Protein-ligand interactions: Discovering potential small-molecule therapies for Alzheimer's disease and investigating the effect of non-natural amino acid incorporation on enzyme-substrate interactions

---

A Dissertation

Presented to

the faculty of the School of Engineering and Applied Sciences

University of Virginia

---

in partial fulfillment

of the requirements for the degree

Doctor of Philosophy

by

H. Edward Wong

August 2015

Defended June 15, 2015

Acknowledgements

This dissertation is dedicated to my mother for her unfailing love. I don't say this enough.

I love you mom.

I would like to thank the following people:

Professor Inchan Kwon, my research advisor, for his guidance, patience and for always challenging me to be my best. I also thank him for opening the door to new opportunities for me. I truly cherish these experiences. It has been an honor to have him as my advisor and look forward to keeping in touch with him.

Professors Michael Shirts, Roseanne Ford, Kyle Lampe, Gordon Laurie, and Michael King for serving on my committee and for providing me with invaluable discussion and insight. I am especially thankful to Professors Michael Shirts and Roseanne Ford for acting as surrogate advisors over the past year. I am grateful to the Chemical Engineering department for the extended financial support and the opportunity to complete my research over the past year and to earn this degree.

My lab mates, Simpson Gregoire, Sung In Lim, Shun Zheng and Jacob Irwin for their support and guidance. It has been a privilege and a humbling experience working with such a talented group of individuals.

Jim Swartz. I cannot thank him enough for taking me under his wings for a short but incredibly formative year in my development as a scientist. It is his poise, patience, and the way he treated everyone with respect and humility that has stayed with me. I also want to graciously thank him for truly believing in me in a time when I wasn't always certain of my own potential.

And last but not least, my family and friends for their love and support. You have helped me navigate through many challenges. You have always given me meaning and purpose. I am blessed to have such good people in my life. And I am especially thankful for my aunt Lin who has always believed in me. I also thank Joe Basconi for not only being a good roommate but a good friend throughout my PhD.

Abstract

Protein-ligand interactions are pivotal and ubiquitous in biological systems. Ligands are small molecules that include therapeutics, substrates, cofactors, inhibitors and many other species that can either influence protein function or be acted upon by a protein. Our research efforts focus on two main areas of study. The first is discovery of potential therapies for treating Alzheimer's disease, directed against amyloid-beta (Aβ) pathology, and the second is developing a better understanding of substrate-enzyme behavior after mutation with genetically encoded non-natural amino acids. Here we describe four works that study protein-ligand interactions.

First, Brilliant Blue G (BBG) was found to be an effective Aβ aggregation modulator and reduces Aβ-associated neurotoxicity by promoting the formation of off-pathway, non-toxic aggregates. Structure-activity analysis between BBG and its three commercially-available analogues (Brilliant Blue R, Brilliant Blue FCF, and Fast Green FCF), revealed that of the group, BBG was the most effective modulator of Aβ aggregation and cytotoxicity, and that its additional methyl groups are important for its enhanced modulating activity. In a follow up study, BBG was also found to disaggregate Aβ40 fibrils.

Second, we found that erythrosine B was able to modulate both Aβ aggregation and Aβ-associated neurotoxicity. Given that this molecule uniquely possesses heavy halogen groups, through structure-function analysis, we demonstrated that halogenation is responsible for the Aβ modulating activities of erythrosine B and its analogues. The specific types, arrangement and placement of the halogen substituents dictated binding attributes, and also the aggregation and cytotocity modulating activity towards Aβ. Analysis by a novel competitive-binding assay with sequence-specific antibodies revealed that erythrosine B and a number of analogues interact with Aβ by binding at its N-terminus.

Third, we discovered that incorporation of 3-(2-naphthyl)-alanine (Nal) at Glu30 in the catalytic domain of murine dihydrofolate reductase (mDHFR) can alter the allosteric cooperativity of the enzyme. Comparison with the closest natural amino acid analogue mutation, Trp at position 30, showed that the behavior promoted by Nal results from its unique size and shape. This is the first report showing that an expanded set of genetically encoded amino acids can alter the cooperativity of an enzyme. Evaluation of enzyme titers also revealed that the altered allosteric cooperative behavior is beneficial to the *E. coli* expression host.

Lastly, we investigated the effects on enzyme function of incorporating Nal, a non-natural amino acid, within the hydrophobic core and solvent-exposed sites of mDHFR. Hydrophobic-core mutants: Through mutational analysis, a computed measure of steric incompatibility was found to have statistically significant monotonic correlations with key kinetic parameters (K_m, k_{cat} and k_{cat}/K_m) of mDHFR. Despite being related structurally, Nal was not an equivalent substitution for Trp and Phe, as it not only caused qualitative secondary structure changes, but also adversely affected catalytic activity, however, without impacting substrate binding. Solvent-exposed-site mutants: Nal, a large hydrophobic residue, could be incorporated at solvent-exposed sites (Phe142 and Phe179) without any adverse affects on the binding (K_m) and catalytic (k_{cat}) components of mDHFR enzymatic function. Results also revealed that structural changes were related to changes in hydrophobicity changes caused by mutation. Statistical analysis revealed that substituting Nal for Glu caused significant deviations in K_m when compared to substitution of Nal at hydrophobic residues by an average of +0.60 μM (Student's t-test, $p < 0.01$). These results demonstrate that mutations that minimize impact to structure can be strategically used to minimize impact on enzyme function.

Table of contents

List of Figures

List of Tables

Chapter 1

Introduction

Preface

The goal of our research is to study the interaction between ligands and proteins. Here, ligand refers to any number of small molecules that can interact with a protein, whether it is a potential small-molecule therapy or an enzyme substrate. This research focuses on two areas where ligands are important to protein function: 1) The discovery and characterization of potential small-molecule therapies for protein aggregation-dependent diseases and 2) the understanding of substrate-enzyme interactions upon incorporation of non-natural amino acids.

Background – Alzheimer's disease, amyloid-beta pathology and therapeutic strategies

Alzheimer's disease

Alzheimer's disease (AD) is the most common form of senile dementia and currently affects roughly 5 million people in the United States (1, 2). It is characterized by the progressive loss of memory, the ability to think, emotional stability and overall cognizance. Ultimately the disease leads to death. In additional to the devastation to the patient, it also carries a heavy emotional and financial burden on loved ones and on society in general. Patients require round-the-clock care during the later stages. And, as the 6th leading cause of death in the United States, nearly $226 billion in direct costs are required annually to treat and care for patients, and to combat the disease (1, 2). While palliative care and symptomatic treatments options are available, a cure or a disease-modifying therapy has yet to be discovered (1, 2). Therefore discovering a cure or a disease-modifying treatment represents a significant and important research challenge.

The hallmarks and driving force of Alzheimer's disease

Diagnosis of the disease is often made by evaluating a patient's emotional, behavioral and cognitive state. A definitive diagnosis, however, requires postmortem biopsy of brain tissue. Although the fundamental cause of AD is still being elucidated, through this procedure, researchers have discovered that atrophy of the brain, and the development of lesions, consisting of amyloid-beta (Aβ) extracellular plaques and *tau* neurofibrillar tangles are hallmarks of the disease (3-5).

Both *tau* and Aβ have natural activities in healthy brain tissue. Aβ activates kinase enzymes (phosphorylation) and acts as a transcription factor, and *tau* stabilizes microtubules for axonal structure and transport (6, 7). However when aggregated, Aβ and hyperphosphorylated *tau* are each cytotoxic and provide a substantial driving force in disease progression. While both Aβ and *tau* have a strong correlation with disease, it is common to find Aβ deposits absent of *tau* tangles (8). But most importantly, Aβ deposits can promote the formation of *tau* neurofibrillar tangles (9-11). And *tau* pathology is considered to occur downstream of Aβ pathology (9-11). Therefore, Aβ represents a particularly important target for therapeutic research (12).

Generation of Aβ

Aβ is produced by the sequential proteolysis of the amyloid precursor protein (APP) by beta and gamma secretase. And depending on the cleavage location, this process forms a number of Aβ isoforms varying in length from 39 to 43 residues (13). The two most common isoforms found in extracellular plaques consist of 40 and 42 residues and are denoted as Aβ40 and Aβ42, respectively. Aβ40 is the most prominent and is nine times more physiologically prevalent in plaques than Aβ42 (14, 15). However, Aβ42 is known to be more toxic and aggregation prone

(14). The toxicity of both Aβ40 and Aβ42 arises from their aggregation propensity towards a fibrillar structure (16-23). And the intermediate conformers that are formed during this pathway are acutely toxic and cause a cascade of biological responses that lead to their associated toxicity and the formation of brain lesions (16-18, 24-29).

Therapeutic strategies

While Aβ production is a naturally occurring process that stays relatively constant throughout an individual's life, AD is associated with an impairment of Aβ clearance from the brain (30, 31). This impairment leads to an accumulation of Aβ which promotes an environment that facilitates the aggregation process (31). Since Aβ is not required for normal function in animal models, a number of strategies have focused on minimizing Aβ load in the brain by reducing the rate of production and/or increasing its rate of clearance (27). These strategies commonly mediate peripheral biological entities that process Aβ or APP. Inhibitors have been developed to minimize the activity of beta and/or gamma secretase, which is effective at reducing the Aβ burden in brain tissue (32, 33). However, this approach also confers side effects as the inhibitors often lack target specificity and also block the activity of the secretases for contiguous biological targets (1). Research for improving Aβ clearance has focused on eliminating microglial dysfunction and/or enhancing proteasome-mediated degradation (34-36). Peptide immunization has been investigated as a means of controlling Aβ levels (37-40). However, incidences of meningoencephalitis have occurred, and pivotal human trials have been halted (40). Because Aβ undergoes various conformational changes through toxic intermediates, a promising therapeutic strategy is to modulate the aggregation process itself.

Amyloid-beta aggregation

Aβ is generated as a monomer with a random amorphous structure. Aggregation occurs by two proposed pathways (41). Unstructured Aβ monomers can associate to form amorphous globular oligomers. These oligomers are transient conformers that can reconfigure to form protofibrils or prefibrils. Monomers can also associate through a seeding mechanism, where individual monomers first transition to a β-turn/β-strand seeding structure that propogates aggregation (17, 23, 41-49). The β-turn/β-strand conformational transition in either the monomer or oligomers is required to proceed to fibrillar species. And this transition is considered a rate limiting step in fibril formation (41, 49, 50).

The hydrophobic effect is a key driving force in the formation of the β-turn in the monomeric unit which brings together the two hydrophobic regions of Aβ (25). The turn region is also further stabilized by the formation of a salt bridge between Asp23 and Lys28. His13 to Lys16 also plays important roles for oligomerization and fibril propagation (25, 51). Once the β-turn motif is formed, subunits self-associate in an anti-parallel manner to produce protofibrils that resemble a β-sheet zipper (25). The mature fibrils that are predominant in plaques are generated by the longitudinal intertwining of protofibrils (51-54). Each of these species in the pathway can be differentiated using microscopy techniques and/or by employing antibodies and small molecules, such at thioflavin T and Congo red, that preferentially recognize specific substructures (55-57). While the propensity of Aβ is to form fibrils ("on-pathway"), in vitro studies have also shown that "off-pathway" species can also be formed depending on the environmental conditions, which indicates that the aggregation process can indeed be modulated (27, 58).

Modulating amyloid-beta aggregation

The change between different aggregation conformations is controlled by high energy transition states. Potential therapies, that modulate Aβ aggregation, exploit the energy landscape, such that by binding, they lower the activation barrier between different conformations or by stabilizing particular aggregation states (24, 27, 59, 60). Ultimately, the goal is to inhibit the formation of acutely toxic aggregates, or to prevent their formation entirely. To this end, research efforts have focused on antibodies and small-molecules.

Antibodies

Antibodies represent a promising approach to controlling Aβ aggregation. They have been shown to both bind and interact with various Aβ aggregate conformations. These antibodies can prevent Aβ aggregation in vitro and are used as detection agents for various aggregate conformers (61-65). However, their general inability to pass through the blood-brain barrier (BBB) has been a major obstacle in their adoption as potential therapeutic agents (66). However, a number of advancements have been made in this area. Recently, a chimeric human-murine low-affinity antibody was developed against the transferrin receptor (TfR). Normally, the wild-type antibody binds to TfR and is then transported across the BBB. The wild-type form, however, has only modest brain uptake, due to its retention at the receptor. But the low affinity mutant exhibited increased brain uptake (67, 68). As proof-of-concept, the mutant anti-TfR was then coupled with a secondary antibody to form a bispecific unit. The mutant anti-TfR was shown to facilitate brain uptake of the secondary antibody (67, 68). However, while antibodies are very promising, their potential immunogenicity still remains an obstacle that could prevent their broad use (27, 69).

Small-Molecules

Due to the immunogenicity concerns with antibodies, small-molecules are particularly promising for further research since they do not have this issue. The identification of potential disease-modifying compounds has focused on groups of molecules with favorable biological compatibility and attributes. These include ones that are antioxidant, anti-inflammatory, FDA-approved, and/or permeable to the blood-brain barrier (27).

Polyphenols

Polyphenols are a highly attractive group of antioxidants (70). Since Aβ toxicity is mediated by the accumulation of hydrogen peroxide and lipid peroxides within cells, polyphenols can potentially counteract this effect (27, 70, 71). Just as importantly, polyphenols are particularly amenable for interacting with Aβ directly. These molecules are found in what are considered antioxidant-rich foods such as green tea, blueberries, red grapes, turmeric, amongst others.

Curcumin was one of the earliest polyphenols studied capable of mediating Aβ and AD symptoms. Curcumin is a yellow curry pigment found in turmeric, which has anti-inflammatory and antioxidant properties thought to be beneficial for treatment and prevention of AD (70). It was found to be a potent modulator of Aβ aggregation. In vitro it inhibited aggregation, and disaggregated Aβ40 fibrils at submicromolar concentrations. It was also able to inhibit Aβ42 oligomer formation at similar concentrations (72, 73). Studies have also shown that the geometry and separation of aromatic moieties within the molecule facilitates its binding to Aβ (74). When applied to AD and Tg2576 mouse brain sections, curcumin preferentially labeled plaque regions.

Moreover, upon oral administration to advanced-stage Tg2576 mice, curcumin not only labeled plaques, but also lowered overall Aβ and plaque burden in brain tissue (73). Currently, curcumin is undergoing phase 2 clinical trials for mild-to-moderate AD, to determine its efficacy towards improving cognitive performance and lowering human brain Aβ loads (75, 76).

Soon after discovery of the benefits of curcumin, researchers continued to focus their search for novel disease-modifying compounds in antioxidant-rich foods (70, 77). When red wine consumption was linked to reduced AD risk, growing interest developed around resveratrol, the primary polyphenolic antioxidant constituent in grapes and red wine (77-79). Resveratrol was shown to inhibit Aβ42 fibril formation and cytotoxicity however it was unable to prevent oligomer formation (80-82). Nonetheless, it was able to restructure Aβ fibrils and oligomers into soluble non-toxic, off-pathway oligomers. It was also found to have varying binding affinity between the monomer and fibrillar Aβ states and the interaction differed between Aβ40 and Aβ42 (80, 82, 83). Resveratrol also mitigated Aβ cytotoxicity and markedly lowered levels of secreted intracellular Aβ from different cell lines, by enhancing degradation rates through a mechanism that involves the proteasome (84, 85). However, it did not reduce the rates of Aβ production or APP processing, as it did not interact with beta or gamma secretase (84, 85). In mouse models, oral administration of resveratrol was found to reduce brain plaque burdens with the most significant improvements occurring in the cortex (-48%), striatum (-89%) and hypothalamus (-90%). Resveratrol and its immediate metabolites, however, were not detectable in the brain (86). Currently, resveratrol is under phase 3 clinical trials for AD and in phase 4 clinical trials for Mild Cognitive Impairment (83, 87, 88).

As the popularity of polyphenols increased, one of the more recent additions to the set of Aβ-modifying molecules is (–)-epigallocatechin gallate (EGCG) (89, 90). EGCG interacts with

unfolded Aβ monomer and promotes the formation of non-toxic off-pathway oligomers. This interaction also extends to the ability to inhibit Aβ and alpha-synuclein fibrillogenesis. EGCG can also restructure mature Aβ and alpha-synuclein fibrils into amorphous aggregates that are non-toxic to mammalian cell models (89, 90). Studies into the mechanism, also found that EGCG preferentially binds β-sheet-rich aggregates which provides the driving force for the conformational changes; however without disassociating them into monomer or smaller aggregates (89-91). EGCG also promoted a number of auspicious biological responses when applied in vivo. EGCG inhibited Aβ42-induced neuronal cell apoptosis (92). In Swedish APP mutant murine neuron-like cells and APP-over-expressing Tg2576 mouse primary neurons, EGCG reduced Aβ generation by enhancing α-secretase activity which promoted the formation of soluble APP N- and C-terminus fragments (93). EGCG was also able to enhance the memory and α-secretase activity in the presenilin-2 AD mouse model (93, 94). Currently, EGCG is in phase 2/3 clinical trials to evaluate whether it slows development of AD-like symptoms and biomarkers in Down's syndrome patients, such as the early formation of Aβ plaques (95, 96).

Congo red

In addition to the polyphenols, a number of novel compounds have been discovered that can modulate Aβ aggregation and its cytotoxicity. One of the first of these molecules was Congo Red (97). While it has not been pursued as a potential therapeutic, it has been studied fairly extensively to understand how small molecule modulators interact with Aβ. In particular, Congo red is commonly used to label Aβ plaques and fibrils (55, 98-100).

It has been shown that Congo red inhibits fibril formation and promotes oligomer formation. It also has the ability to disaggregate Aβ40 fibrils. Congo red binds preferentially

within the grooves of β-pleated sheets in amyloid structures (101, 102). And in particular, NMR studies have shown that it binds to residues 14-26 and 31-37 in Aβ which correspond to the hydrophobic regions (103).

Research objectives and significance

To date, small-molecules have provided the most substantial advancements towards finding a disease-modifying treatment for AD; small-molecule drug candidates are the significant majority in phase 3 and phase 4 clinical trials. Therefore, greater research efforts are needed in small-molecules to identify and to characterize potential disease-modifying treatments for AD.

Therefore, our research focuses on identifying small-molecules that can modulate Aβ pathology. Our goal is to diversify the current set of small-molecule modulators as well as to understand how these small molecules interact with Aβ directly. In particular we are interested in compounds, especially dyes, with high biocompatibility and biological safety profiles that are capable of modulating both Aβ aggregation and cytotoxicity. Initial studies have identified Brilliant Blue G (BB) as being capable of modulating with Aβ. Therefore, we would like to characterize BBG further. Thus the objectives for this research are as follows:

1. **Determine whether Brilliant Blue G is an effective modulator of Aβ aggregation and cytotoxicity.**

2. **Employ structure-activity analysis using a panel of Brilliant Blue G analogues to determine whether certain structural features are important for Aβ modulating activity.**

Recently, we identified erythrosine B, which is approved for human consumption, and which has been shown to modulate both Aβ aggregation and its associated cytotoxicity. Erythrosine B is a unique Aβ modulator in that it possess heavy halogen atoms on its benzoate and xanthene constituents (104). We hypothesize that halogenation is responsible for the modulating activity of erythrosine B. Thus the objectives for this research are as follows:

3. **Employ structure-activity analysis using a panel of erythrosine B analogues to determine whether halogenation generates effective modulators of Aβ aggregation and cytotoxicity.**

4. **Provide insight into the binding interaction between erythrosine B analogues and Aβ.**

We believe that our research will provide insight into how BBG and ERB and their analogues interact with Aβ. These insights will help in the identification, development, and possible engineering of other potential small-molecules as disease-modifying therapies for AD.

Background – Non-natural amino acids and applications

The genetic code

There are 64 potential three-nucleotide codon combinations that can encode for an amino acid. The 20 natural amino acids are encoded by 61 degenerate codons, meaning that certain amino acids are redundantly encoded. And three codons (TAG, amber; TAA, orchre; and TGA, opal) are used to stop protein translation. In order to add a new amino acid to the genetic code, a specific codon that is unique to the new amino acid is required. This means that the 61 codons that encode the canonical amino acids are not ideal for this purpose (105-108). Therefore, the amber stop codon (a rare stop codon) and four-nucleotide codons have been used as target sites for site-specific non-natural amino acid incorporation (109-113). Non-natural amino acids were first incorporated in vitro (114). To accomplish this, the desired non-natural acid was aminoacylated to the amber suppressor tRNA by the appropriate aminoacyl-tRNA synthetase for the non-natural amino acid (115). The aminoacyl-tRNA containing the non-natural amino acid is then added to an *E.coli* cell-free expression system, which contains all of the endogenous translational machinery and an expression vector containing the gene of interest with the TAG mutation at the target site (114). During translation, the non-natural amino acid is incorporated at the target amber stop codon.

Expanding the genetic code of *E. coli*

To accomplish the same feat in vivo, within *E. coli*, additional translational machinery is needed to allow the aminoacylation step to occur inside the cell. Therefore, a functional aaRS/tRNA pair that is specific to the non-natural amino acid and that is orthogonal to the endogenous aaRA/tRNA machinery is required (105-107, 115). Orthogonal aaRS/tRNA pairs are

adopted from other organisms. Pairs from different organisms can have unique recognition units that prevent cross-talk (orthogonality). Through in vitro incorporation studies, a *Methanocaldococcus jannaschii* tyrosyl aaRS/tRNA pair (*Mj*TyrRS/ MjtRNA^{Tyr}) was the first set discovered to be orthoganol to of the endogenous aaRS/tRNA machinery in *E.coli* (115). An engineered tyrosyl tRNA synthetase and cognate nonsense suppressor tRNA (*Mj*TyrRS/ *M*jtRNA$^{Tyr}_{CUA}$) was evolved from this pair. First the anticodon of *Mj*tRNA^{Tyr} was mutated to CUA to create an amber suppressor tRNA (*Mj*tRNA$^{Tyr}_{CUA}$). In order to alter the specificity *Mj*TyrRS for the desired non-natural amino acid, *Mj*TyrRS was evolved through successive rounds of mutational selection. Pairs that could suppress the amber codon were positively selected in the first round (107). In the second round, pairs that were cognate to canonical amino acid were negatively selected. This approach has been generalized for evolving other heterologous orthogonal aaRS/tRNA pairs for site-specific non-natural amino acid incorporation (107, 114, 116, 117).

Expanding the genetic code of eukaryotes

The general technique described above was also used to expand the genetic code of eukaryotes. *Saccharomyces cerevisiae* was the first to have its genetic code expanded to include non-natural amino acids (118-120). The tyrosyl aaRS/tRNA pair from *E. coli* was found to be orthogonal in *S. cerevisiae* and has become a prime engineering candidate to broaden the number of non-natural amino acid for incorporation (118, 119). Non-natural amino acids have since been incorporated in *Bacillus stearothermophilus* and Chinese hamster ovary cells, 293T, and primary neuron cells (107, 111, 117, 121, 122).

Advances of in vivo non-natural amino acid incorporation

A number of advancements in non-natural amino acid incorporation technology have been aimed at improving the expression yield of proteins within which they are contained. Because the amber codon is commonly used, often what limits expression efficiency is competition between release factor 1 and the amber suppressor tRNA ($tRNA_{CUA}$) for the target amber codon. A successful strategy to increase the efficiency of amber suppression is improving the expression or overexpression of $tRNA_{CUA}$ by using host-optimized promoters or multiple copies of the $tRNA_{CUA}$ gene in a single expression construct, respectively (123, 124). These approaches help $tRNA_{CUA}$ to stoichiometrically out-compete release factor 1 for the target amber codon.

Other approaches have looked at altering the incorporation machinery itself. Along these lines, the T and acceptor stem of Mj-tyr-$tRNA_{CUA}$ has been evolved for higher amber suppression efficiency (125). Another example is an orthogonal *E.coli* ribosome that was engineered to have lower activity towards release factor 1, which reduces incidences of premature translation termination (107).

Expression titers have also been increased by genetically altering the expression hosts. Recently a mutant *E.coli* MG1655 expression strain was developed in which all instances of release factor 1 are deleted (126-128). This minimizes any competition that $tRNA_{CUA}$ might have for the amber codon, and allows the non-natural amino acid to be uniquely encoded by the TAG codon. Misacylation of $tRNA_{CUA}$ can also prevent optimal expression yields (129, 130). An auxotrophic *E.coli* expression strain, AFWK (Phe/Trp/Lys auxotroph) has been developed to minimize rates of misacylation of endogenous amino acids that are analogues of non-natural amino acids (131, 132). In addition to improving expression titers, advancements have also been

made towards directed evolution of proteins using non-natural amino acids (133). As a precursor, non-natural amino acids have been applied to phage display selection methods (134).

Applications of site-specific non-natural amino acid incorporation

To date, the application of nAA has focused on providing additional functionality to a target protein that was not possible with natural amino acids. This review focuses on site-specific non-natural amino acid incorporation, which is highly tunable to protein engineering applications (107, 135-138).

One of the first applications of site-specifically incorporated non-natural amino acids was to probe the structure and function of proteins. For this particular application, subtle mutational changes are often required to elucidate the role of a particular amino acid, that site-directed mutagenesis with canonical amino acids often cannot provide. In a compelling example, photoaffinity had shown that up to 9 tyrosine and tryptophan residues of the nicotinic acetylcholine receptor were involved in agonist binding. Their particular roles, however, were unknown (139). Probing these tyrosines with a set of non-natural amino acids revealed that Trp149 of α-subunit was critical for agonist binding involving cation-pi interaction. Since fluorine has an additive effect on cation-pi interaction, further mutation of the Tr149 with fluorinated tryptophan analogues, revealed that the strength of the cation-pi interaction could be manipulated linearly based on the number of fluorine moieties (139).

Fluorinated non-natural amino acids can be used for nuclear magnetic resonance due to the high magnetiogyric ratio of ^{19}F. The ^{19}F-amino acid, trifluoromethyl-L-phenylalanine was site-specifically incorporated and was used as an NMR probe to characterize the protein structure and function of nitroreductase (NTR) and histidinol dehydrogenase (HDH) (140).

Another application of non-natural amino acids has been the rational engineering of the spectral properties of fluorescent proteins. Green fluorescent protein (GFP) contains a unique chromophore consisting of three residues (residues 65-67) (141). The overall β-barrel structure of GFP acts to protect the chromophore from solvent and mediates the electronic interaction between the chromophore and a number of functional residues (141, 142). Endeavors to engineer GFP for different spectral properties, often focuses on mutating the components of the chromophore to analogous residues. For instance mutation of Tyr66 to histidine and tryptophan resulted in a spectral emissions shift from green to blue and cyan, respectively (143, 144). These results indicated that Tyr66 was particularly attractive for site-specifically incorporating a set of tyrosine, phenylalanine and tryptophan analogues. When Tyr66 was replaced with these analogues (p-amino-L-phenylalanine, p-methoxy-L-phenylalanine, p-iodo-L-phenylalanine, p-bromo-L-phenylalanine, and L-3-(2-naphthyl)-alanine), shifts in the fluorescence emissions wavelength were observed and they corresponded to the strength of each non-natural amino acid as an electron-donor (145, 146). This work demonstrates that non-natural amino acids can be used to tailor the properties of proteins, in this particular case, the spectral properties of GFP.

Because a number of non-natural amino acids contain reactive moieties, they can be used for bioconjugation. While the canonical amino acids, lysine, histidine and cysteine, can be used for this purpose, their abundance and prevalence in proteins often results in a lack of target selectivity which yields heterogeneity or non-specific conjugation in the end-product. The protein N- and C-terminus can also be employed as bioconjugation sites. However, these locations are often less than optimal (147, 148). The use of reactive non-natural amino acids overcomes these two major limitations when using the canonical amino acids as conjugation sites. Non-natural amino acids can be site-specifically incorporated, which allows precise

targeting as well as control over the number of conjugation sites (149, 150). Non-natural amino acids can possess three reactive components, terminal ketones, azides, and alkynes, which can be bioorthogonally conjugated by dehydration, Staudinger ligation, or variations of the Huisgen cycloaddition (151-161). Recently, *p*-ethynylphenylalanine and *p*-azido-phenylalanine were used as bioconjugate target proteins to either a functionalized fatty-acid chain or to albumin through a functionalized linker at solvent-accessible sites (152, 162). In both cases, each of the modified proteins had a significantly improved blood circulation half-life. Earlier work has also shown that *p*-azido-phenylalanine can also be used for site-specific glycosylation and PEGylation (163-165). Bioconjugation using genetically encoded non-natural has also been applied to antibody-drug conjugates. *p*-Acetylphenylalanine was site-specifically incorporated into an anti-Her2 antibody fragment and IgG in *E.coli* and mammalian cells, respectively. The target proteins were then conjugated to an auristatin derivative which yielded conjugates that exhibited excellent pharmacokinetics, potent in vitro cytotoxic activity towards Her2-positive cancer cells, and complete tumor regression in treatment models (166, 167).

Non-natural amino acids have also been employed to improve the existing function of enzymes beyond what is possible with the canonical amino acids. NTR-CB1954 is an enzyme-prodrug combination being developed for cancer gene therapy. CB1954 is activated into a cytotoxic form by NTR, in NTR-producing cells. Efforts have been made to improve the ability of NTR to activate CB1954 (168). In particular, the active site Phe124 has been identified as being crucial to NTR function. When mutated with the entire spectrum of canonical amino acids, position 124 was determined to be the most sensitive to mutation, with the F124K mutation was the most active towards CB1954 (168). To determine whether non-natural amino acids could better these results, a panel of Phe analogues was systematically site-specifically incorporated to

replace Phe124. Results showed that *p*-aminophenylalanine was able to improve activity compared to F124K, while *p*-nitrophenylalanine was able to increase the activity of nitroreductase two-fold over that of F124K (169). Recently, efforts have also been made to alter the activity and regioselectivity of the CYP450 family of enzymes which are terminal oxidases in electron transfer chains and have a broad range of substrate targets. Four aromatic unnatural amino acids were incorporated at 11 active-site positions of a catalytically promiscuous CYP102A1. These mutations resulted in significant shifts in regioselectivity, especially for the incorporation of *p*-acetyl-phenylalanine at sites near the heme cofactor. Furthermore, catalytic activity enhancements were also observed with active-site substitutions involving *p*-amino-phenylalanine. And these functional changes could not be reproduced with any of the 20 canonical amino acids (170).

Our group has also been improving and altering the catalytic function of enzymes using non-natural amino acids targeted at the active site. In particular we were able to alter the methotrexate (MTX) inhibition of murine dihydrofolate reductase (mDHFR) by incorporating *p*-bromo-phenylalanine (pBrF) and 3-(2-naphthyl)-alanine (NAl) at Phe31 in the active site. The pBrF mutation was shown to preferentially disrupt MTX binding over that of substrate. Further characterization of the Nal mutation also revealed that it enhanced the specificity of mDHFR for a normally less favorable substrate folic acid (171).

Research objectives and significance

The objectives of our current research efforts are 1) to find new ways that non-natural amino acids can be used to alter or improve enzyme function, and 2) to understand how non-natural amino acids can be incorporated into enzymes in order to maintain function.

Recently, we have identified that mutation of Glu30 with Nal appears to alter the cooperativity of mDHFR. Our specific aims for the first project are as follows:

5. **Determine whether the mutation of Glu30 to 3-(2-naphthyl)-alanine (Nal) alters the catalytic allosteric cooperativity of mDHFR.**

6. **Determine whether the change in allosteric cooperativity of mDHFR that is imparted by the Glu30 to Nal mutation can be replicated with the most similar natural amino acid mutation of Glu30 to Trp.**

If the specific aims can be successfully completed, to our knowledge, this will be the first report demonstrating that mutation with an expanded set of genetically encoded amino acids can alter the catalytic allosteric cooperativity of an enzyme. As the number of biocatalysts increase in number, this research could provide a new method to alter the regulation mechanism of enzymes, and enhance our ability to control how enzymes function alone, and in networks.

For our second objective, we would like to determine how non-natural amino acids can be incorporated into enzymes while maintaining function. The specific aims for this project are as follows:

7. **Investigate how the incorporation of Nal in the hydrophobic core affects the enzymatic function of mDHFR.**

8. **Investigate how the incorporation of Nal in solvent-exposed regions affects the enzymatic function of mDHFR.**

Predicting how mutations affect enzyme function is very difficult. Through this research we hope to establish principles or strategies for mutating hydrophobic core and solvent-exposed sites for maintaining function. This research would greatly improve the accessibility and utility of non-natural amino acids, while improving our understanding of how mutations can made permissively.

Part 1

The discovery, development, and characterization of potential small-molecule therapies for Alzheimer's disease

Chapter 2

A safe, blood-brain barrier permeable triphenylmethane dye inhibits amyloid-beta neurotoxicity by generating non-toxic oligomers

Sections of this chapter contain excerpts from the following publications.

1. **Wong HE**, Qi W, Choi H-M, Fernandez EJ, & Kwon I (2011) A Safe, Blood-Brain Barrier Permeable Triphenylmethane Dye Inhibits Amyloid-β Neurotoxicity by Generating Nontoxic Aggregates. Acs Chemical Neuroscience 2(11):645-657

2. Irwin JA, **Wong HE**, & Kwon I (2013) Different Fates of Alzheimer's Disease Amyloid-beta Fibrils Remodeled by Biocompatible Small Molecules. Biomacromolecules 14(1):264-274.

Abstract

Growing evidence suggests that on-pathway amyloid-beta (Aβ) oligomers are the primary neurotoxic species and directly correlate with the onset of Alzheimer's disease (AD). One promising therapeutic strategy to block disease progression is to reduce levels of these neurotoxic Aβ species using small molecules. While several compounds have been shown to modulate Aβ aggregation, compounds with such activity combined with safety and high blood-brain barrier (BBB) permeability have yet to be reported. Brilliant Blue G (BBG) is a close structural analog of a Food and Drug Administration (FDA)-approved food dye and has recently garnered prominent attention as a potential drug to treat spinal cord injury due to its neuroprotective effects combined with BBB permeability and high degree of safety. In this work, we demonstrate that BBG is an effective Aβ aggregation modulator, that it reduces Aβ-associated cytotoxicity in a dose-dependent manner, and that it acts by promoting the formation of off-pathway, non-toxic aggregates. Comparative studies of BBG and three structural analogs, brilliant blue R (BBR), brilliant blue FCF (BBF) and fast green FCF (FGF), revealed that BBG is most effective, BBR is moderately effective, and BBF and FGF are least effective in modulating Aβ aggregation and cytotoxicity. Therefore, the two additional methyl groups of BBG and other structural differences between the congeners are important in the interaction of BBG with Aβ leading to formation of non-toxic Aβ aggregates. Our findings support the hypothesis that generation of non-toxic oligomers using small molecule modulators is an effective strategy to reduce Aβ cytotoxicity. Furthermore, key structural features of BBG identified through structure-function studies open new avenues into therapeutic design for combating AD.

Introduction

With an ever increasing number of new cases each year, Alzheimer's disease (AD) has become the most common form of senile dementia. The disease is primarily diagnosed in persons over the age of 65 (172). Symptoms manifest in a slow and progressive manner, but are ultimately debilitating and fatal. Currently, 5.3 million people in U.S. are affected by AD, with the number projected to rise to 13.5 million by 2050 (173). Although several U.S. Food and Drug Administration (FDA)-approved drugs temporarily reduce symptoms, no treatment exists that slows or stops progression of AD.

A pathological hallmark of AD is the accumulation of insoluble protein aggregates, composed primarily of neurotoxic amyloid-beta (Aβ). Aβ is created from sequential proteolytic cleavage of the amyloid precursor protein (APP) by the β- and γ-secretases (174). Although a number of Aβ isoforms, with lengths from 39 to 43 residues are generated, Aβ40 and Aβ42 are the most physiologically relevant forms. In AD patients, Aβ40 and Aβ42 are found in approximately a 9:1 ratio, but Aβ42 is more aggregation-prone (14).

According to the original amyloid-cascade hypothesis, conversion of soluble Aβ monomers into insoluble fibrils causes AD onset (175). Recently the amyloid-cascade hypothesis has been further refined. Growing evidence suggests that certain types of soluble Aβ oligomers are more toxic than Aβ fibrils, and their presence correlates strongly with dementia (29, 80, 176, 177). Therefore, reduction of neurotoxic Aβ oligomers represents a promising strategy to inhibit Aβ-associated neurotoxicity.

Numerous small molecules have been studied for their ability to modulate Aβ aggregation and reduce neurotoxicity (41, 178-180). Congo red, an amyloid-structure specific dye, has the ability to modulate fibril formation and reduce neurotoxicity of Aβ (101-103, 181,

182) Besides amyloid-specific dyes, several lipid-based modulators and polyphenols, such as scyllo-inocitol, nordihydroguaiaretic acid, curcumin, epigallocatechin gallate (EGCG) and resveratrol, have been reported to modulate Aβ aggregation and reduce Aβ-associated toxicity (73, 74, 89, 178, 183-186). Although the results from these molecules are encouraging and validate Aβ aggregation modulation as a promising strategy, a practical and effective therapeutic has yet to be identified. Most of small molecule modulators of Aβ aggregation identified are not suitable for AD therapeutic leads because they lack low toxicity or blood-brain barrier (BBB) permeability. Crossing blood-brain barrier is a big challenge in AD drug development; 98% of small molecule drugs and almost 100% of large molecule drugs cannot cross the BBB (187). For example, therapeutic application of Congo red has been hindered by poor blood-brain barrier (BBB) permeability as well as carcinogenicity (97). Although several polyphenol-based Aβ modulators including tannic acid and EGCG are very effective in reducing Aβ neurotoxicity in cell-based assays (89, 188), tannic acid or EGCG do not cross the animal BBB or the human BBB, respectively (189-191). As a result, there remains a strong driving force to identify new small molecule AD therapeutic candidates that modulate Aβ aggregation and are also safe and BBB-permeable.

In this article, we identify a new Aβ modulator with all of these properties. To our knowledge, Aβ modulating capacities of triphenylmethane dyes have not yet been reported. Here we show that brilliant blue G (BBG), a triphenylmethane dye with a demonstrated safety profile (192) and BBB-permeability (193), also substantially removes Aβ cytotoxicity even at below stoichiometric concentration. Brilliant Blue FCF (BBF) is approved by the U.S. Food and Drug Administration (FDA) as a blue food dye and has one of the highest safety profiles amongst the seven currently approved synthetic food dyes. In tests, it exhibited no observable toxicity up to a

daily consumption of 600 mg/kg body mass in healthy animals (194). In the United States, more than six thousand pounds of BBF is produced annually, and daily intake of up to 12.5 mg/kg is tolerable in humans (195). A close structural analog of BBF, Brilliant Blue G (BBG), also has low toxicity and highly favorable biocompatibility, but additionally possesses the ability to cross the blood-brain barrier (Figure 2.1) (192, 193). BBG has recently garnered prominent attention in neuroscience regarding its therapeutic potential to treat acute spinal cord injury. In animal models, systemic administration of BBG reduced damage and expedited recovery after spinal cord injury (193). BBG also confers neuroprotection to the brain by inhibiting adverse inflammatory reactions and mitigating multiple sclerosis symptoms (196, 197). With the possibility for systemic administration into the nervous system with no known adverse side effects, BBG is an attractive candidate Aβ aggregation modulator.

In this article, we explore BBG's ability to modulate Aβ aggregation and reduce neurotoxicity with biochemical, biophysical, and cell-based assays. In particular, we monitored Aβ oligomer formation via immunoblotting using Aβ-conformation specific antibody, A11. Polyclonal A11 antibody reacts with soluble Aβ oligomers, including neurotoxic oligomeric conformers, but not with Aβ monomers and fibrils (20, 80, 198). We report that BBG promotes Aβ monomer conversions into non-toxic aggregates. To begin to identify the structural features of BBG responsible for this activity, we also evaluated the modulating capacities of three close structural analogs of BBG, brilliant blue R (BBR), BBF, and fast green FCF (FGF) on Aβ aggregation and cytotoxicity. Our findings suggest that the structural differences of BBG and BBR from BBF and FGF and two additional methyl groups attached to the triphenylmethane structure of BBG are important for effective modulation of Aβ aggregation and cytotoxicity. Unique interaction modes on Aβ of BBG and BBR are expected to provide a new insight on

molecular mechanism of Aβ aggregation and cytotoxicity. Our findings validate a relatively new hypothesis that generation of non-toxic Aβ oligomers by small molecules is an effective way to reduce Ab-associated neurotoxicity even without preventing Aβ oligomer formation (89, 188). Thus, our work provides evidence of and mechanistic details of reduced Aβ-associated neurotoxicity for a novel type of Aβ aggregation inhibitor that also has encouraging attributes as a therapeutic lead compound.

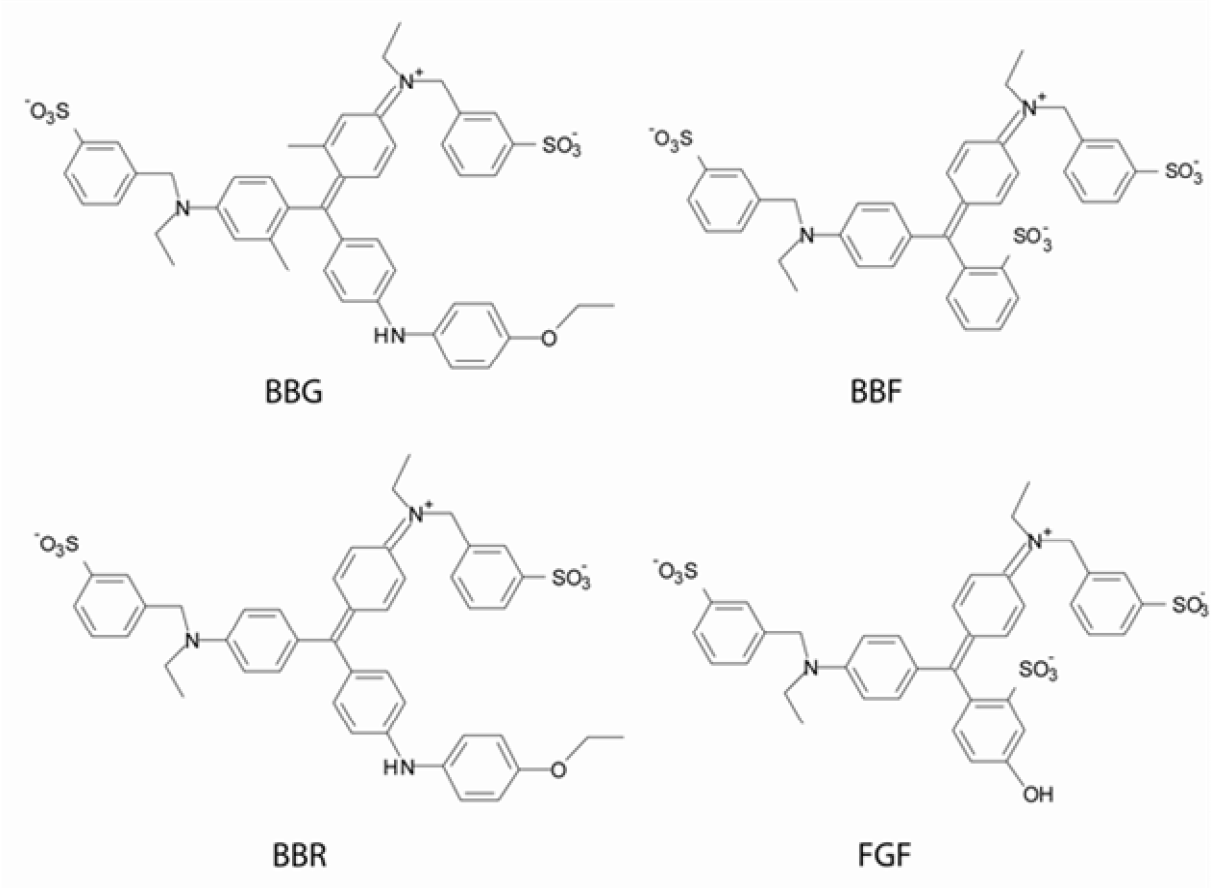

Figure 2.1. Chemical structures of Brilliant Blue G (BBG), Brilliant Blue FCF (BBF), Brilliant Blue R (BBR), and Fast Green FCF (FGF) at neutral pH.

Materials and methods

Materials

Aβ40 was purchased from Anaspec, Inc. (Fremont, CA). Human neuroblastoma SH-SY5Y cells were obtained from ATCC (Manassas, VA). Polyclonal A11 anti-oligomer and horseradish peroxidase (HRP)-conjugated anti-rabbit IgG antibodies were obtained from Invitrogen (Carlsbad, CA). 4G8 antibody was obtained from Abcam (Cambridge, MA). Monoclonal 6E10 was obtained from Millipore (Billerica, MA). ECL advance chemi-luminescence kit was obtained from GE Healthcare Life Sciences. All other chemicals were obtained from Sigma-Aldrich (St. Louis, MO) unless otherwise noted.

Aβ Sample Preparation

Aβ40 samples were prepared as described earlier (199-201). Aβ40 was dissolved in 0.1 % triflouroacetic acid (TFA) to obtain a 1.0 mM stock solution, which was then incubated for 1 hour at room temperature without agitation. The freshly prepared 1.0 mM stock Aβ40 solution was diluted with phosphate buffered saline (PBS) solution (10 mM NaH_2PO_4 and 150 mM NaCl at pH 7.4) to obtain a 50 μM Aβ solution. 50 μM Aβ samples were then incubated at 37 °C for the desired time.

Dot blotting

2 μL Aβ40 samples were spotted onto a nitrocellulose membrane and were allowed to dry at room temperature. The nitrocellulose membrane was incubated in 5 % skim milk dissolved in 0.1 % Tween 20, Tris-buffered saline (TBS-T) solution for one hour. The 5% milk TBS-T solution was removed and the membrane was washed three times for 5 minutes each with

TBS-T solution. The membrane was then incubated in antibody solution for 1 hour. The 4G8, A11 and 6E10 antibodies were diluted in 0.5 % milk TBS-T solution according to the manufacturer's recommendation. After incubation the membrane was washed three times for 5 minutes using TBS-T solution. When a peroxidase (HRP)-conjugated antibody (4G8) was used as the primary antibody, membranes were coated with 2 mL of detection agent from the ECL Advance Detection Kit (GE Healthcare, Waukesha, WI) and the fluorescence was visualized. Otherwise, the membrane was incubated in (1:5000 dilution in 0.5% milk TBS-T) HRP-conjugated IgG for one hour. Then the membrane was washed three times for 5 minutes each with TBS-T solution and the same detection method as previously described was used. The blot images were captured using a BioSpectrum imaging system (UVP, Upland, CA).

Thioflavin T (ThT) Fluorescence Assay

5 μL of 50 μM Aβ40 sample solution was diluted in 250 μL of 10 μM ThT (dissolved in PBS) in 96-well plates. The resulting ThT fluorescence of Aβ sample was measured at an emission wavelength of 485 nm using an excitation wavelength of 450 nm using a Synergy 4 UV-Vis/fluorescence multi-mode microplate reader (Biotek, Winooski, VT).

Transmission Electron Microscopy (TEM)

10 μL Aβ sample was adsorbed onto a formvar mesh grid for 1 min. The grids were then negatively stained with 2 % uranyl acetate for 45 sec., blotted dry and viewed on a Jeol JEM1230 Transmission Electron Microscope at the Advanced Microscopy Laboratory at the University of Virginia operated at 80 kV.

Cytotoxicity Assay

50 mg of 3-(4,5-Dimethylthiazol-2-yl)-2,5-diphenyltetrazolium bromide (MTT) obtained from Millipore (Billerica, MA) was dissolved overnight at 4 ^{o}C in 10 mL of PBS. The MTT solution was then sterile filtered. Human neuroblastoma SH-SY5Y cells were cultured in a humidified 5 % CO_2/air incubator at 37 ^{o}C in DMEM 12:1:1 modified media with 10 % fetal bovine serum and 1 % penicillin-streptomycin (Thermofisher, Waltham, MA). 25,000 SH-SY5Y cells were seeded into 96-well plates and incubated for 48 hours. After incubation, the culture medium was replaced with 100 µL of fresh media, and 10 µL of the Aβ sample was added to each well to obtain a final Aβ concentration of 5 µM. Cells were incubated for an additional 48 hours. The media was then aspirated and replaced with 50 µL of fresh media. 10 µL of the sterile MTT solution was added, and cells were incubated for 6 hours at 37 ^{o}C in the dark. After incubation 200 µL of DMSO was added to each well to dissolve the reduced MTT, and the absorbance was measured at 506 nm using a Synergy 4 UV-Vis/fluorescence multi-mode microplate reader.

Results and discussion

Modulation of Aβ Aggregation by BBG

In order to evaluate the aggregation modulation capability of BBG, we employed dot-blotting, TEM and the ThT fluorescence assay. TEM and ThT fluorescence assays are widely used to monitor Aβ aggregation. TEM images provide morphological information of Aβ aggregates. ThT is a dye that fluoresces at 485 nm when it binds to amyloid fibrils (57, 74, 202). Therefore, ThT fluorescence measurement is an efficient tool to monitor the progression of fibril formation. However, the ThT assay is not very effective in detecting soluble oligomers that are

known to be more neurotoxic than amyloid fibrils (29, 80, 176, 177). Furthermore, the diversity of Aβ aggregate morphologies and differing levels of neurotoxicity (203, 204) represent a challenge for correlating the aggregate morphology observed by TEM to Aβ-associated neurotoxicity. Recently dot-blotting with Aβ-specific antibodies was successfully used to detect and distinguish the spectrum of Aβ conformer species (20, 80, 198, 205-207). In particular, the oligomer-specific antibody, A11, is useful for detecting neurotoxic Aβ intermediates. A11 is a polyclonal antibody that reacts with soluble on-pathway toxic oligomers (198, 206). Previously it was shown that Aβ-associated toxicity could be mitigated by reducing the presence A11-reactive species (80, 89). Alternatively, 4G8 is an Aβ-sequence-specific monoclonal antibody (208-211) which has an epitope that lies within amino acids 17 to 24 of Aβ. The 4G8 epitope corresponds to a region of the Aβ peptide that is known to form β-sheet structures. During transition from monomers and low molecular weight oligomers to fibrils, β-sheet stacking buries the 4G8 epitope and ultimately limits 4G8 antibody binding. This leads to a dramatic loss of the 4G8 signal which can thereby be used to detect extensive fibril network structure formation (212). Lastly, 6E10 is a monoclonal antibody that recognizes residues 1-16 of Aβ, the N-terminus of Aβ (206, 212). Although the 6E10 antibody was originally thought to bind various Aβ species equally strongly, recent studies indicate that the 6E10 antibody binds to different Aβ species with different binding affinities (41, 61, 206). Similar to the 4G8 antibody, the 6E10 antibody binding affinity to fibrils is a few times lower than those of oligomers and monomers. According to the structural model of Aβ40 fibril proposed by Grigorieff et. al., two pairs of Aβ protofibrils intertwine adjacently to form a fibril (213). In their model, the N-terminus of the each protofibril is interlocked to form a fibril, which can bury the 6E10 epitope upon fibril formation. We

performed dot-blotting using a panel of Aβ-specific antibodies, together with traditional TEM and ThT fluorescence assay, to monitor the formation of neurotoxic Aβ oligomers and fibrils.

Two pathologically important Aβ isoforms, Aβ42 and Aβ40, have been widely used to evaluate the modulating capacities of numerous small molecules on Aβ aggregation and cytotoxicity (214-218). We used the more abundant isoform, Aβ40, in this study. Aβ samples were prepared by incubating 50 μM of Aβ40 monomer from 0 to 3 days at 37 °C without shaking either in the absence (control) or presence of BBG as described previously (199-201). In order to detect even weak modulating effect of BBG on Aβ aggregation, we chose 150 μM of BBG (3x BBG), which is three times higher than concentration of Aβ (50 μM). Aβ samples were taken periodically during incubation, and subjected to dot-blotting, ThT fluorescence assay, and TEM.

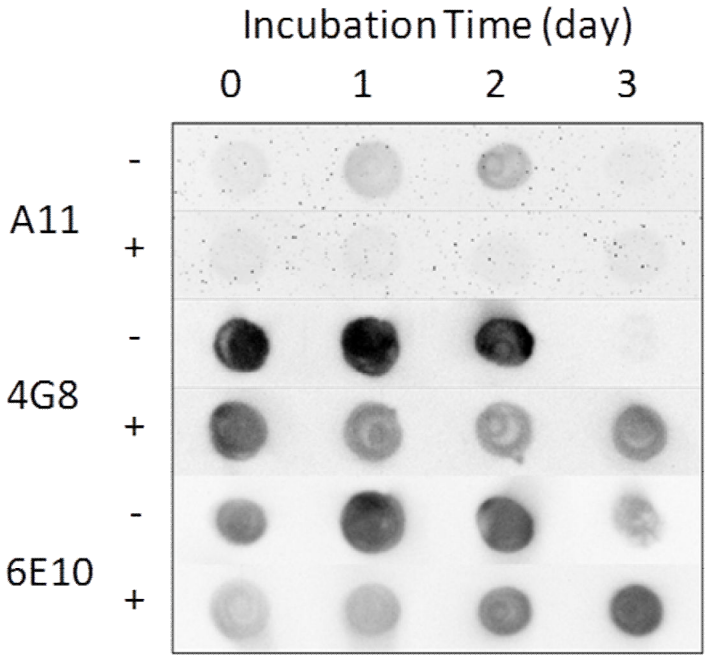

Figure 2.2. Monitoring Aβ aggregation by dot blotting. Oligomer-specific A11 antibody and Aβ-sequence specific antibodies, 4G8 and 6E10, were used.

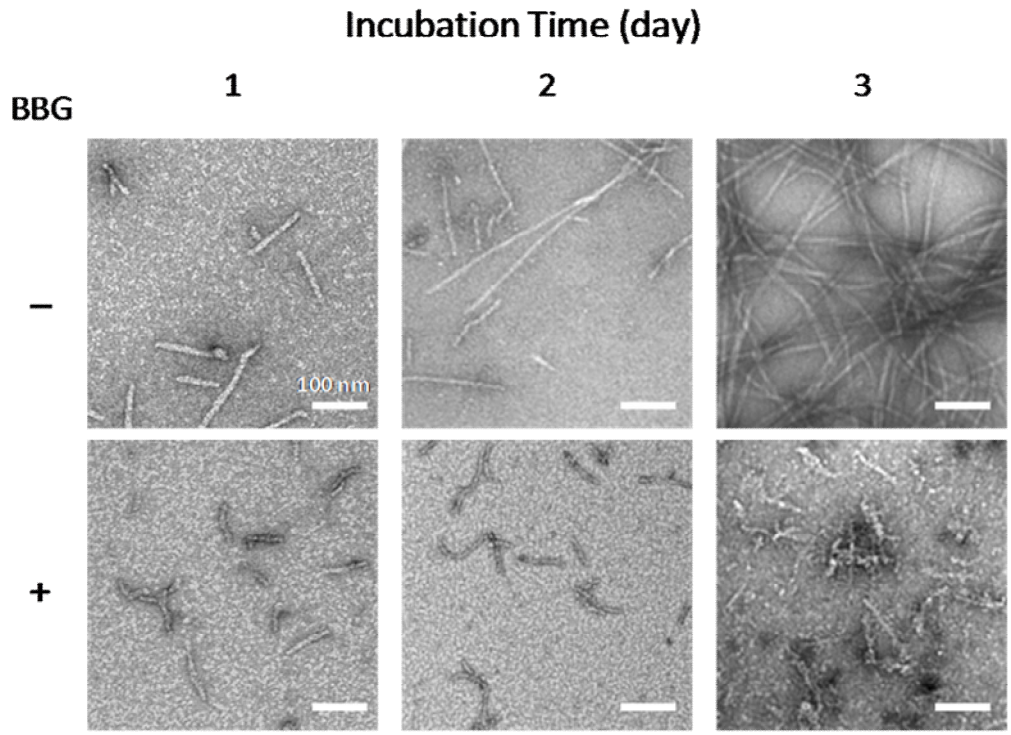

Figure 2.3. Monitoring Aβ aggregate and fibril formation by TEM. 50 μM Aβ was incubated in the absence (-) (top panels) or presence of 3x BBG (+) (bottom panels) for 1 to 3 days at 37 °C. Presence of oligomers and protofibrils (Top-left); protofibrils and isolated fibrils (Top-middle); fibril mesh network (Top-right*);* oligomers and protofibrils (Bottom-left); protofibrils (Bottom-middle); protofibrils (Bottom-right). Scale bar is 100 nm.

In the absence of BBG, dot-blotting results indicated that the majority of A11-reactive Aβ oligomers formed between day 1 and 2 (Figure 2.2; Figure 2.8A). However, when Aβ monomer was co-incubated with BBG, A11-reactive signals remain very low throughout the duration of the study. However, reduction of the A11-reactive signals at day 1 and 2 did not result from a loss of Aβ moieties, as supported by the sustained 6E10 signal at days 1 and 2 compared to day 0 (Figure 2.2; Figure 2.8C). In the absence of BBG, the 6E10 signal increases at days 1 and 2 from day 0 and then decreases at day 3 (Figure 2.2 as well as "no dye" portion of Figure 2.8C). This variation can be explained by the weaker binding affinity of 6E10 for Aβ monomers and fibrils compared to Aβ oligomers as described previously (61). In the presence of 3x BBG, the 6E10

signal at day 3 was very strong suggesting the idea that Aβ oligomers rather than Aβ fibrils were predominant in the sample. In the Aβ control sample, the majority of 4G8 signal was lost between day 2 and 3 (Figure 2.2; Figure 2.8B), implying that the majority of 4G8 epitopes were buried due to compact stacking of β-sheet structures, a prototypical feature of amyloid fibrils (212). However, in the presence of 3x BBG, a significant 4G8 signal at day 3 was observed, which also supports the idea that Aβ fibril mesh networks were not formed. These findings imply that BBG effectively inhibits the formation of A11-reactive Aβ oligomers and Aβ fibrils, the most toxic Aβ species.

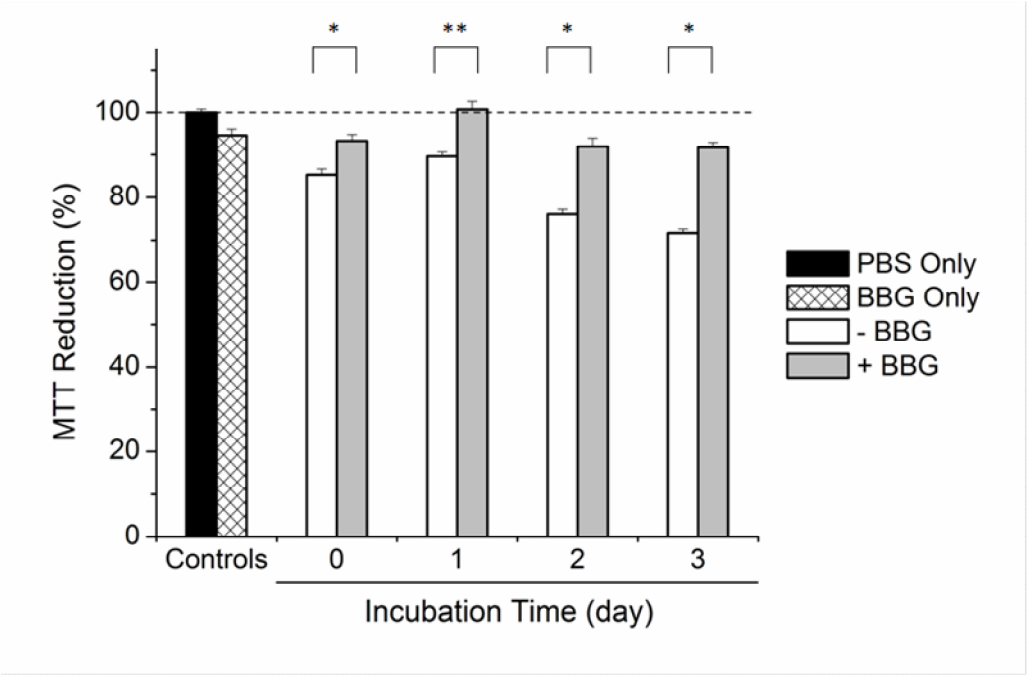

Figure 2.4. Viability of neuroblastoma SH-SY5Y cells incubated with pre-formed Aβ samples in the absence or presence of BBG. Preformed Aβ aggregates were prepared by incubating 50 μM of Aβ monomer in the absence or presence of BBG at 37 °C for 0 to 3 days, as indicated in the graph. Aggregates were then administered to SH-SY5Y cells at a final concentration of 5 μM. After 48 hours, mitochondrial metabolic activity was measured using MTT reduction. Cells administered with PBS as a control (*Black*), 3x BBG (15μM) dye only (*White with pattern*), Aβ incubated without BBG (*White*), Aβ incubated with 3x BBG (*Grey*). Values represent means ± standard deviation ($n \geq 3$). Values are normalized to the viability of cells administered with PBS only. Two-sided Student's t-tests were applied to the data. * $P < 0.001$, ** $P < 0.005$.

Next we characterized the morphology of the Aβ species formed with and without BBG using negative-stain TEM. TEM images clearly show a distinct morphological difference between Aβ samples incubated in the absence and those in the presence of 3x BBG (Figure 2.3). At day 1, in the absence of BBG, small oligomers (~100 nm in length) were formed (Figure 2.3, top-left), which is consistent with the dot-blotting results showing that A11-reactive Aβ aggregates were formed at day 1. Interestingly, even in the presence of 3x BBG, small oligomers (~100 nm in length) were predominantly observed (Figure 2.3, bottom-left panel). Despite the morphological similarities, the Aβ aggregates prepared with 3x BBG possessed substantially lower immunoreactivity to A11 antibody than those prepared without BBG. These findings imply that at day 1, the low A11 reactivity of Aβ samples co-incubated with BBG resulted from formation of A11-unreactive Aβ oligomers, rather than a complete inhibition of Aβ aggregation.

At day 2, a mixture of oligomers and long protofibrils was observed in the absence of BBG (Figure 2.3, top-middle; Figure 2.9A), which indicates that some Aβ oligomers are converted into protofibrils. However, in the presence of 3x BBG, small oligomers (less than 100 nm) were still predominantly observed similar to day 1 (Figure 2.3, bottom-middle; Figure 2.9B).

At day 3, the Aβ sample prepared in the absence of BBG exhibited only long mature fibrils in a meshed network (Figure 2.3, top-right), which is consistent with dot-blotting and ThT fluorescence results.. Here, ThT fluorescence sharply increased beginning at 48 hr (Figure 2.7), which was interpreted to be the onset of amyloid formation. In dramatic contrast, in the presence of 3x BBG, TEM showed that oligomers (~100 nm) remained the predominant species (Figure 2.3, bottom-right), which supports the idea that co-incubation of 3x BBG stops or at least substantially slow down Aβ aggregation process. Morphological similarities among the BBG-

treated Aβ aggregates observed at days 1, 2 and 3 are consistent with very weak A11-reactivity of the BBG-treated samples at least until day 3. These findings support that BBG is an efficient aggregation modulator. BBG reduces the formation of A11-reactive Aβ aggregates by generating A11-unreactive Aβ oligomers. The results also show that BBG suppresses fibril formation for at least three days.

Dose-Dependent Modulation of Aβ Aggregation by BBG

To further characterize the aggregation modulation capabilities of BBG, we evaluated BBG dose-dependent aggregation using dot-blotting and ThT fluorescence assay. 50μM Aβ was co-incubated at 37 °C with various BBG concentrations ranging from 0.001x (50 nM) to 10x (500 μM). Dot-blotting results of Aβ samples using three Aβ-specific antibodies (A11, 4G8, and 6E10) are shown in Figure 2.6. When Aβ was co-incubated with less than 0.1x BBG (5 μM), no observable changes were found in the A11 immunoblotting patterns (Figure 2.6A). However, co-incubation with 0.5x BBG or greater resulted in a reduction in the concentration of A11-reactive species formed, over the course of the study, confirming previous results. Since A11-reactive Aβ species were most abundant at day 2, we wanted to quantify inhibition of A11-reactive Aβ species formation (Figure 2.6D). Therefore, for day 2, integrated A11 dot-blot signal intensities were plotted against BBG concentrations. A half-maximal value of inhibitory concentration (IC_{50}) of 0.72x BBG was derived from the data fitting to a sigmoid curve (R^2=0.99).

In the absence of BBG, the 6E10 antibody stained Aβ oligomers, monomers, and fibrils in decreasing order of intensity, which is consistent with a few fold weaker binding to Aβ fibrils by the 6E10 compared to oligomers as described previously (61). In Figure 2.6B and C, BBG at concentration below 1x increases 4G8 and 6E10 signals at day 3. These results are consistent

with enhanced accessibility of the 4G8 and 6E10 epitopes due to BBG-induced conversion of Aβ aggregates from fibril mesh networks to oligomers. However, as the concentration of BBG increases above 1x, 4G8 and 6E10 reactive signals decrease. Finally, in the presence of 10x BBG, the 4G8- and 6E10-reactive signals both very weak compared to those observed in the absence of BBG, suggesting that both 4G8 and 6E10 epitopes were substantially lost partially due to direct binding of BBG to the 4G8 and 6E10 epitopes. The 4G8 epitope corresponds to a hydrophobic patch of the Aβ that is known to form β-sheet structures. The 6E10 epitope is the N-terminus of Aβ carrying both positive and negative charges. Therefore, we speculate that BBG preferentially binds to the hydrophobic patch of Aβ and weakly binds to the charged N-terminus of Aβ via electrostatic interaction.

Inhibition of Aβ-associated Cytotoxicity by BBG

Next, we sought to determine whether the conversion of A11-reactive aggregates into off-pathway aggregates reduces Aβ-associated neurotoxicity. In order to evaluate the cytotoxicity of Aβ species, we employed the MTT-reduction assay and neuroblastoma SH-SY5Y cells, widely used for this purpose (80, 185, 219-224). Preformed Aβ aggregates were prepared by incubating Aβ monomers in the absence or presence of 3x BBG at 37 °C for the specified time duration. The preformed aggregates were then administered to neuroblastoma SH-SY5Y cells for 48 hours, and subsequent cell viability was measured by MTT reduction. Before testing the cytotoxicity of Aβ samples, we first determined whether BBG by itself is cytotoxic to neuroblastoma SH-SY5Y cells. In the presence of 3x BBG dye (15 μM), SH-SY5Y cell viability was 95% without any BBG, quite consistent with the good biocompatibility and low toxicity observed in animals (192, 193).

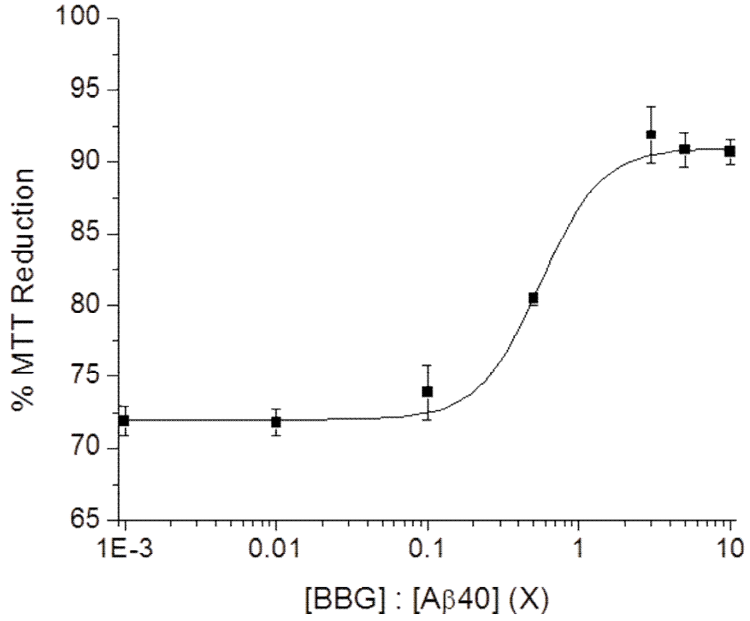

Figure 2.5. Dose-dependence of inhibition of Aβ-associated cytotoxicity by BBG. Preformed Aβ aggregates were prepared by incubating 50 μM of Aβ monomer in the presence of varying concentrations of BBG (0.001x, 0.01x, 0.1x, 0.5x, 1x, 3x, 5x, and 10x) at 37 °C for 2 days. Aβ aggregates were then administered to SH-SY5Y cells at a final concentration of 5 μM. After incubation, mitochondrial metabolic activity was measured after 48 hours using MTT reduction. Values represent means ± standard deviation ($n \geq 3$). Values are normalized to the viability of cells administered with PBS only. The data were fitted to a sigmoid curve ($R^2 = 0.99$).

Next we evaluated Aβ-associated toxicity. At day 0, Aβ monomers (5 μM) caused a mild reduction (15%) in cell viability (Figure 2.4). However, in the presence of 3x BBG (15 μM), viability recovered to 93% ($P < 0.001$), which is similar to the viability of 3x BBG dye alone without Aβ monomer (95%). This finding indicates that 3x BBG eliminates the cytotoxicity of Aβ monomers (5 μM). At day 1, in the presence of 3x BBG, the Aβ sample exhibited cell viability of 101 %, significantly higher than the cell viability (90%) of Aβ samples without BBG ($P < 0.001$) (Figure 2.4). These findings support the hypothesis that BBG can counteract the

cytotoxicity of Aβ sample and that BBG-induced Aβ oligomers observed by TEM were non-toxic.

At day 2, in the absence of BBG, cell viability decreased to 76%. This can likely be attributed to an increased concentration of A11-reactive toxic oligomers and to the emergence of amyloid fibrils (Figure 2.4). Although amyloid fibrils are less toxic than A11-reactive toxic oligomers, the toxicity of amyloid fibrils is reportedly higher than that of monomers (29, 80). In the presence of BBG, cell viability was significantly improved to 92% ($P < 0.001$), consistent with the reduction of A11-reactive Aβ species in the dot-blot results (Figure 2.2) and lack of observable fibrils in the TEM image (Figure 2.3). These results suggested that a decrease in the concentration of A11-reactive species correlates with a decrease in Aβ-associated toxicity.

At day 3, in the absence of BBG, addition of the preformed Aβ aggregates reduced the cell viability to 72%. Although the A11-reactive signal dropped after day 2, the reduced viability was most probably caused by the predominant amyloid fibrils converted from both small fraction of toxic A11-reactive aggregates and probably more dominant toxic non-A11 reactive large intermediates. Ishii and co-workers showed that Aβ aggregates larger than 50 kDa were five times less toxic than Aβ aggregates smaller than 50 kDa (29). Based on dot-blotting, ThT fluorescence and TEM, the vast majority of fibrils were formed almost exclusively after day 2 (Figure 2.2, 2.3, and 2.7). Consequently, at day 3, fibrils were the major toxic moieties. However, when Aβ was incubated with 3x BBG, cell viability significantly recovered to 92% ($P < 0.001$), which is comparable to the viability of cells incubated only with 3x BBG, without Aβ. Based on the cell viability results, we concluded that 3x BBG completely mitigates Aβ-associated cytotoxicity. Moreover, these findings suggest that the majority of oligomers and protofibrils formed in the presence of 3x BBG observed in TEM in fact are non-toxic and

structurally distinct from toxic Aβ species formed in the absence of BBG. This confirms that BBG reduces Aβ-associated toxicity by promoting the conversion of Aβ monomer to off-pathway, non-toxic intermediates.

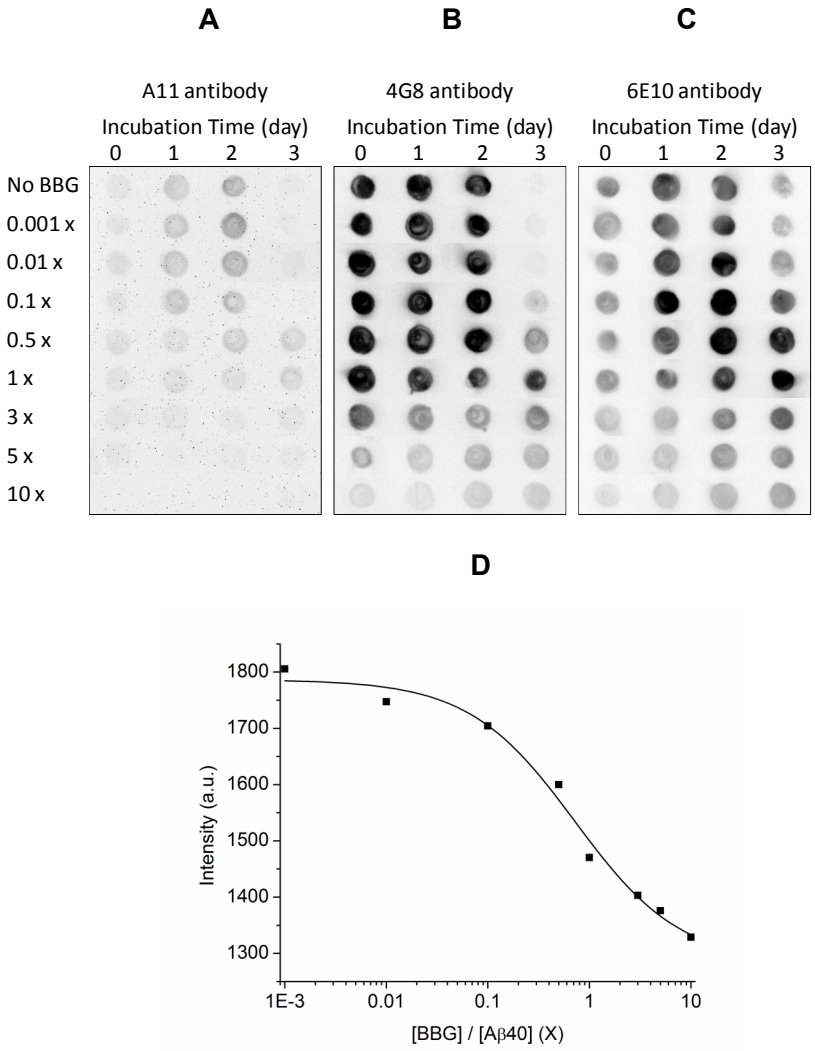

Figure 2.6. Dose-dependence of Aβ aggregation modulation by BBG. 50 μM of Aβ monomer was incubated at 37 °C in the absence (No BBG) or presence of the indicated concentrations of BBG (from 0.001x to 10x) for up to 3 days. Samples were taken on the indicated day and spotted onto a nitrocellulose membrane. Each membrane was immunostained with the A11 (*A*), 4G8 (*B*), or 6E10 (*C*) antibody. The blot images were taken by a UVP BioSpectrum imaging system. The blot image of A11-reactive signal of Aβ samples incubated with varying concentrations of BBG for two days was processed by ImageJ (NIH). The data were fitted to a sigmoid curve ($R^2 = 0.99$) *(D)*.

Dose-Dependent Inhibition of Aβ-Associated Cytotoxicity by BBG

In order to evaluate dose-dependent ability of BBG to inhibit Aβ-associated cytotoxicity, preformed Aβ aggregates were prepared by incubating Aβ monomer in the absence (control) or presence of varying concentrations of BBG from 0.001x to 10x at 37 °C for 2 days. The resulting preformed species were administered to SH-SY5Y cells and viability was measured after 48 hours using MTT reduction. From 0.001x (5.0 nM) to 0.1x (0.5 μM) BBG, cell viability (approximately 72%) was comparable to that of the control. However, cell viability dramatically improved when 0.5x BBG (2.5 μM) or greater was co-incubated with Aβ (Figure 2.5). Consequently, from 3x to 10x BBG, cell viability was maintained in the range of 91 to 93%. When the data were fitted to a sigmoid dose-dependent curve (R^2 = 0.99), a half maximal effective concentration (EC_{50}) value of 0.55x BBG was obtained. This value corresponded almost exactly to the significant reduction in the Aβ-associated cytotoxicity observed at 0.5x BBG. These results clearly demonstrate that BBG inhibits Aβ-associated cytotoxicity in a dose-dependent manner.

Based on the results described earlier, it is obvious that BBG inhibits formation of A11-reactive Aβ oligomers and Aβ-associated cytotoxicity in a dose-dependent manner. Furthermore, the EC_{50} value (0.55x BBG) derived from Aβ-associated cytotoxicity sigmoidal regression (Figure 2.5) corresponds well to the IC_{50} values (0.72x BBG) derived from the sigmoidal regression of inhibition of A11-reactive Aβ species formation by BBG (Figure 2.6D). Therefore, we conclude that the inhibition of Aβ-associated cytotoxicity directly correlates with the aggregation modulation effects of BBG. Furthermore, considering that BBG-induced oligomers are non-toxic, reduction of Aβ-associated cytotoxicity is attributed to BBG-induced, non-toxic oligomer formation.

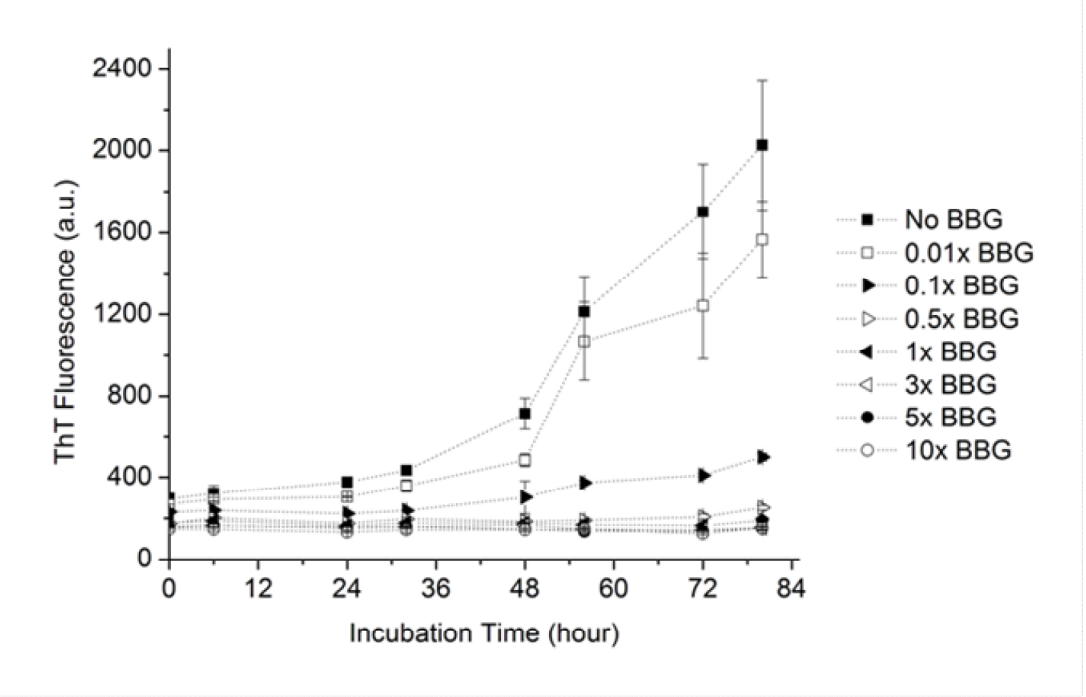

Figure 2.7. Time course of ThT fluorescence of Aβ samples with varying concentrations of BBG. 50μM of Aβ monomer was incubated at 37 °C in the absence (no BBG) or presence of the indicated concentrations of BBG (from 0.001x to 10x) for up to 80 hours. 5 μL of Aβ sample was taken at 0, 6, 24, 32, 48, 54, 72 and 80 hours for ThT fluorescence analysis. ThT fluorescence was measured in arbitrary units (a.u.). Values represent means ± standard deviation (n = 3).

Bias of ThT Fluorescence Reading at High Concentration of BBG

We used ThT binding to verify the onset of fibril formation at varying concentrations of BBG. As BBG concentration was increased ThT fluorescence of Aβ sample decreased accordingly (Figure 2.7), consistent with our findings and observations at 3x BBG. In order to quantify the inhibition of ThT fluorescence by BBG, we plotted ThT fluorescence versus BBG concentrations from 10^{-5}x to 10x BBG (Figure A1). Data fitting to a sigmoid curve ($R^2 = 0.99$) generated an IC_{50} value of 0.03x BBG, which is one order of magnitude lower than those determined for the inhibition of A11-reactive species formation by BBG. To explain this discrepancy, we hypothesized that ThT fluorescence reading was biased due to either spectral

interference of BBG on ThT fluorescence measurement or competitive binding of BBG to ThT binding sites on amyloid fibrils. Carver et al. reported that curcumin and quercetin significantly skewed ThT fluorescence measurements via spectral interference, where alternatively resveratrol introduced a measurement bias by competing with ThT for amyloid fibril binding sites (225). Since BBG at neutral pH has negligible absorbance at both 450 nm (excitation wavelength of ThT fluorescence) and 485 nm (emission wavelength of ThT fluorescence) (226), spectral interference was ruled out as a source of the bias. Next, to determine whether BBG and ThT competitively bind to the same sites, we measured the ThT fluorescence of preformed amyloid fibrils that were momentarily mixed with varying concentrations of BBG immediately prior to addition of ThT (Figure A2). As BBG concentration increased, ThT fluorescence decreased accordingly. When the data were fitted to a sigmoidal curve ($R^2 = 0.99$), an IC_{50} value of 0.16x BBG was obtained. From this we concluded that the ThT fluorescence measurements of Aβ samples co-incubated with BBG can be biased since BBG at high concentrations can interfere with ThT binding to amyloid fibrils. Consequently, the ThT fluorescence assay should be used with caution at high concentrations of BBG.

Modulation of Aβ aggregation by BBG analogs

In order to determine whether any structural features of BBG are critical in modulating Aβ aggregation and cytotoxicity, modulation of Aβ aggregation by three close structural analogs of BBG (BBR, BBF and FGF) were examined by dot blotting and TEM analysis. The four compounds (BBG, BBR, BBF, and FGF) are congeners sharing the common triphenylmethane structure. Both BBF and FGF are the FDA-approved food dyes (227). Similar to BBG, BBR is commonly used to stain proteins in protein electrophoresis. However, the chemical structure of

BBR differs from BBG by lacking two methyl groups attached to triphenylmethane (Figure 2.1). Both BBF and FGF have three benzenesulfonate functional groups, whereas BBG and BBR have two benzenesulfonate functional groups and one uncharged diphenylamine group (Figure 2.1). FGF differs from BBF with only one hydroxyl functional group attached to one of the benzenesulfonate functional groups (Figure 2.1).

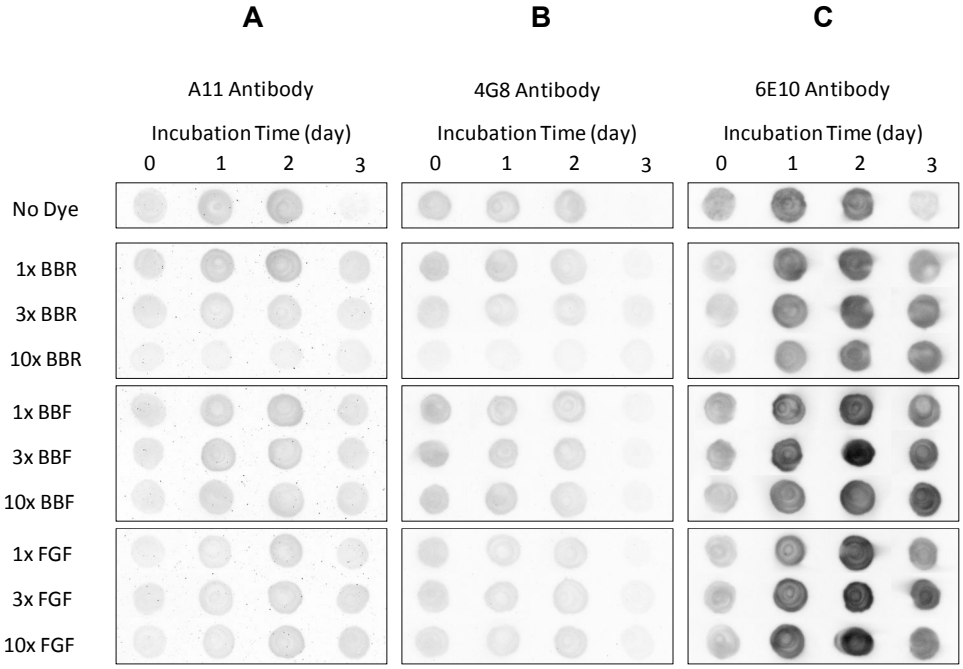

Figure 2.8. Modulation of Aβ aggregation by BBG analogs, BBR, BBF and FGF. 50 μM of Aβ monomer was incubated at 37 °C in the absence (No Dye) or presence of the indicated concentrations of BBR, BBF or FGF (1x, 3x, and 10x) for up to three days. Samples were taken on the indicated day and spotted onto a nitrocellulose membrane. Each membrane was immunostained with the A11 (*A*), 4G8 (*B*), or 6E10 (*C*) antibody.

Three different concentrations (1x, 3x, and 10x) of each BBG analog were co-incubated with 50 μM of Aβ up to three days and the immuno-reactivities of the Aβ samples were monitored by A11, 4G8, and 6E10 Aβ-specific antibodies. Similar to BBG, BBR reduced toxic A11-reactive Aβ species. In the presence of 3x BBR, the A11-reactive Aβ signal became less than half the A11-reactive signal of Aβ sample incubated without any dye, though 1x BBR did

not make a substantial change in the A11-reactive signal (Figure 2.8A). Co-incubation of 10x BBR with the Aβ samples led to almost complete elimination of the A11-reactive species. However, considering that even 1x BBG substantially reduced A11-reactive signal (Figure 2.6A), BBR is less effective than BBG in reducing A11-reactive species. Similar to 10x BBG, 10x BBR substantially reduced the 4G8-reactive signal, which suggests that both BBR and BBG bind to the hydrophobic patch (4G8 epitope) of Aβ in a similar fashion (Figure 2.8B). In contrast, even at 10x BBR, there was no substantial reduction of the 6E10-reactive signal, which suggests that BBR interaction mode of Aβ is different from that of BBG (Figure 2.6C and 2.8C). These results suggest that BBR reduces A11-reactive toxic species, but the interaction mode of BBR with Aβ is different from that of BBG.

In sharp contrast to BBG, both BBF and FGF exhibited little or minor changes in the immuno-reactivities of the Aβ samples against the A11 and 4G8 antibodies from the Aβ samples incubated without any dye (Figure 2.8A to C). In particular, even 10x BBF and 10x FGF did not show any substantial reduction of the neurotoxic A11-reactive Aβ species. At day 3, the Aβ samples incubated with either BBF or FGF exhibited strong 6E10 signals, whereas Aβ aggregates formed in the absence of any dye exhibits very weak 6E10 signals (Figure 2.8C). These 6E10 epitope accessibility results suggest that BBF- or FGF-induced Aβ protofibrils and fibrils have conformations different from those of Aβ protofibrils and fibrils formed in the absence of any dye.

Morphology of Aβ aggregates formed after two days in the absence (no dye control) or in the presence of one of BBG congeners was analyzed by negative-stain TEM (Figure 2.9). Similar to BBG, co-incubation of 10x BBR promotes short oligomer formation (less than 100 nm), but inhibits amyloid fibril formation (Figure 2.9B and C). In contrast, both BBF and FGF induce

formation of the mixture of long fibrils and protofibrils, whereas the Aβ aggregates incubated with BBG for two days are predominantly curvilinear oligomers (Figure 2.9B, D, and E). In contrast, morphology of the Aβ aggregates formed in the presence of either BBF (Figure 2.9D) or FGF (Figure 2.9E) are similar to that of the Aβ aggregates formed in the absence of any dye (Figure 2.9A), which is consistent with the dot-blot results that there are little or minor differences in the immuno-reactivities of the Aβ aggregates formed in the absence or in the presence of BBF or FGF. These results strongly suggest that the both BBG and BBR effectively modulate Aβ aggregation by promoting short oligomer formation but inhibiting fibril formation. In contrast, both BBF and FGF are not as effective in modulating Aβ aggregation as BBG and BBR, but promote formation of the mixture of protofibrils and fibrils.

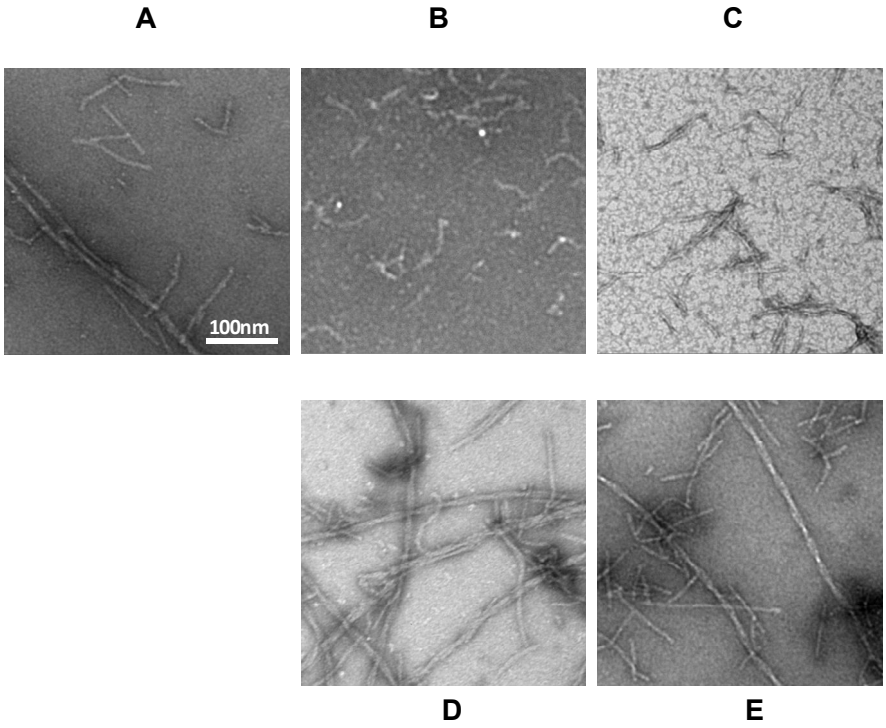

Figure 2.9. TEM images of 50 μM of Aβ incubated for two days at 37 °C in the absence of any dye (*A*), or in the presence of 10x BBG (*B*), 10x BBR (*C*), 10x BBF (*D*), or 10x FGF (*E*). Scale bar is 100 nm.

Modulation of Aβ cytotoxicity by BBG analogs. Modulating effects of the BBG analogs on Aβ-associated cytotoxicity were also evaluated by MTT reduction assay of SH-SY5Y cells (Figure 2.10). Similar to 3x BBG, co-incubation of 3x BBR with Aβ samples recovers the viability of SH-SY5Y cells from 76% to 97% (Figure 2.10), which is consistent with the reduced neurotoxic A11-reactive signal of the Aβ aggregates at 3x BBR (Figure 2.8A). However, compared with 1x BBG, co-incubation of 1x BBR exhibits less increase in the SH-SY5Y cell viability (86%) consistent with lower reduction of A11-reactive signal. These findings support the idea that BBR reduces Aβ-associated cytotoxicity but is less effective than BBG.

In contrast, BBF and FGF are less effective in modulating the Aβ-cytotoxicity than BBG and BBR. Even at 3x BBF and FGF, the SH-SY5Y cell viability was 80% and 86%, respectively, which is higher than the cell viability without any dye but 10% lower than the cell viability with either 3x BBG or 3x BBR. A moderate reduction of Aβ cytotoxicity produced by BBF or FGF may be due to increased conversion of more toxic oligomers into less toxic fibrils (Figure 2.9D and E). Investigations are underway to reveal the underlying mechanisms for this behavior.

Based on our findings, we identify several important structural features of BBG on modulating Aβ aggregation and cytotoxicity. Although all four triphenylmethane-based BBG and analogs exhibit modulating ability on Aβ aggregation, structural differences of BBG and BBR from BBF and FGF (one additional diphenylamine group and one less benzenesulfonate group) are responsible for the unique interaction mode of BBG and BBR on Aβ leading to formation of non-toxic Aβ aggregates. In particular, one sulfonate group connected to triphenylmethane is expected to perturb pi-pi stacking interaction by an electron withdrawing sulfur atom. Furthermore, considering that BBG is more effective in modulating Aβ aggregation

and cytotoxicity than BBR, the two additional methyl groups in BBG should also be considered important.

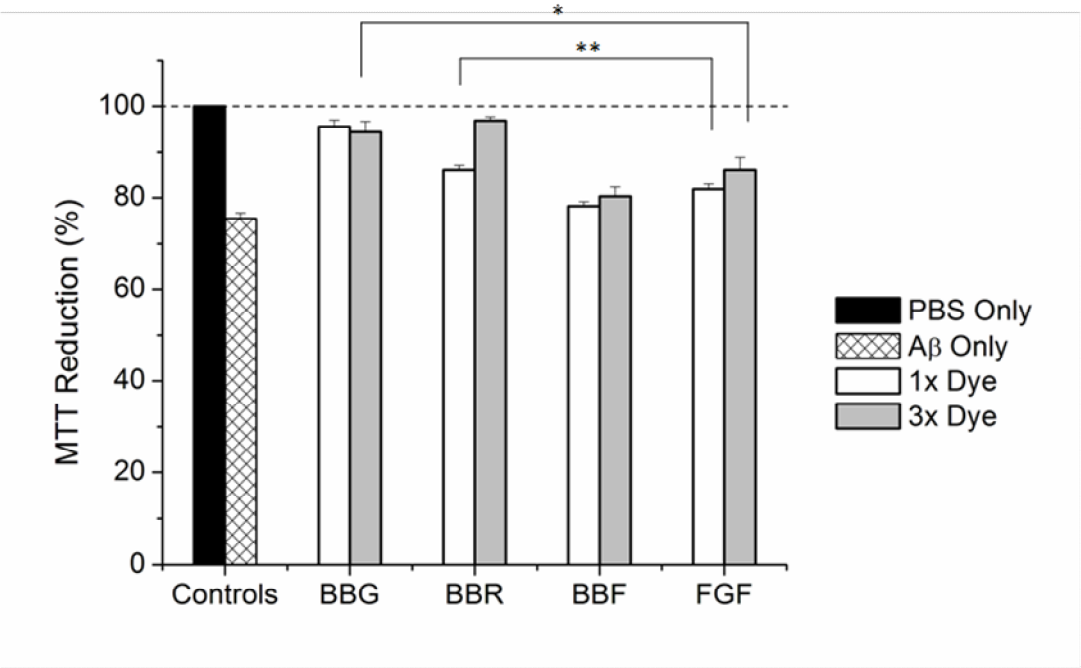

Figure 2.10. Viability of neuroblastoma SH-SY5Y cells incubated with pre-formed Aβ samples in the presence of BBG or BBG analogs (BBR, BBF, and FGF). Preformed Aβ aggregates were prepared by incubating 50 μM of Aβ monomer in the presence of BBG or BBG analogs at 37 °C for two days, as indicated in the graph. Aggregates were then administered to SH-SY5Y cells at a final concentration of 5 μM. After 48 hours, mitochondrial metabolic activity was measured using MTT reduction. Cells administered with PBS as a control (*Black*), Aβ samples incubated without BBG (*White with pattern*), Aβ samples incubated with 1x dye (*White*) or 3x dye (*Grey*). Values represent means ± standard deviation ($n \geq 3$). Values are normalized to the viability of cells administered with PBS only. Two-sided Student's t-tests were applied to the data. * $P < 0.001$, ** $P < 0.01$.

Taken together, our results conclusively establish that BBG effectively reduces neurotoxic A11-reactive Aβ intermediates by inducing the formation of non-toxic Aβ aggregates. BBG inhibited the formation of A11-reactive Aβ aggregates in a dose-dependent manner. The IC_{50} value in the inhibition of A11-reactive Aβ aggregate formation by BBG after two-day incubation was 0.72x BBG. Negative-stain TEM, ThT fluorescence assay and dot-blotting assay results

strongly support the idea that BBG promotes the formation of A11-unreactive, off-pathway Aβ oligomers and protofibrils, but inhibits the formation of amyloid fibrils. 15 μM of BBG (3x BBG) conferred only a minor cytotoxicity (5%) to neuroblastoma SH-SY5Y cells, which is approximately one third of the cytotoxicity of 5 μM of Aβ monomer. At 3x BBG, Aβ-associated cytotoxicity was completely suppressed throughout the duration of our study (three days). BBG effectively inhibits Aβ-associated cytotoxicity in a dose-dependent manner. The EC_{50} value of inhibition of Aβ-associated cytotoxicity by BBG was 0.55x BBG. These results strongly support the idea that the inhibition of Aβ-associated cytotoxicity by BBG directly correlates with the reduction of neurotoxic A11-reactive Aβ aggregates by BBG. Comparative studies of BBG and BBG analogs on modulation of Aβ aggregation and cytotoxicity revealed that the structural differences of BBG and BBR from BBF and FGF are critical for the unique interaction of BBG and BBR with Aβ. Furthermore, considering that BBG is more effective in modulating Aβ aggregation and cytotoxicity than BBR, the two additional methyl groups attached to the triphenylmethane structure in BBG are also important. The inhibitory effects of BBG on Aβ-associated cytotoxicity as well as highly favorable biocompatibility and BBB-permeability make BBG a promising lead compound for future AD therapeutic development.

Chapter 3

Halogenation generates effective modulators of amyloid-beta aggregation and neurotoxicity

Sections of this chapter contain excerpts from the following publications.

1. **Wong HE**, Irwin JA, & Kwon I (2013) Halogenation Generates Effective Modulators of Amyloid-Beta Aggregation and Neurotoxicity. PLoS One 8(2):e57288.

2. **Wong HE** & Kwon I (2011) Xanthene Food Dye, as a Modulator of Alzheimer's Disease Amyloid-beta Peptide Aggregation and the Associated Impaired Neuronal Cell Function. PLoS One 6(10).

3. Irwin JA, **Wong HE**, & Kwon I (2013) Different Fates of Alzheimer's Disease Amyloid-beta Fibrils Remodeled by Biocompatible Small Molecules. Biomacromolecules 14(1):264-274.

4. Irwin JA, **Wong HE**, & Kwon I (2015) Determining binding sites of polycyclic aromatic small molecule-based amyloid-beta peptide aggregation modulators using sequence-specific antibodies. Analytical Biochemistry 470:61-70.

Abstract

Halogenation of organic compounds plays diverse roles in biochemistry, including selective chemical modification of proteins and improved oral absorption/blood-brain barrier permeability of drug candidates. Moreover, halogenation of aromatic molecules greatly affects aromatic interaction-mediated self-assembly processes, including amyloid fibril formation. Perturbation of the aromatic interaction caused by halogenation of peptide building blocks is known to affect the morphology and other physical properties of the fibrillar structure. Consequently, in this article, we investigated the ability of halogenated ligands to modulate the self-assembly of amyloidogenic peptide/protein. As a model system, we chose amyloid-beta peptide (Aβ), which is implicated in Alzheimer's disease, and a novel modulator of Aβ aggregation, erythrosine B (ERB). Considering that four halogen atoms are attached to the xanthene benzoate group in ERB, we hypothesized that halogenation of the xanthene benzoate plays a critical role in modulating Aβ aggregation and cytotoxicity. Therefore, we evaluated the modulating capacities of four ERB analogs containing different types and numbers of halogen atoms as well as fluorescein as a negative control. We found that fluorescein is not an effective modulator of Aβ aggregation and cytotoxicity. However, halogenation of either the xanthenes or benzoate ring of fluorescein substantially enhanced the inhibitory capacity on Aβ aggregation. Such Aβ aggregation inhibition by ERB analogs except rose bengal correlated well to the inhibition of Aβ cytotoxicity. To our knowledge, this is the first report demonstrating that halogenation of aromatic rings substantially enhance inhibitory capacities of small molecules on Aβ-associated neurotoxicity via Aβ aggregation modulation.

Introduction

Halogenation has been widely used to provide organic compounds including biomolecules with new properties. Introduction of aryl halides into proteins allows chemical modification via versatile palladium catalyzed cross-coupling reactions with terminal alkene or alkyne reaction partners (228, 229), and facilitates monitoring structural changes of protein (230, 231). Halogen groups are often inserted during hit-to-lead or lead-to-drug conversions for several reasons, including enhanced antagonistic/agnostic effects due to improved oral absorption/blood-brain barrier permeability (232). Furthermore, it was reported that halogenation of aromatic molecules greatly affects aromatic interaction-mediated self-assembly processes (233). Aromatic interaction plays an important role in a broad spectrum of molecular self-assemblies (230, 234-236). In particular, aromatic interaction is considered one of critical contributors to forming cross-stacked β-sheet structure, so called, amyloid fibrillar structure (237, 238). Planar aromatic interaction stabilizes the fibrillar structure and determines the direction and orientation of amyloid fibrils (239, 240). Therefore, perturbation of the aromatic interaction caused by halogenation of aromatic building block affects the morphology and physical properties of the fibrillar structure (230).

Herein, we have investigated whether halogenation of ligands can also affect self-assembly of amyloid-beta peptide (Aβ), which is implicated in Alzheimer's disease (AD). A pathological hallmark of AD is the accumulation of insoluble protein aggregates, composed primarily of fibrillar Aβ aggregates. According to the revised amyloid-cascade hypothesis, certain types of soluble Aβ oligomers and protofibrils are more toxic than Aβ fibrils and correlate well with dementia (29, 80, 176, 177). Therefore, modulation of Aβ aggregation using small molecules is considered a promising way to eliminate Aβ associated toxicity (41, 73, 74,

89, 178, 179, 183-186, 188, 230, 241-244). We recently reported that red food dye erythrosine B (ERB) is a novel modulator of Aβ-aggregation in vitro and Aβ neurotoxicity (245). The good biocompatibility and possibility of systemic administration make ERB an attractive inhibitor of Aβ neurotoxicity (246, 247). Considering that ERB has multiple aromatic rings attached to four electronegative halogen atoms (Figure 3.1), we hypothesize that the modulatory capacity of ERB on Aβ aggregation is attributed to halogen atoms. In order to validate our hypothesis that halogen atoms are key chemical structures for Aβ aggregation modulation, we evaluated the modulating capacities of four ERB congeners containing different type and number of halogen atoms, eosin Y (EOY), eosin B (EOB), rose bengal (ROB), and phloxine B (PHB) (Figure 3.1). We also evaluated fluorescein (FLN), which has the same xanthene benzoate backbone similar to ERB but lacks a halogen atom, as a negative control. If halogenation of aromatic rings is indeed effective in modulating Aβ aggregation and cytotoxicity, it will enhance our understanding of molecular mechanism of amyloid formation and facilitate discovery and design of a new series of halogenated small molecule modulators of amyloidogenic peptides/proteins.

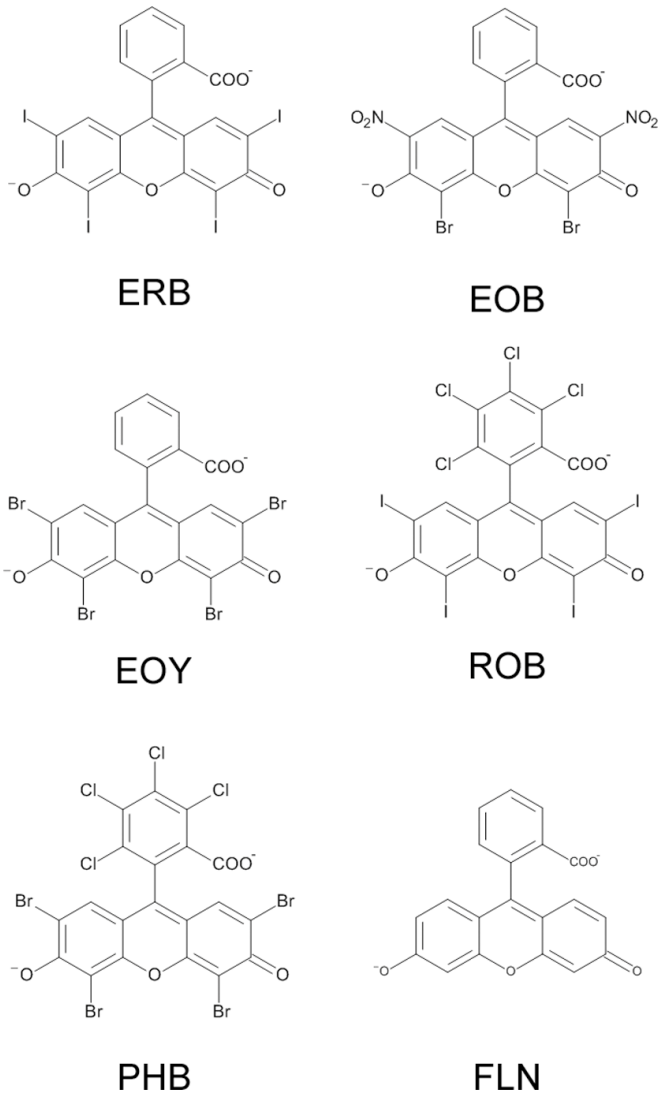

Figure 3.1. Chemical Structure of erythrosine B (ERB), eosin Y (EOY), eosin B (EOB), rose Bengal (ROB), phloxine B (PHB), and fluorescein (FLN) at neutral pH.

Materials and Methods

Materials

Aβ40 was purchased from Anaspec Inc. (Fremont, CA) and Selleck Chemicals (Houston, TX). Human neuroblastoma SH-SY5Y cells were obtained from the American Type Culture Collection (ATCC; Manassas, VA). Polyclonal A11 anti-oligomer and horseradish peroxidase (HRP)-conjugated anti-rabbit IgG antibodies were obtained from Invitrogen (Carlsbad, CA). 4G8

antibody was obtained from Covance (Dedham, MA). Polyclonal OC antibody and 3-(4,5-dimethylthiazol-2-yl)-2,5-diphenyltetrazolium bromide (MTT) was obtained from Millipore (Billerica, MA). Nitrocellulose membranes and ECL advance chemiluminescence detection kit were obtained from GE Healthcare Life Sciences (Waukesha, WI). Eosin Y was purchased from Acros Organics (Geel, Belgium). All other chemicals were obtained from Sigma-Aldrich (St. Louis, MO) unless otherwise noted.

Aβ Aggregation

Aβ40 stock was prepared as described previously (245, 248) except the pretreatment using hexafluoroisopropanol (HFIP). It has been reported that HFIP increases the α-helix content of a protein and is a strong disaggregating solvent of Aβ (20, 249). Lyophilized Aβ40 was dissolved in 100 % HFIP (1 mM) and incubated at room temperature for 2 hours. HFIP was evaporated under a constant stream of nitrogen, and the peptide was reconstituted in phosphate buffered saline (PBS) solution (10 mM NaH_2PO_4 and 150 mM NaCl, pH 7.4) to a concentration of 50 μM. If needed, the HFIP treated peptide was dissolved in 100 mM NaOH (2 mM Aβ) prior to dilution in PBS. Erythrosine B, eosin Y, eosin B, rose bengal, phloxine B, and fluorescein were dissolved in PBS. Concentrated dye stock solutions were added to the peptide solutions. The Aβ40 peptide samples were incubated at 37 ˚C in the absence or in the presence of the dye.

Thioflavin T (ThT) Assay

5 μL of Aβ sample (50 μM) was dissolved in 250 μL of ThT (10 μM). Fluorescence was measured in 96-well microtiter plates (Fisher Scientific, Pittsburgh, PA) using a Synergy 4 UV-

Vis/fluorescence multi-mode microplate reader (Biotek, VT) with an excitation and emission wavelength of 438 nm and 485 nm, respectively.

Transmission Electron Microscopy (TEM)

TEM was performed as reported previously (245, 248). Aβ samples (10 μL of 50 μM Aβ) were placed on 200 mesh formvar coated/copper grids, absorbed for 1 minute, and blotted dry with filter paper. Grids were then negatively stained with 2% uranyl acetate solution, blotted dry, and then inspected with a JEOL 1010 Transmission Electron Microscope operated at 60 kV.

Dot Blotting

Dot blotting was performed as reported previously (245, 248). 2 μL Aβ samples were spotted onto nitrocellulose membranes and were dried at room temperature. A solution of 0.1 % Tween 20 in Tris-buffered saline (TBS-T) solution (0.1% Tween 20, 20 mM Tris, 150 mM NaCl, pH 7.4) was prepared. Each nitrocellulose membrane was blocked at room temperature for 1 hour (5 % milk TBS-T) and washed with TBS-T. Each membrane was then incubated with antibody (HRP-conjugated 4G8, A11, or OC antibody) in 0.5% milk TBS-T for 1 hour at room temperature and washed with TBS-T. After immuno-staining with HRP-conjugated 4G8, the membranes were coated with ECL advance detection agent (based on manufacturer specifications) and visualized. Alternatively, all other membranes were incubated with HRP-conjugated IgG in 0.5 % milk TBS-T for 1 hour and washed with TBS-T. Signal detection was performed as aforementioned using the ECL Advance Detection kit and was visualized using a Biospectrum imaging system (UVP, Upland, CA). HRP-conjugated 4G8 and OC were applied at a 1:25000 dilution while A11 and HRP-conjugated IgG were applied at a 1:10000 dilution.

MTT Reduction Assay

MTT reduction assay was performed as reported previously (245, 248). SH-SY5Y cells were cultured in a humidified 5 % CO2/air incubator at 37 ˚C in DMEM/F 12:1:1 containing 10 % fetal bovine serum and 1 % penicillin-streptomycin. 20000 to 25000 cells were seeded into each well of a 96-well microtiter plate (BD, Franklin Lakes, NJ) and allowed to acclimate for 3 days. 10 μL of Aβ sample was added to each well and incubated for 2 days. The cells were washed by replacing the culture media with fresh media and incubating for 1 hour. The wash media was replaced with fresh media. 10 μL of MTT was added to each well and incubated in the dark for 6 hours at 37 ˚C. After incubation, reduced MTT was dissolved with 200 μL of DMSO. After reduced MTT dissolution, the absorbance was measured at 506 nm using a Synergy 4 UV-Vis/fluorescence multi-mode microplate reader (Biotek, VT).

Circular Dichroism (CD)

CD analysis of Aβ samples was performed as described previously (102, 217). Aβ sample was diluted 1:10 using double distilled water. Samples were measured using a Jasco J710 spectropolarimeter with a 1 mm path length. The reported spectrum for each sample was the average of at least 5 measurements and the background was subtracted using appropriate controls. In case of samples containing any dye, the background spectra were obtained using controls containing the same concentration of the dye.

Aβ Binding Assay

The binding of ERB, EOY, ROB, PHB, and FLN to Aβ40 was assessed using modified assays based on emission fluorescence quenching techniques described in the literature (250-253). The concentration of each of the dyes was fixed at 20 μM. In order to evaluate fluorescence quenching of the dye upon binding to Aβ40, Aβ40 was mixed with the dye in a final concentration of 0 to 25 μM in citrate buffer at pH 4.5. The excitation wavelengths used are as follows: ERB – 317 nm, EOY – 480 nm, ROB – 510 nm, PHB – 500 nm, and FLN – 432 nm. The emission wavelengths where the data were collected are as follows: ERB – 548 nm, EOY – 536 nm, ROB – 565 nm, PHB – 555 nm, and FLN – 512 nm. With FLN, fluorescence quenching was also investigated due to binding to bovine serum albumin (BSA - New England Biolabs, Ipswich, MA) by mixing with FLN in a final concentration of 0 to 25 μM BSA in citrate buffer at pH 4.5. Where appropriate, the dissociation constant, K_d, was determined using the non-linear regression curve fitting to Eq. 1 shown below. In Eq. 1, n is the number of binding sites, and [D] is the molar concentration of free dye.

$$\bar{n} = \frac{n[D]}{K_d + [D]} \qquad \textit{Eq. 1}$$

Where, $\bar{n}$ is the average number of dye molecules bound to protein molecule and thus is calculated as shown in Eq. 2.

$$\bar{n} = \frac{X[D_t]}{[P_t]} \qquad \textit{Eq. 2}$$

And, [D_t] and [P_t] are the total molar dye (set at 20 μM) and Aβ40 concentrations, respectively and X is the fraction of dye bound to Aβ40 at each Aβ40 concentration, calculated as shown in Eq. 3. In Eq. 3, F_{free}, $F_{obs.}$, and F_0 correspond to the free 20 μM dye fluorescence, fluorescence

observed at a certain Aβ40 concentration, and the fully quenched fluorescence values, respectively.

$$X = \frac{F_{free} - F_{obs.}}{F_{free} - F_0} \qquad Eq.\ 3$$

We assessed the binding of EOB to Aβ40 and BSA, using an absorbance technique described in the literature based on the observation that upon protein binding (254), the absorbance maximum of EOB shifts from 514 to 530 ± 5 nm. The concentration of EOB was fixed at 20 μM. Aβ40 and BSA concentrations were varied from 0 to 60 μM and 0 to 25 μM, respectively, and the absorbance was measured at 530 nm. Citrate buffer at pH 4.5 was also used for the EOB binding assay.

Sequence-Specific Antibody Immunostaining.

Dot blotting was performed as reported previously.(245, 255-257) 2 μL Aβ40 peptide samples were spotted onto nitrocellulose membranes and were dried at room temperature. A solution of 0.1 % Tween 20 in Tris-buffered saline (TBS-T) solution (0.1% (v/v) Tween 20, 20 mM Tris, 150 mM NaCl, pH 7.4) was prepared. Each nitrocellulose membrane was blocked at room temperature for 1 hour (5 % (w/v) milk TBS-T) and washed with TBS-T. Each membrane was then incubated with an Aβ sequence-specific primary antibody (HRP-conjugated 4G8, HRP-conjugated 6e10, 12C3, 2H4, Anti-Aβ-22-35, or 11A50-B10 antibody) in 0.5% (w/v) milk TBS-T for 1 hour at room temperature and washed with TBS-T. After immunostaining with HRP-conjugated 4G8 and 6e10 primary antibodies, the membranes were coated with ECL Prime detection agent (based on manufacturer specifications) and visualized. Alternatively, all other

membranes were incubated with the appropriate HRP-conjugated anti-mouse or anti-rabbit IgG secondary antibody in 0.5 % (w/v) milk TBS-T for 1 hour and washed with TBS-T. Signal detection was performed as aforementioned using the ECL Prime Detection kit and was visualized using a Biospectrum imaging system. HRP-conjugated 4G8, 6e10, and IgG secondary antibodies along with the 11A50-B10 antibody were applied at a 1:10000 dilution, while the 2H4, 12C3, and Anti-Aβ-22-35 antibodies were applied at a 1:7000 dilution. When appropriate, the resulting dot blot intensities were quantified using Image J.

Results and Discussion

ERB, EOY, and PHB Substantially Inhibit Aβ-Associated Cytotoxicity

In order to evaluate the modulation capability of ERB and its analogs (EOY, EOB, PHB, and ROB), we employed the widely-used MTT reduction assay (80, 185, 219, 220, 245, 248). Aβ aggregates were prepared by incubating Aβ monomers with or without 3x ERB analog. In the absence of any ERB analog, Aβ aggregation was monitored by ThT fluorescence assay. The ThT fluorescence of Aβ aggregates started to increase at day 4 and reached the plateau at day 6 (Figure 3.2A), indicating that Aβ protofibrils and fibrils were primarily formed from day 4. In order to evaluate cytotoxicity of Aβ aggregates containing Aβ intermediates, we chose Aβ samples incubated for 5 days in the absence or presence of 3x ERB analog. The preformed Aβ aggregates were then administered to neuroblastoma SH-SY5Y cells, and cell viability was determined by MTT reduction (Figure 3.2B). We determined whether Aβ monomer or ERB analog is cytotoxic to neuroblastoma SH-SY5Y cells, and the results are shown in Figure 3.2B. Aβ monomers (5 μM) caused a mild reduction (11%) in the cell viability. All ERB analogs (15 μM) except ROB also caused only mild reduction in the cell viability ranging from 0 to 8%.

However, 3x ROB substantially reduced the cell viability (34%). ROB has been tested to ablate certain types of cancer cells including melanoma (258, 259), and so it is not surprising that ROB is cytotoxic to SH-SY5Y cells.

Next, we determined the cytotoxicity of Aβ monomers incubated with or without ERB analog for 5 days, and the results are shown in Figure 3.2B. 5 μM of Aβ aggregates without any ERB analog (Aβ control) substantially reduced the cell viability to 63%. Co-incubation of Aβ monomers in the presence of 3x EOB (15 μM) resulted in an SH-SY5Y cell viability was 65%, which is not significantly different from that of Aβ control. However, co-incubation of Aβ monomer with 3x ERB, EOY, or PHB significantly increased the cell viability (around 21%). In the presence of 3x ROB, cell viability was 70%, which is only 7% higher than that of the Aβ control. The MTT reduction assay results clearly indicate that 3x ERB, EOY, and PHB can substantially inhibit Aβ-associated cytotoxicity but 3x EOB cannot. The Aβ monomers incubated with 3x ROB (15 μM) led to a substantial reduction in the cell viability (30%). However, since 3x ROB alone (no Aβ) was intrinsically toxic and led to a similar reduction in cell viability (34%), it is difficult to gauge the effect that 3x ROB coincubation had on Aβ-induced cytotoxicity. In order to clarify this, we repeated the MTT cell viability assay, this time comparing the results obtained using 2.5 μM and 5 μM Aβ, both with corresponding concentrations of 3x ROB (7.5 μM and 15 μM, respectively – Figure B1; Panels A and B in the Supporting Information). Since the ThT fluorescence of the Aβ aggregates reach a plateau at day 6, the Aβ aggregates in day 3 were used as Aβ intermediate controls. When 5 μM Aβ and 15 μM ROB was used, we again observed a substantial reduction in cell viability upon the addition of 3x ROB alone and Aβ intermediate controls compared to Aβ monomer and PBS samples (Figure C1; Panel A). However, when concentrations of 2.5 μM Aβ and 7.5 μM ROB were applied to

the cells, the intrinsic cytotoxicity of ROB alone (no Aβ) was greatly reduced to approximately the level of the Aβ monomer control (Figure C1; Panel B). These results allowed us to interpret the true effect ROB had on Aβ-induced toxicity. Similar to EOB, coincubation of Aβ monomers with 3x ROB for 3 days did not significantly alleviate the Aβ-associated cytotoxicity displayed by the Aβ intermediate control. Next, in order to investigate the effect that dye binding to Aβ had on Aβ-associated toxicity, Aβ intermediates from day 3 of aggregation were mixed with 3x ROB and immediately added to the SH-SY5Y cells. As with coincubation, the results showed that ROB binding to Aβ did not alleviate the associated toxicity (Figure C1; Panels A and B). In addition, since the Aβ intermediates mixed with 3x ROB immediately prior to addition to the cells showed similar cell viability to the Aβ intermediate control, we concluded that the intrinsic toxicity of ROB and Aβ are not additive.

It should be noted that careful execution of the MTT reduction assay and interpretation of the results is required due to several factors. The first potential issue is that Aβ induces expedited exocytosis of reduced MTT. Several reports have shown that Aβ aggregates can facilitate reduced crystalline MTT deposition on the cell surface leading to decreased MTT uptake (260-262). In our previous studies, there was good correlation between MTT reduction and cell viability which was corroborated by Alamar blue reduction, which maintains solubility upon reduction (248). Therefore, the MTT reduction assay was considered valid with the described cell line and Aβ preparation method. The second issue relates to potential spectral interference between the dyes being investigated and reduced MTT. In order to minimize this potential issue, all viability assays incorporated thorough washing steps, as detailed in the Methods section. To validate the thoroughness of the washing steps, residual dye concentrations were quantified. The results showed that less than 3% of residual dye remained in the wells after washing (Table B1 in

the Supporting Information). Next, we quantified the interference effect these quantities might have on the final MTT absorbance measurement. Our results showed that the interference was less than 5% for all dyes (Table B1 in the Supporting Information), which is consistent with the random uncertainty of the MTT assay (4 to 6%) in Figure 3.2B and Figure B1, which indicates that the dyes do not cause significant spectral interference in the MTT assays.

By correlating the chemical structures of ERB analogs and their inhibitory capacities on Aβ cytotoxicity, we deduced the following. First, EOY, which contains four bromine atoms in the same locations as the four iodine atoms in ERB, exhibited similar inhibitory capacities on Aβ cytotoxicity as ERB. However, EOB, which contains two nitro groups in the place of the two bromine atoms in the xanthene group of EOY, did not show any significant inhibitory capacity on Aβ cytotoxicity. Therefore, these findings clearly indicate that either bromine or iodine atoms in the two positions of xanthene group are critical for Aβ cytotoxicity inhibition. Second, PHB, which contains four extra chlorine atoms in the benzoate ring structure present in EOY, exhibits significant inhibitory capacities on Aβ cytotoxicity (similar to EOY). The third conclusion we made was in regards to ROB, which did not eliminate Aβ-associated cytotoxicity. ROB differs from ERB in that it is outfitted with four extra chlorine atoms in the benzoate ring and differs from PHB in that the bromine atoms on the xanthene group are replaced with iodine. The ROB results clearly indicate that not only the presence, but also the specific position of the halogenation, is important in determining the potency in inhibiting Aβ-cytotoxicity.

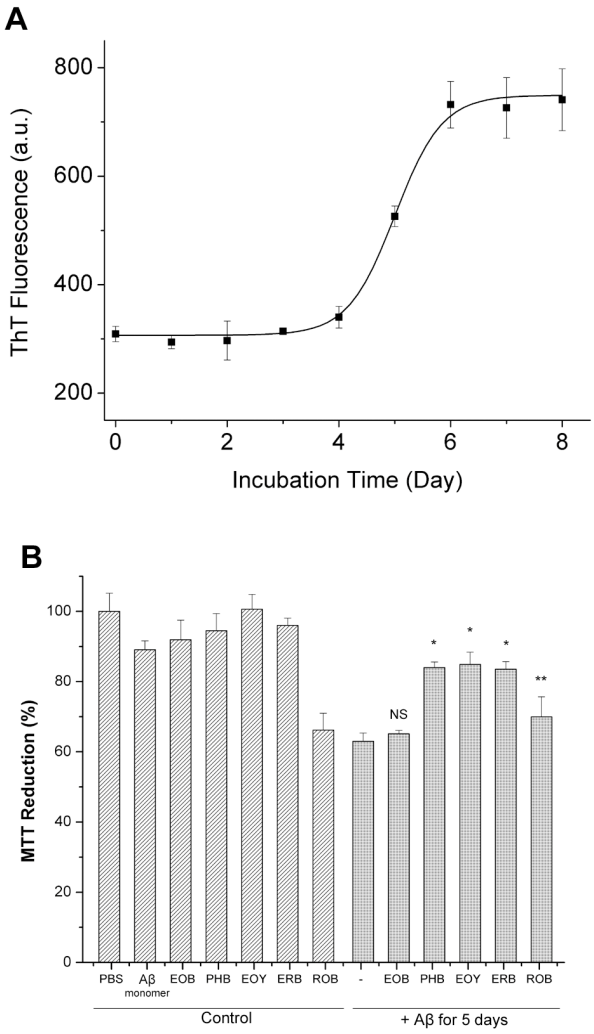

Figure 3.2. Monitoring Aβ aggregation by ThT fluorescence assay and measuring Aβ-associated cytotoxicity using MTT reduction assay. (A) Time course of ThT fluorescence of Aβ samples. 50 μM of Aβ monomer was incubated at 37 °C. 5 μL of Aβ sample was taken daily for 8 dyes for ThT fluorescence analysis. ThT fluorescence was measured in arbitrary units (a.u.). Values represent means ± standard deviation (n = 3). (B) Viability of neuroblastoma SH-SY5Y cells incubated with ERB analog controls and pre-formed Aβ samples in the absence or presence of ERB analog. Preformed Aβ aggregates were prepared by incubating 50 μM of Aβ monomer in the absence or presence of ERB analog (EOB, PHB, EOY, ERB, EOY, or ROB) at 37 °C for 5 days. Aggregates were then administered to SH-SY5Y cells at a final concentration of 5 μM. After 48 hours, MTT reducing activity was measured. Values represent means ± standard deviation ($n \geq 3$). Values are normalized to the viability of cells administered with PBS only. Two-sided Student's t-tests were applied to the MTT reduction data of Aβ aggregates in the presence of ERB analog at day 5 compared to that of the Aβ only control. (NS; Not significant, *; $P < 0.001$, **; $P < 0.05$).

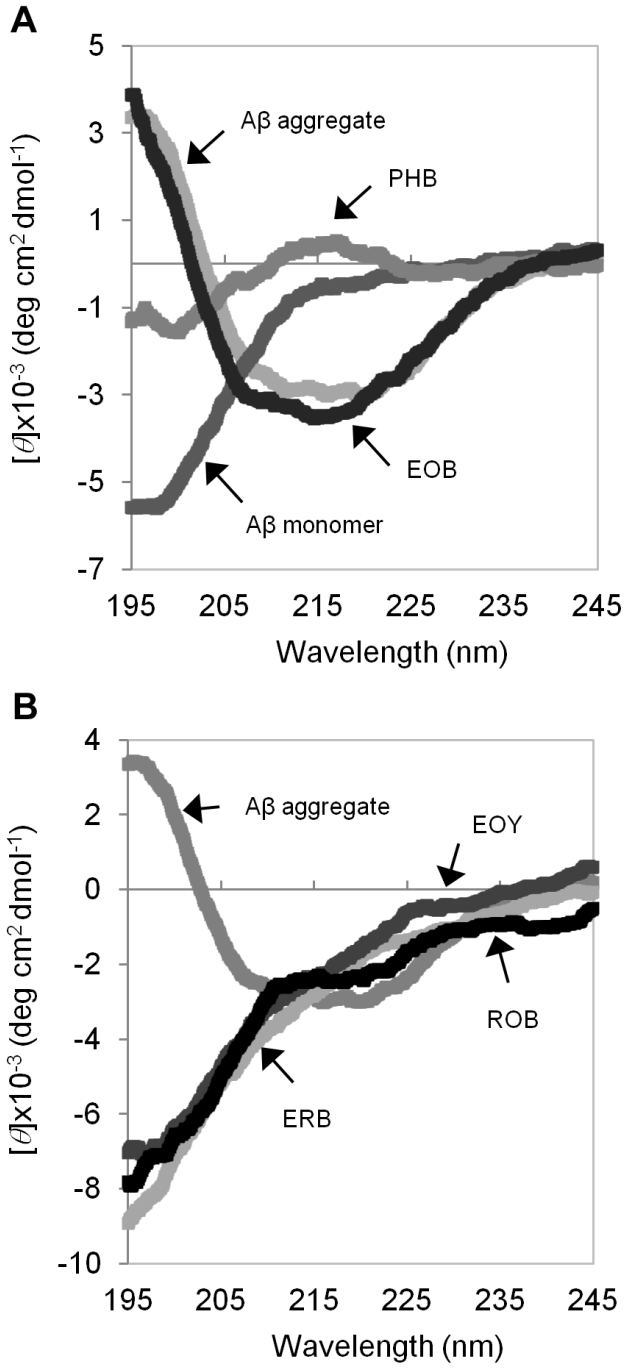

Figure 3.3. CD spectra of Aβ monomer and preformed Aβ aggregates. (A) CD spectra of Aβ monomer, Aβ aggregates formed in the absence or presence of 10x EOB or PHB for 5 days at 37 °C. (B) CD spectra of Aβ aggregates formed in the absence or presence of 10x EOY, ERB, or ROB for 5 days at 37 °C.

Aβ Monomers Aggregate to Form Prefibrillar and Fibrillar Aggregates

In order to determine whether Aβ cytotoxicity inhibition by ERB analogs is associated with Aβ aggregation modulation, we characterized the Aβ aggregates formed in the absence or presence of each ERB analog using CD, TEM, and dot-blot assays. CD analysis has been widely used to monitor secondary structure changes of proteins (14, 263-265). The CD spectrum of Aβ monomer did not exhibit any spectral feature of α-helix and β-sheet, but showed typical features of dominantly disordered structure (Figure 3.3A). The CD spectrum of Aβ aggregates at day 5 exhibited the typical signatures of β-sheet structure, including a minimum at 217 nm (Figure 3.3A), which indicate that disordered Aβ monomers aggregated into β-sheet rich fibrillar aggregates.

The TEM image of Aβ monomers incubated for 5 days also clearly show the existence of the Aβ aggregates consisting of protofibrils and short fibrils (Figure 3.4; Panel Aβ only). Recently, dot-blotting with Aβ-specific antibodies was widely used to detect the spectrum of Aβ aggregates with different conformations (20, 80, 198, 205-207, 242). OC is a polyclonal antibody that reacts with neurotoxic fibrillar oligomers, protofibrils and fibrils (80, 206). It was shown that Aβ-associated toxicity could be eliminated by reducing the OC-reactive species (80). Dot-blot assay using the OC antibody confirmed the existence of fibrillar structure at day 5 (Figure 3.5; Panel OC). 4G8 is an Aβ-sequence-specific monoclonal antibody (208-211) of which epitope is known to be residues 17 to 24 of Aβ. During transition from monomers to fibrils, β-sheet stacking buries the 4G8 epitope and ultimately limits 4G8 antibody access to the epitope leading to a significant reduction in the 4G8 reactivity (245, 248, 266). Therefore, the reduction in 4G8 reactivity of Aβ aggregates at days 5 and 6 can be attributed to the formation of fibrils and the lateral fibril stacking (Figure 3.5; Panel 4G8). A11 is a polyclonal antibody that reacts

with disordered prefibrillar aggregates (80). The weak A11-reactivity of the Aβ aggregates at day 5 indicate that content of disordered prefibrillar Aβ aggregates was low (Figure C2 in Supporting Information). Therefore, the CD, TEM, and dot-blot results using Aβ-specific antibodies clearly show that the Aβ aggregates at day 5 mainly consist of fibrillar aggregates including protofibrils and short fibrils.

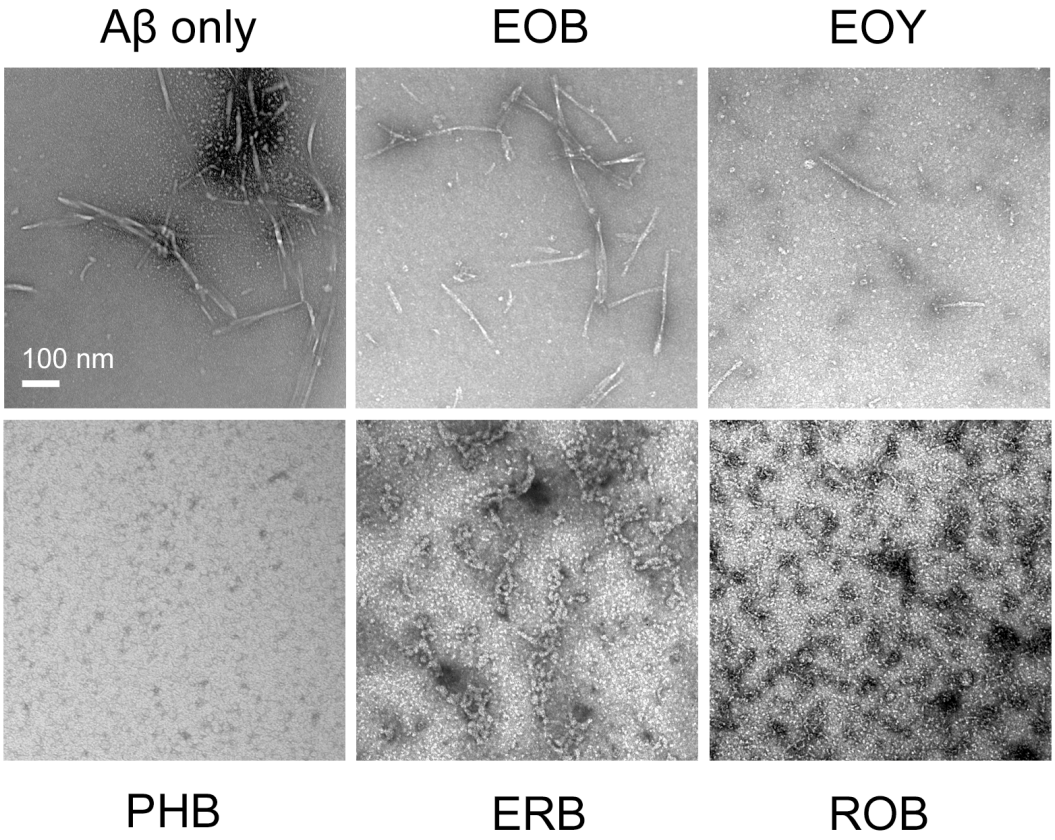

Figure 3.4. TEM images of 50 μM of Aβ incubated for five days at 37 °C in the absence of any dye (Aβ only), or in the presence of 3x EOB, EOY, PHB, ERB, or ROB. Scale bar is 100 nm.

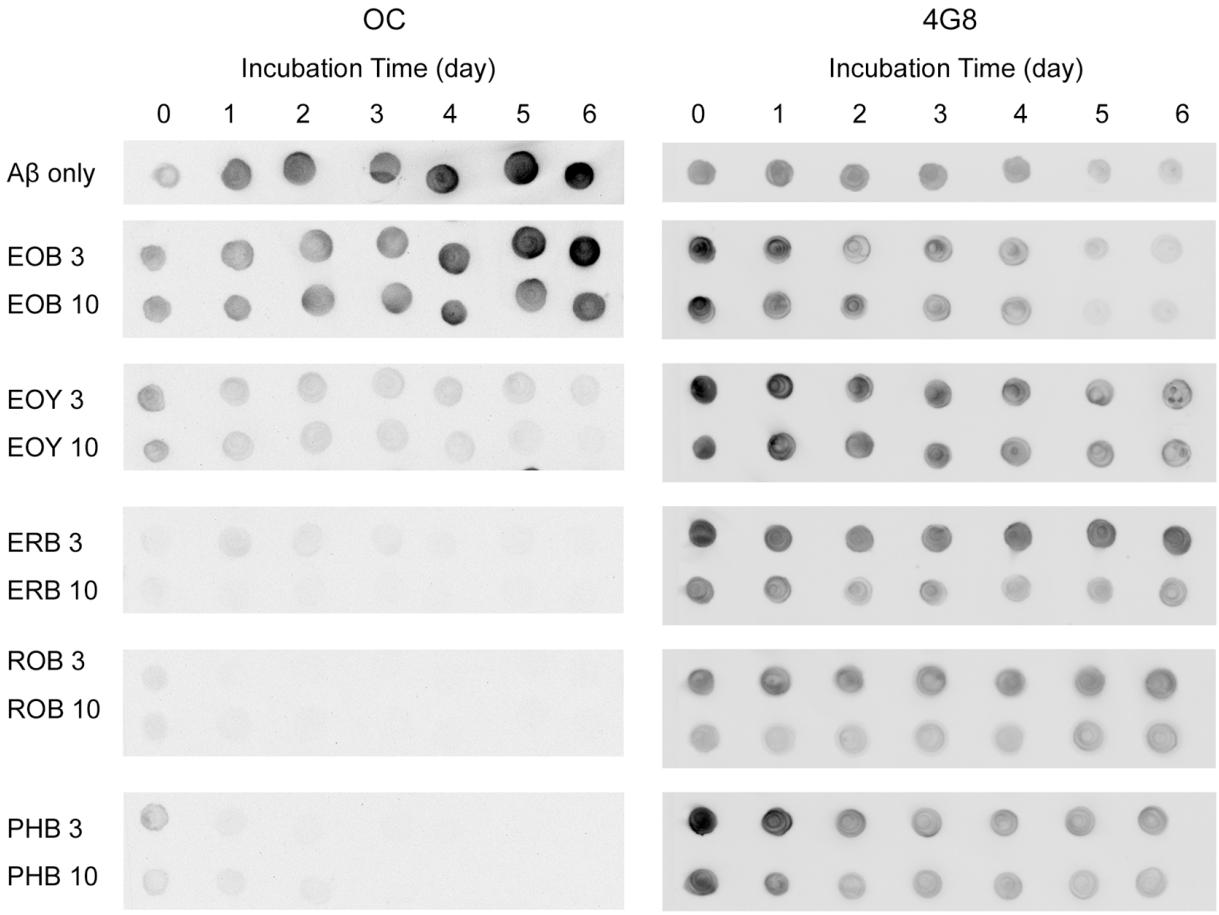

Figure 3.5. Modulation of Aβ aggregation by ERB and ERB analogs. 50 μM of Aβ monomer was incubated at 37 °C in the absence (Aβ only) or presence of 3x and 10x ERB analogs (EOB, EOY, ERB, ROB, and PHB) for up to 6 days. For each antibody, all samples were spotted onto one nitrocellulose membrane. Each membrane was immuno-stained with the OC or 4G8 antibody. For clearer presentation of the data, the sections of each membrane were cut and re-arranged.

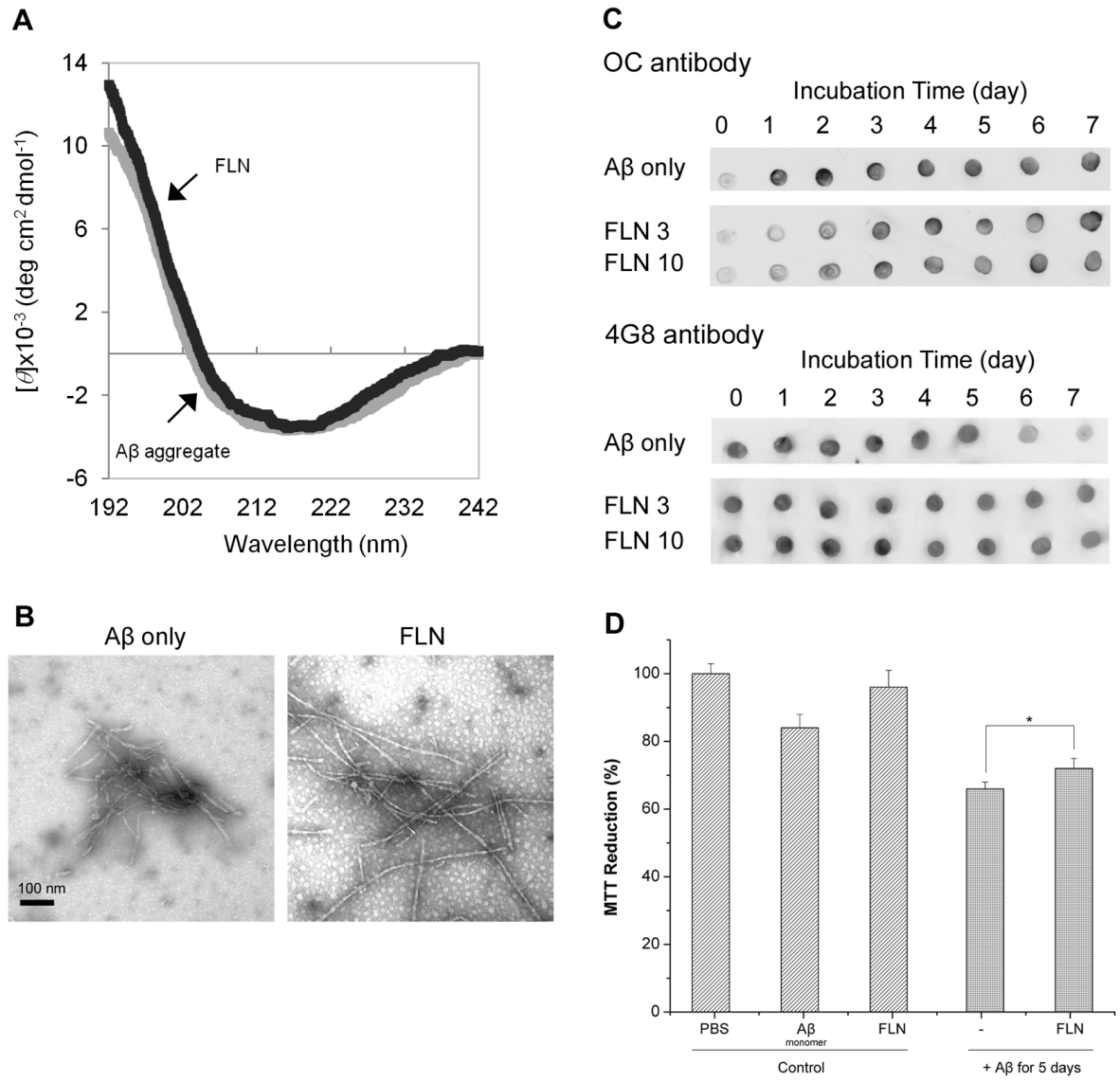

Figure 3.6. Modulation of Aβ aggregation and cytotoxicity by FLN. (A) CD spectra of Aβ monomer incubated for 7 days at 37 °C in the absence (Aβ aggregate) or presence of 10x FLN (FLN). (B) TEM images of 50 μM of Aβ incubated for seven days at 37 °C in the absence of any dye (Aβ only), or in the presence of 3x FLN. Scale bar is 100 nm. (C) Dot blot images of Aβ aggregates formed without (Aβ only) or with 3x and 10x FLN using OC and 4G8 antibodies. For each antibody, all samples were spotted onto one nitrocellulose membrane. Each membrane was immuno-stained with the OC or 4G8 antibody. For clearer presentation of the data, the sections of each membrane were cut and re-arranged. (D) Viability of neuroblastoma SH-SY5Y cells. Three controls (PBS buffer, Aβ monomer, and FLN) and two Aβ aggregates formed in the absence or presence of 3x FLN at 37 °C for 5 days. Values represent means ± standard deviation ($n \geq 3$). Values are normalized to the viability of cells administered with PBS buffer only. Two-sided Student's t-tests were applied to the MTT reduction data. (*; $P = 0.013$).

EOB Does Not Modulate Aβ Aggregation, but PHB Substantially Inhibits Aβ Aggregation

Next, we characterized the Aβ aggregates formed in the presence of 3x or 10x EOB. The CD spectrum of Aβ aggregates formed with EOB exhibits dominant β-sheet structure, possibly fibrillar structures, similar to that of Aβ control (Figure 3.3A). The TEM images also show that the EOB-induced Aβ aggregates have protofibrils and short fibrils similar to the Aβ control (Figure 3.4; Panels EOB and Aβ only). Furthermore, the EOB-induced Aβ aggregates exhibit immuno-reactivity against OC-, 4G8-, and A11-antibodies similar to those of the Aβ control from days 0 to 6 (Figure 3.5; Figure B2 in Supporting Information). The CD, TEM, and dot-blot assay results clearly indicate that the co-incubation of EOB with Aβ monomer does not substantially affect Aβ aggregation process, which is consistent with the MTT reduction results showing that the cytotoxicity of the EOB-induced Aβ aggregates was comparable to that of Aβ control (Figure 3.2B). These findings indicate that addition of two nitro groups and two bromine atoms to xanthene benzoate does not enhance modulatory capacity on Aβ aggregation and cytotoxicity. However, considering the possibility of negative effects of two nitro groups on the modulatory capacity of halogenated xanthene benzoates, we also tested the other xanthene benzoate derivatives which contain only halogen atoms.

In case of PHB, the CD, TEM, and dot-blot assay results clearly indicate that co-incubation of Aβ monomer with PHB significantly inhibits the Aβ aggregation process (Figures 3.3A, 3.4, and 3.5). First, the CD spectrum of the Aβ monomers co-incubated with PHB for 5 days do not show any typical features of α-helical and β-sheet structure strongly indicating that the PHB-induced Aβ species has the disordered structure (Figure 3.3A). In the TEM image of the PHB-induced Aβ species, no Aβ aggregates were observed (Figure 3.4; Panel PHB)

indicating no large molecular weight aggregates are present in the Aβ sample. Since no aggregates were detected in the TEM image, the dot-blot assays using fibrillar or disordered oligomer-specific antibodies (OC- or A11-antibodies) were employed to monitor formation of Aβ oligomers. The Aβ monomers co-incubated with either 3x or 10x PHB exhibit neither OC- nor A11-reactivity, indicating that the PHB-induced Aβ species were neither fibrillar nor disordered prefibrillar Aβ oligomers (Figure 3.5 Panel OC; Figure B2 in the Supporting Information). Therefore, the TEM, CD, and dot-blot assay results strongly support the idea that co-incubation of PHB significant inhibits formation of any Aβ oligomers/higher molecular weight aggregates, but allows maintaining Aβ monomer-like structural features. Considering that Aβ monomer is known to be a non-toxic species (80, 245, 248), the substantial reduction of Aβ-associated cytotoxicity by co-incubating Aβ monomer with PHB can be attributed to the Aβ monomer-like structure of the PHB-induced Aβ species.

EOY, ERB, and ROB Substantially Inhibit Fibrillar Structure Formation

We then characterized the Aβ aggregates formed in the presence of 3x or 10x EOY, ERB, or ROB. The three CD spectra of the Aβ aggregates formed with one of the three ERB congeners (10x EOY, ERB, and ROB) were almost overlapped (Figure 3.3B), indicating that the secondary structure contents of the Aβ aggregates are similar. The negative epllipticity value over all ranges of wavelength and the strong negative ellipticity values below 200 nm indicate the typical features of denatured proteins (267) or disordered Aβ aggregates induced by small molecules (80, 89). Therefore, the CD analysis results support the idea that the three Aβ aggregates formed with EOY, ERB, and ROB have an increased disordered structure content but a decreased β-sheet structure (possibly fibrillar structure) compared to Aβ control. However, the

overlapped CD spectra of the Aβ samples with the three 10x dyes make it difficult to determine relative Aβ-aggregation modulating capacities of the three dyes. Therefore, the CD spectrum of the Aβ aggregates formed with a lower concentration (3x) of EOY, ERB, or ROB was also obtained (Figure C3 in Supporting Information). The estimated β-sheet content, possibly fibrillar structure, of the Aβ samples with the three dyes based on the ellipticity value around 217 nm is in descending order of EOY, ERB and ROB. The TEM images of the three Aβ aggregates formed with EOY, ERB, and ROB also show that the morphology of the three Aβ aggregates are quite different from that of Aβ control (Figure 3.4). The EOY-induced Aβ aggregates are primarily small protofibrils in the length of 20 to 40 nm and a small portion of ~ 100 nm straight protofibrils (Figure 3.4; Panel EOY), whereas the Aβ control mainly consisted of protofibrils and fibrils in the length of > 300 nm (Figure 3.4; Panel Aβ only). The ERB-induced Aβ aggregates are curvilinear aggregates protofibrils, suggesting that the disordered structure content is higher than that of the Aβ control (Figure 3.4; Panel ERB). The ROB-induced Aβ aggregates also appeared as curvilinear protofibrils, but are thinner than the ERB-induced Aβ aggregates (Figure 3.4; Panel ROB). Dot-blot assays using the OC and A11 antibodies were employed to estimate the relative amount of fibrillar and prefibrillar aggregates in the Aβ samples. At day 5, the EOY-, ERB-, and ROB-induced Aβ aggregates were in descending order of OC-reactivity (Figure 3.5; Panel OC), which is quite consistent with the trend found in the CD analysis (Figure C3 in the Supporting Information). In contrast, the ROB-, ERB-, and EOY-induced Aβ aggregates were in the descending order of A11-reactivity (Figure C2 in Supporting Information). Since the ROB-induced Aβ aggregates exhibit very high A11-reactivity, we investigated whether there was any spectral interference of all ERB analogs with the dot-blot assay using the A11 antibody. The

ERB congeners alone as well as the A11-reactive Aβ aggregates were spotted to a nitrocellulose membrane and then the A11-reactivity of the samples was determined. Only ROB exhibits a significant A11-reactivity comparable to those of Aβ samples (Figure C4 in Supporting Information). Therefore, caution should be taken to interpret A11-reactivity of Aβ samples containing ROB. None of the ERB congeners exhibit a significant immuno-reactivity against the OC and 4G8 antibodies (data not shown). The decrease in the OC-reactivity of the ERB analogs can be directly interpreted as a decrease in the fibrillar structure content, but the increase in the A11-reactivity of the ROB-induced should not be interpreted as an increase in the prefibrillar content.

For all three ERB congeners (EOY, ERB and ROB), the CD spectra, TEM images, and dot-blot assay using OC-antibody clearly indicate that there was a substantial of reduction in the fibrillar structure. Combined with the MTT reduction assay results (Figure 3.2B), such a reduction in the fibrillar structure can be attributed to a reduction in the Aβ-associated cytotoxicity for EOY and ERB. Although the A11-reactivity of the ROB-induced Aβ aggregates is greater than that of the Aβ control, the A11-reactivity is most likely overestimated. It is also interesting to note that even though ROB did not reduce Aβ-associated cytotoxicity in the MTT assay, these results show that it is clearly a potent inhibitor of the Aβ-aggregation.

FLN Does Not Effectively Modulate Aβ Aggregation and Cytotoxicity

Investigating the modulatory capacities of ERB congeners on Aβ cytotoxicity and aggregation reveals that even a subtle change in their chemical structure from the ERB structural template can affect their modulatory capacities. In order to further validate our hypothesis that the modulatory capacities of the ERB congeners are related with the presence of halogen atoms,

we also evaluated the modulatory capacities of FLN as a negative control without any halogen atoms (Figure 3.1). The CD spectrum of the FLN-induced Aβ aggregates clearly exhibits the typical features of β-sheet rich structure (Figure 3.6A). The TEM image of the FLN-induced Aβ aggregates also indicates that protofibrils and fibrils are dominant species similar to the Aβ control (Figure 3.6B). Furthermore, the OC-reactivity of the Aβ aggregates formed with FLN at days 5 and 6 are very comparable to those of the Aβ control (Figure 3.6C), indicating that the FLN-induced Aβ aggregates had fibrillar aggregates as much as the Aβ control. The 4G8-reactivity of the FLN-induced Aβ aggregates with FLN remained unchanged up to day 7, whereas the 4G8-reactivity of the Aβ control dropped at day 5. Such a slightly higher 4G8-reactivity of the FLN-induced Aβ aggregates at day 5 is likely because the FLN-induced fibrils are not laterally stacked and so allow the 4G8 binding to its epitope better than the Aβ control. The CD, TEM, and dot-blot assay results conclusively demonstrate that FLN does not modulate the Aβ aggregation as much as EOY, ERB, or ROB.

Next, we investigated whether FLN affects the Aβ-associated cytotoxicity. Similar to the ERB analogs, Aβ monomers were incubated in the absence of or presence of FLN for 5 days, and the resulting aggregates were subjected to the MTT reduction assay. The viability of the SH-SY5Y cells treated with the Aβ control (5 μM) was 66% (Figure 3.6D). Co-incubation of the Aβ monomer with FLN led to a small increase in the cell viability (6%) (Figure 3.6D), but the difference was only marginally significant ($P = 0.013$), while ERB, EOY, and PHB led to a substantial increase in the cell viability ($P < 0.001$). The MTT assay results indicate that FLN did not substantially eliminate Aβ cytotoxicity, which is consistent with the fact that FLN did not modulate Aβ aggregation.

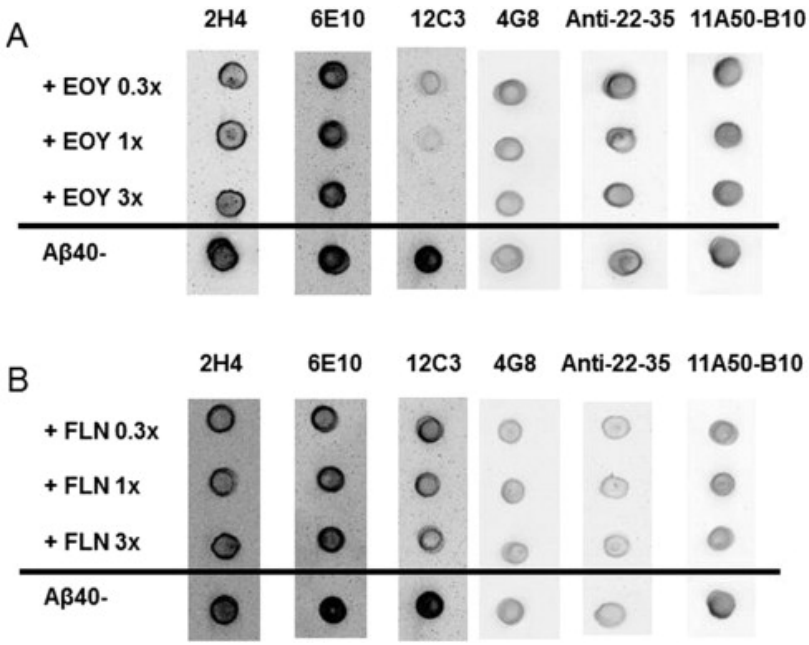

Figure 3.7. Less halogenated xanthene benzoate ligand binding site identification using sequence-specific antibody panel. Shown are representative dot blotting results of Aβ40 monomers mixed with (+ ligand) or without (Aβ40-) 0.3 to 3× molar excess concentrations of EOY (A) or FLN (non-halogenated, weakly binding control molecule) (B) for the six sequence-specific antibodies and then dotted within 5 min after mixing. For better ease of viewing, each antibody was developed on a separate membrane and then cut and pasted for the compiled results.

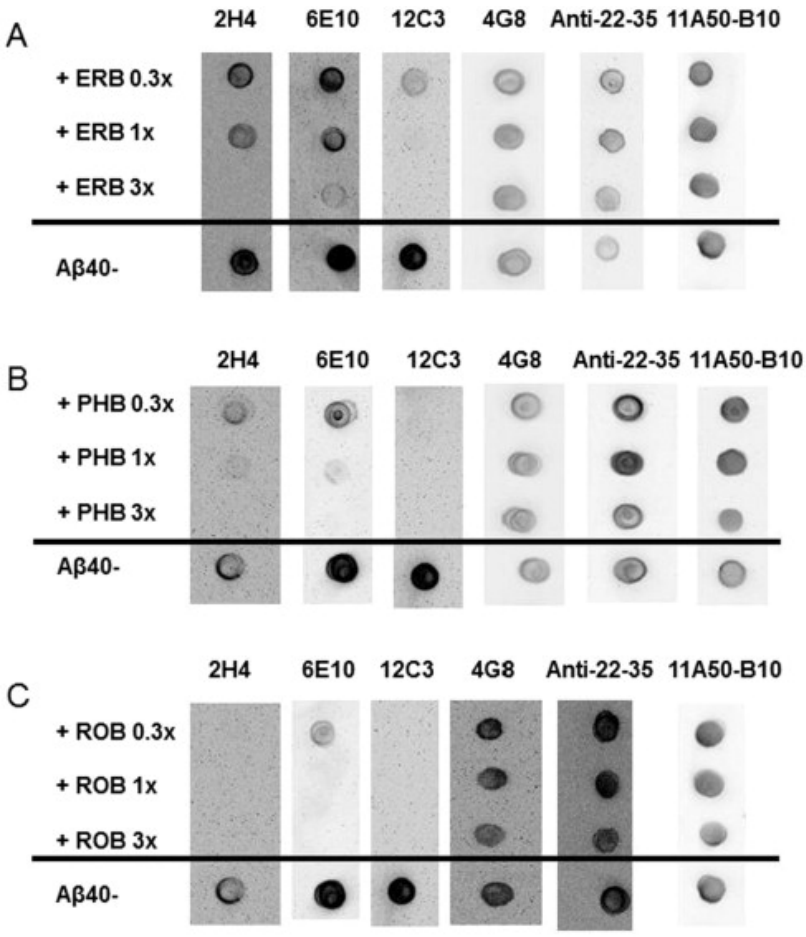

Figure 3.8. More extensively halogenated xanthene benzoate ligand binding site identification using sequence-specific antibody panel. Shown are representative dot blotting results of Aβ40 monomers mixed with (+ ligand) or without (Aβ40-) 0.3 to 3× molar excess concentrations of ERB (A), PHB (B), or ROB (C) for the six sequence-specific antibodies and then dotted within 5 min after mixing. For better ease of viewing, each antibody was developed on a separate membrane and then cut and pasted for the compiled results.

Table 3.1. Binding properties of ERB analogs to Aβ40 monomers.

Dye (20 μM)	ERB	EOY	PHB	ROB	EOB	FLN
Dissociation Constant (μM)	3.35	0.14	0.89	1.36	Poor Binding	Poor Binding
Number of binding sites	2.1	1.4	1.4	2.0	Poor Binding	Poor Binding

Halogenation of Xanthene Benzoate Generates Efficient Binders of Aβ

Having discovered from the CD, TEM, and dot-blotting results that ROB, PHB, ERB, and EOY (but not EOB and FLN) are potent inhibitors of Aβ aggregation, we then investigated possible correlations between these inhibition results and the binding affinity of the dyes to Aβ. Dissociation constant (K_d) values and the number of binding sites were calculated for ROB, PHB, ERB, and EOY using fluorescence quenching of 20 μM concentrations of the dyes upon binding to Aβ (Table 3.1). The results showed that EOY most strongly binds Aβ among the dyes used in this study. Intriguingly, the FLN (negative control lacking halogen atoms) quenching results showed that FLN has exceptionally poor binding affinity for Aβ with less than 3% of the dye bound even in the presence of an excess molar concentration of 25 μM Aβ (Figure C5 A in the Supporting Information). In order to maintain consistency with the other five small molecules, our first preference was to employ a similar fluorescence quenching technique to assess the binding of 20 μM EOB (analog of EOY with replacement of the two bromine atoms close to benzoate group in EOY with two nitro groups) to Aβ40. Despite varying reports in the literature about the fluorescence of the EOB molecule (250-253) and trying various solvents and pH conditions (acids, bases, alcohols), in our hands, the EOB fluorescence was too low for use in the quenching assay. Therefore, we employed an assay based on the characteristic shift in the absorbance maximum of EOB upon protein binding. The results showed that like FLN, EOB weakly binds Aβ with less than 3% of the dye bound even in the presence of an excess molar concentration of 25 μM Aβ (Figure C5 B in the Supporting Information). The number of binding sites on Aβ40 for the four dyes (RRB, EOY, ROB, and PHB) ranges between 1.5 and 2 suggesting that these dyes interact with multiple sites of Aβ40. The multiple binding sites may

explain different properties of the Aβ aggregates induced by the dyes. Since EOB and FLN displayed very poor binding affinity to Aβ and were also poor inhibitors of Aβ aggregation, it clearly demonstrates that halogenation is very effective in generating molecules that tightly bind and consequently modulate the aggregation of Aβ.

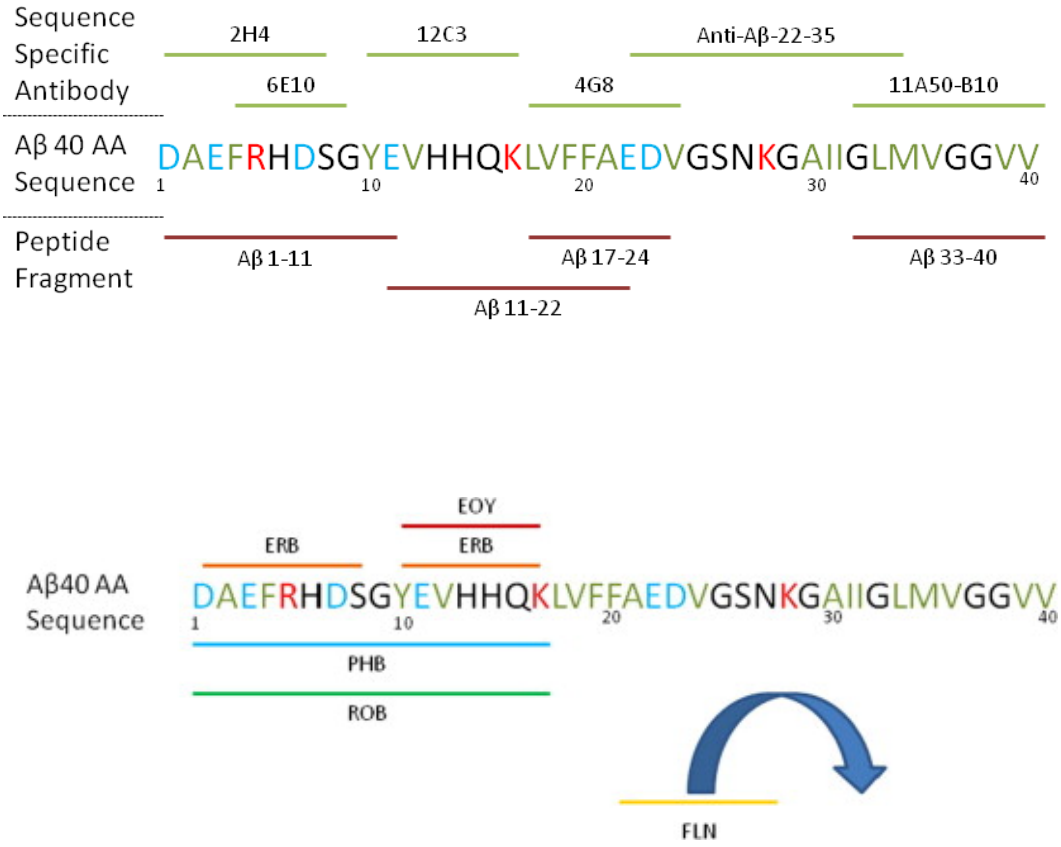

Figure 3.9. Summary of strong binding sites for Aβ40 aggregation modulating ligands. FLN (weakly binding, non-aggregation-modulating control molecule) does not strongly bind. ERB, EOY, PHB, and ROB all strongly bind to the common loci of AAs 10–16 on Aβ40. ERB, PHB, and ROB also bind strongly to other sites on the N terminus. The top panel shows the binding location and coverage of the sequence-specific antibodies. The lower panel shows the binding location of ERB, EOY, PHB and ROB.

Heavy Halogen Atoms Play a Key Role in Modulating Aβ Aggregation

Taken together, the TEM, CD, dot-blot, dye binding, and MTT reduction assay results indicate that FLN (negative control) without any halogen atom does not bind and modulate the Aβ aggregation and cytotoxicity, whereas ERB congeners (ERB, EOY, PHB) containing multiple halogen atoms substantially modulated the Aβ aggregation and effectively reduced the Aβ cytotoxicity. Considering that FLN has a polyphenol-like structure but is a very poor Aβ aggregation modulator, the molecular mechanism underlying the Aβ aggregation modulation by ERB congeners was different from those of polyphenols. The assay results strongly support the idea that halogen atoms in the ERB congeners play an important role in the modulating Aβ aggregation, and in the case of ERB, PHB, and EOY, ultimately Aβ cytotoxicity. Having established this, the next issue becomes determining which specific features of halogen atoms are critical in modulating the Aβ aggregation.

From the CD, TEM, and dot-blot results of FLN and ERB analogs, several trends were found. First, the electronegativity of the halogen atoms/functional groups attached to xanthene group play an important role in Aβ aggregation modulation. Although the results clearly show that EOY (which has four bromine atoms attached to the xanthene group) and ERB (which has four iodine atoms attached to the xanthene group) are both potent inhibitors of Aβ fibril formation, ERB was slightly more effective than EOY at reducing the formation of fibrillar structures in the dot blotting and TEM assays. Furthermore, when the two bromine atoms close to benzoate group in the EOY structure are replaced with the two nitro groups in EOB, the inhibitory capacities of the small molecule on Aβ fibril formation are eliminated. Therefore, the order of Aβ fibril formation inhibitory capacity by xanthenes constituent group is I (ERB) > Br (EOY) > NO_2 (EOB). Because of this, either the electronegativity or size of the functional group

attached to xanthene ring can be attributed to the inhibitory capacity of the ERB analogs. The order of the electronegativity and size of three atoms/groups is NO_2 > Br > I or NO_2 > I > Br, respectively. Therefore, we concluded that the inhibitory capacities are inversely proportional to the electronegativity of functional group attached to xanthene group rather than size, which is consistent with the recent findings on organofluorine Aβ aggregation inhibitors (268). Second, PHB and ROB (both of which contain four chlorine atoms on the benzoate group in addition to xanthenes group structures of EOY and ERB, respectively) led to the potent inhibitory capacities on Aβ aggregation compared to the non-halogenated control molecules, EOB and FLN. This indicates that either polarity change or steric hindrance caused by four chlorine atoms added to the benzoate group resulted in the enhanced inhibitory capacities. However, ROB does not reduce Aβ cytotoxicity, suggesting that both the location and type of halogen atoms on the xanthene benzoate affects the extent of Aβ cytotoxicity inhibition.

Despite the two bromine atoms attached to xanthene benzoate group, EOB is not an effective modulator of Aβ aggregation and cytotoxicity, Alternatively, we speculate that two nitro groups in EOB offset the positive effects of two bromine atoms on the modulatory capacity. Although more studies are required to clearly understand why EOB is not an effective modulator, other halogenated xanthene benzoates without any nitro group clearly exhibited the enhanced modulatory capacity on Aβ aggregation over the xanthene benzoate without any halogen atom (FLN).

Competitive antibody binding analysis reveals that EOY, ERB, PHB, and ROB bind at the N-terminus of Aβ

Previously, we had determined that sequence-specific antibodies were useful for detecting small molecule binding locations on Aβ monomer (36). Tangential to developing a method for determining the small-molecule binding sites using sequence-specific antibodies, we investigated the binding mode for EOY, ERB, PHB and ROB, the four small molecules which were shown to have strong binding interaction with Aβ. These three xanethene benzoate analogs were also shown to be effective modulators and Aβ aggregation and cytotoxicity.

For this purpose we employed a panel of sequence specific antibodies with known binding locations shown in the top panel of Figure 3.9. When Aβ monomer was briefly pre-incubated with EOY, ERB, PHB or ROB, gently washed and immediately dot blotted, we found that a lack of signal for a particular antibody corresponded to a location where the small molecules had bound.

Based on the immunostaining results, we found that each of the small-molecules prevented the 12C3 antibody from binding, indicating a binding locale within amino acid residues 11-16 (Figure 3.7 and 3.8). Since EOY only disrupted 12C3 binding, this suggests that this is its only binding site (Figure 3.7). ERB was also shown to block 2H4 binding while permitting some 6E10 binding. This suggests that ERB has a second binding site which corresponds to amino acid residues 1-4 (Figure 3.8).

PHB, and ROB, on the other hand, exhibited a different binding mode. In addition to blocking 12C3 binding, they also blocked 2H4 and 6E10 binding (Figure 3.8). This suggests that these small molecules have a fairly large binding area consisting of the first sixteen residues. The summary of results is shown in the bottom panel of Figure 3.9. These results corroborate our previous gand shown in Table 3.1. The fact that ROB was found to have two binding sites

suggests that the two sites are non-overlapping and each binding site is partially located within the overlapping region of the antibody binding sites (Figure 3.9).

Conclusions

In this article, our investigation has conclusively established that ERB and two ERB analogs (EOY and PHB) effectively reduce Aβ-associated neurotoxicity by modulating Aβ aggregation. In the case of ROB, while modulating capacities of ROB on Aβ aggregation are prominent, it was not capable of alleviating Aβ-associated neurotoxicity. Comparative studies of ERB and ERB analogs on modulation of Aβ aggregation and cytotoxicity revealed that FLN is not an effective modulator, but adding four heavy halogen atoms (either Br or I) to the xanthene group substantially enhanced the modulatory capacities on Aβ aggregation and cytotoxicity. Adding four Cl atoms to the benzoate group also significantly enhanced the Aβ aggregation modulation. In particular, co-incubation of PHB that contains four bromine atoms in the xanthene group and four chlorine atoms in the benzoate generates the low-molecular-weight Aβ species with disordered structure similar to Aβ monomer, which makes PHB a unique Aβ aggregation modulator. Considering that halogen atoms play an important role in modulating Aβ aggregation and cytotoxicity, ERB analogs are considered a new type of Aβ modulators, halogenated small molecules. To our knowledge, this is the first report demonstrating the heavy halogen atoms added to multiple aromatic rings can confer inhibitory capacities on Aβ-associated cytotoxicity. Our studies can open a door to convert a poor Aβ aggregation modulator into an effective one by adding heavy halogen atoms and serves as guidance to discover or design novel Aβ aggregation modulators. Considering that ERB analogs are effective modulators of α-synuclein implicated in

Parkinson's disease (269), halogenation of small molecules might be a general way to obtain effective modulators of other amyloidogenic peptides and proteins.

Part 2

Investigating enzyme-substrate interaction upon non-natural amino acid incorporation

Chapter 4

An active site mutation with an expanded set of genetically encoded amino acids alters allosteric cooperativity in murine dihydrofolate reductase

Abstract

Cooperative allosteric enzyme control is fundamental to the regulation of biological systems. This control mechanism affords both efficient energy and resource utilization. Dihydrofolate reductase (DHFR) is an important allosterically-active enzyme found in all organisms. The primary function of DHFR is the reduction of dihydrofolate to form tetrahydrofolate. Dihydrofolate reductase metabolism at low substrate concentrations (≤ 200 μM DHF) has Michaelis-Menten kinetics, which is absent of cooperativity. Here we show that wild-type murine DHFR (mDHFR) exhibits positive cooperativity (Hill number, h = 4.0 ± 1.0) at higher substrate concentrations (> 200 μM DHF). The $mDHFR^{E30Nal}$ mutant exhibited continuous positive cooperative kinetics (Hill number, h = 3.5 ± 0.5) throughout the entire concentration range (0 – 1200 μM DHF). Unlike the wild-type, at low DHF concentrations (≤ 200 μM), $mDHFR^{E30Nal}$ kinetics are non-Michaelis-Menten. There is an upward curvature which is consistent with the positive cooperativity (sigmoidal) observed at higher DHF concentrations. A tryptophan mutant $mDHFR^{E30W}$ was created to determine whether the closest natural amino acid anologue to Nal could promote the same behavior. Despite having significantly lower activity, $mDHFR^{E30W}$ exhibited similar kinetic behavior to wild-type, and not $mDHFR^{E30Nal}$, across the entire DHF concentration range (0 – 1200 μM). And consequently it retained Michaelis-Menten kinetics at low DHF concentrations (≤ 200 μM). This indicates that $mDHFR^{E30Nal}$ was able to alter cooperativity at low DHF concentrations (≤ 200 μM) due to its unique size and shape. Because Trp and Nal can only weakly hydrogen bond with DHF, impairing hydrogen bonding between position 30 and DHF is not sufficient alone to alter cooperativity. As each of the mDHFR variants share a similar K_h value, and $mDHFR^{E30W}$ and $mDHFR^{E30Nal}$ share similar k_{cat} values at high DHF concentrations (> 200uM), suggests that the

E30Nal mutation may "lock" mDHFR into a shared conformation that is conducive to cooperativity, and inherently present in mDHFR at high DHF concentrations (> 200 μM DHF). We also found that the E30Nal mutation was highly beneficial to the *E.coli* expression host which allowed disproportionately higher titers than the E30W mutant. To our knowledge this is the first report showing that an expanded set of genetically encoded amino acids can alter the allosteric cooperativity of an enzyme. In particular, this work also shows that non-natural amino acids can elicit responses that are not possible with a similar natural amino acid due to their subtle differences in shape and size.

Introduction

Allostery is a protein regulation mechanism in which the binding of an effector molecule affects another site of the protein (270-275). As biological systems have been evolved for homeostasis, allostery is incredibly important as it enables the control and regulation of energy and resource utilization to maximize efficiency and productivity (272, 276). A number of model proteins have harnessed the power of allosteric control. A classical example is hemoglobin, the oxygen-transport protein in red blood cells. The binding of carbon dioxide at the allosteric site reduces the affinity of hemoglobin for oxygen. Allostery provides hemoglobin its bifunctionality to not only carry oxygen throughout the body but also to take up carbon dioxide for expulsion (277, 278). Another model of allosteric regulation is aspartate carbamoyltransferase (ATCase) which catalyzes the first step in the pyrimidine biosynthesis pathway (279). ATCase has a number of effectors. Binding of the substrate causes ATCase to shift towards the catalytically active state. CTP, an end-product of the pathway, however, causes a decrease in catalytic velocity. And ATP, the product of the parallel purine biosynthesis pathway enhances catalysis (279, 280).

Enzymes typically exhibit hyperbolic enzyme kinetics, which has classically been modeled by the Michaelis-Menten equation (Equation 1) (281).

The Michaelis-Menten (hyperbolic) model for non-cooperative enzyme kinetics:

$$v = \frac{k_{cat}[E][S]}{K_m + [S]} \qquad (1)$$

[E] and [S] are the enzyme and substrate concentration, respectively. k_{cat} is the substrate turnover rate and K_m is the substrate concentration at half-maximal velocity. This simple but elegant model describes the general reaction mechanism by which product is formed upon enzyme and substrate binding. For this type of mechanism, there is no cooperative communication between various regions of the enzyme that can be detected through the kinetics. Allosteric systems, however, can possess cooperativity between sites that can be observed in the reaction kinetics. Cooperative kinetics is generally modeled by the Hill equation which takes on a sigmoidal shape (Equation 2) (271).

The Hill (sigmoidal) model for enzyme kinetics with allosteric cooperativity:

$$v = \frac{k_{cat}[E][S]^h}{{K_h}^h + [S]^h} \qquad (2)$$

For the Hill equation, k_{cat} and K_h are analogous to the Michaelis-Menten parameters k_{cat} and K_m, respectively, while h, the Hill coefficient, numerically describes the degree of cooperativity. Cooperative regulation often acts analogously to feedback and feedforward control (271, 274). An effector can be activating (positive cooperativity) and cause an enhancement to kinetics, or it can be inhibiting (negative cooperativity) and cause a suppression of enzyme activity. Positive cooperativity is present when $h > 1$. Alternatively, negative cooperativity is present when $h < 1$. And when $h = 1$, the Hill equation simplifies to the Michaelis-Menten equation (282).

A number of publications have demonstrated that mutations can alter the allosteric cooperativity of certain enzymes. Often, these mutations are within the catalytic domain. One

example is the mutation of key active-site arginine residues of phosphofructokinase (PFK). The reverse reaction of PFK is characterized by Michaelis-Menten kinetics which is absent of cooperativity. However, mutations of the Arg162 and Arg243 to serine were able to promote positive cooperativity for the reverse reaction, which is evident by the resulting Hill numbers being greater than one (283, 284). Chorismate mutase (CM) from yeast is another well studied allosteric enzyme. Mutational studies have shown that two different catalytic-domain substructures, a loop (residues 212 – 226) and a helix region (reisdues 227 – 251) are independently responsible for the sensitivity of CM towards its two allosteric effectors, tyrosine and tryptophan (285). Mutations can also remove signs of cooperativity in the kinetics. This was accomplished by mutating glutamate and histidine residues in the active site domain of insulin-degrading enzyme, which rendered the enzyme insensitive to its effector (286).

Dihydrofolate reductase (DHFR) is also allosterically-active. The cofactor, NADPH, facilitates the binding of the substrate, dihydrofolate (DHF) (287-290). NADPH mediates the opening and occlusion of the active site through the motion of loop regions (290). Moreover, it has been shown that a network of residues control the overall structure (291, 292). However, cooperativity has not been evident in the enzyme kinetics at lower, more physiologically-relevant, substrate concentrations, where DHF reduction kinetics is normally characterized (293-298). In this regime, the kinetics follows the Michaelis-Menten model where cooperativity is absent (288, 293, 296, 299-307). However, while probing the active site residues through mutation, we discovered that the mutation of Glu30 to 3-(2-naphthyl)-alanine (Nal) (E30Nal), from an expanded set of genetically encoded amino acids, alters the cooperativity of murine DHFR (mDHFR) (Figure 4.1) (308). The objectives of this work are 1) to characterize the kinetic and cooperative behavior of the mDHFR^{E30Nal} mutant and to demonstrate that it is

different from that of wild-type mDHFR, and 2) to compare the kinetic and cooperative behavior between the E30Nal and E30W mutation to determine if the same response can be reproduced with the most structurally similar natural amino acid.

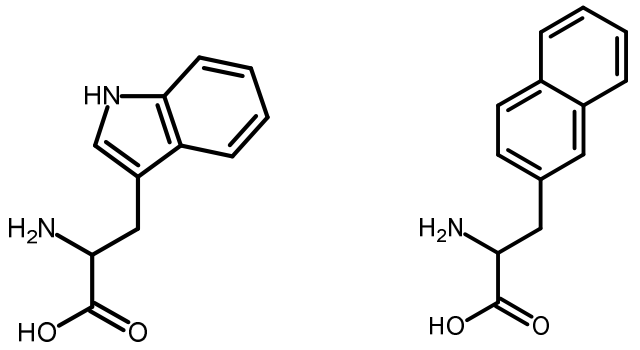

Trp Nal

Figure 4.1. Structures of tryptophan (Trp) and 3-(2-naphthyl)-alanine (Nal).

Materials and Methods

Materials

3-(2-naphthyl)-alanine (Nal) was obtained from Chem-Impex (Wood Dale, IL). The twenty natural amino acids, ampicillin, kanamycin, *L*-(–)-fucose, and 2,5-dihydroxybenzoic acid (DHB) were purchased from Sigma-Aldrich (St.Louis, MO). Dihydrofolic acid (DHF), nicotinamide adenine dinucleotide phosphate (NADPH), and isopropyl β-D-1-thiogalactopyranoside (IPTG) were purchased from Santa Cruz Biotechnologies (Dallas, TX). Sequencing-grade modified trypsin was procured from Promega (Madison, WI). Nickel-nitrilotriaceticacid affinity column resin (Ni-NTA column) and plasmid pQE16 were obtained from Qiagen (Valencia, CA). C18 ZipTip pipette tips were obtained from Millipore (Billerica, MA). All other chemicals, unless otherwise noted, were purchased from Fisher Scientific (Pittsburg, PA) and were used without additional purification.

Expression of wild-Type mDHFR and mDHFR^{E30W}

Wild-type mDHFR and mDHFR^{E30W} are encoded in pQE16-mDHFR^{WT} and pQE16-mDHFR^{E30W}. Each pQE16 plasmid containing the gene for either wild-type mDHFR or mDHFR^{E30W} was transformed into the AFWK (Phe, Trp, Lys auxotroph) *E.coli* expression strain. The enzymes were expressed in M9-20AA media (6 g/L Na_2HPO_4, 3 g/L KH_2PO_4, 0.5 g/L NaCl, 0.1 mM $CaCl_2$, 1 mM $MgSO_4$, 0.4 % glucose, 50 mg/L of each of the 20 natural amino acids) supplemented with 100 mg/mL ampicillin. The cells were grown to OD_{600} = 1.0 and induced with a final concentration of 1 mM IPTG. Cells were harvested after overnight induction at 32 ˚C. The mDHFR being used has the residues MRGSGI appended to the N-terminus and the hexahistidine purification tag located on the C-terminus (171).

Expression of mDHFR^{E30Nal}

The two plasmids pQE16-30Amb_mDHFR-yPheRS^{naph}/pREP4-ytRNA$^{Phe}_{CUA_UG}$ were co-transformed into the AFWK *E.coli* host. The cells were grown in M9-20AA, supplemented with 100 mg/mL ampicillin and 50 mg/mL kanamycin, until OD_{600} = 1.0. Cells were harvested and centrifuged at 4,500 x g for 8 mins. The resulting cell pellet was resuspended and gently washed with 0.9 % NaCl and centrifuged again at 4,500 x g for 8 mins. The resulting cell pellet was resuspended in M9-17AA (6 g/L Na_2HPO_4, 3 g/L KH_2PO_4, 0.5 g/L NaCl, 0.1 mM $CaCl_2$, 1 mM $MgSO_4$, 0.4 % glucose, 0.05 g/L of each of the natural amino acids except phenylalanine, tryptophan, and lysine, which were supplemented at a final concentration of 25 µM, 50 µM and 100 µM, respectively. The M9-17AA was then supplemented with 3 mM of Nal. After incubation at 37 ˚C for 10 mins, induction was initiated by the addition of IPTG to the culture at

a final concentration of 1 mM. The cells were allowed to induce overnight at 32 ˚C. The mDHFR being used has the residues MRGSGI appended to the N-terminus and the hexahistidine purification tag located on the C-terminus (171).

Protein purification

Purification of the mDHFR variants including wild-type was performed using Ni-NTA resin per manufacturer (Qiagen, Venlo, Limburg). The manufacturer protocol was followed with the exception that 20 mM and 40 mM imidazole were used in the lysis and wash buffers, respectively.

Determination of protein concentration

Purity of purified mDHFR variants was determined by analyzing SDS-PAGE protein gels. The protein gel images were taken using a UVP BioSpectrum imager (Upland, CA) and then analyzed by VisionWorks image analysis software. Protein concentration was determined by absorbance measurements at 280 nm, using a calculated extinction of 24,750 $cm^{-1}M^{-1}$ (171).

Confirmation of in vivo Nal Incorporation by MALDI-TOF/MS

Incorporation of Nal in $mDHFR^{E30Nal}$ was confirmed by MALDI-TOF/MS with tryptic digestion. 1 µL of 1 µg/µL trypsin (in 50 mM acetic acid) was added to 10 µL of 5 µM $mDHFR^{E30Nal}$ in elution buffer (50 mM NaH_2PO_4, 300 mM NaCl, and 250 mM imidazole, pH = 8.0). Upon addition, the sample was incubated at 37 ˚C overnight. 12 µL of 5 % trifluoroacetic acid was added to stop the reaction. Digested peptides solutions were desalted using C18 Ziptips according to the manufacturer's protocol (EMD-Millipore, Darmstadt, Germany). 20 mg/mL of

2,5-dihydroxybenzoic acid and 2 mg/mL of L-fucose dissolved in 10 % ethanol was used as the matrix for MS analysis using a Microflex MALDI-TOF/MS (Bruker, Billerica, MA) (171).

Dihydrofolic acid (DHF) reduction kinetics

NADPH-dependent mDHFR reduction of DHF was monitored by measuring the decrease in absorbance at 340 nm using a Synergy four multimode microplate reader (BioTek, Winooski, VT) following manufacturer protocol (Sigma-Aldrich, St. Louis, MO). Reactions were carried out in MTEN buffer 50 mM 2-(N-morpholino)ethanesulfonic acid (MES), 25mM tris(hydroxymethyl) aminomethane (Tris), 25 mM ethanolamine, and 800 mM sodium chloride, pH 7.5). For determining kinetics at low DHF concentrations, the final reaction contained 0 – 200 μM of dihydrofolate (DHF), 300 μM of NADPH, and 5 to 100 nM enzyme, which was added to initiate the reaction. For determining kinetics at high DHF concentrations, the final reaction contained 0 – 1200 μM of dihydrofolate (DHF), 3000 μM of NADPH, and 5 to 100 nM enzyme, which was added to initiate the reaction. Enzyme was pre-incubated with NADPH for 10 minutes prior to addition. All measurements were performed in at least triplicates. Reaction rates with respect to substrate concentration were fit to either the Michaelis-Menten model or the Hill model to obtain kinetic parameters (171, 309). The extinction coefficient for NADPH-dependent DHF reduction reaction is 12,300 M^{-1}/cm at 340 nm at 25 ˚C (310, 311).

Results and Discussion

Hereinafter, mutations will be denoted as E30W, where the E represents the native site residue, 30 denotes the position of the mutation site (based on numbering for PDB:ID 1U72) and Nal and W represent 3-(2-naphthyl)-alanine and tryptophan (Trp), respectively (Figure 4.1).

Preparation of wild-type mDHFR and mutants

mDHFR variants were prepared using the methods described by Zheng (171). Each of the variants were successfully expressed and purified as evident by a clear protein band for mDHFR at 23.5 kDa on SDS-PAGE (Figure 4.2). For $mDHFR^{E30Nal}$ and $mDHFR^{E30W}$, since both Trp and Nal differ in mass from Glu by no more than 68 Da, the protein band migration distance was not noticeably attenuated as a result of the relatively minor mass contribution of Nal or Trp.

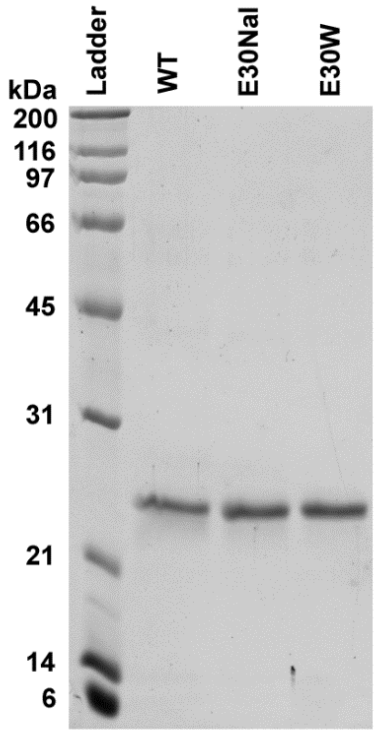

Figure 4.2. SDS-PAGE of purified wild-type mDHFR (WT), $mDHFR^{E30Nal}$ (E30Nal), and $mDHFR^{E30W}$ (E30W). Samples were run on a 12% polyacrylamide gel and stained with Coomassie Blue.

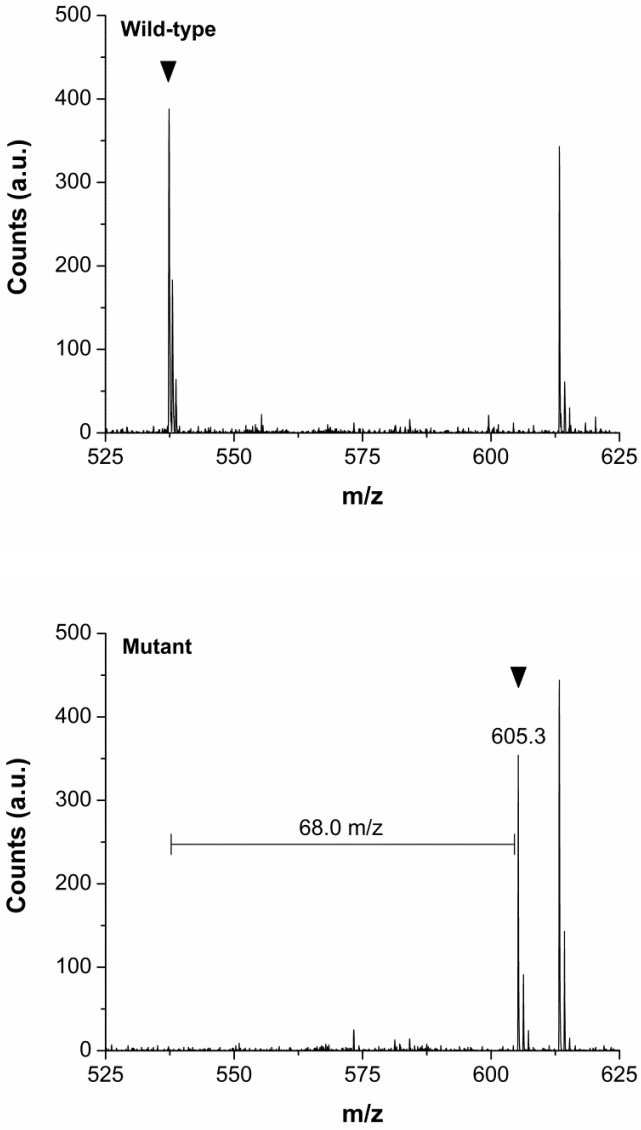

Figure 4.3. Confirmation of in vivo Nal incorporation at position 30 by MALDI-TOF/MS. The residue numbering corresponds to positions based on PDB ID:1U72. The top panel shows the spectrum for the tryptic digest of wild-type mDHFR. The peak corresponding to the wild-type fragment with glutamic acid at position 30 (containing residues 29 – 32) is denoted by the arrow at 537.3 m/z. The bottom panel shows the spectrum for the tryptic digest of $mDHFR^{E30Nal}$. The peak corresponding to the fragment containing Nal at position 30 (containing residues 29 – 32) is denoted by the arrow at 605.3 m/z. The horizontal line denotes the difference in mass between the Nal-containing mutant fragment and the corresponding wild-type fragment. a.u. denotes arbitrary units.

Verification of in vivo Nal incorporation at position 30 of mDHFR by MALDI-TOF/MS

Nal incorporation was accomplished using the engineered, heterologous, orthogonal yPheRS^{naph}/ytRNA$^{Phe}_{CUA_UG}$ pair that is highly specific to Nal. Additionally, the AFWK *E. coli* expression strain, which is a Phe, Trp, and Lys auxotroph, was used to preclude misacylation of ytRNA$^{Phe}_{CUA_UG}$, thus preventing the formation of the most likely misincorporation products with Phe and Trp at the target site. To further confirm the successful expression of mDHFR^{E30Nal}, site-specific in vivo incorporation of Nal at position 30 was verified by MALDI-TOF/MS analysis (171, 308). Nal was successfully incorporated and yielded a unique fragment mass of 605.3 m/z (Figure 4.3, bottom panel). The corresponding wild-type fragment was found at 537.3 m/z (Figure 4.3, top panel). As expected, the difference in mass of the two fragments, 68.0 m/z, was equivalent to the mass difference between Nal and glutamic acid which is 68.0 ± 1.0 m/z. This indicates that Nal was successfully incorporated at position 30 in mDHFR. Also the corresponding wild-type fragment and fragments pertaining to misincorporation of Phe and Trp were not observed in the mutant spectra indicating that Nal was incorporated efficiently at position 30 (Figure 4.3, bottom panel).

The E30Nal mutation shows evidence of cooperativity at low DHF concentrations (0 – 200 μM)

The primary function of mDHFR is to reduce DHF to tetrahydrofolate (THF) (288). Previously, under 200 μM DHF, wild-type mDHFR has been shown to possess Michaelis-Menten kinetics (Equation 1) (171, 288, 293, 296-305, 310-313). Here, as expected, wild-type mDHFR was verified to have Michaelis-Menten kinetics (Figure 4.4A) (314). Wild-type k_{cat} and K_m were determined to be 2.93 ± 0.02 s^{-1} and 2.16 ± 0.18 μM, respectively (Table 4.1). The

coefficient of determination (r^2) for this regression was found to be 0.997 indicating a good fit (Figure 4.4A).

Alternatively, $mDHFR^{E30Nal}$ kinetics exhibited an upward curvature, which suggests a positive cooperative mechanism (Figure 4.4B). This type of kinetic behavior cannot be physically described by the single binding mode and the single reaction energy landscape of the Michaelis-Menten model. To verify the enzyme-dependent nature of this kinetic response, two sets of measurements (0 – 200 μM DHF) were obtained at different $mDHFR^{E30Nal}$ concentrations (50 nM and 100 nM). As expected for an enzyme-dependent response, at 50 nM $mDHFR^{E30Nal}$, for each DHF concentration, the corresponding reaction velocity was approximately half of that of 100 nM $mDHFR^{E30Nal}$ (Figure 4.4B). At both enzyme concentrations, since only DHF concentration was varied, DHF appeared to bolster the rate of its own metabolism which is suggestive of homotropic activation.

To ensure that hysteresis and transient behavior did not bias DHF reduction rates and produce a false-positive cooperative kinetic response for $mDHFR^{E30Nal}$, in addition to pre-incubating each mDHFR sample with NADPH (prior to initiation of the reaction), reaction rates were monitored for up to an hour to ensure that measurements had been made at steady-state. Reaction rates did not show aberrant hystoretic or transient behavior that is normally characterized in mDHFR by a sudden rise or fall in catalytic activity (Figure 4.5) (313, 315).

Due to the suspected cooperative nature of DHF metabolism by $mDHFR^{E30Nal}$, a preliminary regression against the Hill model (Equation 2) was performed (274, 282, 316). Since by up to 200 μM DHF, a saturation (maximum) reaction velocity had not been reached, kinetic parameters could not be obtained for this portion of the kinetics (0 – 200 μM DHF) (Figure 4.4B). Nonetheless, the regression against the Hill model provided a good fit for both the 50 nM

and 100 nM enzyme concentration results. The coefficient of determination (r^2) was found to be 0.999 for both sets of results (Figure 4.4B). This demonstrates that up to 200 μM of DHF, wild-type and mDHFR^{E30Nal} are governed by fundamentally different catalytic regulation mechanisms. While wild-type innately follows Michaelis-Menten kinetics, which is non-cooperative, mDHFR^{E30Nal} displays both non-Michaelis-Menten kinetics and evidence of cooperativity.

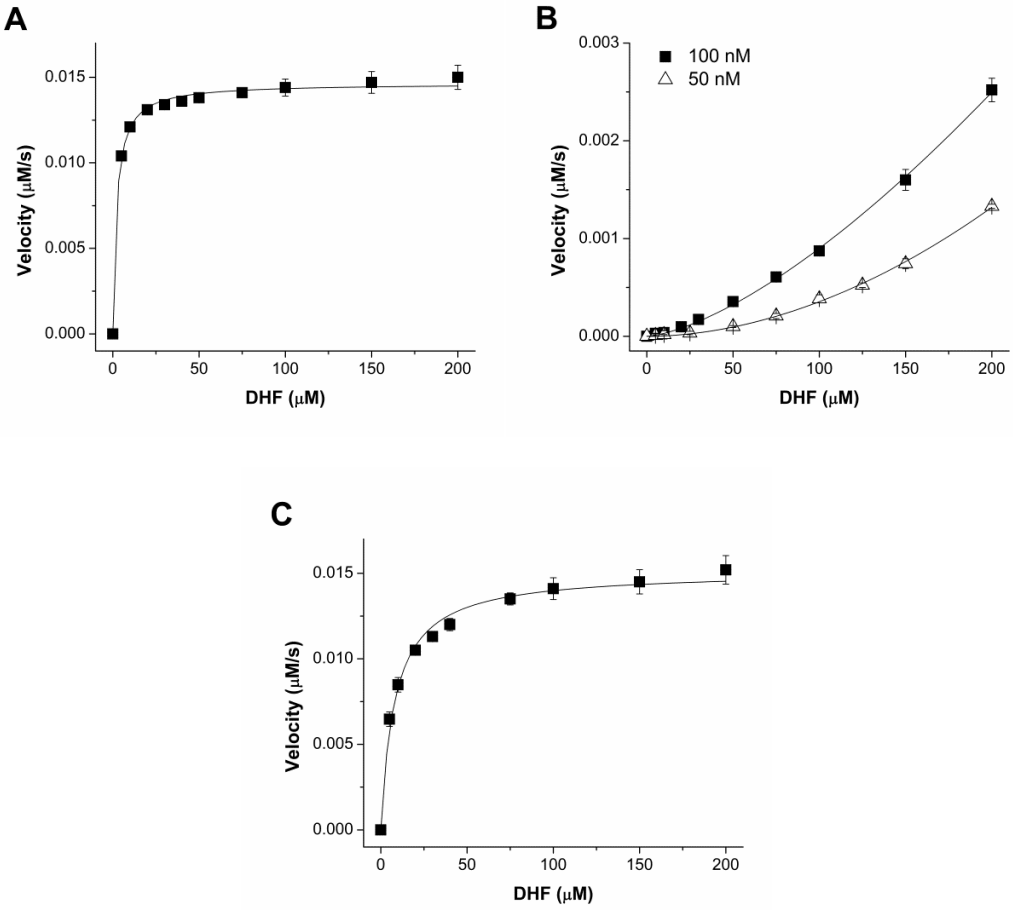

Figure 4.4. mDHFR reaction kinetics at low DHF concentrations (0 – 200 μM DHF). (A) 5 nM wild-type mDHFR (B) 50 nM and 100 nM mDHFR^{E30Nal}, and (C) 100 nM mDHFR^{E30W} were used for kinetic measurements. Reactions were conducted using varying DHF concentrations (0 – 200 μM) and 300 μM of NADPH. Hyperbolic (Michaelis-Menten) regression was performed on wild-type mDHFR and mDHFR^{E30W} kinetics. Sigmoidal (Hill) regression was performed on mDHFR^{E30Nal} kinetics. Error bars denote standard errors (n = 3).

Table 4.1. Michaelis-Menten kinetic parameters for DHF reduction (0 - 200 μM DHF).

Variant	mDHFR^{WT}	mDHFR^{E30Nal}	mDHFR^{E30W}
k_{cat} (s^{-1})	2.93 ± 0.02		0.15 ± 0.003
K_m (μM)	2.16 ± 0.18	Non-Michaelis-Menten Kinetics	8.37 ± 0.77
k_{cat}/K_m (s^{-1}/μM)	1.36 ± 0.11		0.018 ± 0.002
r^2	0.997		0.991

1) WT denotes wild-type.
2) Reactions were conducted with DHF concentrations from 0 – 200 μM and 300 μM NADPH.
3) For mDHFR^{E30Nal}, kinetics did not fit regression to the Michaelis-Menten equation.
4) r^2 is the coefficient of determination. Standard errors are reported (n= 3).

Table 4.2. Hill kinetic parameters for DHF reduction (0 - 1200 μM DHF).

Variant	mDHFR^{WT}	mDHFR^{E30Nal}	mDHFR^{E30W}
k_{cat} (s^{-1})	426 ± 24	1.11 ± 0.09	1.17 ± 0.13
K_h (μM)	511 ± 32	650 ± 41	533 ± 67
k_{cat}/K_h (s^{-1})	0.83 ± 0.06	0.0017 ± 0.0001	0.0024 ± 0.0003
h	4.0 ± 1.0	3.5 ± 0.5	2.7 ± 0.7
r^2	0.998	0.996	0.994

1) WT denotes wild-type.
2) Reactions were conducted with DHF concentrations from 0 – 1200 μM and 3000 μM of NADPH..
3) Regression was performed against the Hill (sigmoidal) model for allosteric cooperativity.
4) r^2 is the coefficient of determination. Standard errors are shown (n = 3).

mDHFR^{E30Nal} has one kinetic mode while wild-type mDHFR has two

In the effort to determine kinetic parameters for mDHFR^{E30Nal}, the substrate concentration range was expanded for kinetic measurements in order to find the maximum (saturation) velocity. The maximum velocity was approached at approximately 1200 μM DHF (Figure 4.6A). Expectedly, mDHFR^{E30Nal} kinetics possessed hallmark features of a continuous sigmoidal response across the entire substrate concentration range (0 – 1200 μM) (Figure 4.6A). Upon regression against the Hill model, the kinetic parameters, k_{cat}, K_h and h were determined to be 1.11 ± 0.09 s^{-1}, 650 ± 41 μM, and 3.5 ± 0.5, respectively (Table 4.2). Since h was greater than one, this verifies that mDHFR^{E30Nal} strongly exhibits positive cooperativity. The coefficient of determination for this regression was found to be 0.996 indicating a good fit. Since for the

kinetic measurements, only DHF concentration was varied, this indicates that mDHFR^{E30Nal} DHF metabolism occurs via homotropic activation.

At substrate concentrate concentrations of up to 200 μM DHF, wild-type mDHFR functioned by Michaelis-Menten kinetics. But like mDHFR^{E30Nal}, it also exhibited the onset of a global maximum velocity at approximately 1200 μM DHF (Figure 4.6B). The activity increase after the first saturation velocity plateau at 200 μM DHF indicates that wild-type mDHFR has additional modes of associating with and reducing DHF. Since the strength of additional modes of association with the same ligand cannot increase without help from an effector molecule, this indicates that above 200 μM DHF, a cooperative mechanism is present. Similarly, stepwise activity increases, such as the transition at 200 μM DHF for a single enzyme system are not possible without a change to the reaction energy landscape (309, 317, 318).

Therefore, the Hill model was applied to obtain wild-type kinetic parameters at high DHF concentrations (> 200 μM DHF). Since cooperativity is present only at higher DHF concentrations, to obtain an accurate representation of the cooperativity, points below 200 μM DHF were excluded from the regression (Figure 4.6B). For wild-type, k_{cat} and K_h were determined to be 426 ± 24 s^{-1} and 511 ± 32 μM, respectively. The Hill coefficient, h, was determined to be 4.0 ± 1.0 (Table 4.2). The coefficient of determination for the regression was found to be 0.998 which indicates a good fit. And with $h > 1$, this indicates that, at higher DHF concentrations, wild-type mDHFR is innately governed by positive cooperativity as well, and also has a significantly higher catalytic activity than mDHFR^{E30Nal} (282, 316).

While DHF metabolism by mDHFR^{E30Nal} occurs continuously by positive cooperativity, over the entire substrate concentration range, wild-type mDHFR has two distinct reaction modes (Figure 4.6B). For wild-type, at lower concentrations (≤ 200 μM) DHF reduction occurs by

Michaelis-Menten kinetics which is absent of cooperativity (Figure 4.4A). And as DHF concentration is increased, kinetics is regulated allosterically by positive cooperativity (> 200 μM DHF) (Figure 4.6B). The fact that wild-type and mDHFR^{E30Nal} have similar K_h (500 μM and 650 μM, respectively) and h (4.0 and 3.5, respectively) values, and both reached their global maximum velocity at around 1200 μM DHF illustrates that the E30Nal mutation is responsible not only for lowering activity but also for altering the cooperativity at low DHF concentrations (≤ 200 μM) (Figure 4.6A and 4.6B).

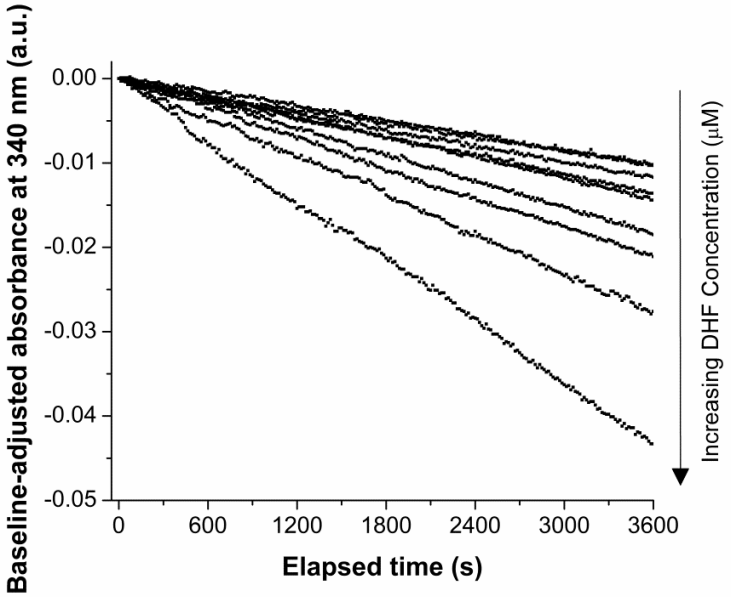

Figure 4.5. Representative baseline-adjusted kinetic measurements for mDHFR^{E30Nal} at varying DHF concentrations (5 – 200 μM). Absorbance measurements at 340 nm were taken 10 minutes after pre-incubation of mDHFR^{E30Nal} with NADPH. The final NADPH concentration was 300 μM. Values were baseline-adjusted so that each measurement start point equals zero on the y-axis (n = 1). Arbitrary units, a.u.

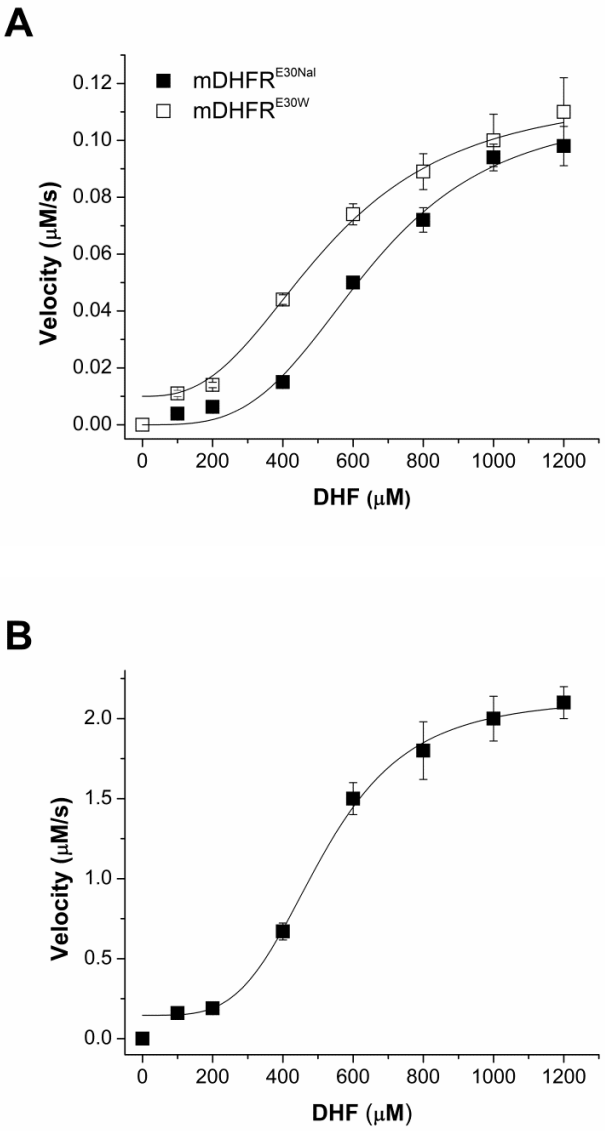

Figure 4.6. mDHFR reaction kinetics at high DHF concentrations (0 – 1200 μM DHF). (A) 100 nM mDHFR^{E30Nal} and 100 nM mDHFR^{E30W} and (B) 5 nM wild-type mDHFR were used for reactions. Reactions were conducted with 0 – 1200 μM of DHF and 3000 μM of NADPH. Sigmoidal (Hill) regression was performed on the saturation kinetics for each mDHFR variant. Wild-type mDHFR and mDHFR^{E30W} kinetics were regressed without points below 200 μM DHF. Error bars denote standard errors (n = 3).

The change in allosteric cooperativity is caused by the particular shape and size of Nal

To determine if the change in cooperativity was attributable to a unique feature of Nal, we created mutant $mDHFR^{E30W}$ (mutation of Glu30 to Trp) as a basis for comparison (Figure 4.1). Tryptophan, like Nal, is a bulky planar hydrophobic amino acid. It has two conjugated aromatic rings and is the natural amino acid with the most similar size and shape to Nal. We expected that if a natural-amino-acid mutation could replicate the cooperative regulation behavior found in $mDHFR^{E30Nal}$, it would be $mDHFR^{E30W}$.

However, interestingly, $mDHFR^{E30W}$ mimicked wild-type and not $mDHFR^{E30Nal}$ behavior. Up to 200 μM DHF, $mDHFR^{E30W}$ followed Michaelis-Menten kinetics (Figure 4.4C). For this concentration range, the k_{cat} and K_m of $mDHFR^{E30W}$ were determined to be 0.15 ± 0.003 s^{-1} and 8.37 ± 0.77 μM, respectively (Table 4.1). The coefficient of determination for this regression was found to be 0.994 and indicates a good fit. Since Trp can only weakly hydrogen bond the pteridin substituent of DHF, the higher K_m for $mDHFR^{E30W}$ compared to that of wild-type is consistent with a lower binding affinity caused by impaired hydrogen bonding between Trp30 and DHF (319, 320). The lower k_{cat} also corroborates previous findings, which demonstrated that Glu30 is involved in DHF metabolism (296, 319, 321, 322).

When the DHF concentration range was expanded, $mDHFR^{E30W}$, similarly to the other two variants, also reached a maximum velocity plateau at approximately 1200 μM DHF (Figure 4.6A). In a similar manner to wild-type, $mDHFR^{E30W}$ was regressed with the Hill model and velocities measured below 200 μM were excluded. k_{cat}, K_h and h were determined to be 1.17 ± 0.13 s^{-1}, 533 ± 67 μM and 2.7 ± 0.7, respectively (Table 4.2). The coefficient of determination was found to be 0.994, indicating a good fit. Like wild-type, $mDHFR^{E30W}$ also possessed two modes of reducing DHF. Interestingly, although in the low DHF regime (≤ 200 μM),

mDHFR^{E30W} possessed a weaker DHF binding affinity (higher K_m) than wild-type, all three variants shared a similar K_h and h value. This indicates that while Glu30 is important for substrate turnover, unencumbered hydrogen bonding between position 30 and DHF is not critical for substrate binding at high concentrations (> 200 μM). Instead hydrogen bonding is more pertinent at low substrate concentrations, evident by the unique binding behaviors of each variant at low DHF concentration (0 – 200 μM DHF). Also since Trp and Nal have weaker hydrogen bonding potential than glutamate, this indicates that impairing hydrogen bonding alone was not sufficient to mediate the regulation change asserted by the E30Nal mutation (323).

Most importantly, it is clear that for mDHFR^{E30Nal}, the replacement of Michaelis-Menten kinetics with allosteric cooperativity at low DHF concentrations is a direct result of the size and shape of Nal because the same response could not be replicated with mutation to Trp. Nal is larger than Trp, and contains two 6-membered rings while Trp has a 5- and 6-membered ring. Although both are planar, the orientation and carbon connectivity of the aromatic rings are unique between the two residues.

The cooperative attribute of mDHFR^{E30Nal} is favorable for the expression host

DHFR is an essential enzyme that generates tetrahydrofolic acid which is a *de novo* precursor to purines, thymidylic acid and certain amino acids. It has been shown that expression of recombinant mDHFR is beneficial to *E.coli* expression hosts, and that mDHFR expression titers have a positive linear correlation with catalytic efficiency (307, 322). Based on the Hill regressions, mDHFR^{E30W} and mDHFR^{E30Nal} shared similar catalytic efficiencies, despite being far less productive than wild-type (by 384 and 364-fold, respectively) (Table 4.2). However, there was a marked discrepancy between catalytic efficiency and expression yields for these two

variants. For mDHFR^{E30W}, expression titers were merely 4% of wild-type expression titers, which is consistent with its low catalytic efficiency (Table 4.3). However, mDHFR^{E30Nal} expression titers were disproportionately higher at nearly half (48%) of wild-type expression titers (Table 4.3). Since the regulation mechanism at ≤ 200 μM DHF is the most significant difference between mDHFR^{E30Nal} and mDHFR^{E30W}, this suggests that the cooperative nature of mDHFR^{E30Nal} at low substrate concentrations (0 – 200 μM) is a highly favorable attribute that is beneficial to the expression host. The mechanism behind this behavior, however, is still unknown.

Table 4.3. Wild-type mDHFR and variant expression/purification relative yields.

Variant	**mDHFR^{WT}**	**mDHFR^{E30Nal}**	**mDHFR^{E30W}**
Relative Yield (%)	100	48 ± 9	4 ± 1

1) Yields were determined after Ni-NTA purification and are relative to wild-type DHFR (DHFR^{WT}). WT denotes wild-type.
2) Standard errors are reported (n = 3).

Discussion

One striking feature of the mDHFR (Wild-type mDHFR, mDHFR^{E30W} and mDHFR^{E30Nal}) variants is that they share a similar reaction landscape at high DHF concentrations; consequently they result in similar K_h and h values. This result suggests that mDHFR^{E30Nal} may share a similar conformation to those of wild-type mDHFR and mDHFR^{E30W} at high DHF concentrations (>200 μM DHF) (290, 324). Especially between mDHFR^{E30Nal} and mDHFR^{E30W}, this phenomenon would be expected because Trp and Nal are structural analogues. However, since mDHFR^{E30Nal} has one continuous cooperative catalytic mode across the entire measured substrate concentration range, this suggests that the E30Nal mutation may "lock" mDHFR into the inherent conformation that is present at high DHF concentrations which is conducive to

cooperativity. This is consistent with the Monod-Wyman-Changeux model which suggests that cooperativity is possible when an enzyme can take on discrete conformations (274, 303, 317, 324, 325).

While mDHFR is allosterically active, it is not apparent why the mutation of Glu30 to Nal would alter its cooperativity (270, 271, 273-275, 290, 326, 327). To find clues, we looked at other allosterically regulated enzymes with cooperativity. Based on the comparison of several well characterized enzymes, key residues that are involved in cooperativity often share a number of similar attributes. This commonality would make sense since sequence similarity has been used to identify allosterically-active residues (275, 316, 326, 328). Comparison of these residues shows that they are 1) located in the catalytic domain, 2) stabilize the catalytic state through intramolecular interactions, and 3) are involved in the transition of the enzyme conformation from the inactive (T, tight) to active (R, relaxed) state. For example, residues that are involved in allosteric coopertivity, Arg162 and Arg243 in PFK, Thr226 in CM and Gln231 in ATCase are each located in the catalytic domain. These residues also hydrogen bond with their respective substrate or allosteric effector molecule. Most importantly, these residues are involved in the transition between the T and R enzymatic states (317, 318).

Glu30 also shares a number of these characteristics. Like the other residues involved in cooperativity, Glu30 resides in the catalytic domain of mDHFR. Glu30 also hydrogen bonds with dihydrofolate (DHF). And lastly, its equivalent residue in *E. coli* DHFR, Asn27, is involved in the conformational transition between the T and R states, which suggests that Glu30 plays a similar if not the same role (303-305, 312, 316, 329) . We hypothesize that these similar attributes may be indicators of residues, like Glu30 that are allosterically-active and may be involved with cooperativity.

Conclusions

Here we have identified a mDHFR mutant containing the E30Nal mutation that has a different catalytic regulation scheme than its wild-type counterpart. Previous, mutational and structural analysis of mDHFR has shown that Glu30 is responsible for both substrate binding and catalytic function. Previous work has shown that at low DHF substrate concentrations (≤ 200 μM) mDHFR is governed by Michaelis-Menten kinetics. We have expanded upon this work to evaluate higher substrate concentrations (> 200 μM) and have shown that wild-type mDHFR is inherently governed by two catalytic modes that are substrate-concentration-dependent. Wild-type was governed by Michaelis-Menten and homotropic activation at low (≤ 200 μM) and high (>200 μM) DHF concentrations, respectively. Alternatively, $mDHFR^{E30Nal}$ had one continuous catalytic regulation mechanism for the entire substrate range (0 – 1200 μM) and exhibited homotropic activation. The $mDHFR^{E30W}$ mutant was created to determine whether it could replicate the behavior of the E30Nal mutation. $mDHFR^{E30W}$, however, mimicked wild-type and not $mDHFR^{E30Nal}$. $mDHFR^{E30W}$ had two catalytic modes that are substrate-concentration-dependent. And finally, $mDHFR^{E30W}$ was governed by Michaelis-Menten and homotropic activation at low (≤ 200 μM) and high (>200 μM) DHF concentrations, respectively. These results demonstrate that incorporation of Nal at position 30 alters the cooperativity of mDHFR. This change is driven by the particular shape and size of Nal, since the same attribute could not be reproduced when Glu30 was mutated to the most similar natural amino acid analogue, Trp. Furthermore, since both Trp and Nal can only weakly hydrogen bond with the pteridin substituent of DHF, impairing the hydrogen bond alone between position 30 and DHF is not sufficient to alter the cooperativity of mDHFR. Furthermore, examination of expression titers

showed that despite having low catalytic efficiency (since 30 is important for catalytic turnover), homotropic activation was extremely beneficial to the expression host based on the relatively high expression titers of $mDHFR^{E30Nal}$. This work demonstrates that although non-natural amino acids possess an array of chemical properties, simply based on the subtle changes to shape, non-natural amino acids have the ability to fill roles that natural amino acids cannot. To our knowledge this is the first report showing that an expanded set of genetically encoded amino acids can alter the cooperativity of an enzyme.

Chapter 5

Strategizing the selection and placement of an expanded set of amino acids for maintaining enzyme function

Abstract

The ability to incorporate non-natural amino acids (nAAs) during protein synthesis has greatly broadened the protein engineering space by providing new building blocks with unique structures, chemistry and reactivity, not found in natural amino acids. General knowledge of how mutations affect enzyme function is limited. With the increasing diversity of residues available for protein synthesis, understanding how mutations affect enzyme function is crucial. Here, we investigate how nAAs can be incorporated into enzymes while minimizing the impact on function. The goals are two-fold; 1) to increase the accessibility and utility of nAAs for protein engineering applications, and 2) to provide insight into how mutations outside of the active site can affect enzyme function. 3-(2-naphthyl)-alanine (Nal) was strategically incorporated at positions in the hydrophobic core and at solvent-exposed regions in murine dihydrofolate reductase (mDHFR). Six hydrophobic core mutants (V50Nal, I51Nal, V112Nal, W113Nal, F134Nal, and V135Nal) and six solvent-exposed site mutants (V43Nal, E44Nal, F142Nal, E143Nal, F179Nal, and E180Nal) were created, to investigate the effect of mutation on enzyme function caused by changes in steric compatibility and change in hydrophobicity, for each region respectively. Hydrophobic-core mutants: The Lennard-Jones repulsive (LJR) score, a measure of steric incompatibility, calculated using RosettaDesign, was found to have a positive linear correlation with the absolute deviation in K_m from that of wild-type (Pearson's correlation coefficient, r = 0.831; p = 0.041). The kinetic parameters, k_{cat} and k_{cat}/K_m were found to have a negative monotonic correlation with the LJR score, based on the Spearman correlation coefficient (ρ = –0.886; p = 0.019). Despite being related structurally, Nal was not an equivalent substitution for Trp and Phe as it caused structural changes and adversely affected catalytic activity, however, without impacting K_m. Solvent-exposed-site mutants: Nal, a large

hydrophobic residue, could be incorporated at solvent-exposed sites (Phe142 and Phe179) without any adverse affects on the binding (K_m) and catalytic (k_{cat}) components of mDHFR function. As expected, changes in secondary structure were also found to trend with HDMNR. Statistical analysis revealed that substituting Nal for Glu caused significant deviations in K_m when compared to substitution of Nal at hydrophobic residues by an average of +0.60 μM (Two-tailed, unpaired, Student's t-test, $p < 0.01$). For the solvent-exposed site, a trend or correlation catalytic activity and any other parameter, investigated here, was not observed. Collectively, these results indicate that mutations that are intended to minimize structural changes can be used to strategically minimize impact on enzyme function.

Introduction

Protein engineering has been used extensively to create useful proteins with improved, modified and/or added function. The ability to engineer a protein to a particular state or to possess a desired attribute depends on the sequence and structure space. The advent of technology to genetically encode and incorporate non-natural amino acid (nAA) into proteins has greatly expanded the protein engineering space by increasing the number and diversity of residues available for protein synthesis and mutation. Originally only the 20 natural amino acids could be used in protein biosynthesis. Now, over 50 nAAs have been successfully incorporated in vivo into various protein targets (105, 114, 118, 171, 330). A significant advantage of using nAAs is that they possess unique, structure, chemistry and reactivity compared to the natural amino acids.

Site-specific incorporation of nAAs has been used for a range of protein engineering applications. For example, due to the high magnetiogyric ratio of ^{19}F, fluorinated nAAs have been used as NMR probes to determine the structure and function of nitroreductase (NTR) and histidinol dehydrogenase (140). Tyrosine, phenylalanine and tryptophan analogues, (*p*-amino-L-phenylalanine, *p*-methoxy-L-phenylalanine, *p*-iodo-L-phenylalanine, *p*-bromo-L-phenylalanine, and 3-(2-naphthyl)-alanine have been used to substitute Tyr66, a chromophore residue of green fluorescent protein (GFP) (131, 144-146). These substitution mutations were able to alter the spectral properties of GFP, yielding shifts in fluorescence emission wavelengths corresponding to the strength of each nAA as an electron donor (131, 144-146), which demonstrated that strategic nAA selection and placement could be used to tailor protein function. The use of nAAs has also been applied to improving the properties of enzymes beyond the limits of natural amino acids. For the enzyme-prodrug combination, NTR-CB1954, being developed for cancer gene

therapy, Phe124 of NTR, through mutation with the entire spectrum of natural amino acids was shown to be the most sensitive site for improving NTR catalytic activity towards CB1954 (168). Site-specific incorporation of *p*-aminophenylalanine at Phe124 was able to increase the activity of NTR for CB1954 two-fold over the best natural amino acid mutation, F124K (169). A group of bioorthogonally reactive nAAs, containing terminal ketones, azides, and alkynes have been developed for bioconjugation applications (148, 149, 151, 153-155, 157, 164). Since nAA incorporation can be targeted to specific locations in a protein, they can be used to create specific and homogeneous conjugation products, which are often not possible with methods using natural amino acids, such as cysteine and lysine (150, 158, 160, 161). Bioconjugation of fatty acids and polyethylene glycol (PEGylation) at reactive nAA sites have improved the blood-circulation longevity of pharmaceutically-relevant enzymes and antibodies without loss of function (152, 163, 166). Additional functionalities have also been covalented added to proteins, such as the bioconjugation of an auristatin derivative, a cancer drug, to an anti-Her2 antibody fragment and IgG, for targeted drug delivery against Her2-positive cancer cells. nAAs have also been used to alter enzyme properties. In CYP102A1, a catalytically promiscuous cytochrome P450, four aromatic unnatural amino acids were site-specifically incorporated at 11 active-site positions resulting in certain mutants exhibiting significant shifts in regioselectivity and improvements to catalytic activity (170). Also, the replacement of Phe31 of murine dyhydrofolate reductase with 3-(2-naphthyl)-alanine and *p*-bromo-phenylalanine were capable of altering specificity of mDHFR for a less favorable substrate, folic acid, and reducing its binding affinity to an artificial inhibitor (methotrexate), respectively (136, 171).

However, in general one of the primary obstacles in protein engineering is being able to correctly predict how mutations will affect enzyme function. This is especially a challenge when

applying non-natural amino acids, which have a diversity of structures and chemistries, and where rational or semi-rational design is still commonly employed (136, 140, 145, 152, 162, 169, 171, 331-334). With the increasing diversity of residues available for protein synthesis, understanding how mutations affect enzyme function is crucial. Therefore, the goal of this work is to investigate how nAAs can be permissively incorporated into enzymes. Enzymes are a particularly attractive test platform, since enzyme function is a two step process involving an obligate substrate binding step and a catalysis step. Both of these steps can be characterized simultaneously to evaluate the effects of nAA incorporation on function. For this work, murine dihydrofolate reductase (mDHFR) was used as the model protein. Numerous crystal structures for DHFR are resolved, and the enzyme kinetics has been extensively characterized (291, 293, 295-298, 307, 335-339). mDHFR function will be characterized though the saturation kinetics of DHF metabolism which will be fit to the Michaelis-Menten equation to obtain the kinetic parameters K_m and k_{cat}, to evaluate the impact of nAA incorporation on the binding and biocatalytic components of mDHFR function, respectively. Here we focus primarily on the effect of site-specific incorporation nAAs into the hydrophobic core and solvent-exposed regions as these two regions are common to almost all globular proteins and have similar characteristics from protein to protein. Also these two regions are commonly studied. Active site residues are excluded from this research effort since enzyme function and the role of active-site residues vary.

Since enzymes require their structure to function properly, we hypothesize that mutations that are intended to minimize structural changes will have a lesser impact on mDHFR function (340-353). Since the structure of the hydrophobic core is governed by its sequence and steric compatibility, six nAA incorporation sites were selected from the hydrophobic core of the

mDHFR in order to investigate how the steric compatibility of a hydrophobic non-natural amino acid affects mDHFR function (340-353). Since hydrophobic residues govern protein surface structure, six mutations were selected from solvent-exposed regions to investigate how changes in hydrophobicity at these sites affect mDHFR function (340, 341, 343, 345). Two non-natural amino acids, *p*-bromo-phenylalanine (pBrF) and 3-(2-naphthyl)-alanine (Nal), and their corresponding aminoacyl tRNA synthetase/tRNA pairs, used to incorporate them, were available to us for this work (131, 132). As Nal is larger than pBrF, we selected it for our work. Given that Nal is bulky residue that is larger than any natural amino acid it can be used to manipulate both the sterics of the hydrophobic core and hydrophobicity of solvent-exposed sites.

Materials and Methods

Materials

3-(2-naphthy)-alanine (Nal) was obtained from Chem-Impex (Wood Dale, IL). The twenty natural amino acids, ampicillin, kanamycin, *L*-(–)-fucose, and 2,5-dihydroxybenzoic acid (DHB) were purchased from Sigma-Aldrich (St.Louis, MO). Dihydrofolic acid (DHF), nicotinamide adenine dinucleotide phosphate (NADPH), and isopropyl β-D-1-thiogalactopyranoside (IPTG) were purchased from Santa Cruz Biotechnologies (Dallas, TX). Sequencing-grade trypsin was procured from Promega (Madison, WI). Nickel-nitrilotriaceticacid (Ni-NTA) affinity column resin and plasmid pQE16 were obtained from Qiagen (Valencia, CA). C18 ZipTip pipette tips were obtained from Millipore (Billerica, MA). All other chemicals, unless otherwise noted, were purchased from Fisher Scientific (Pittsburgh, PA) and were used without additional purification.

Expression of wild-Type mDHFR

Wild-type DHFR encoded on the plasmid pQE16-mDHFR^{WT}-yPheRS^{naph} was expressed in M9-20AA media (6 g/L Na_2HPO_4, 3 g/L KH_2PO_4, 0.5 g/L NaCl, 0.1 mM $CaCl_2$, 1 mM $MgSO_4$, 0.4 % glucose, 50 mg/L of each of the 20 natural amino acids) supplemented with 100 mg/mL ampicillin. The pQE16 plasmid containing the mDHFR gene was transformed into the AFWK host. The cells were grown to OD_{600} = 1.0 and induced with a final concentration of 1 mM IPTG. Cells were harvested after overnight induction at 32 ˚C.

Expression of mDHFR Nal variants

In order to express the Nal variants, the two plasmids pQE16-XXAmb_mDHFR-yPheRS^{naph} and pREP4-ytRNA$^{Phe}_{CUA_UG}$ were co-transformed into the *E. coli* AFWK host. Here XX represents the corresponding position of amber codon suppression based on PDB ID: 1U72 (296). The cells were then grown in M9-20AA, supplemented with 100 mg/mL ampicillin and 50 mg/mL kanamycin, until OD_{600} = 1.0. Cells were harvested and centrifuged at 4,500 x g for 8 mins. The resulting cell pellet was resuspended and gently washed with 0.9 % NaCl and centrifuged again at 4,500 x g for 8 mins. The resulting cell pellet was resuspended in M9-17AA (6 g/L Na_2HPO_4, 3 g/L KH_2PO_4, 0.5 g/L NaCl, 0.1 mM $CaCl_2$, 1 mM $MgSO_4$, 0.4 % glucose, 0.05 g/L of each of the natural amino acids except phenylalanine, tryptophan and lysine which were supplemented at 25 µM, 50 µM and 100 µM, respectively (152). The M9-17AA was then supplemented with 3 mM of Nal. After incubation at 37 ˚C for 10 mins, induction was initiated by the addition of IPTG to the culture at a final concentration of 1mM. The cells were induced overnight at 32 ˚C. The mDHFR being used has the residues MRGSGI at to the N-terminus and a hexahistidine purification tag at the C-terminus (171).

Protein purification

Purification of the mDHFR variants including wild-type was performed using Ni-NTA resin per manufacturer protocol (Qiagen, Venlo, Limburg). The manufacturer protocol was followed with the exception that 20 mM and 40 mM imidazole were used in the lysis and wash buffers, respectively (171).

Determination of protein purity and concentration

The yield and purity of the purified DHFR variants were determined by analyzing SDS-PAGE protein gels. The protein gel images were taken using a UVP BioSpectrum imager (Upland, CA) and then analyzed by VisionWorks image analysis software. Protein concentration was determined by absorbance measurements at 280 nm, using a calculated extinction coefficient of 24,750 $cm^{-1}M^{-1}$ (171).

Confirmation of in vivo Nal incorporation by MALDI-TOF/MS

Incorporation of Nal was confirmed by MALDI-TOF/MS after enzymatic digestion of each variant. 1 µL of 1 µg/µL trypsin (in 50 mM acetic acid) or 1 µL of 1 µg/µL of chymotrypsin (in 50 mM acetic acid) was added to 10 µL of 5 µM each DHFR variant in elution buffer (50 mM NaH_2PO_4, 300 mM NaCl, and 250 mM imidazole, pH = 8.0). Upon addition the sample was incubated at 37 ˚C overnight. 12 µL of 5 % trifluoroacetic acid was added to quench the reaction. Digested peptides solutions were desalted using C18 Ziptips according to the manufacturer's protocol (EMD-Millipore, Darmstadt, Germany). 20 mg/mL of 2,5-dihydroxybenzoic acid and 2 mg/mL of L-fucose dissolved in 10 % ethanol was used as the

matrix for MS analysis using a Microflex MALDI-TOF/MS (Bruker, Billerica, MA). Variants V43Nal, E44Nal, V50Nal, I51Nal, F134Nal, V135Nal, F179Nal, and E180Nal were digest by trypsin. V112Nal, W113Nal, F142Nal, and E143Nal were digested by chymotrypsin (171).

Dihydrofolic acid (DHF) reduction kinetics

NADPH-dependent mDHFR reduction of DHF was monitored by measuring the decrease in absorbance at 340 nm using a Synergy four multimode microplate reader (BioTek, Winooski, VT) following manufacturer protocol (Sigma-Aldrich, St. Louis, MO). To determine DHF reduction kinetic parameters, 60 μM of NADPH and varying concentrations of dihydrofolate (DHF) (0 – 40 μM) were dissolved in MTEN buffer (50 mM 2-(N-morpholino)ethanesulfonic acid (MES), 25 mM tris(hydroxymethyl)aminomethane (Tris), 25 mM ethanolamine, and 800 mM sodium chloride, pH 7.5). Reactions were initiated by the addition of enzyme to a final concentration of 2 to 100 nM (depending on the variant). Enzyme was pre-incubated with NADPH for 10 minutes prior to addition. Bovine serum albumin (BSA) was added to each reaction at a final concentration of 0.1 mg/mL (310, 311). While BSA has previously been used in the DHFR kinetic assay (310, 311), a supplemental experiments used for validating BSA use in the kinetic assay is located in the Supporting Information section Appendix D (Figure D1 – D3). All measurements were performed in at least triplicates. Reaction rates with respect to substrate concentration were fitted against the classical Michaelis-Menten model in order to determine kinetic parameters, k_{cat}, K_m, and k_{cat}/K_m (171, 293-298). The extinction coefficient for NADPH-dependent DHF reduction reaction is 12,300 M^{-1}/cm at 340 nm at 25 ˚C (310, 311).

Circular Dichroism

Eluted mDHFR was desalted on a PD-10 column (GE Healthcare, Pittsburgh, PA) per manufacture protocol and then diluted using 10 mM phosphate buffer to a final concentration of 2 μM enzyme. Samples were measured using a Jasco J-710 spectropolarimeter with a 1 mm path length. The reported spectrum for each sample was an average of at least 5 measurements and the solvent background spectrum was subtracted. CD sprectra were only obtained for V43Nal, E44Nal, W113Nal, F134Nal, F142Nal, E143Nal, F179Nal, and E180Nal, because expression/purification titers were too low for V50Nal, I51Nal, V112Nal, and V135Nal to conduct the analysis (354).

Computational analysis of conformational stability and mutational steric compatibility

Computational analysis of the conformational stability of mDHFR after non-natural amino acid incorporation was performed using the molecular modeling program RosettaDesign, version 3.4 (355, 356). The energy score output of RosettaDesign is a linear sum of the Lennard-Jones potential, the Lazaridis-Karplus solvation energy, an empirical hydrogen bonding potential, the internal energy of sidechain rotamers, the Coulombic electrostatic energy potential, the energetic favorability of a specific amino acid based on φ/ψ angles, and a unique reference energy for each amino acid (355-357). For a given crystal structure, RosettaDesign uses a Monte Carlo method to simulate residue annealing by scanning through a large number of rotamers for a given non-natural amino acid (from the SwissSidechain database) to minimize the energy score output. For this analysis, a fixed-backbone technique was used (358). A fixed backbone technique has previously been used successfully for computational design of proteins (359-365). Since a crystal structure for wild-type mDHFR bound to either DHF or folic acid (FOL) is not available, the human DHFR (hDHFR) structure (PDB ID: 2W3M) was used instead. The

hDHFR structure is highly homologous to that of mDHFR, and the two have greater than 95% sequence conservation (296, 339).

Results and discussion

Part I: Non-natural amino acid incorporation within the hydrophobic core

Selection of non-natural amino acids for site-specific incorporation in the hydrophobic core

In order to investigate the effect of mutation within the core, we looked at the available hydrophobic non-natural amino acids (nAA) that have previously been incorporated successfully (107, 136, 308, 366). Of those, two hydrophobic nAAs, *p*-bromophenylalanine (pBrF) and 3-(2-naphthyl)-alanine (Nal) and their corresponding engineered aminoacyl tRNA synthetase/tRNA pairs were available to us for this work (131, 132, 308). While the lower size spectrum of hydrophobic residues is well covered by the natural amino acids, the use of larger sidechains is limited only by the ability to engineer suitable corresponding heterologous orthogonal suppressor tRNA and aminoacyl tRNA synthetase pairs (171, 367, 368). This presented an opportunity to investigate whether larger hydrophobic amino acids could be successfully incorporated into the core while maintaining enzyme function (346). Nal, a bulky hydrophobic Phe/Trp analogue, was selected for this purpose (Figure 5.1) (308). Nal has two conjugated rings and is larger in mass and van der Waals volume than any natural amino acid, as well as pBrF (Figure 5.1) (369). Nal also comes from one of the largest families of nAAs, the Trp/Tyr/Phe analogues, that are extensively used for protein engineering applications involving non-natural amino acids (136).

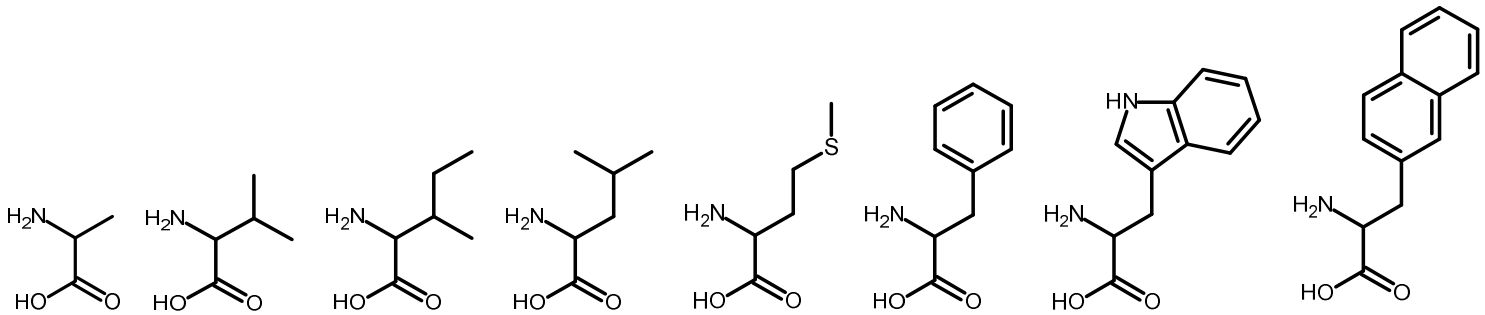

Ala	Val	Ile	Leu	Met	Phe	Trp	Nal
86.4Å^3	121.0 Å^3	138.3 Å^3	138.3 Å^3	139.5 Å^3	159.0 Å^3	178.7 Å^3	199.7 Å^3

Figure 5.1. Structures and the calculated van der Waals volumes of hydrophobic amino acids in order of increasing size. Van der Waals volumes were calculated using the method described by Zhao (369).

Table 5.1. Parameters derived from computational and crystal structure analysis.

Variant	Wild-type	W113Nal	V112Nal	F134Nal	V135Nal	I51Nal	V50Nal
fa_rep (kcal/mol)	14.1 ± 0.5	66.5 ± 0.7	121.3 ± 34.8	59.7 ± 2.3	77.9 ± 1.5	96.7 ± 0.6	121.4 ± 1.2
DTS (Å)	NA	9	12	6	7	8	8

1) fa_rep is the Lennard-Jones repulsive score derived by computational analysis (RossettaDesign 3.4) using a fixed-backbone method using PDB ID: 2W3M. Standard errors are reported (n = 3).
2) DTS, distance to the substrate. Distances represent the lowest edge-to-edge distance from the native residue to the substrate and are binned to a whole number. For example, 8Å represents an actual edge-to-edge distance between 8 to 9 Å.
3) NA, not applicable.

Table 5.2. Michaelis-Menten kinetic Parameters for mDHFR NADPH-dependent DHF reduction.

Variant	Wild-type	W113Nal	V112Nal	F134Nal	V135Nal	I51Nal	V50Nal
k_{cat} (s^{-1})	3.66 ± 0.02	2.95 ± 0.002	0.029 ± 0.0001	1.46 ± 0.0002	0.32 ± 0.0004	0.028 ± 0.0002	0.020 ± 0.0002
K_m (µM)	1.94 ± 0.08	2.10 ± 0.19	2.61 ± 0.12	1.87 ± 0.19	1.47 ± 0.08	3.01 ± 0.11	3.43 ± 0.24
k_{cat}/K_m (µM/s)	1.9 ± 0.1	1.4 ± 0.1	0.011 ± 0.001	0.78 ± 0.08	0.22 ± 0.01	0.0092 ± 0.001	0.0058 ± 0.0004
Rel. k_{cat}/K_m (%)	100.0	74.5 ± 12.7	0.6 ± 0.05	41.4 ± 8.1	11.7 ± 1.2	0.5 ± 0.05	0.3 ± 0.04
$\|\Delta K_m\|$ (µM)	NA	0.16	0.67	0.07	0.47	1.07	1.49

1) Rel. k_{cat}/K_m is the relative catalytic efficiency of the particular variant compared to that of wild-type.
2) Reactions were conducted with DHF concentrations of 0 – 40 µM and 60 µM of NADPH.
3) $|\Delta K_m|$ is the absolute difference between the K_m of the mutant mDHFR and that of wild-type mDHFR
4) Standard errors are shown (n = 3).

Selection of hydrophobic-core incorporation sites

To select mutation sites, we calculated the accessible solvent area (ASA), a common practice used to locate residues of the hydrophobic core (343, 370). Since solvent accessibility is highly restricted within this area, we restricted our selection to residues (PDB ID: 1U72) with ASA less than or equal to 2.0 % (296, 343, 370). To eliminate bias that can be associated with using only a single algorithm, we calculated ASA values using three different published calculators to ensure that values were in close accordance with one another (ASA-View, CUPSAT and SDM) (371-373). The ASA cutoff criteria limited selection to include five hydrophobic regions. While this selection criterion may not encompass all core residues, this method nearly guarantees the selection of only hydrophobic core residues, especially to ones that are buried with limited accessibility to solvent (343, 370, 374). Additionally, we excluded active site and binding pocket residues in order to minimize direct interaction with the substrate and cofactor, which is not being studied herein. The ASA criterion was also verified to naturally exclude residues that are exposed to bulk solvent. We also excluded core residues that are involved in sidechain-sidechain and sidechain-backbone hydrogen bonding pairs, as these residues are normally crucial to structure and function (323, 375).

With the aforementioned criteria, selection was narrowed to the β-strand portion of the core (296). From here, we carefully selected three pairs of adjacent mutations sites, one pair from each region, for site-specific incorporation of Nal. Between mutants of adjacent sites, confounding variables such as differences in location-dependent behavior and local structural environment are expected to be minimized and this facilitates pairwise comparison (340, 341, 343, 376, 377). Each adjacent pair of mutation sites consists of a small valine residue and larger hydrophobic residue. Valine was selected as the smaller residue since it represents an

intermediate hydrophobic residue size, and because it serves as a common residue to facilitate comparison across regions. The size difference between valine and the adjacent residue allows comparison to determine whether the residue **s**ize **d**ifference between the **m**utant and **n**ative **r**esidue (SDMNR) is an important variable that can impact enzyme function. Positions Val50, Ile51, Val112, Trp113, Phe134, and Val135 were selected (based on position numbering for PDB:ID 1U72) (296). Therefore, six mutants were created, with Nal site-specifically incorporated only at the target site. Since Nal is an analogue to Trp and Phe, Trp113 and Phe134 serve as conservative mutation sites based on size and shape.

Hereinafter mutations are denoted as, for example, V135Nal, where V is the native site residue valine, 135 is the position of the target incorporation site and Nal represents 3-(2-naphthyl)-alanine. Natural amino acids are denoted with single letters. This nomenclature is used to denote both the mutations and mutants.

Preparation of Nal variants

The mDHFR variants were prepared using a modified version of the method described by Zheng (171). mDHFR variants were successfully expressed and purified as evidenced by a clear protein band at 23.5 kDa on SDS-PAGE (Figure 5.2). As was the case, since Nal only differs in mass from Val, Ile, Phe and Trp (native residues of Nal incorporation sites) by no more than 97.9 Da, the protein migration distance was not noticeably attenuated from the relatively minor mass contribution of Nal incorporation.

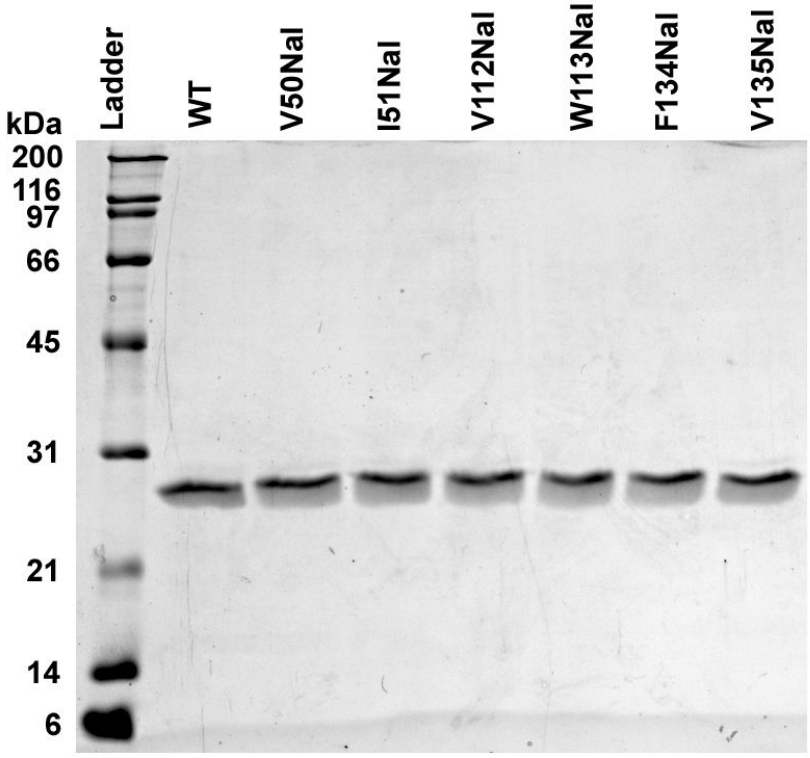

Figure 5.2. SDS-PAGE showing purified wild-type mDHFR and hydrophobic core mutants. WT denotes wild-type. Samples were run on a 12% polyacrylamide gel and stained with Coomassie blue.

Verification of in vivo Nal incorporation by MALDI-TOF/MS

Nal incorporation was accomplished using the engineered, heterologous, orthogonal yPheRS^{naph}/ytRNA$^{Phe}_{CUA_UG}$ pair that is highly specific to Nal (131, 308). Additionally, the AFWK *E. coli* expression strain, which is a Phe, Trp, and Lys auxotroph, was used to preclude misacylation of ytRNA$^{Phe}_{CUA_UG}$, thus preventing the formation of the most likely misincorporation products with Phe and Trp at the target site (131). In vivo site-specific incorporation of Nal at each target site was verified by MALDI-TOF/MS. Prior to MALDI-TOF/MS, each variant was enzymatically digested by either trypsin or chymotrypsin to produce a fingerprint of peptide fragments of known length and mass. Successful incorporation yields a

Nal-containing fragment with monoisotopic mass equivalent to the monoisotopic mass of the native fragment plus the difference in mass between Nal and the native site residue (171).

MALDI-TOF/MS analysis confirmed the successful incorporation of Nal at each location. For V50Nal and I51Nal, the expected monoisotopic masses for the Nal-containing fragments were 1156.6 m/z (residues 47 - 55) and 1142.5 m/z (residues 47 - 55), respectively. The actual monoisotopic masses for the Nal-containing fragments were found to be 1156.4 m/z and 1142.1 m/z for V50Nal and I51Nal, respectively (Figure 5.3A and 5.3B). For V112Nal and W113Nal, the expected monoisotopic masses for the Nal-containing fragments were 1164.5 m/z (residue 107 - 121) and 946.4 m/z (residues 106 - 113), respectively. The actual monoisotopic masses for the Nal-containing fragments were found to be 1164.5 m/z and 946.5 m/z for V112Nal and W113Nal, respectively (Figure 5.4A and 4B). For F134Nal and V135Nal, the expected monoisotopic masses for the Nal-containing fragments were 685.3 m/z (residue 133 - 137) and 733.3 m/z (residues 133 - 137), respectively. The actual monoisotopic masses for the Nal-containing fragments were found to be 685.4 m/z and 733.4 m/z for F134Nal and V135Nal, respectively (Figure 5.5A and 5.5B). The masses for each of the Nal-containing fragments were within ± 1.0 m/z of the expected monoisotopic masses, which is within the standard error for MALDI-TOF/MS measurements and indicates that Nal was successfully incorporated at each target position. Masses corresponding to Nal-containing fragments were not observed in the wild-type spectra indicating that the Nal-containing fragment for each variant is unique and each arises from in vivo incorporation Nal at the correct position. Also the corresponding wild-type fragment and fragments pertaining to misincorporation of Phe and Trp were not observed in the mutant spectra indicating that Nal was incorporated efficiently (131).

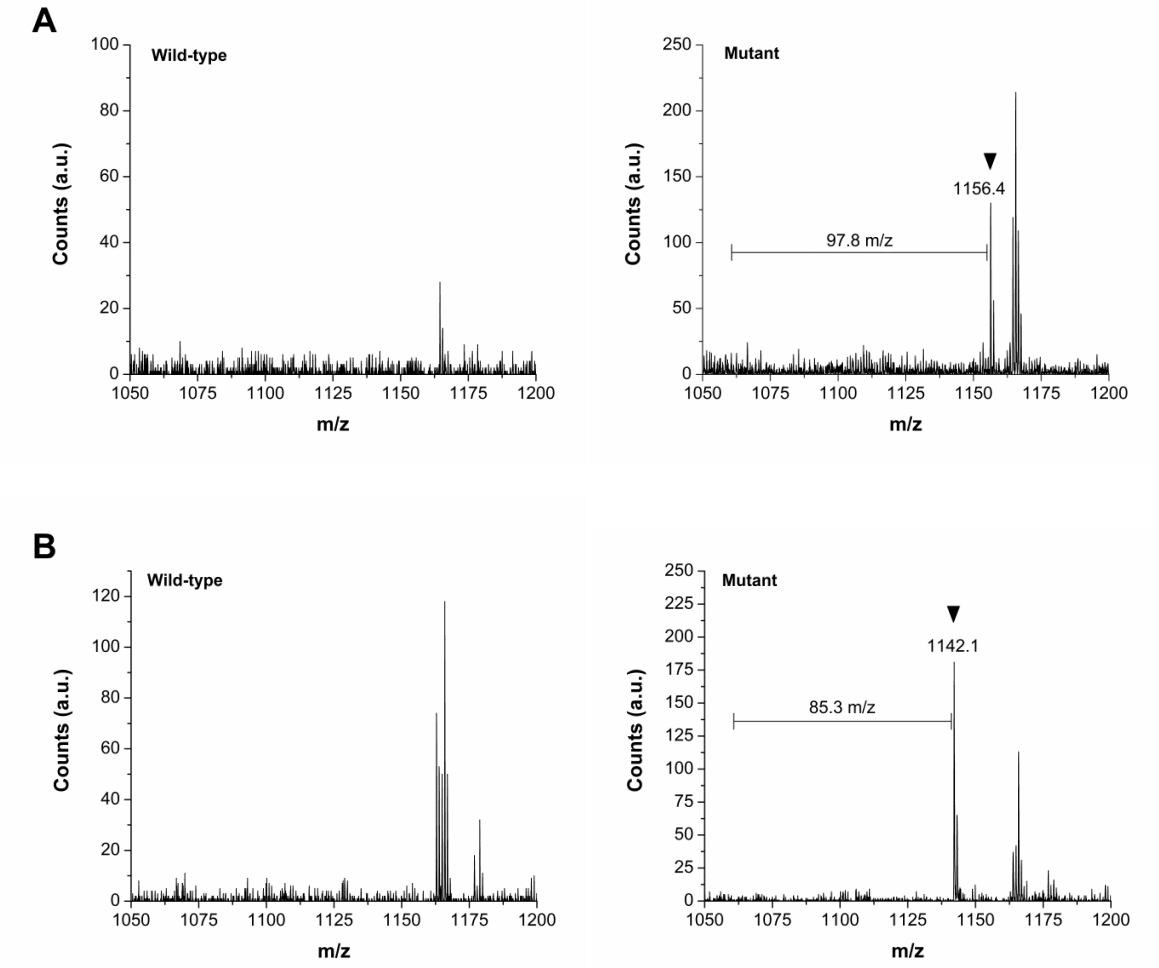

Figure 5.3. Confirmation of in vivo Nal incorporation by MALDI-TOF/MS for hydrophobic core mutants. The mass spectroscopy spectra verifying incorporation of Nal at the target site for mutant A) V50Nal (residues 47 - 55) and B) I51N (residues 47 - 55). For each sample, the left panel shows the spectrum of the wild-type enzymatic digest. The right panel shows the spectrum of the mutant enzymatic digest with the Nal-containing fragment. In the right panel, the peak corresponding to the Nal-containing fragment is indicated by the arrow. In the left panel, if present, the counterpart wild-type fragment with the native residue is marked by an arrow. The residue numbering corresponds to PDB ID:1U72. The horizontal bar indicates the mass difference between the Nal-containing fragment and corresponding wild-type fragment with the native residue. a.u. denotes arbitrary units.

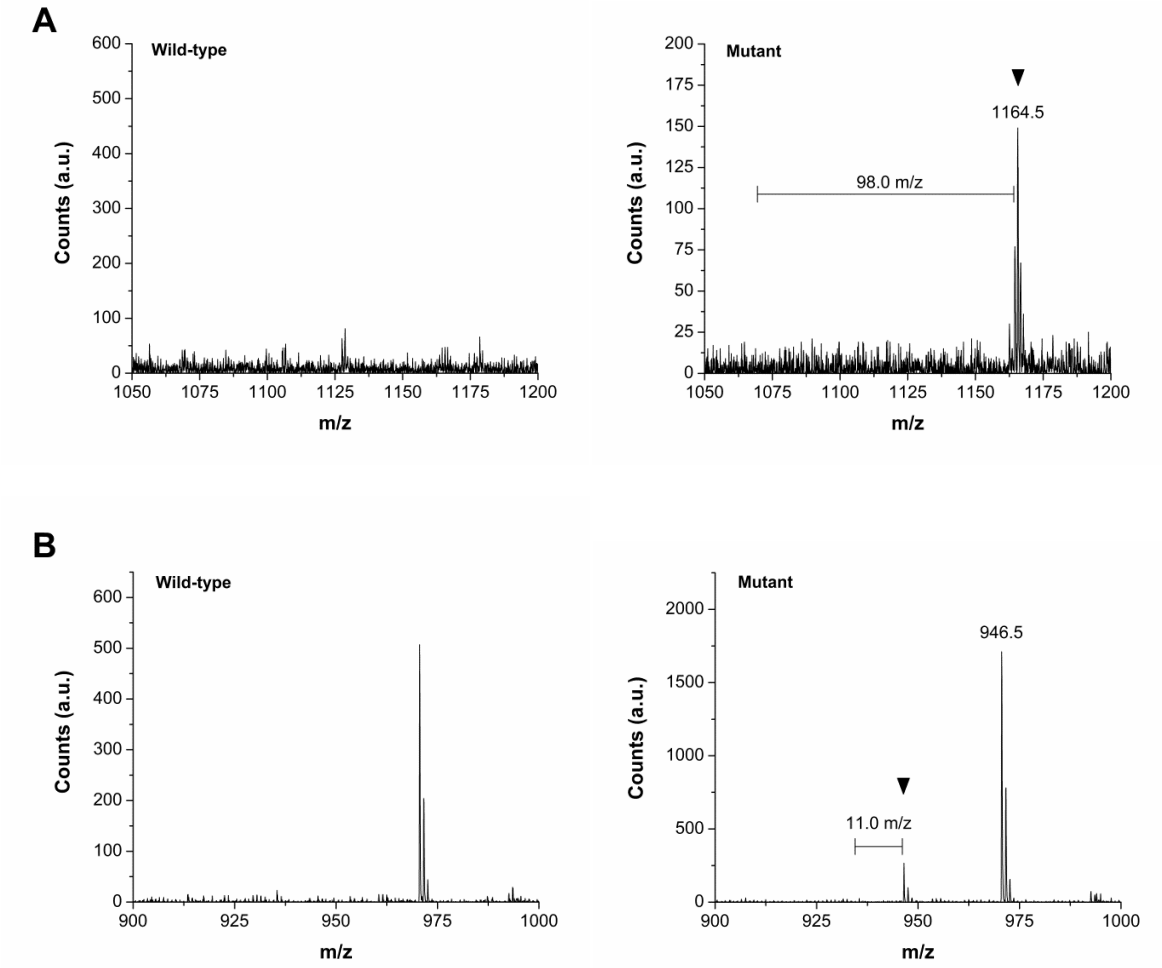

Figure 5.4. Confirmation of in vivo Nal incorporation by MALDI-TOF/MS for hydrophobic core mutants. The mass spectroscopy spectra verifying incorporation of Nal at the target site for mutant A) V112Nal (residues 112 - 121) and B) W113Nal (residues 106 - 113). For each sample, the left panel shows the spectrum of the wild-type enzymatic digest. The right panel shows the spectrum of the mutant enzymatic digest with the Nal-containing fragment. In the right panel, the peak corresponding to the Nal-containing fragment is indicated by the arrow. In the left panel, if present, the counterpart wild-type fragment with the native residue is marked by an arrow. The residue numbering corresponds to PDB ID:1U72. The horizontal bar indicates the mass difference between the Nal-containing fragment and corresponding wild-type fragment with the native residue. a.u. denotes arbitrary units.

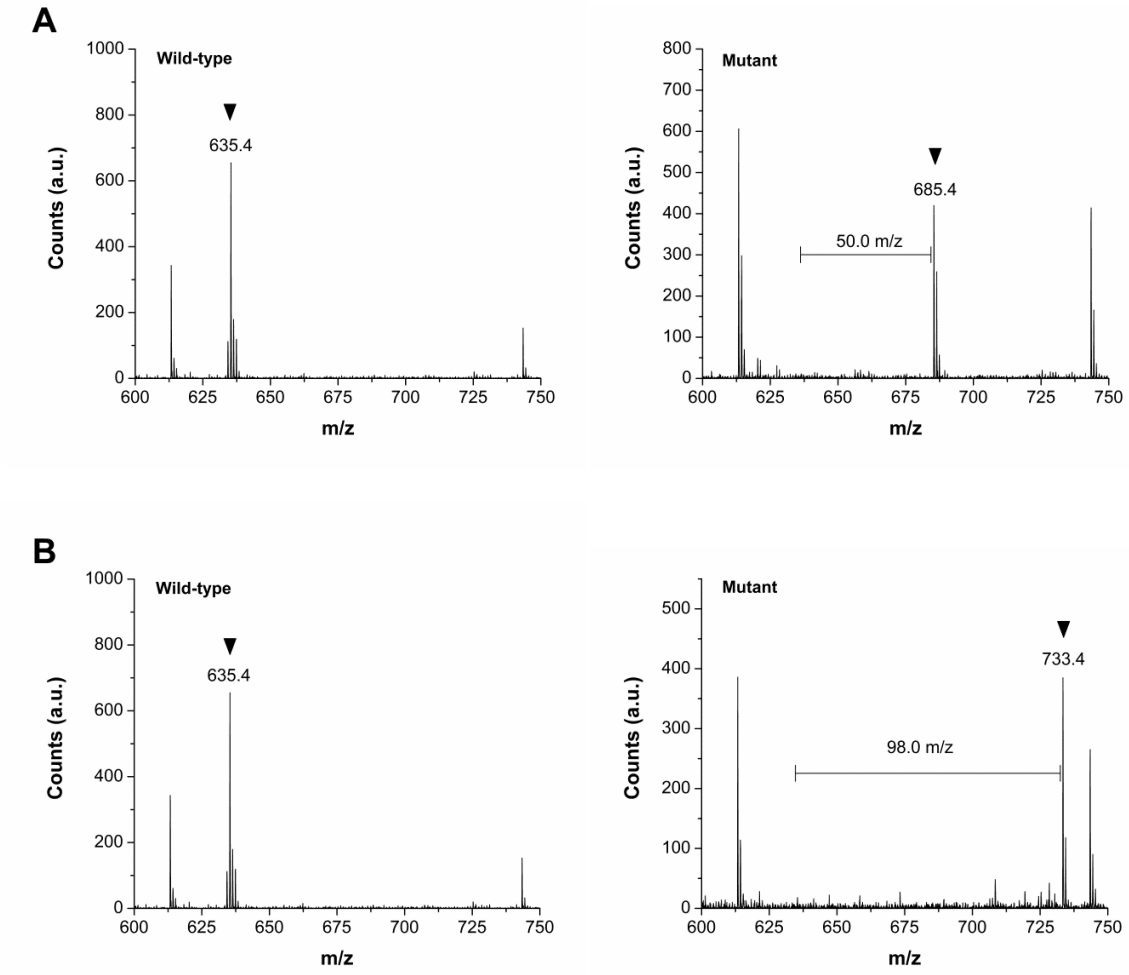

Figure 5.5. Confirmation of in vivo Nal incorporation by MALDI-TOF/MS for hydrophobic core mutants. The mass spectroscopy spectra verifying incorporation of Nal at the target site for mutant A) F134Nal (residues 133 - 137) and B) V135Nal (residues 133 - 137). For each sample, the left panel shows the spectrum of the wild-type enzymatic digest. The right panel shows the spectrum of the mutant enzymatic digest with the Nal-containing fragment. In the right panel, the peak corresponding to the Nal-containing fragment is indicated by the arrow. In the left panel, if present, the counterpart wild-type fragment with the native residue is marked by an arrow. The residue numbering corresponds to PDB ID:1U72. The horizontal bar indicates the mass difference between the Nal-containing fragment and corresponding wild-type fragment with the native residue. a.u. denotes arbitrary units.

Computational analysis of the steric compatibility of Nal incorporation

Computational analysis using RosettaDesign was performed to evaluate the steric compatibility of Nal at each incorporation site. The RosettaDesign fa_rep output is the Lennard-Jones repulsive (LJR) score, which is a measure of the deviation of atom distances from optimality (355). Higher scores reflect a scenario where atoms are closer than the distance preferred by van der Waals forces. The LJR score is a measure of the steric compatibility of a mutation and, for a fixed-backbone technique, also represents the available free energy to drive structural changes to a more stable protein fold (357, 378-381). The RosettaDesign LJR score has previously been used to evaluate the folding stability of hSOD1 and was used successfully to predict mutations for both favorable and unfavorable conformational interactions (364, 365).

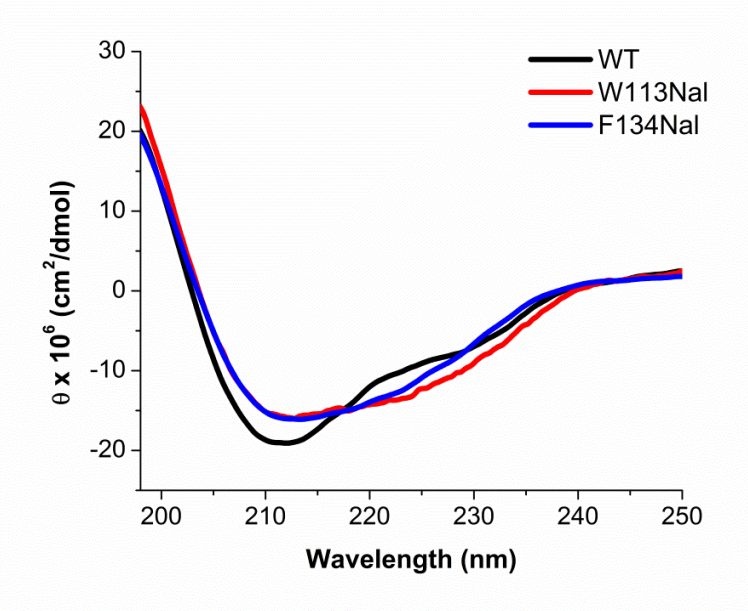

Figure 5.6. Evaluation of secondary structure changes by far-UV circular dichroism. Spectra for Wild-type, denoted WT (Black), W113Nal (red), and F134Nal (blue) are shown over the wavelength range of 195-250 nm. Spectra were obtained by averaging at least n = 5 measurements.

The conservative mutations, W113Nal and F134Nal are not completely sterically compatible and cause structural changes to mDHFR

When compared to the wild-type mDHFR score (14.1 ± 0.5 kcal/mol), the higher LJR scores observed for W113Nal (66.5 ± 0.7 kcal/mol) and F134Nal (59.7 ± 2.3 kcal/mol) indicate an increase in steric incompatibility and this is consistent with the qualitative changes to secondary structure (Figure 5.6) (343, 382). This suggests that, despite being analogues, the size difference between Nal and Trp/Phe are significant (Figure 5.1) and a structural change is required to accommodate Nal at the two corresponding positions. Nal is slightly larger than Trp because it is composed of two six-member rings while Trp is constructed of a five- and six-member ring. When compared to the phenyl substituent of Phe, the naphthyl substituent of Nal has an additional 6-membered ring (341, 343, 344, 383, 384). These results are consistent with a previous findings showing that Nal is not sterically equivalent to Phe (171).

The degree of steric incompatibility (LJR score) is related to the size difference between the mutant and the native residue

Mutants of adjacent sites (W113Nal/V112Nal, F134Nal/V135Nal and I51Nal/V50Nal) were compared pairwise to minimize effects associated with location-dependence (291, 296, 300, 302, 312, 321, 337, 385, 386). It was observed that, the mutation with the smaller SDMNR of each pair (W113Nal, F134Nal and I51Nal) consistently exhibited a lower LJR score than its adjacent counterpart (V112Nal, F135Nal and V50Nal) with the larger SDMNR (Figure 5.1 and Table 5.1). As would be expected, these results indicate that between mutants of adjacent sites, the mutation with the smaller SDMNR is more sterically compatible. In other words, the degree of steric incompatibility (LJR score) is related to the SDMNR. This corroborates our hypothesis

that minimizing the SDMNR reduces steric incompatibility (382). Since CD spectra could not be obtained for V50Nal, I51Nal, V112Nal, and V135Nal due to low expression/purification yields, for these mutants, therefore the LJR scores could not be related to structural changes.

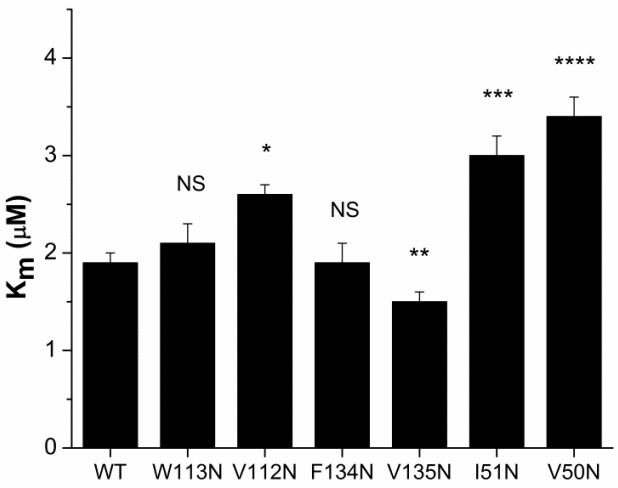

Figure 5.7. Michaelis-Menten constants (K_m) for DHF for wild-type mDHFR and hydrophobic core mutants. K_m values were derived from the Michaelis-Menten model based on saturation kinetics. WT denotes wild-type mDHFR. Error bars denote the standard error (n = 3). Here N denotes Nal. The two-tailed, unpaired Students' t-test *p*-values are for comparison of the mutant with wild-type. For A) (*; $p = 0.001$), (**; $p = 0.002$), (***; $p = 0.0006$), and (****; $p = 0.0005$). Not significant, NS.

Evaluating the impact of Nal incorporation on mDHFR substrate binding

Next, we wanted to examine how the incorporation of Nal affected enzyme function. Substrate binding is the obligate step in all enzymatic reactions before biocatalysis can occur (288). Since reduction of DHF by mDHFR follows Michaeli-Menten kinetics within the measured substrate concentration range (0 – 40 μM DHF) (288, 293, 296-305, 310-313, 324, 337, 387, 388), K_m, the inverse measure of binding affinity, was used to evaluate the effect of Nal incorporation on the substrate binding component of enzyme function.

W113Nal and F134Nal affect the secondary structure mDHFR, but not substrate binding affinity

K_m values for the conservative mutations, W113Nal and F134Nal, were statistically indistinguishable from that of wild-type mDHFR ($p > 0.05$) (Table 1). This indicates that the two conservative mutations did not affect DHF binding affinity despite being less sterically compatible than their respective native residues and also causing secondary structure changes (Table 5.1 and Figure 5.6). Therefore the difference in size and shape between Nal and Trp/Phe is substantial enough to cause structural changes (Table 5.1 and Figure 5.6); however, at positions 113 and 133, the SDMNR and the resulting sterics were not sufficient to alter the binding affinity between DHF and mDHFR (Figure 5.1).

DHF binding affinity is dependent on the steric compatibility of the mutation

The packed structure of the hydrophobic core is held together predominantly by van der Waals interactions, and it is strongly dependent on both the steric compatibility and the configuration of its residues (343, 346, 375). The hydrophobic core structure is highly sensitive to mutations that promote conformational strain or cavitations (341). Moreover, enzyme-substrate binding affinity is sensitive to structural changes and can be affected by either a change to the binding site structure itself or by a change in the structure outside the binding site that alters the stability of the substrate-bound conformation (288, 389, 390). DHF is known to interact with specific active site side-chains (Ile7, Leu22, Glu30, Phe31 and Asn64) in a highly specific configuration requiring hydrogen bonding with Glu30 and Asn64 (306, 319). As expected, a number of mutations have been shown to affect binding site structure and binding affinity of DHFR through the propagation of structural changes between the mutation and

binding site (288, 292, 306, 385, 391-394). Therefore, we suspect that there is a link between the steric compatibility of a mutation in the hydrophobic core and changes in substrate binding affinity.

To determine whether the steric compatibility of a mutation in the hydrophobic core is an important variable that affects substrate binding, mutants of adjacent sites were compared pairwise. The LJR score did not trend with K_m itself. Instead, we observed, that between mutants of adjacent sites, the LJR score trended with the absolute difference between the K_m of the mutant and that of wild-type ($|\Delta K_m|$). Nal incorporation at the larger native residue (Trp113, Phe134 and Ile51), mutations with lower LJR scores (better steric compatibility), consistently resulted in a lower $|\Delta K_m|$ than the corresponding mutant of the adjacent valine site (Val112, Val135, Val50), with higher LJR scores (Table 5.1 and Table 5.2). Also, the difference in the K_m values between mutants of adjacent sites was found to be statistically significant ($p < 0.05$).

Moreover, K_m and $|\Delta K_m|$ did not trend or correlate with the distance of the mutation site from the active site (DTS) (Table 5.1and Table 5.2), nor did they trend or correlate with ASA which was kept relatively constant through a rigorous mutation selection process (Table 5.2) (341, 375). Because the dependence of K_m on DTS and ASA were determined to be inconsequential, this indicates that DHF binding affinity is in fact dependent on the steric compatibility of the mutation (343, 375).

Absolute changes in K_m has a positive correlation with the Lennard-Jones repulsive score of the mutations

To determine whether there was a correlation between the LJR score and $|\Delta K_m|$, we calculated the Pearson's correlation coefficient (PCC), r, which is used to evaluate the linearity

between two variables. From this analysis, r was determined to be 0.831 and the corresponding *p*-value was found to be equal to 0.041 (Figure D4A). Since the *p*-value was less than 0.05 and the r value was greater than zero, the statistical analysis indicates that a statistically significant positive correlation is present between the LJR score and $|\Delta K_m|$ (Figure D4A). While the sample size was small, it was taken into account during calculation of the PCC and *p*-value (343, 375, 395). Collectively, these results indicate that steric compatibility is predictive to the degree to which K_m changes but not its directionality. A similar phenomenon has been observed in a number of cases where the protein stability correlates both positively or negatively with ligand binding affinity (396). This phenomenon, however, is not well understood. Nonetheless, since the LJR score is a linear term in the protein stability calculation (RosettaDesign) (356), our results suggest that for hydrophobic core mutants, steric compatibility of the mutation plays a significant role in the relationship between protein stability and substrate binding affinity (396).

DHF binding affinity is sensitive to the location of the mutation

To determine whether the location of the mutation was an important factor that affected K_m values, the effect of Nal incorporation at each of the valines from the three regions were compared with one another. Val50, Val112 and Val135 are located approximately 8 Å, 12 Å and 8 Å from the active site binding pocket, respectively (Table 5.1). When we compared the distance of the mutation site from the active site with the K_m values, there was no observable correlation (Table 5.1). Since, between the Val sit mutants, differences in K_m were observed, this suggests that location is an important factor that determines how, and the degree to which a mutation affects enzyme function. This is to be expected since numerous mutational studies and

analyses of sequence conservation have shown that location is an important factor that determines how a mutation affects function (171, 296, 299-301, 312, 337, 340, 387).

Since the K_m value of the V50Nal mutation was significantly higher than that of V135Nal, and because these two mutation sites are equidistant from the active site, this suggests that Val50 is more sensitive to Nal incorporation than Val135. The LJR scores indicate that the local structural environment at position 50 is less sterically compatible for Nal than that at position 135, which would explain the sensitivity. Although additional studies are needed, location-dependence may also explain why the V135Nal mutation exhibited a higher DHF binding affinity than that of wild-type mDHFR. Without additional structural information, it is difficult to determine why each mutation behaved accordingly (288, 296, 397).

Evaluating the effect of NAl incorporation on catalytic function

Next, we evaluated the impact of each mutation on catalytic function. The primary role of DHFR in all organisms is the formation of THF through the reduction of DHF in a hydride transfer reaction aided by the cofactor NADPH (288, 306, 310, 311). This process is modeled by the Michaelis-Menten equation (288, 293, 296-305, 310-313, 324, 337, 387, 388). The kinetic parameters k_{cat} and k_{cat}/K_m, are the substrate turnover rate and catalytic efficiency, respectively, and are used to evaluate the effect of each mutation on function.

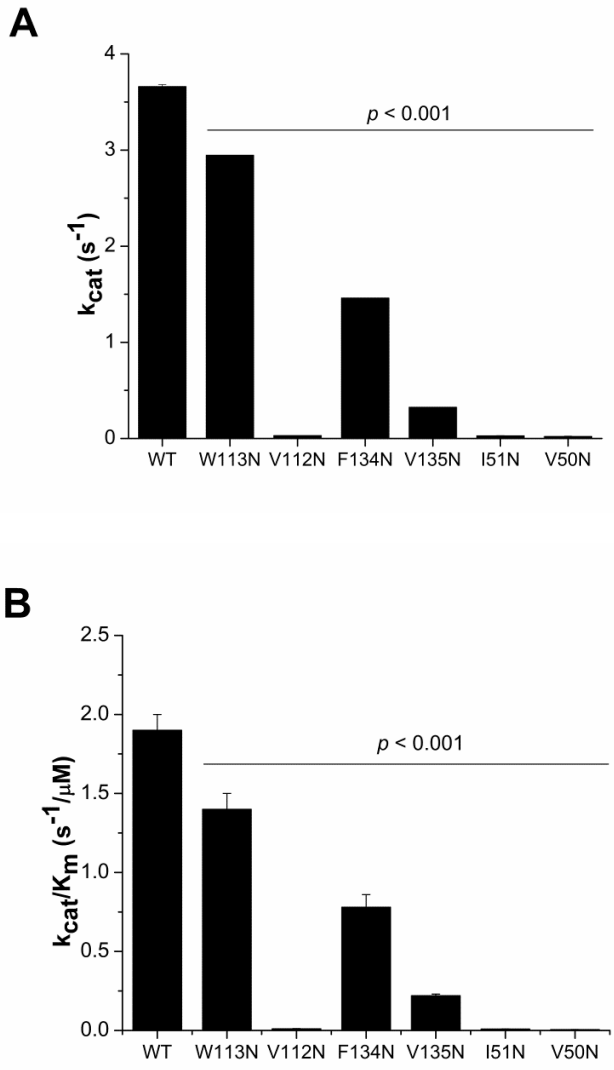

Figure 5.8. Substrate turnover rate (k_{cat}) and catalytic efficiency (k_{cat}/K_m) for DHF reduction for wild-type mDHFR and hydrophobic core mutants. The kinetic parameters A) k_{cat} and B) k_{cat}/K_m were derived from the Michaelis-Menten equation. Values were obtained from averaging values from at least n = 3 samples. Error bars denote the standard error. Here N denotes Nal. The two-tailed, unpaired Students' t-test was used to calculate *p*-values for comparison between mutants with wild-type mDHFR.

The Trp113 and F134 are important for catalytic function and mutation to Nal adversely impacts catalytic function

While the conservative mutations, W113Nal and F134Nal, did not impact binding affinity, they were capable of adversely affecting mDHFR catalytic function. This was evident by the decrease in the substrate turnover rate (k_{cat}), and also the catalytic efficiency (k_{cat}/K_m) (Table 5.2, Figure 5.8A, and Figure 5.8B). Since the binding affinity was left unaffected when compared to wild-type, this suggests that the active site structures of both mutants remained intact in the wild-type conformation. At the same time, since Trp113 and Phe134 are located outside of the active site, the observed decrease in catalytic activity indicates that the two positions are important for catalytic function and/or that the incorporation of Nal at these positions causes structural changes at regions that are important for catalytic function (292, 385, 398).

Based on the inspection of the crystal structure (PDB ID:1U72), it is not apparent how these two positions might be important to function (296). Both are located in the rigid β-sheet core of mDHFR and are not directly associated with loop regions that are essential for catalytic function (288). However, since secondary structure changes were observed for these two mutations, this corroborates findings that have shown that preservation of the mDHFR core structure is important for catalytic function (399).

Substrate turnover rate decreases monotonically with the Lennard-Jones repulsive score

To evaluate the effect of the mutational steric compatibility on catalytic function, the k_{cat} value of mutants of adjacent incorporation sites were compared in a pairwise manner. Between the adjacent sites, mutations with the lower LJR scores consistently retained a higher substrate

turnover rate and catalytic efficiency. W113Nal, F134Nal and I51Nal had 102, 4.6 and 1.4 -fold, higher substrate turnover rates, respectively, than their counterpart mutant at the valine site. Consequently, this same trend was observed between the LJR score and catalytic efficiency, k_{cat}/K_m.

When we calculated the Pearson's correlation coefficient for k_{cat} as a function of the LJR score, the r and corresponding *p*-value were determined to be -0.739 and 0.093, respectively. Since, $p > 0.05$, this indicates that the LJR score does not correlate linearly with k_{cat}. Since the r value was relatively high ($-1 \leq r \leq +1$), we suspected that a monotonic correlation might be present instead. Therefore, we calculated the Spearman rho correlation coefficient, ρ, which was determined to be –0.886 with a corresponding *p*-value equal to 0.019 (Figure D4B). Since, $\rho < 0$ and $p < 0.05$, this indicates that k_{cat} has a decreasing monotonic trend with respect to the LJR score, and this occurs in a non-linear manner (Figure D4B). The same correlation was observed between k_{cat}/K_m and the LJR score. Since DHF binding is an obligate step in the reaction pathway, we also compared changes in K_m with those in k_{cat} (288). However, no apparent trend was observed.

Steric incompatibility can affect enzyme function in a number of ways. It can occur by disruption of structure. At the extreme, this mechanism is evident in misfolded and denatured enzymes which have no function. Steric incompatibility can also affect enzyme function by decreasing the dynamic range of motion of an enzyme. Protein dynamics have increasingly been shown to be important for enzyme function (317, 329, 396-398, 400). Structural features such as loop regions are known to mediate catalytic function of mDHFR. For example, the opening and occlusion of loop regions around the active site during the unbinding of product and NADP+ are rate limiting steps in the catalytic pathway (288, 290, 291, 300, 301, 397, 398). Also mutation of

Gly121 in DHFR has been shown to decrease the dynamic range of motion thus inhibiting catalysis (300, 302, 387). Therefore, we suspect that the hydrophobic core mutations affect mDHFR function through one of these mechanisms. However, further studies involving structural analysis are necessary to elucidate the appropriate mechanism.

Part II: Non-natural amino acid incorporation at solvent-exposed sites

Selection of non-natural amino acid for site-specific incorporation at solvent-exposed sites

Since hydrophobic residues dictate the structure of solvent-exposed and surface regions, we wanted to evaluate whether hydrophobic non-natural amino acids can be incorporated at the surface while maintaining function (343). An important motivation for investigating hydrophobic residues is that one of the largest groups of non-natural amino acids consists of Phe/Trp analogues, which are often used for engineering applications (136, 171). In particular a subset have reactive groups, such as azido, alkyne, and terminal keto moieties that are commonly employed as points of chemical bioconjugation (148, 153, 162). These reactive residues require solvent exposure for efficient bioconjugation to occur (152, 162). Because bioconjugation is intended to covalently add function to a protein, the incorporation of reactive non-natural amino acids should ideally be innocuous to inherent enzyme function (152, 162). Given that these reactive groups are anchored by a large hydrophobic structure, this coincides with the goal to determine whether large hydrophobic nAAs can be permissively incorporated at solvent-exposed regions of proteins. Since a number of the Trp/Phe analogues are larger than any of the natural amino acids, this also presented an opportunity to determine if hydrophobic residues, especially ones that are larger than the natural amino acids, can be permissively incorporated at solvent

exposed sites. Of the two hydrophobic nAA available to us (pBrF and Nal), Nal was selected for this investigation (131, 132, 308). Nal is a bulky hydrophobic non-natural amino acid that is larger than any natural amino acid.

Selection of solvent-exposed incorporation sites

In order to investigate the effect of Nal incorporation at solvent-exposed sites, mDHFR was used as the model protein due to the extensive characterization background of DHFR (152, 288, 293, 295, 297-306, 311-313, 319, 337-339, 387, 393, 401, 402). Surface exposed residues can vary greatly in polarity, charge and size. In order to minimize the number of variables being compared, and to focus primarily on the importance of the **h**ydrophobic **d**ifference between the **m**utant and **n**ative **r**esidues (HDMNR), selection of incorporation sites was narrowed to adjacent sites containing a hydrophobic residue and the negatively charged glutamic acid (Glu) residue. This selection method facilitates pairwise comparison between mutants of adjacent sites, by minimizing the effect of confounding variables such as location-dependence (340, 341, 343, 376, 377). Glu was selected because, in mDHFR, it has the highest diversity of adjacent hydrophobic residues, and it is the second most prevalence (16 residues) amongst charged and polar residues (296). Fixing the charged residue selection is also convenient since surface stability has a stronger dependence on the total number of charged interactions with bulk solvent rather than type of charge (343). Therefore selecting a charged residue other than Glu is not expected to yield significantly different results. Of the charged natural amino acids, Glu also has the approximate average frequency of occurrence in vertebrates (5.8%) which suggests that it is unlikely to have specialized function (403). Furthermore, it is one of the most hydrophilic natural amino acids (404, 405). Sites Val43, Glu44, Phe142, Glu143, Phe179 and Glu180 were selected

(with position numbering based on PDB:ID 1U72) (296). Therefore, six mutants were created, and for each mutant, Nal was site-specifically incorporated only at the desired target site. Of these sites, Val43 and Phe179 have previously been used as incorporation sites for *p*-ethynylphenylalanine (152, 406). And Phe142 was selected because it is a relatively solvent accessible Phe in mDHFR. These incorporation sites are located at three distinct vertices of mDHFR ranging from approximately 8 to 20 Å from the substrate binding pocket (Table 5.3 and Figure 5.9) (296).

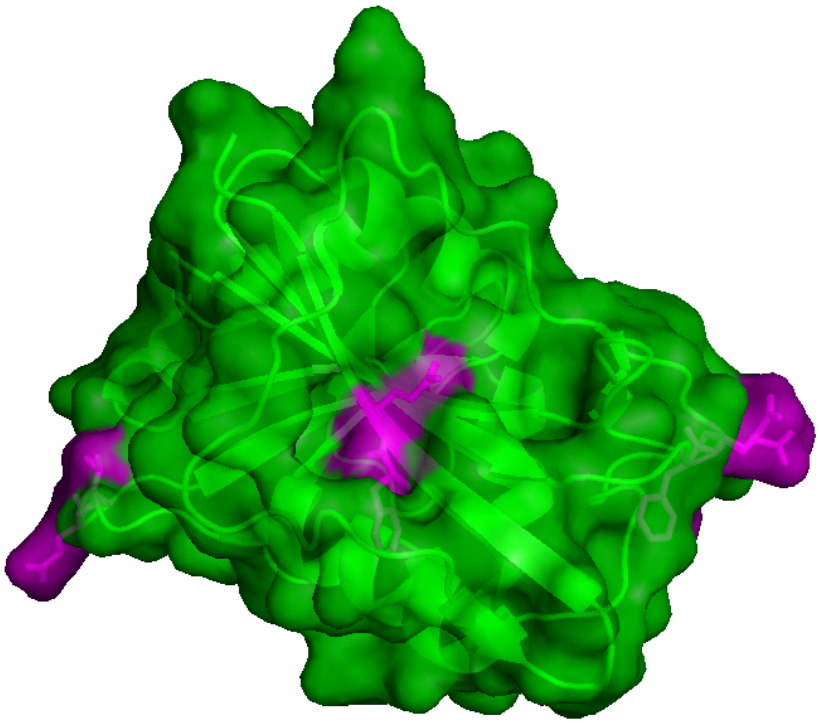

Figure 5.9. Surface map of mDHFR showing the locations of Nal incorporation sites at solvent-exposed regions. The image shows the surface map of DHFR along with the cartoon backbone (PDB ID:1U72). The solvent exposed residues that were selected for replacement by Nal are colored magenta, while all other residues are colored green.

Table 5.3. mDHFR parameters and characteristics

Variant	WT	V43Nal	E44Nal	F142Nal	E143Nal	F179Nal	E180Nal
$[\theta]_{212}/[\theta]_{222}$	1.8	1.5	1.3	1.7	0.8	1.7	1.2
DTB (Å)	NA	19	20	12	14	8	9
ASA	NA	0.52	1.09	0.19	0.89	0.10	0.18

1) $[\theta]_{212}/[\theta]_{222}$,the molar ellipticity ratio between signals at 212 nm and 222 nm from circular dichroism measurements (n = 3).
2) DTS, distance to the substrate. Distances represent the lowest edge-to-edge distance from the native residue to the substrate and are binned to a whole number. For example, 8Å represents an actual edge-to-edge distance between 8 to 9 Å.
3) ASA is the average accessible solvent area obtained from three published calculators, ASA-View, CUPSAT and SDM.
4) NA, not applicable.

Table 5.4. Michaelis-Menten kinetic parameters for mDHFR NADPH-dependent DHF reduction.

Variant	WT	V43Nal	E44Nal	F142Nal	E143Nal	F179Nal	E180Nal
k_{cat} (s^{-1})	3.66 ± 0.02	2.35 ± 0.04	3.51 ± 0.03	5.67 ± 0.01	0.958 ± 0.01	4.29 ± 0.01	1.91 ± 0.01
K_m (μM)	1.94 ± 0.12	2.07 ± 0.07	2.51 ± 0.14	2.13 ± 0.07	2.44 ± 0.10	2.16 ± 0.06	2.69 ± 0.08
k_{cat}/K_m (s^{-1}/uM)	1.9 ± 0.1	1.0 ± 0.1	1.4 ± 0.1	2.7 ± 0.1	0.39 ± 0.02	2.0 ± 0.1	0.71 ± 0.02
Rel. k_{cat}/K_m (%)	100.0	52.7 ± 2.2	74.3 ± 4.1	141.6 ± 4.6	20.8 ± 0.9	105.8 ± 3.1	37.7 ± 1.1

5) Rel. k_{cat}/K_m is the relative catalytic efficiency of the particular variant compared to that of wild-type.
6) Reactions were conducted with DHF concentrations of 0 – 40 μM and 60 μM of NADPH.
7) Standard errors are shown (n = 3).

Preparation of Nal variants

Variants were prepared using the method described by Zheng (171). Each of the variants were successfully expressed and purified as evident by a clear protein band for DHFR and its variants at 23.5 kDa on SDS-PAGE (Figure 5.10). As was the case, since Nal only differs in mass from Glu, Val, and Phe (the native residues of mutation sites), by no more than 97.9 Da, the protein migration distance was not expected to be noticeably attenuated from the relatively minor mass contribution of Nal incorporation.

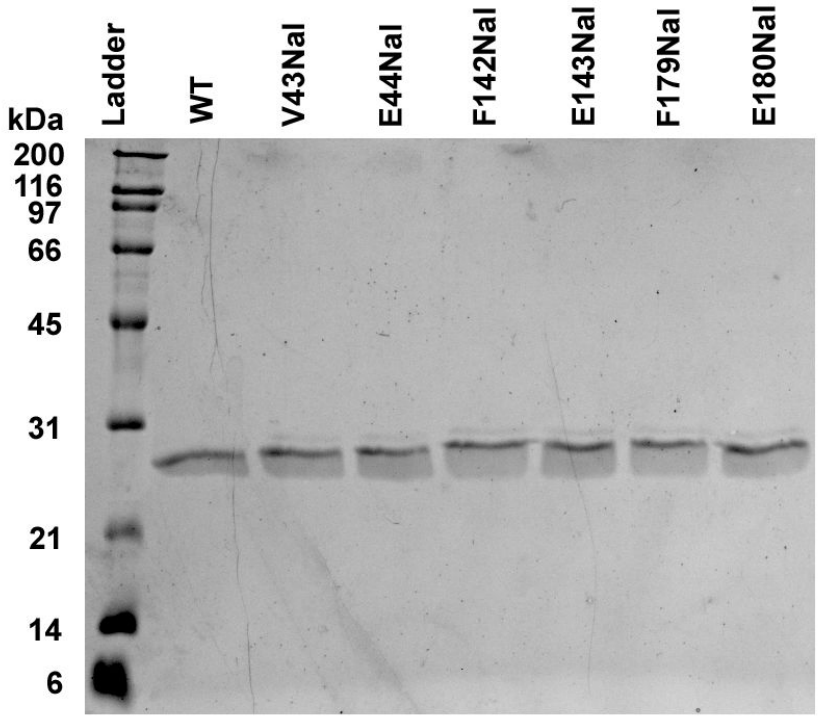

Figure 5.10. SDS-PAGE of purified wild-type mDHFR and hydrophobic core mutants. WT denotes wild-type. Samples were run on a 12% polyacrylamide gel and stained with Coomassie blue.

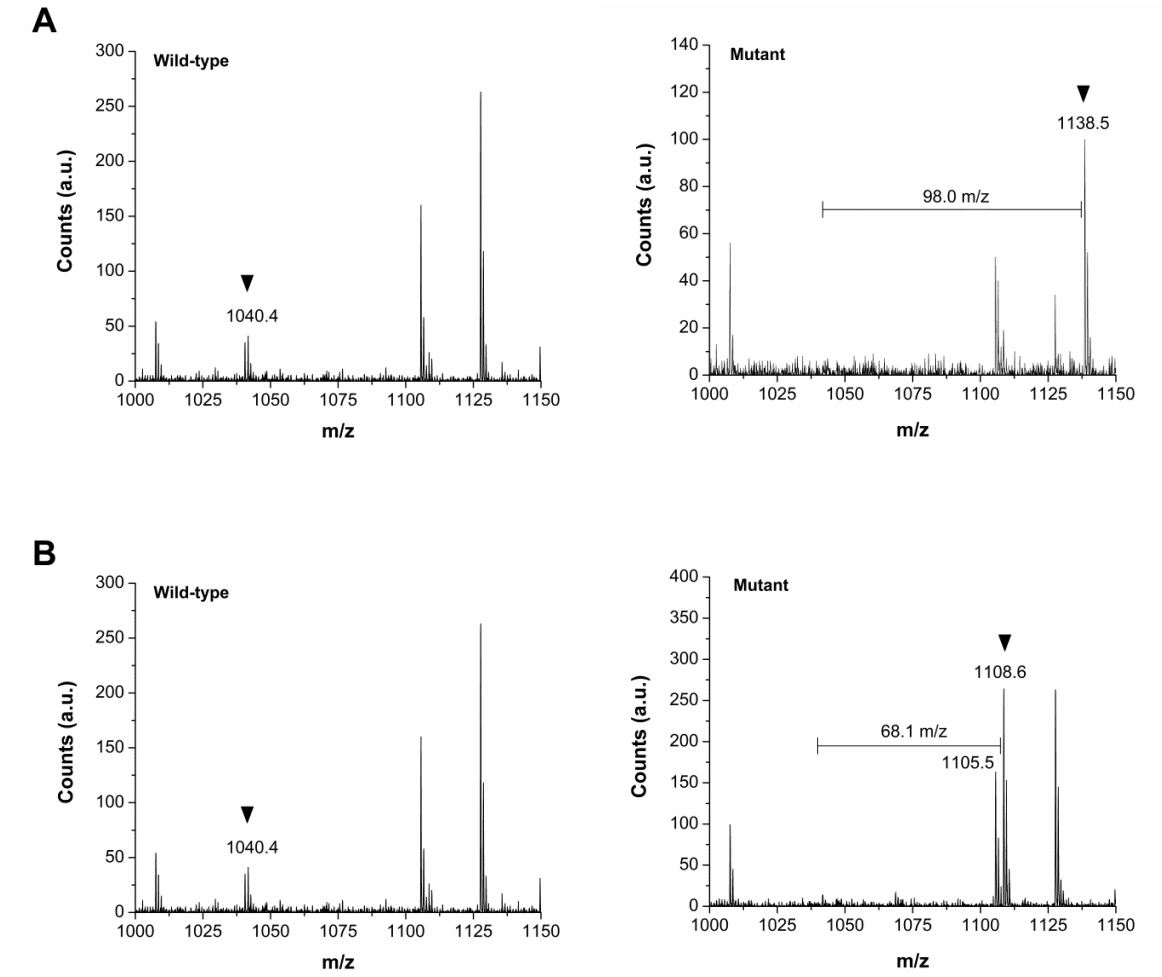

Figure 5.11. Confirmation of in vivo Nal incorporation by MALDI-TOF/MS for hydrophobic core mutants. The mass spectroscopy spectra verifying incorporation of Nal at the target site for mutant A) V43Nal (residues 37 - 46) and B) E44Nal (residues 37 - 46). For each sample, the left panel shows the spectrum of the wild-type enzymatic digest. The right panel shows the spectrum of the mutant enzymatic digest with the Nal-containing fragment. In the right panel, the peak corresponding to the Nal-containing fragment is indicated by the arrow. In the left panel, if present, the counterpart wild-type fragment with the native residue is marked by an arrow. The residue numbering corresponds to PDB ID:1U72. The horizontal bar indicates the mass difference between the Nal-containing fragment and corresponding wild-type fragment with the native residue. a.u. denotes arbitrary units.

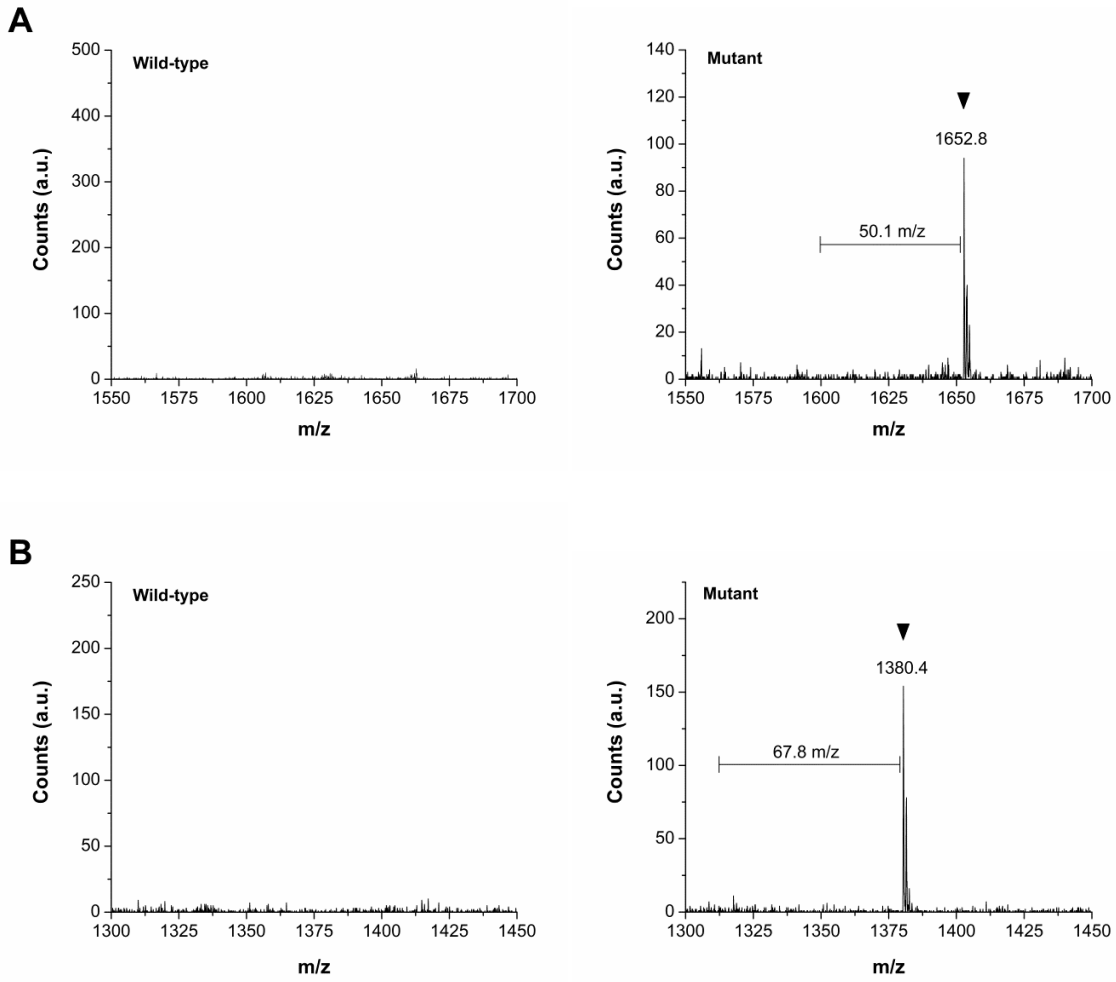

Figure 5.12. Confirmation of in vivo Nal incorporation by MALDI-TOF/MS for hydrophobic core mutants. The mass spectroscopy spectra verifying incorporation of Nal at the target site for mutant A) F142Nal (residues 135 - 147) and B) E143Nal (residues 143 - 153). For each sample, the left panel shows the spectrum of the wild-type enzymatic digest. The right panel shows the spectrum of the mutant enzymatic digest with the Nal-containing fragment. In the right panel, the peak corresponding to the Nal-containing fragment is indicated by the arrow. In the left panel, if present, the counterpart wild-type fragment with the native residue is marked by an arrow. The residue numbering corresponds to PDB ID:1U72. The horizontal bar indicates the mass difference between the Nal-containing fragment and corresponding wild-type fragment with the native residue. a.u. denotes arbitrary units.

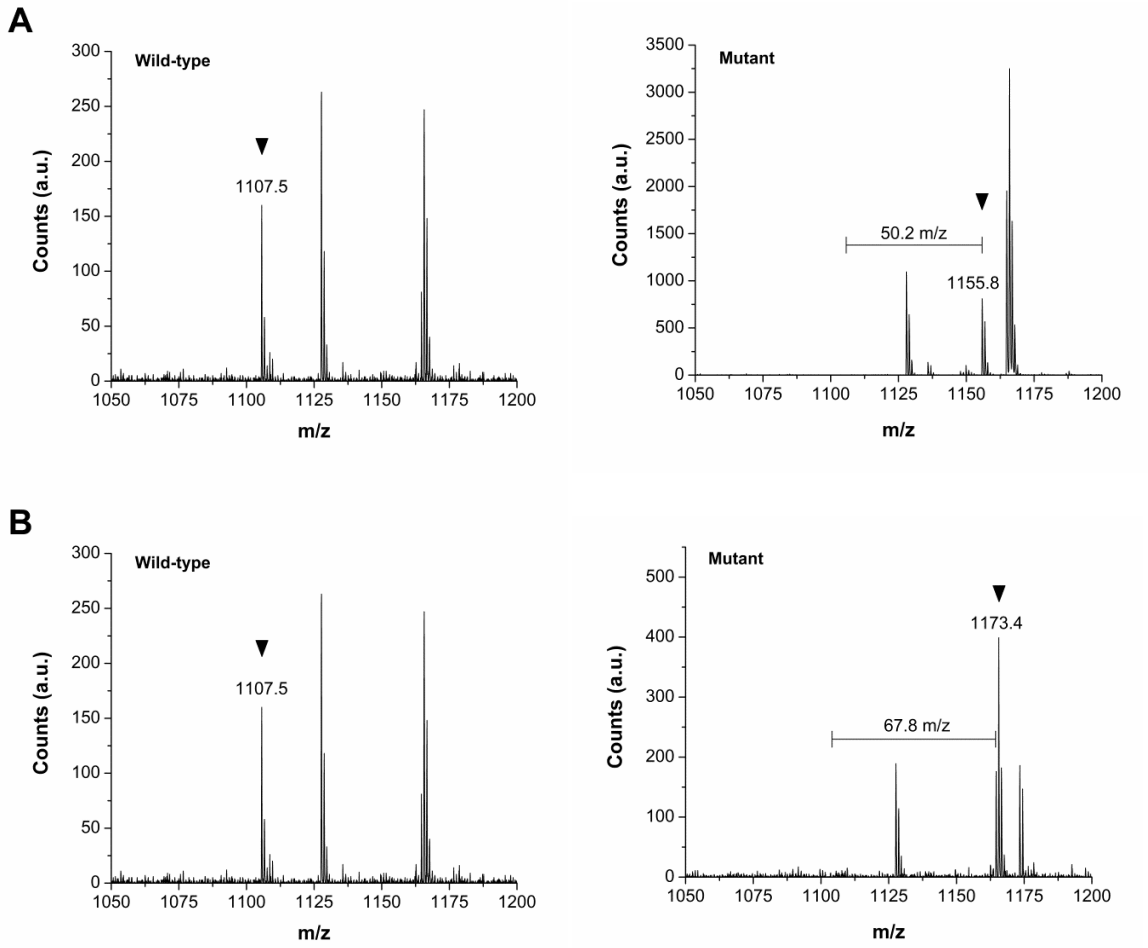

Figure 5.13. Confirmation of in vivo Nal incorporation by MALDI-TOF/MS for hydrophobic core mutants. The mass spectroscopy spectra verifying incorporation of Nal at the target site for mutant A) F179N (residues 177 - 184) and B) E180Nal (residues 177 - 184). For each sample, the left panel shows the spectrum of the wild-type enzymatic digest. The right panel shows the spectrum of the mutant enzymatic digest with the Nal-containing fragment. In the right panel, the peak corresponding to the Nal-containing fragment is indicated by the arrow. In the left panel, if present, the counterpart wild-type fragment with the native residue is marked by an arrow. The residue numbering corresponds to PDB ID:1U72. The horizontal bar indicates the mass difference between the Nal-containing fragment and corresponding wild-type fragment with the native residue. a.u. denotes arbitrary units.

Verification of in vivo Nal incorporation at solvent-exposed sites by MALDI-TOF/MS

Nal incorporation was accomplished using the engineered, heterologous, orthogonal yPheRS^{naph}/ytRNA$^{Phe}_{CUA_UG}$ pair that is highly specific to Nal (131, 308). Additionally, the AFWK *E. coli* expression strain, which is a Phe, Trp, and Lys auxotroph, was used to preclude misacylation of ytRNA$^{Phe}_{CUA_UG}$, thus preventing the formation of the most likely misincorporation products with Phe and Trp at the target site (131). In vivo site-specific incorporation of Nal at each target site was verified by MALDI-TOF/MS. Prior to MALDI-TOF/MS, each variant was enzymatically digested by either trypsin or chymotrypsin to produce a fingerprint of peptide fragments of known length and mass. Successful incorporation yields a Nal-containing fragment with monoisotopic mass equivalent to the monoisotopic mass of the native fragment plus the difference in mass between Nal and the native site residue (171).

MALDI-TOF/MS analysis confirmed the successful incorporation of Nal at each location. For V43N and E44N the expected monoisotopic masses for the Nal-containing fragments were 1138.4 m/z (residues 37 - 46) and 1108.5 m/z (residues 37 - 46). The actual monoisotopic masses for the Nal-containing fragments were found to be 1138.5 m/z and 1108.6 m/z for V43Nal and E44Nal, respectively (Figure 5.11A and Figure 5.11B). For F142Nal and E143Nal, the expected monoisotopic masses for the Nal-containing fragments were 1652.6 m/z (residue 135 - 147) and 1380.6 m/z (residues 143 - 153), respectively. The actual monoisotopic masses for the Nal-containing fragments were found to be 1652.8 m/z and 1380.4 m/z for F142Nal and E143Nal, respectively (Figure 5.12A and Figure 5.12B). For F179Nal and E180Nal, the expected monoisotopic masses for the Nal-containing fragments were 1155.5 m/z (residue 177 - 184) and 1173.5 m/z (residues 177 - 184), respectively. The actual monoisotopic masses for the Nal-containing fragments were found to be 1155.8 m/z and 1173.4 m/z for

F179Nal and E180Nal, respectively (Figure 5.13 A and Figure 5.13B). The masses for each of the Nal-containing fragments were within ± 1.0 m/z of the expected monoisotopic masses, which is within the standard error for MALDI-TOF/MS measurements and indicates that Nal was successfully incorporated at each target position. Masses corresponding to Nal-containing fragments were not observed in the wild-type spectra indicating that the Nal-containing fragment for each variant is unique and each arises from in vivo incorporation Nal at the correct position. Also the corresponding wild-type fragment and fragments pertaining to misincorporation of Phe and Trp were not observed in the mutant spectrum indicating that Nal was incorporated efficiently (131).

Characterizing the secondary structure changes caused by the incorporation of Nal

Far-UV circular dichroism (195 nm to 250 nm) was performed to evaluate changes in secondary structure caused by Nal incorporation (354, 402). Wild-type mDHFR contains 33% β-sheet (15 β-strands) character and 21% α-helical (6 helices) character (296, 297, 342, 354). Due to the high β-sheet nature, the wild-type mDHFR spectrum is highlighted by a β-sheet minimum at 212 nm. It also possesses a distinct shoulder at 222 nm associated with α-helical structure (Figure 5.14A) (354, 402). The molar ellipticity ratio between signals at 212 nm and 222 nm ($[\theta]_{212}/[\theta]_{222}$) can be used to assess the impact of a mutation on the secondary structure of a protein based on changes in β-strand and α-helix content (Table 5.3) (354, 402, 407).

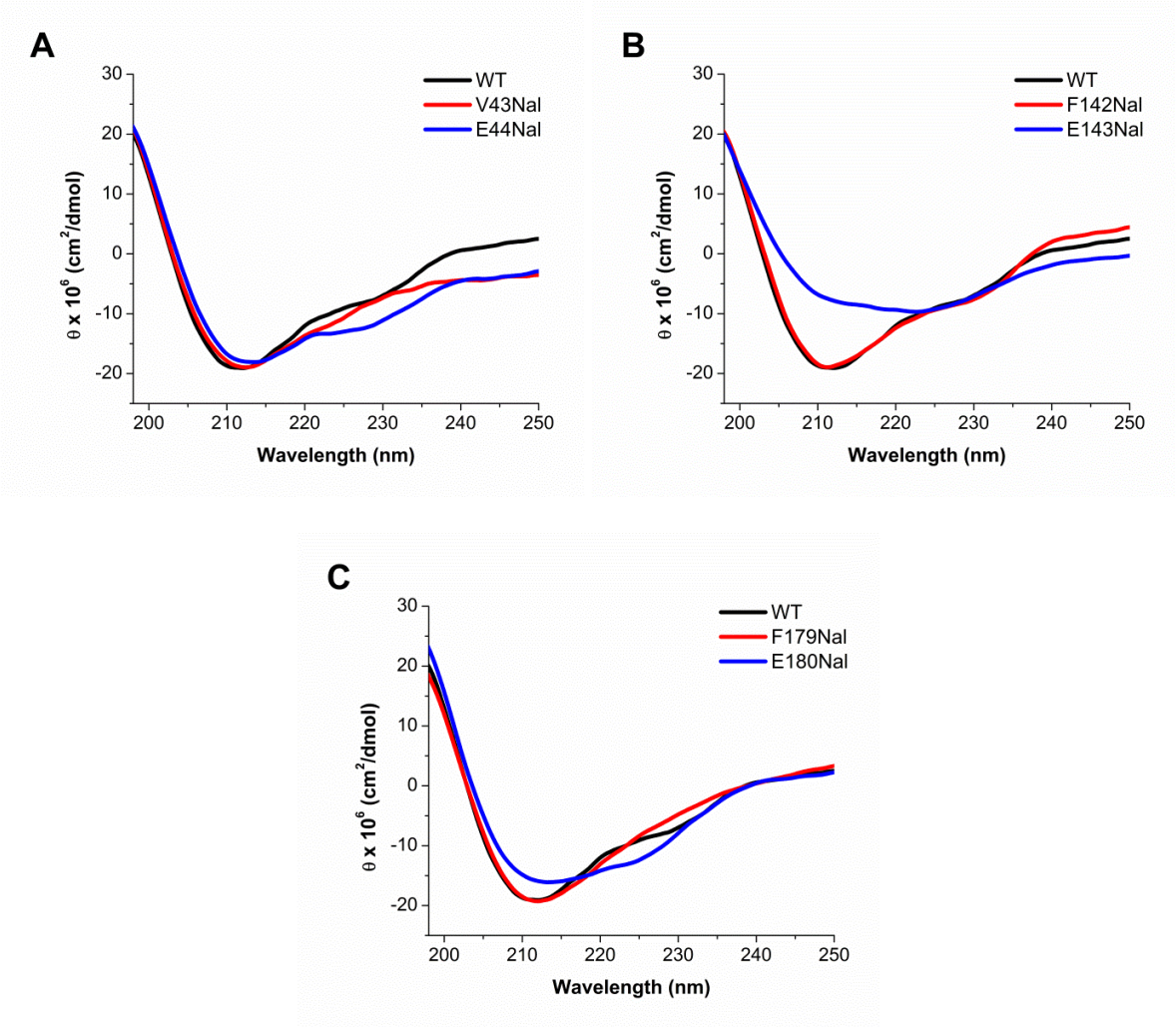

Figure 5.14. Evaluation of secondary structure changes by far-UV circular dichroism. Spectra for A) Wild-type, V43Nal, E44Nal, B) wild-type, F142Nal, E143Nal, C) wild-type, F179Nal, E180Nal over the wavelength range of 195 - 250 nm.

From these results we observed that between mutants of adjacent sites, the substitution of hydrophobic residues with Nal consistently maintained a higher $[\theta]_{212}/[\theta]_{222}$ ratio than the substitution of Nal at the counterpart Glu sites. In each case, incorporation of Nal at the Glu sites increased the ratio of α-helix to β-strand structures. Since Nal is a bulky hydrophobic residue, it can be reasonably inferred that the hydrophobicity scale amongst the residues involved this study is, (Nal, Phe) > Val >> Glu, and therefore incorporation of Nal at Glu causes a greater increase in

hydrophobicity than incorporation of Nal at one of the hydrophobic residues. In each case where the hydrophobic content was significantly increased, through the incorporation of Nal at a charged Glu residue, more severe structural changes were observed. This is consistent with the idea that hydrophobic residues govern the structure of solvent-exposed regions (343). These results indicate that the HDMNR is an important variable at solvent-exposed sites that affects protein structure. These results also confirm our hypothesis that the mutations with higher HDMNR are more likely to cause structural changes.

Evaluating the effect of Nal incorporation on DHF binding affinity

Next, we wanted to examine how the incorporation of Nal affected enzyme function. Substrate binding is the obligate step in all enzymatic reactions before biocatalysis can occur. Since reduction of DHF by mDHFR follows Michaeli-Menten kinetics within the measured substrate concentration range (0 – 40 μM DHF) (288, 293, 296-305, 310-313, 324, 337, 387, 388), K_m, the inverse measure of binding affinity, was used to evaluate the effect of Nal incorporation on the substrate binding component of enzyme function.

Mutations that minimized the HDMNR minimized changes to DHF binding affinity.

Based on the K_m values, V43Nal, F142Nal and F179Nal maintained the same DHF binding affinity as wild-type, as the values were statistically indistinguishable ($p > 0.05$) from one another (Table 5.4 and Figure 5.15). Alternatively incorporation of Nal at each of the glutamic acid sites displayed a different response. For the E44Nal, E143Nal and E180Nal mutations, K_m values noticeably deviated from that of wild-type mDHFR by +0.54 μM, +0.50 μM and +0.75 μM, respectively with $p \leq 0.01$ (Table 5.4 and Figure 5.15). Similarly, the

difference in K_m values between adjacent mutations sites was also found to be statistically significant ($p \leq 0.01$). A two-tailed, unpaired, Student's t-test was employed to determine whether the difference in K_m values between the substitution of Nal at the hydrophobic sites and the charged Glu sites was statistically significant. The *p*-value for the analysis was determined to be 0.006 which indicates that the difference is indeed statistically significant. This indicates that the mutations that minimized the HDMNR minimized changes to DHF binding affinity.

We also considered whether the distance between the incorporation site and substrate binding pocket was a significant factor that lead to the observed trend between mutants of adjacent incorporation sites. Differences in K_m values were found to be independent of the distance of the mutation from the active site, since the two values did not correlate with one another (Table 5.3 and Table 5.4). However, between mutants of adjacent sites, ASA was found to trend negatively with K_m values (341, 375). This is expected since ASA is a variable that has been shown to be important to how mutations affect structure and function (343, 375). Lastly between mutants of adjacent sites, $[\theta]_{212}/[\theta]_{222}$ was also found to trend negatively with K_m values. These results collectively suggest that structural changes are responsible for the deviations in the K_m from that of wild-type. These trends are consistent with studies that have shown that distal mutations and structural changes can affect DHF binding affinity (287, 290, 292, 386, 392). However, more extensive structural information is required to evaluate how these changes in binding affinity occur. Nonetheless these results suggest that creating mutations that are intended to minimize changes in structure is a viable strategy for minimizing changes in the binding component of enzyme function.

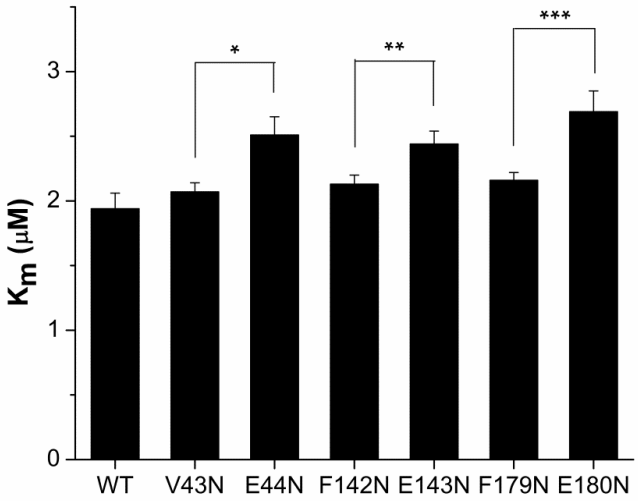

Figure 5.15. Michaelis-Menten constants (K_m) for DHF reduction for wild-type mDHFR and mutants at solvent-exposed sites. K_m values were derived from the Michaelis-Menten model. WT denotes wild-type mDHFR. Error bars denote the standard error (n = 3). Here, N denotes Nal. The unpaired, two-tailed, Student's t-test was used to obtain *p*-values. (*; $p = 0.008$), (**; $p = 0.01$), and (***; $p = 0.006$).

Evaluating the effect of Nal incorporation solvent-exposed sites on catalytic function

Next, we evaluated the impact of each mutation on catalytic function. The primary role of DHFR in all organisms is the formation of tetrahydrofolate (THF) through the reduction of DHF in a hydride transfer reaction aided by the cofactor NADPH (288, 306, 310, 311). This process has hyperbolic reaction kinetics which is modeled by the Michaelis-Menten equation (288, 293, 296-305, 310-313, 324, 337, 387, 388). The kinetic parameters k_{cat} and k_{cat}/K_m, are the substrate turnover rate and catalytic efficiency, respectively, and are used to evaluate the effect of each mutation on function.

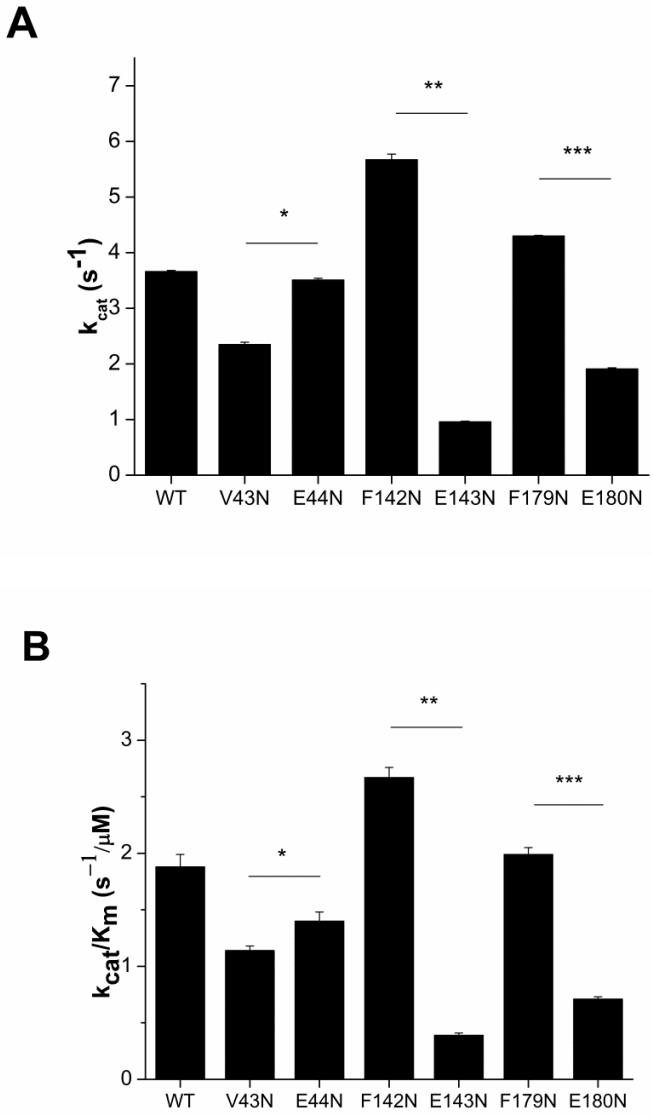

Figure 5.16. Substrate turnover rate (k_{cat}) and catalytic efficiency (k_{cat}/K_m) for mutations at surface exposed sites. A) k_{cat}, and B) k_{cat}/K_m are shown. WT denotes wild-type mDHFR. Error bars denote the standard error (n = 3). Here, N denotes Nal. Unpaired, two-tailed, Student's t-test was performed to obtain *p*-values. For A) (*; $p < 0.001$), (**; $p < 0.001$), and (**; $p < 0.001$). For B) (*; $p < 0.005$), (**; $p < 0.001$), and (**; $p < 0.001$).

Large hydrophobic non-natural amino acids can be incorporated at solvent-exposed sites without loss of enzyme function

Of the mutations, F142Nal and F179Nal were completely functionally permissive mutations. They exhibited the same substrate binding affinity as that of wild-type mDHFR and they exhibited relative catalytic efficiencies of 141.6 ± 4.6 % and 105.8 ± 3.1 %, respectively Table 5.4 and Figure 5.16A and 5.16B). This clearly indicates that a hydrophobic non-natural amino acid such as Nal, that are larger than any of the natural amino acid can be incorporated at solvent-exposed sites without loss of enzymatic function.

Since F142Nal did not disrupt substrate binding affinity or secondary structure, but exhibited an increase in the substrate turnover rate, this suggests that the Phe142 is in a functionally-relevant region or site outside of the active site. This is indeed the case. The F142Nal mutation is located in the catalytically-relevant F-G loop which is involved in opening and occlusion of the active site (288, 408). Since the secondary structure of F142Nal is nearly identical to that of wild-type, the increase in catalytic activity is unlikely to have resulted from a structure change (288, 292, 300, 385, 401). However since opening and occlusion of the active site is involved in a number of rate-limiting steps, including NADP+ and THF release, the F142Nal mutation likely enhances the rate of one of these processes (288, 292, 300, 336, 385).

Mutant catalytic function does not trend with any other parameter

When we compared the substrate turnover rates (k_{cat}) and catalytic efficiencies (k_{cat}/K_m) between the adjacent mutations, a trend was not apparent (Table 5.4 and Figure 5.16A and 5.16B). While the F142Nal and F179Nal retained significantly higher catalytic efficiency than their adjacent counterparts, this was not the case between V43Nal and E44Nal. E44Nal exhibited

a higher k_{cat} and k_{cat}/K_m than V43Nal (Figure 5.16B). The catalytic behavior of V43Nal and E44Nal and catalytic function did not trend or correlate with any of the parameters including HDMNR, $[\theta]_{212}/[\theta]_{222}$ or K_m (Table 5.3 and Table 5.4). Since the short loop region containing the two mutations is not well characterized, it is difficult to evaluate why the two mutations behaved accordingly therefore further studies are required to elucidate the role of these positions. However we suspect that Val43 and Glu44 are located on a functional loop region.

Conclusions

The goal of this research effort was to improve the understanding of how non-natural amino acids can be permissively incorporated into enzymes in order to maintain function. What is learned here can also be applied broadly to mutations, involving both natural and non-natural amino acids. In particular we focused our efforts on two regions, the hydrophobic core and the solvent-exposed sites which are present in almost all globular proteins. We hypothesized that mutations that are intended to minimize structural changes may be able to minimize impact on mDHFR enzyme function.

For the hydrophobic core, the conservative mutations W113Nal and F134Nal were not completely sterically compatible compared to their native site residues which lead to secondary structure changes. Nal is not an equivalent substitution for Trp and Phe, likely because of its larger size. The steric incompatibility, however, was unable to affect DHF binding. Nonetheless these two mutations were able to affect the catalytic activity of mDHFR which suggests that Trp113 and Phe134 are important to catalytic function. The steric incompatibility (LJR score calculated by the by RosettaDesign) of a given Nal substitution was found to have a linear positive correlation with $|\Delta K_m|$, the absolute difference between the K_m of the mutant and that of

wild-type. This correlation is likely due to the fact that substrate binding affinity is closely related to the structure and conformation of an enzyme. Statistical analysis also revealed that k_{cat} and k_{cat}/K_m have a negative non-linear monotonic correlation with the LJR score. While the Pearson's correlation coefficient was not found to be significant, indicating non-linearity, the Spearman rho correlation coefficient ρ and corresponding *p*-value were determined to be 0.886 and 0.019, respectively. The results suggest that both the binding and catalytic component of mDHFR enzymatic function are dependent on the steric compatibility of a mutation. These results suggest that, for hydrophobic core, mutations that are intended to minimize structural changes can be used strategically to minimize the impact on mDHFR enzyme function.

For solvent-exposed sites, two mutations F142Nal and F179Nal were found to be completely functionally permissive as both mutations did not affect substrate binding affinity and were innocuous to catalytic function. F142Nal was able to enhance substrate turnover to 142% when compared to wild-type, while F179Nal maintained wild-type mDHFR catalytic activity. These results demonstrate that hydrophobic non-natural amino acids, that are larger than any ofo the natural amino acids can be incorporated at solvent-exposed sites without loss of function. The incorporation of Nal at hydrophobic residues caused less severe changes in β-sheet and α-helix secondary structure content than incorporation at Glu sites. There was also a statistically significant difference in how Nal incorporation at hydrophobic residues and hydrophilic (Glu) residues affect the substrate binding component of enzyme function. Incorporation of Nal at Glu weakened DHF binding affinity whereas incorporation of Nal at hydrophobic sites did not. Based on the unpaired, two-tailed, Student's t-test, this difference (+0.60 μM) was found to be statistically significant. Collectively, these results suggest that the incorporation of Nal at hydrophobic residue and Glu yielded different responses, due to the changes in structure that are

associated with the change in hydrophobicity upon mutation. Finally, a correlation could not be found between changes in catalytic activity (k_{cat} and k_{cat}/K_m) and any of other parameters (HDMNR, ASA, $[\theta]_{212}/[\theta]_{222}$ and K_m) studied here. This suggests that other factors, that we could not identify here, play an important role in enzymes function.

With this work we have elucidated whether large hydrophobic non-natural amino acids can be permissively incorporated into two important parts of globular proteins, the hydrophobic core and solvent-exposed sites. We have demonstrated that mDHFR enzyme function is dependent on the steric compatibility of a mutation and also changes in hydrophobicity. These results can be used to aid the design of future studies to look at other parameters and variables that may be important to enzyme function.

Chapter 6

Project summary and recommendations

Project Summary

The goal of this dissertation research is to study the interaction between ligands and proteins. This research effort focused on two areas where ligands are important to protein function: 1) The discovery and characterization of potential small-molecule therapies for protein aggregation-dependent diseases and 2) the understanding of substrate-enzyme interactions upon incorporation of non-natural amino acids.

All research objectives were completed:

1. **Determine whether Brilliant Blue G (BBG) is an effective modulator of Aβ aggregation and cytotoxicity.**

2. **Employ structure-activity analysis using a panel of Brilliant Blue G analogues to determine whether certain structural features are important for Aβ modulating activity.**

BBG was found to be an effective aggregation modulator and reduces Aβ-associated cytotoxicity by promoting the formation of off-pathway, non-toxic aggregates. Structure-activity analysis between BBG and its three commercially-available analogues (Brilliant Blue R (BBR), Brilliant Blue FCF (BBF), and Fast Green FCF (FGF)), revealed that of the group, BBG was the most effective modulator of Aβ aggregation and cytotoxicity, and that its additional methyl groups are important for its enhanced modulating activity. In a follow up study, BBG was also

found to disaggregate Aβ40 fibrils. Currently, we are investigating the effects of BBG in AD mouse models.

3. **Employ structure-activity analysis using a panel of erythrosine B (ERB) analogues to determine if halogenation generates effective modulators of Aβ aggregation and cytotoxicity.**

4. **Provide insight into the binding interaction between erythrosine B analogues and Aβ.**

ERB was found to be an effective modulator of Aβ aggregation and cytotoxicity. The unhalogenated analogue fluorescein was ineffective as an Aβ aggregation and cytotoxicity modulator. Halogenation of either the benzoate or xanthene substituent of fluorescein base structure was able to impart Aβ modulating activity to the molecule, which demonstrates that halogenation generates effective modulators of Aβ. Additionally, the other analogues were characterized as well. Competitive binding studies using sequence specific antibodies also revealed that ERB and a number of its analogues bind at the N-terminus of Aβ monomer.

5. **Determine whether the mutation of Glu30 to 3-(2-naphthyl)-alanine (Nal) alters the catalytic allosteric cooperativity of mDHFR.**

6. **Determine whether the change in allosteric cooperativity of mDHFR that is imparted by the Glu30 to Nal mutation can be replicated with the most similar natural amino acid mutation of Glu30 to Trp.**

Mutation of Glu30 to Nal was shown to alter the coopertivity of mDHFR at low substrate concentrations (0 – 200 μM DHF). At these substrate concentrations, wild-type mDHFR, and the $mDHFR^{E30W}$, the mutant with the most similar natural amino acid, exhibited Michaelis-Menten kinetics, while $mDHFR^{E30Nal}$ was shown to have non-Michaelis-Menten kinetics. Since mutation of Glu30 with the most structurally similar natural amino acid (Trp) could not replicate the behavior found with $mDHFR^{E30Nal}$, this indicated that the size and shape difference between Nal and Trp is responsible for altering the cooperativity of mDHFR.

7. **Investigate how the incorporation of Nal in the hydrophobic core affects the enzymatic function of mDHFR.**

8. **Investigate how the incorporation of Nal in solvent-exposed regions affects the enzymatic function of mDHFR.**

Hydrophobic-core mutants: The Lennard-Jones repulsive score, a measure of steric incompatibility, calculated using RosettaDesign, was found to have a positive linear correlation with the absolute deviation in K_m from that of wild-type (Pearson's correlation coefficient, r = 0.831; p = 0.041). Also, the kinetic parameters, k_{cat} and k_{cat}/K_m were found to have a negative monotonic correlation with the LJR score, based on the Spearman correlation coefficient (ρ = –

0.886; $p = 0.019$). Despite being related structurally, Nal was not an equivalent substitution for Trp and Phe, as it not only caused structural changes, but also adversely affected catalytic activity, however, without impacting K_m. Solvent-exposed-site mutants: Nal, a large hydrophobic residue, could be incorporated at solvent-exposed sites (Phe142 and Phe179) without any adverse affects on the binding (K_m) and catalytic (k_{cat}) components of mDHFR enzyme function. Statistical analysis revealed that substituting Nal for Glu caused significant deviations in K_m when compared to substitution of Nal at hydrophobic residues by an average of +0.60 μM (Two-tailed, unpaired, Student's t-test, $p < 0.01$). A correlation or trend between various parameters and catalytic activity was not found.

Recommendations for future studies

Chapters 2 and 3

The next milestone for this research effort is to determine whether these small-molecules can be used to modulate Aβ42. While Aβ40 is the most physiologically prevalent Aβ isoform, Aβ42 is widely regarded as more toxic and aggregation prone. The two isoforms have a similar aggregation pathway but have been shown to have different sensitivity to small-molecule modulators. A potential therapy that is capable of modulating Aβ40 but not Aβ42 would be limited in its ability to function as a complete disease-modifying treatment option. Also, understanding the differences in interaction between a modulator and Aβ40/Aβ2 would ultimately help in directing the search and design of novel and effective Aβ modulators, and disease-modifying therapies.

Chapter 4

Based on this work, a number of exciting research avenues present themselves. Structural changes are an integral part of allostery and cooperative communication in enzymes. While the E30Nal mutation was shown to promote homotropic activation of mDHFR at low concentrations, the structural mechanism for this change in cooperative behavior is not yet understood. Evidence from the kinetic parameters suggests that $mDHFR^{E30Nal}$ has a similar conformation as $mDHFR^{WT}$ and $mDHFR^{E30W}$ in their high substrate concentration catalytic states. This similarity would suggest that the E30Nal mutation "locks" the mDHFR conformation in the high-DHF (>200 μM) conformation even at low DHF concentrations (≤ 200 μM). Further studies are needed to confirm this. We believe that structural analysis, either with high-resolution methods such as nuclear magnetic resonance imaging and low-resolution methods like circular dichroism can both provide insight into the structural similarities and differences between each of the variants. These techniques can also provide important information on structural intermediates, reaction transition states, and new DHF binding modes.

Understanding both the mechanism and strategies for altering cooperativity in enzymes could greatly enhance our ability to control them for a wide variety of engineering applications. Along these lines, we have also compared Glu30 to a number of residues in other allosterically-active enzymes that are involved in cooperativity. These residues all seem to share a number of characteristics. We believe that it would be incredibly useful to determine whether this set of observations holds true by testing the hypothesis towards other allosterically-active enzymes. In addition, we hope that, what has been learned here can be applied to high-value enzymes.

Chapter 5

Our recommendations for future studies are intended to address a number of research limitations that were observed in this work and reflect changes that would be made if the study was re-conducted. These limitations are listed numerically as follows:

1) Sample size – limitation in statistical analysis power and the ability to test wider sequence and structure spaces
2) Enzyme model – limitation in sequence and structure space, and expression yield

In this research effort, we focused our efforts to determine how changes in two parameters, steric compatibility and hydrophobicity at the hydrophobic core and solve-exposed sites, respectively, affected enzyme function. However, these are only single parameters out of many that can affect enzyme function and the exact relationship between these parameters and enzyme function is still unknown. Therefore, evaluating for the presence of trends and relationships requires statistical analysis. To perform more rigorous statistical analysis, a larger sample size, with more mutations, is required. While smaller sample sizes can be used with statistical analysis like the Student's t-test, the law of large numbers indicates that statistical power and greater confidence in results is achieved with larger sample sizes. This is also related to the fact that the standard error of the mean is inversely proportional to the square root of the sample size. Furthermore, larger sample sizes would allow us to test more subtle changes in parameters with greater confidence. It is important to note that similar studies that have investigated the effect of point mutations on enzyme function have often used hundreds and up to thousands of mutations. However, this is not feasible for this project given the time constraints and technical constraints of using nAAs.

An example where a larger sample size would have been crucial was while determining whether the changes in catalytic activity at the solvent exposed sites were dependent on changes in hydrophobicity. A larger sample size might have elucidated a trend or correlation. For the calculation of the Pearson's correlation coefficient (PCC), larger sample sizes can greatly reduce the need for a high PCC coefficient, since the *p*-value derived from the PCC is dependent on sample size. And lastly, a larger sample size could have been used to identify the shape of the negative monotonic correlation between the catalytic parameters k_{cat} and k_{cat}/K_m with the LJR score.

To estimate the sample size that would allow us to take advantage of a wider range of statistical tools, we looked at the number of samples required for pairwise difference analysis, where samples are matched/paired to minimize the effect of confounding variables. These types of analysis methods require the most data points. Chi-squared analysis is often used for pairwise comparisons, and it requires a minimum of 5 expected outcomes per variable/pair/category. Therefore, a sample size of at least 20 mutants is required to test a single parameter that yields two types of expected outcomes (i.e. high/low or true/false). 30 mutants are required if there are three types of expected outcomes (higher/equal/lower). Therefore a minimum of 10 pairs of adjacent mutants would be selected from each region (hydrophobic and solvent-exposed) (40 total mutants) if the study were re-conducted with slightly more lax but similar time and resource constraints, or the number of parameters being studied can be reduced. However, 15 pairs of adjacent mutants would be selected from each region (60 total mutants) for a full study.

While DHFR is an extensively studied enzyme, it possesses a number of limitations. One limitation of using DHFR is that it has a low diversity of highly solvent-exposed hydrophobic residues. This limited our ability to test a broad range of hydrophobic residues at solvent-

exposed sites. Therefore, a larger monomeric enzyme may be better suited as a test platform. This would not only afford greater residue diversity for solvent-exposed sites but in principle also for the hydrophobic core. It would also be expected that the increase in sequence space would also increase the structure space, the diversity of local structural environments and/or the number of functionally-relevant residues. Mannitol dehydrogenase (MDH) would be a prime candidate since it is larger than DHFR and has previously been characterized by our group.

A general limitation of using nAAs is that expression yields are often low. This was found to be the case with mDHFR using the current expression system setup. Because of this we were limited in our ability to perform circular dichroism on a number of mutants. One way to bypass this issue would be to select a higher yielding enzyme, staying with the current expression system. Another method would be to use a new expression system/strain such as C321ΔA.exp. C321ΔA.exp is a release factor 1-deleted *E. coli* strain and has been shown to improve expression titers significantly. Most importantly it has been tested in our lab. However, successs of this approach will also depend on the fidelity of the existing aminoacyl tRNA synthetase/tRNA pair for Nal since C321ΔA.exp is not auxotrophic for Phe, Trp, and Lys. Given that MDH expression yields using the C321ΔA.exp are high, compared to mDHFR yields with the current system, it would be recommended to switch to the MDH as the target enzyme using the C321ΔA.exp expression system.

References

1. Citron M (2010) Alzheimer's disease: strategies for disease modification. *Nature Reviews Drug Discovery* 9(5):387-398.

2. Citron M (2004) Strategies for disease modification in Alzheimer's disease. *Nature Reviews Neuroscience* 5(9):677-685.

3. LeVine H (2004) Alzheimer's beta-peptide oligomer formation at physiologic concentrations. *Analytical Biochemistry* 335(1):81-90.

4. Atamna H (2009) Amino acids variations in Amyloid-beta peptides, mitochondrial dysfunction, and new therapies for Alzheimer's disease. *Journal of Bioenergetics and Biomembranes* 41(5):457-464.

5. Roychaudhuri R, Yang M, Hoshi MM, & Teplow DB (2009) Amyloid beta-Protein Assembly and Alzheimer Disease. *Journal of Biological Chemistry* 284(8):4749-4753.

6. Goedert M, Crowther RA, & Garner CC (1991) Molecular characterization of microtubule-associated proteins-tau and map2. *Trends in Neurosciences* 14(5):193-199.

7. Bailey JA, Maloney B, Ge Y-W, & Lahiri DK (2011) Functional activity of the novel Alzheimer's amyloid beta-peptide interacting domain (A beta ID) in the APP and BACE1 promoter sequences and implications in activating apoptotic genes and in amyloidogenesis. *Gene* 488(1-2):13-22.

8. Selkoe DJ (2001) Alzheimer's disease: Genes, proteins, and therapy. *Physiological Reviews* 81(2):741-766.

9. Ma QL*, et al.* (2009) beta-Amyloid Oligomers Induce Phosphorylation of Tau and Inactivation of Insulin Receptor Substrate via c-Jun N-Terminal Kinase Signaling: Suppression by Omega-3 Fatty Acids and Curcumin. *Journal of Neuroscience* 29(28):9078-9089.

10. Busciglio J, Lorenzo A, Yeh J, & Yankner BA (1995) Beta-amyloid fibrils induce tau-phosphorylation and loss of microtubule-binding. *Neuron* 14(4):879-888.

11. De Felice FG*, et al.* (2008) Alzheimer's disease-type neuronal tau hyperphosphorylation induced by A beta oligomers. *Neurobiology of Aging* 29(9):1334-1347.

12. Naslund J*, et al.* (2000) Correlation between elevated levels of amyloid beta-peptide in the brain and cognitive decline. *Jama-Journal of the American Medical Association* 283(12):1571-1577.

13. Shoji M*, et al.* (1992) Production of the Alzheimer amyloid-beta protein by normal proteolytic processing. *Science* 258(5079):126-129.

14. Bitan G*, et al.* (2003) Amyloid beta-protein (A beta) assembly: A beta 40 and A beta 42 oligomerize through distinct pathways. *Proceedings of the National Academy of Sciences of the United States of America* 100(1):330-335.

15. Hasegawa K, Yamaguchi I, Omata S, Gejyo F, & Naiki H (1999) Interaction between A beta(1-42) and A beta(1-40) in Alzheimer's beta-amyloid fibril formation in vitro. *Biochemistry* 38(47):15514-15521.

16. Bernstein SL*, et al.* (2009) Amyloid-beta protein oligomerization and the importance of tetramers and dodecamers in the aetiology of Alzheimer's disease. *Nature Chemistry* 1(4):326-331.

17. Bitan G, Fradinger EA, Spring SM, & Teplow DB (2005) Neurotoxic protein oligomers - what you see is not always what you get. *Amyloid-Journal of Protein Folding Disorders* 12(2):88-95.

18. Kirkitadze MD, Bitan G, & Teplow DB (2002) Paradigm shifts in Alzheimer's disease and other neuro degenerative disorders: The emerging role of oligomeric assemblies. *Journal of Neuroscience Research* 69(5):567-577.

19. Glabe CG (2006) Common mechanisms of amyloid oligomer pathogenesis in degenerative disease. *Neurobiology of Aging* 27(4):570-575.

20. Kayed R*, et al.* (2003) Common structure of soluble amyloid oligomers implies common mechanism of pathogenesis. *Science* 300(5618):486-489.

21. Tomic JL, Pensalfini A, Head E, & Glabe CG (2009) Soluble fibrillar oligomer levels are elevated in Alzheimer's disease brain and correlate with cognitive dysfunction. *Neurobiology of Disease* 35(3):352-358.

22. Lesne S*, et al.* (2006) A specific amyloid-beta protein assembly in the brain impairs memory. *Nature* 440(7082):352-357.

23. Glabe CG (2008) Structural Classification of Toxic Amyloid Oligomers. *Journal of Biological Chemistry* 283(44):29639-29643.

24. Stefani M & Dobson CM (2003) Protein aggregation and aggregate toxicity: new insights into protein folding, misfolding diseases and biological evolution. *Journal of Molecular Medicine-Jmm* 81(11):678-699.

25. Ahmed M*, et al.* (2010) Structural conversion of neurotoxic amyloid-beta(1-42) oligomers to fibrils. *Nature Structural & Molecular Biology* 17(5):561-U556.

26. Bitan G, Lomakin A, & Teplow DB (2001) Amyloid beta-protein oligomerization - Prenucleation interactions revealed by photo-induced cross-linking of unmodified proteins. *Journal of Biological Chemistry* 276(37):35176-35184.

27. Walsh DM, Klyubin I, Fadeeva JV, Rowan MJ, & Selkoe DJ (2002) Amyloid-beta oligomers: their production, toxicity and therapeutic inhibition. *Biochemical Society Transactions* 30:552-557.

28. Cleary JP, *et al.* (2005) Natural oligomers of the amyloid-protein specifically disrupt cognitive function. *Nature Neuroscience* 8(1):79-84.

29. Chimon S, *et al.* (2007) Evidence of fibril-like beta-sheet structures in a neurotoxic amyloid intermediate of Alzheimer's beta-amyloid. *Nat. Struct. Mol. Biol.* 14(12):1157-1164.

30. Mawuenyega KG, *et al.* (2010) Decreased Clearance of CNS beta-Amyloid in Alzheimer's Disease. *Science* 330(6012):1774-1774.

31. Shoghi-Jadid K, *et al.* (2002) Localization of neurofibrillary tangles and beta-amyloid plaques in the brains of living patients with Alzheimer disease. *American Journal of Geriatric Psychiatry* 10(1):24-35.

32. Dovey HF, *et al.* (2001) Functional gamma-secretase inhibitors reduce beta-amyloid peptide levels in brain. *Journal of Neurochemistry* 76(1):173-181.

33. Kounnas MZ, *et al.* (2010) Modulation of gamma-Secretase Reduces beta-Amyloid Deposition in a Transgenic Mouse Model of Alzheimer's Disease. *Neuron* 67(5):769-780.

34. Kopec KK & Carroll RT (1998) Alzheimer's beta-amyloid peptide 1-42 induces a phagocytic response in murine microglia. *Journal of Neurochemistry* 71(5):2123-2131.

35. Hickman SE, Allison EK, & El Khoury J (2008) Microglial dysfunction and defective beta-amyloid clearance pathways in aging Alzheimer's disease mice. *Journal of Neuroscience* 28(33):8354-8360.

36. Fang F, *et al.* (2010) RAGE-dependent signaling in microglia contributes to neuroinflammation, A beta accumulation, and impaired learning/memory in a mouse model of Alzheimer's disease. *Faseb Journal* 24(4):1043-1055.

37. Sigurdsson EM, Scholtzova H, Mehta PD, Frangione B, & Wisniewski T (2001) Immunization with a nontoxic/nonfibrillar amyloid-beta homologous peptide reduces Alzheimer's disease-associated pathology in transgenic mice. *American Journal of Pathology* 159(2):439-447.

38. Schenk D, *et al.* (1999) Immunization with amyloid-beta attenuates Alzheimer disease-like pathology in the PDAPP mouse. *Nature* 400(6740):173-177.

39. Lambert MP, *et al.* (2001) Vaccination with soluble A beta oligomers generates toxicity-neutralizing antibodies. *Journal of Neurochemistry* 79(3):595-605.

40. Ferrer I, Rovira MB, Guerra MLS, Rey MJ, & Costa-Jussa F (2004) Neuropathology and pathogenesis of encephalitis following amyloid-beta immunization in Alzheimer's disease. *Brain Pathology* 14(1):11-20.

41. Necula M, Kayed R, Milton S, & Glabe CG (2007) Small molecule inhibitors of aggregation indicate that amyloid beta oligomerization and fibrillization pathways are independent and distinct. *J. Biol. Chem.* 282(14):10311-10324.

42. Chromy BA*, et al.* (2003) Self-assembly of A beta(1-42) into globular neurotoxins. *Biochemistry* 42(44):12749-12760.

43. Yu LP*, et al.* (2009) Structural Characterization of a Soluble Amyloid beta-Peptide Oligomer. *Biochemistry* 48(9):1870-1877.

44. Tomaselli S*, et al.* (2006) The alpha-to-beta conformational transition of Alzheimer's A beta-(1-42) peptide in aqueous media is reversible: A step by step conformational analysis suggests the location of beta conformation seeding. *Chembiochem* 7(2):257-267.

45. Jarrett JT, Berger EP, & Lansbury PT (1993) The C-terminus of the beta-protein is critical in amyloidogenesis. *Alzheimers Disease: Amyloid Precusor Proteins, Signal Transduction, and Neuronal Transplantation,* Annals of the New York Academy of Sciences, eds Nitsch RM, Growdon JH, Corkin S, & Wurtman RJ), Vol 695, pp 144-148.

46. Shivaprasad S & Wetzel R (2004) An intersheet packing interaction in A beta fibrils mapped by disulfide cross-linking. *Biochemistry* 43(49):15310-15317.

47. O'Nuallain B, Williams AD, Westermark P, & Wetzel R (2004) Seeding specificity in amyloid growth induced by heterologous fibrils. *Journal of Biological Chemistry* 279(17):17490-17499.

48. Nelson R*, et al.* (2005) Structure of the cross-beta spine of amyloid-like fibrils. *Nature* 435(7043):773-778.

49. Lomakin A, Chung DS, Benedek GB, Kirschner DA, & Teplow DB (1996) On the nucleation and growth of amyloid beta-protein fibrils: Detection of nuclei and quantitation of rate constants. *Proceedings of the National Academy of Sciences of the United States of America* 93(3):1125-1129.

50. Fezoui Y & Teplow DB (2002) Kinetic studies of amyloid beta-protein fibril assembly - Differential effects of alpha-helix stabilization. *Journal of Biological Chemistry* 277(40):36948-36954.

51. Serpell LC (2000) Alzheimer's amyloid fibrils: structure and assembly. *Biochimica Et Biophysica Acta-Molecular Basis of Disease* 1502(1):16-30.

52. Luhrs T*, et al.* (2005) 3D structure of Alzheimer's amyloid-beta(1-42) fibrils. *Proceedings of the National Academy of Sciences of the United States of America* 102(48):17342-17347.

53. Walsh DM, *et al.* (1999) Amyloid beta-protein fibrillogenesis - Structure and biological activity of protofibrillar intermediates. *Journal of Biological Chemistry* 274(36):25945-25952.

54. Finder VH & Glockshuber R (2007) Amyloid-beta aggregation. *Neurodegenerative Diseases* 4(1):13-27.

55. Maezawa I, *et al.* (2008) Congo red and thioflavin-T analogs detect A beta oligomers. *Journal of Neurochemistry* 104(2):457-468.

56. Groenning M, *et al.* (2007) Study on the binding of Thioflavin T to beta-sheet-rich and non-beta-sheet cavities. *Journal of Structural Biology* 158(3):358-369.

57. Khurana R, *et al.* (2005) Mechanism of thioflavin T binding to amyloid fibrils. *J. Struct. Biol.* 151(3):229-238.

58. Shen CL & Murphy RM (1995) Solvent effects on self-assembly of beta-amyloid peptide. *Biophysical Journal* 69(2):640-651.

59. Dobson CM (2003) Protein folding and misfolding. *Nature* 426(6968):884-890.

60. Chiti F & Dobson CM (2006) Protein misfolding, functional amyloid, and human disease. *Annual Review of Biochemistry* 75:333-366.

61. Mamikonyan G, *et al.* (2007) Anti-A beta(1-11) antibody binds to different beta-amyloid species, inhibits fibril formation, and disaggregates preformed fibrils but not the most toxic oligomers. *Journal of Biological Chemistry* 282(31):22376-22386.

62. Kayed R, *et al.* (2010) Conformation dependent monoclonal antibodies distinguish different replicating strains or conformers of prefibrillar A beta oligomers. *Molecular Neurodegeneration* 5:10.

63. Kayed R & Glabe CG (2006) Conformation-dependent anti-amyloid oligomer antibodies. *Amyloid, Prions, and Other Protein Aggregates, Pt C,* Methods in Enzymology), Vol 413, pp 326-344.

64. Glabe CG (2004) Conformation-dependent antibodies target diseases of protein misfolding. *Trends in Biochemical Sciences* 29(10):542-547.

65. Kayed R, *et al.* (2007) Fibril specific, conformation dependent antibodies recognize a generic epitope common to amyloid fibrils and fibrillar oligomers that is absent in prefibrillar oligomers. *Molecular Neurodegeneration* 2.

66. Pardridge WM (2007) Blood-brain barrier delivery. *Drug Discovery Today* 12(1-2):54-61.

67. Atwal JK, *et al.* (2011) A Therapeutic Antibody Targeting BACE1 Inhibits Amyloid-beta Production in Vivo. *Science Translational Medicine* 3(84).

68. Yu YJ, *et al.* (2011) Boosting Brain Uptake of a Therapeutic Antibody by Reducing Its Affinity for a Transcytosis Target. *Science Translational Medicine* 3(84).

69. Harding FA, Stickler MM, Razo J, & DuBridge RB (2010) The immunogenicity of humanized and fully human antibodies Residual immunogenicity resides in the CDR regions. *Mabs* 2(3):256-265.

70. Ramassamy C (2006) Emerging role of polyphenolic compounds in the treatment of neurodegenerative diseases: A review of their intracellular targets. *European Journal of Pharmacology* 545(1):51-64.

71. Behl C, Davis JB, Lesley R, & Schubert D (1994) Hydrogen-peroxide mediates amyloid-beta protein toxicity. *Cell* 77(6):817-827.

72. Ono K, Hasegawa K, Naiki H, & Yamada M (2004) Curcumin has potent anti-amyloidogenic effects for Alzheimer's beta-amyloid fibrils in vitro. *Journal of Neuroscience Research* 75(6):742-750.

73. Yang FS, *et al.* (2005) Curcumin inhibits formation of amyloid beta oligomers and fibrils, binds plaques, and reduces amyloid in vivo. *J. Biol. Chem.* 280(7):5892-5901.

74. Reinke AA & Gestwicki JE (2007) Structure-activity relationships of amyloid beta-aggregation inhibitors based on curcumin: Influence of linker length and flexibility. *Chemical Biology & Drug Design* 70(3):206-215.

75. Shin J, Kepe V, Barrio JR, & Small GW (2011) The Merits of FDDNP-PET Imaging in Alzheimer's Disease. *Journal of Alzheimers Disease* 26:135-145.

76. Mecocci P & Polidori MC (2012) Antioxidant clinical trials in mild cognitive impairment and Alzheimer's disease. *Biochimica Et Biophysica Acta-Molecular Basis of Disease* 1822(5):631-638.

77. Anekonda TS (2006) Resveratrol - A boon for treating Alzheimer's disease? *Brain Research Reviews* 52(2):316-326.

78. Lindsay J, *et al.* (2002) Risk factors for Alzheimer's disease: A prospective analysis from the Canadian Study of Health and Aging. *American Journal of Epidemiology* 156(5):445-453.

79. Sun AY, Wang Q, Simonyi A, & Sun GY (2010) Resveratrol as a Therapeutic Agent for Neurodegenerative Diseases. *Molecular Neurobiology* 41(2-3):375-383.

80. Ladiwala ARA, *et al.* (2010) Resveratrol Selectively Remodels Soluble Oligomers and Fibrils of Amyloid A beta into Off-pathway Conformers. *J. Biol. Chem.* 285(31):24228-24237.

81. Feng Y, *et al.* (2009) Resveratrol inhibits beta-amyloid oligomeric cytotoxicity but does not prevent oligomer formation. *Neurotoxicology* 30(6):986-995.

82. Ge J-F, Qiao J-P, Qi C-C, Wang C-W, & Zhou J-N (2012) The binding of resveratrol to monomer and fibril amyloid beta. *Neurochemistry International* 61(7):1192-1201.

83. Li F, Gong Q, Dong H, & Shi J (2012) Resveratrol, A Neuroprotective Supplement for Alzheimer's Disease. *Current Pharmaceutical Design* 18(1):27-33.

84. Jang JH & Surh YJ (2003) Protective effect of resveratrol on beta-amyloid-induced oxidative PC12 cell death. *Free Radical Biology and Medicine* 34(8):1100-1110.

85. Marambaud P, Zhao HT, & Davies P (2005) Resveratrol promotes clearance of Alzheimer's disease amyloid-beta peptides. *Journal of Biological Chemistry* 280(45):37377-37382.

86. Karuppagounder SS*, et al.* (2009) Dietary supplementation with resveratrol reduces plaque pathology in a transgenic model of Alzheimer's disease. *Neurochemistry International* 54(2):111-118.

87. Patel KR*, et al.* (2011) Clinical trials of resveratrol. *Resveratrol and Health,* Annals of the New York Academy of Sciences, eds Vang O & Das DK), Vol 1215, pp 161-169.

88. Smoliga JM, Baur JA, & Hausenblas HA (2011) Resveratrol and health - A comprehensive review of human clinical trials. *Molecular Nutrition & Food Research* 55(8):1129-1141.

89. Ehrnhoefer DE*, et al.* (2008) EGCG redirects amyloidogenic polypeptides into unstructured, off-pathway oligomers. *Nat. Struct. Mol. Biol.* 15(6):558-566.

90. Bieschke J*, et al.* (2010) EGCG remodels mature alpha-synuclein and amyloid-beta fibrils and reduces cellular toxicity. *Proceedings of the National Academy of Sciences of the United States of America* 107(17):7710-7715.

91. Rezai-Zadeh K*, et al.* (2008) Green tea epigallocatechin-3-gallate (EGCG) reduces beta-amyloid mediated cognitive impairment and modulates tau pathology in Alzheimer transgenic mice. *Brain Research* 1214:177-187.

92. Lee JW*, et al.* (2009) Green Tea (-)-Epigallocatechin-3-Gallate Inhibits beta-Amyloid-Induced Cognitive Dysfunction through Modification of Secretase Activity via Inhibition of ERK and NF-kappa B Pathways in Mice. *Journal of Nutrition* 139(10):1987-1993.

93. Rezai-Zadeh K*, et al.* (2005) Green tea epigallocatechin-3-gallate (EGCG) modulates amyloid precursor protein cleavage and reduces cerebral amyloidosis in Alzheimer transgenic mice. *Journal of Neuroscience* 25(38):8807-8814.

94. De Strooper B*, et al.* (1998) Deficiency of presenilin-1 inhibits the normal cleavage of amyloid precursor protein. *Nature* 391(6665):387-390.

95. Mereles D & Hunstein W (2011) Epigallocatechin-3-gallate (EGCG) for Clinical Trials: More Pitfalls than Promises? *International Journal of Molecular Sciences* 12(9):5592-5603.

96. de la Torre R & Dierssen M (2012) Therapeutic approaches in the improvement of cognitive performance in Down syndrome: past, present, and future. *Down Syndrome: from Understanding the Neurobiology to Therapy* 197:1-14.

97. Frid P, Anisimov SV, & Popovic N (2007) Congo red and protein aggregation in neurodegenerative diseases. *Brain Res. Rev.* 53(1):135-160.

98. Nordberg A (2004) PET imaging of amyloid in Alzheimer's disease. *Lancet Neurology* 3(9):519-527.

99. Klunk WE, Jacob RF, & Mason RP (1999) Quantifying amyloid beta-peptide (A beta) aggregation using the Congo red A beta (CR-A beta) spectrophotometric assay. *Analytical Biochemistry* 266(1):66-76.

100. Irwin JA, Wong HE, & Kwon I (2015) Determining binding sites of polycyclic aromatic small molecule-based amyloid-beta peptide aggregation modulators using sequence-specific antibodies. *Analytical Biochemistry* 470:61-70.

101. Lorenzo A & Yankner BA (1994) Beta-amyloid neurotoxicity requires fibril formation and is inhibited by congo red. *Proceedings of the National Academy of Sciences of the United States of America* 91(25):12243-12247.

102. Bose PP*, et al.* (2010) Effects of Congo Red on A beta(1-40) Fibril Formation Process and Morphology. *ACS Chem. Neurosci.* 1(4):315-324.

103. Pedersen MO*, et al.* (2010) NMR Reveals Two-Step Association of Congo Red to Amyloid beta in Low-Molecular-Weight Aggregates. *J. Phys. Chem. B* 114(48):16003-16010.

104. Wong HE & Kwon I (2011) Xanthene Food Dye, as a Modulator of Alzheimer's Disease Amyloid-beta Peptide Aggregation and the Associated Impaired Neuronal Cell Function. *Plos One* 6(10).

105. Wang L, Brock A, Herberich B, & Schultz PG (2001) Expanding the genetic code of Escherichia coli. *Science* 292(5516):498-500.

106. Wang L, Xie J, & Schultz PG (2006) Expanding the genetic code. *Annual Review of Biophysics and Biomolecular Structure,* Annual Review of Biophysics), Vol 35, pp 225-249.

107. Young TS & Schultz PG (2010) Beyond the Canonical 20 Amino Acids: Expanding the Genetic Lexicon. *Journal of Biological Chemistry* 285(15):11039-11044.

108. Zeng Y, Wang W, & Liu WR (2014) Towards Reassigning the Rare AGG Codon in Escherichia coli. *Chembiochem* 15(12):1750-1754.

109. Shim SH*, et al.* (2009) Two-dimensional IR spectroscopy and isotope labeling defines the pathway of amyloid formation with residue-specific resolution. *Proceedings of the National Academy of Sciences of the United States of America* 106(16):6614-6619.

110. Hohsaka T, Ashizuka Y, Taira H, Murakami H, & Sisido M (2001) Incorporation of nonnatural amino acids into proteins by using various four-base codons in an Escherichia coli in vitro translation system. *Biochemistry* 40(37):11060-11064.

111. Niu W, Schultz PG, & Guo J (2013) An Expanded Genetic Code in Mammalian Cells with a Functional Quadruplet Codon. *Acs Chemical Biology* 8(7):1640-1645.

112. Anderson JC*, et al.* (2004) An expanded genetic code with a functional quadruplet codon. *Proceedings of the National Academy of Sciences of the United States of America* 101(20):7566-7571.

113. Neumann H, Wang K, Davis L, Garcia-Alai M, & Chin JW (2010) Encoding multiple unnatural amino acids via evolution of a quadruplet-decoding ribosome. *Nature* 464(7287):441-444.

114. Noren CJ, Anthonycahill SJ, Griffith MC, & Schultz PG (1989) A A general-method for site-specific incorporation of unnatural amino-acids into proteins. *Science* 244(4901):182-188.

115. Liu DR, Magliery TJ, Pasternak M, & Schultz PG (1997) Engineering a tRNA and aminoacyl-tRNA synthetase for the site-specific incorporation of unnatural amino acids into proteins in vivo. *Proceedings of the National Academy of Sciences of the United States of America* 94(19):10092-10097.

116. Wang L & Schultz PG (2001) A general approach for the generation of orthogonal tRNAs. *Chemistry & Biology* 8(9):883-890.

117. Liu W, Brock A, Chen S, Chen S, & Schultz PG (2007) Genetic incorporation of unnatural amino acids into proteins in mammalian cells. *Nature Methods* 4(3):239-244.

118. Chin JW*, et al.* (2003) An expanded eukaryotic genetic code. *Science* 301(5635):964-967.

119. Edwards H & Schimmel P (1990) A bacterial amber suppressor in saccharomyces-cerevisiae is selectively recognized by a bacterial aminoacyl-transfer RNA-synthetase. *Molecular and Cellular Biology* 10(4):1633-1641.

120. Sakamoto K*, et al.* (2002) Site-specific incorporation of an unnatural amino acid into proteins in mammalian cells. *Nucleic Acids Research* 30(21):4692-4699.

121. Wang W, *et al.* (2007) Genetically encoding unnatural amino acids for cellular and neuronal studies. *Nature Neuroscience* 10(8):1063-1072.

122. Hino N, Hayashi A, Sakamoto K, & Yokoyama S (2006) Site-specific incorporation of non-natural amino acids into proteins in mammalian cells with an expanded genetic code. *Nature Protocols* 1(6):2957-2962.

123. Chen S, Schultz PG, & Brock A (2007) An improved system for the generation and analysis of mutant proteins containing unnatural amino acids in Saccharomyces cerevisiae. *Journal of Molecular Biology* 371(1):112-122.

124. Ryu YH & Schultz PG (2006) Efficient incorporation of unnatural amino acids into proteins in Escherichia coli. *Nature Methods* 3(4):263-265.

125. Guo J, Melancon CE, III, Lee HS, Groff D, & Schultz PG (2009) Evolution of Amber Suppressor tRNAs for Efficient Bacterial Production of Proteins Containing Nonnatural Amino Acids. *Angewandte Chemie-International Edition* 48(48):9148-9151.

126. Johnson DBF, *et al.* (2012) Release Factor One Is Nonessential in Escherichia coli. *Acs Chemical Biology* 7(8):1337-1344.

127. Lajoie MJ, *et al.* (2013) Genomically Recoded Organisms Expand Biological Functions. *Science* 342(6156):357-360.

128. Johnson DBF, *et al.* (2011) RF1 knockout allows ribosomal incorporation of unnatural amino acids at multiple sites. *Nature Chemical Biology* 7(11):779-786.

129. Wang Q & Wang L (2008) New methods enabling efficient incorporation of unnatural amino acids in yeast. *Journal of the American Chemical Society* 130(19):6066-+.

130. Young TS, Ahmad I, Yin JA, & Schultz PG (2010) An Enhanced System for Unnatural Amino Acid Mutagenesis in E. coli. *Journal of Molecular Biology* 395(2):361-374.

131. Kwon I & Tirrell DA (2007) Site-specific incorporation of tryptophan analogues into recombinant proteins in bacterial cells. *Journal of the American Chemical Society* 129(34):10431-10437.

132. Kwon I, Wang P, & Tirrell DA (2006) Design of a bacterial host for site-specific incorporation of p-bromophenylalanine into recombinant proteins. *Journal of the American Chemical Society* 128(36):11778-11783.

133. Brustad EM & Arnold FH (2011) Optimizing non-natural protein function with directed evolution. *Current Opinion in Chemical Biology* 15(2):201-210.

134. Tian F, Tsao M-L, & Schultz PG (2004) A phage display system with unnatural amino acids. *Journal of the American Chemical Society* 126(49):15962-15963.

135. Link AJ, Mock ML, & Tirrell DA (2003) Non-canonical amino acids in protein engineering. *Current Opinion in Biotechnology* 14(6):603-609.

136. Zheng S & Kwon I (2012) Manipulation of enzyme properties by noncanonical amino acid incorporation. *Biotechnology Journal* 7(1):47-60.

137. Liu CC*, et al.* (2008) Protein evolution with an expanded genetic code. *Proceedings of the National Academy of Sciences of the United States of America* 105(46):17688-17693.

138. Johnson JA, Lu YY, Van Deventer JA, & Tirrell DA (2010) Residue-specific incorporation of non-canonical amino acids into proteins: recent developments and applications. *Current Opinion in Chemical Biology* 14(6):774-780.

139. Kearney PC*, et al.* (1996) Agonist binding site of the nicotinic acetylcholine receptor: Tests with novel side chains and with several agonists. *Molecular Pharmacology* 50(5):1401-1412.

140. Jackson JC, Hammill JT, & Mehl RA (2007) Site-specific incorporation of a F-19-amino acid into proteins as an NMR probe for characterizing protein structure and reactivity. *Journal of the American Chemical Society* 129(5):1160-1166.

141. Ormo M*, et al.* (1996) Crystal structure of the Aequorea victoria green fluorescent protein. *Science* 273(5280):1392-1395.

142. Yang F, Moss LG, & Phillips GN (1996) The molecular structure of green fluorescent protein. *Nature Biotechnology* 14(10):1246-1251.

143. Chalfie M, Tu Y, Euskirchen G, Ward WW, & Prasher DC (1994) Green fluorescent protein as a marker for gene-expression. *Science* 263(5148):802-805.

144. Heim R, Prasher DC, & Tsien RY (1994) Wavelength mutations and posttranslational autoxidation of green fluorescent protein. *Proceedings of the National Academy of Sciences of the United States of America* 91(26):12501-12504.

145. Wang L, Xie JM, Deniz AA, & Schultz PG (2003) Unnatural amino acid mutagenesis of green fluorescent protein. *Journal of Organic Chemistry* 68(1):174-176.

146. Wang F, Niu W, Guo J, & Schultz PG (2012) Unnatural Amino Acid Mutagenesis of Fluorescent Proteins. *Angewandte Chemie-International Edition* 51(40):10132-10135.

147. Stephanopoulos N & Francis MB (2011) Choosing an effective protein bioconjugation strategy. *Nature Chemical Biology* 7(12):876-884.

148. Francis MB & Carrico IS (2010) New frontiers in protein bioconjugation Editorial overview. *Current Opinion in Chemical Biology* 14(6):771-773.

149. de Graaf AJ, Kooijman M, Hennink WE, & Mastrobattista E (2009) Nonnatural Amino Acids for Site-Specific Protein Conjugation. *Bioconjugate Chemistry* 20(7):1281-1295.

150. Rashidian M, Dozier JK, & Distefano MD (2013) Enzymatic Labeling of Proteins: Techniques and Approaches. *Bioconjugate Chemistry* 24(8):1277-1294.

151. Wu P, *et al.* (2009) Site-specific chemical modification of recombinant proteins produced in mammalian cells by using the genetically encoded aldehyde tag. *Proceedings of the National Academy of Sciences of the United States of America* 106(9):3000-3005.

152. Lim SI, Mizuta Y, Takasu A, Kim YH, & Kwon I (2014) Site-Specific Bioconjugation of a Murine Dihydrofolate Reductase Enzyme by Copper(I)-Catalyzed Azide-Alkyne Cycloaddition with Retained Activity. *Plos One* 9(6).

153. Wang Q, *et al.* (2003) Bioconjugation by copper(I)-catalyzed azide-alkyne 3+2 cycloaddition. *Journal of the American Chemical Society* 125(11):3192-3193.

154. Jewett JC & Bertozzi CR (2010) Cu-free click cycloaddition reactions in chemical biology. *Chemical Society Reviews* 39(4):1272-1279.

155. Tron GC, *et al.* (2008) Click chemistry reactions in medicinal chemistry: Applications of the 1,3-dipolar cycloaddition between azides and alkynes. *Medicinal Research Reviews* 28(2):278-308.

156. Baskin JM, *et al.* (2007) Copper-free click chemistry for dynamic in vivo imaging. *Proceedings of the National Academy of Sciences of the United States of America* 104(43):16793-16797.

157. Moses JE & Moorhouse AD (2007) The growing applications of click chemistry. *Chemical Society Reviews* 36(8):1249-1262.

158. Wu P, *et al.* (2004) Efficiency and fidelity in a click-chemistry route to triazole dendrimers by the copper(I)-catalyzed ligation of azides and alkynes. *Angewandte Chemie-International Edition* 43(30):3928-3932.

159. Kolb HC & Sharpless KB (2003) The growing impact of click chemistry on drug discovery. *Drug Discovery Today* 8(24):1128-1137.

160. Kolb HC, Finn MG, & Sharpless KB (2001) Click chemistry: Diverse chemical function from a few good reactions. *Angewandte Chemie-International Edition* 40(11):2004-+.

161. Sletten EM & Bertozzi CR (2009) Bioorthogonal Chemistry: Fishing for Selectivity in a Sea of Functionality. *Angewandte Chemie-International Edition* 48(38):6974-6998.

162. Lim SI, *et al.* (2013) Site-specific fatty acid-conjugation to prolong protein half-life in vivo. *Journal of Controlled Release* 170(2):219-225.

163. Chen H, *et al.* (2011) High-level production of uricase containing keto functional groups for site-specific PEGylation. *Biochemical Engineering Journal* 58-59:25-32.

164. Fang Z, *et al.* (2011) Designing and Engineering of a Site-specific Incorporation of a Keto Group in Uricase. *Chemical Biology & Drug Design* 78(3):353-360.

165. Pasut G & Veronese FM (2012) State of the art in PEGylation: The great versatility achieved after forty years of research. *Journal of Controlled Release* 161(2):461-472.

166. Axup JY, *et al.* (2012) Synthesis of site-specific antibody-drug conjugates using unnatural amino acids. *Proceedings of the National Academy of Sciences of the United States of America* 109(40):16101-16106.

167. Chari RVJ, Miller ML, & Widdison WC (2014) Antibody- Drug Conjugates: An Emerging Concept in Cancer Therapy. *Angewandte Chemie-International Edition* 53(15):3796-3827.

168. Grove JI, *et al.* (2003) Generation of Escherichia coli nitroreductase mutants conferring improved cell sensitization to the prodrug CB1954. *Cancer Research* 63(17):5532-5537.

169. Jackson JC, Duffy SP, Hess KR, & Mehl RA (2006) Improving nature's enzyme active site with genetically encoded unnatural amino acids. *Journal of the American Chemical Society* 128(34):11124-11127.

170. Kolev JN, Zaengle JM, Ravikumar R, & Fasan R (2014) Enhancing the Efficiency and Regioselectivity of P450 Oxidation Catalysts by Unnatural Amino Acid Mutagenesis. *Chembiochem* 15(7):1001-1010.

171. Zheng S & Kwon I (2013) Controlling Enzyme Inhibition Using an Expanded Set of Genetically Encoded Amino Acids. *Biotechnology and Bioengineering* 110(9):2361-2370.

172. Brookmeyer R, Gray S, & Kawas C (1998) Projections of Alzheimer's disease in the United States and the public health impact of delaying disease onset. *Am. J. Public Health* 88(9):1337-1342.

173. Alzheimer's_Association (2010) 2010 Alzheimer's Disease Facts and Figures. in *Alzheimer's & Dementia*.

174. Sinha S & Lieberburg I (1999) Cellular mechanisms of beta-amyloid production and secretion. *Proc. Natl. Acad. Sci. USA* 96(20):11049-11053.

175. Hardy JA & Higgins GA (1992) Alzheimers disease - the amyloid cascade hypothesis. *Science* 256(5054):184-185.

176. Ladiwala ARA, *et al.* (2010) Resveratrol Selectively Remodels Soluble Oligomers and Fibrils of Amyloid A beta into Off-pathway Conformers. *Journal of Biological Chemistry* 285(31):24228-24237.

177. McLean CA, *et al.* (1999) Soluble pool of A beta amyloid as a determinant of severity of neurodegeneration in Alzheimer's disease. *Ann. Neurol.* 46(6):860-866.

178. Hawkes CA, Ng V, & McLaurin J (2009) Small Molecule Inhibitors of A beta-Aggregation and Neurotoxicity. *Drug Dev. Res.* 70(2):111-124.

179. Hamaguchi T, Ono K, & Yamada M (2006) Anti-amyloidogenic therapies: strategies for prevention and treatment of Alzheimer's disease. *Cell. Mol. Life Sci.* 63(13):1538-1552.

180. Thapa A*, et al.* (Biflavonoids Are Superior to Monoflavonoids in Inhibiting Amyloid-beta Toxicity and Fibrillogenesis via Accumulation of Nontoxic Oligomer-like Structures. *Biochemistry* 50(13):2445-2455.

181. Burgevin MC*, et al.* (1994) Neurotoxicity of beta-amyloid analog peptides on rat hippocampal neuronal cultures. *J. Neurochem.* 63:S74-S74.

182. Podlisny MB*, et al.* (1998) Oligomerization of endogenous and synthetic amyloid beta-protein at nanomolar levels in cell culture and stabilization of monomer by congo red. *Biochemistry* 37(11):3602-3611.

183. McLaurin J, Golomb R, Jurewicz A, Antel JP, & Fraser PE (2000) Inositol stereoisomers stabilize an oligomeric aggregate of Alzheimer amyloid beta peptide and inhibit A beta-induced toxicity. *J. Biol. Chem.* 275(24):18495-18502.

184. McLaurin J*, et al.* (2006) Cyclohexanehexol inhibitors of A beta aggregation prevent and reverse Alzheimer phenotype in a mouse model. *Nat. Med.* 12(7):801-808.

185. Feng Y*, et al.* (2009) Resveratrol inhibits beta-amyloid oligomeric cytotoxicity but does not prevent oligomer formation. *Neurotoxicology* 30(6):986-995.

186. Moss MA, Varvel NH, Nichols MR, Reed DK, & Rosenberry TL (2004) Nordihydroguaiaretic Acid Does Not Disaggregate beta-Amyloid(1-40) Protofibrils but Does Inhibit Growth Arising from Direct Protofibril Association. *Molecular Pharmacology* 66(3):592-600.

187. Pardridge WA (2009) Alzheimer's disease drug development and the problem of the blood-brain barrier. *Alzheimers. Dement.* 5(5):427-432.

188. Ladiwala ARA, Dordick JS, & Tessier PM (2010) Aromatic Small Molecules Remodel Toxic Soluble Oligomers of Amyloid beta through Three Independent Pathways. *J. Biol. Chem.* 286(5):3209-3218.

189. Zini A*, et al.* (2006) Do flavan-3-ols from green tea reach the human brain? *Nutr. Neurosci.* 9(1-2):57-61.

190. Yazawa K*, et al.* (2006) Distinct mechanisms underlie distinct polyphenol-induced neuroprotection. *Febs Letters* 580(28-29):6623-6628.

191. Diniz A*, et al.* (2007) Permeability profile estimation of flavonoids and other phenolic compounds by biopartitioning micellar capillary chromatography. *J. Agric. Food Chem.* 55(21):8372-8379.

192. Remy M, *et al.* (2008) An in vivo evaluation of Brilliant Blue G in animals and humans. *Br. J. Ophthalmol.* 92(8):1142-1147.

193. Peng WG, *et al.* (2009) Systemic administration of an antagonist of the ATP-sensitive receptor P2X7 improves recovery after spinal cord injury. *Proc. Natl. Acad. Sci. U. S. A.* 106(30):12489-12493.

194. Borzelleca JF, Depukat K, & Hallagan JB (1990) Lifetime toxicity carcinogenicity studies of FD&C blue No.1 (brilliant blue FCF) in rats and mice. *Food Chem. Toxicol.* 28(4):221-234.

195. Borzelleca Joseph F & Hallagan John B (1992) Safety and Regulatory Status of Food, Drug, and Cosmetic Color Additives. *Food Safety Assessment,* ACS Symposium Series, (American Chemical Society), Vol 484, pp 377-390.

196. Ryu JK & McLarnon JG (2008) Block of purinergic P2X(7) receptor is neuroprotective in an animal model of Alzheimer's disease. *Neuroreport* 19(17):1715-1719.

197. Matute C, *et al.* (2007) P2X(7) receptor blockade prevents ATP excitotoxicity in oligodendrocytes and ameliorates experimental autoimmune encephalomyelitis. *Journal of Neuroscience* 27(35):9525-9533.

198. Hu Y, *et al.* (2010) A strategy for designing a peptide probe for detection of beta-amyloid oligomers. *ChemBioChem* 11(17):2409-2418.

199. Qi W, *et al.* (2008) Simultaneous monitoring of peptide aggregate distributions, structure, and kinetics using amide hydrogen exchange: Application to A beta(1-40) fibrillogenesis. *Biotechnol. Bioeng.* 100(6):1214-1227.

200. Qi W, Zhang AM, Good TA, & Fernandez EJ (2009) Two Disaccharides and Trimethylamine N-Oxide Affect A beta Aggregation Differently, but All Attenuate Oligomer-Induced Membrane Permeability. *Biochemistry* 48(37):8908-8919.

201. Zhang A, Qi W, Good TA, & Fernandez EJ (2009) Structural differences between A beta(1-40) intermediate oligomers and fibrils elucidated by proteolytic fragmentation and hydrogen/deuterium exchange. *Biophysical Journal* 96(3):1091-1104.

202. LeVine H (1999) Quantification of beta-sheet amyloid fibril structures with thioflavin T. *Amyloid, Prions, and Other Protein Aggregates,* Methods in Enzymology), Vol 309, pp 274-284.

203. Dahlgren KN, *et al.* (2002) Oligomeric and fibrillar species of amyloid-beta peptides differentially affect neuronal viability. *J. Biol. Chem.* 277(35):32046-32053.

204. Shafrir Y, Durell SR, Anishkin A, & Guy HR (2010) Beta-barrel models of soluble amyloid beta oligomers and annular protofibrils. *Proteins-Structure Function and Bioinformatics* 78(16):3458-3472.

205. Chen YR & Glabe CG (2006) Distinct early folding and aggregation properties of Alzheimer amyloid-beta peptides A beta 40 and A beta 42 - Stable trimer or tetramer formation by A beta 42. *J. Biol. Chem.* 281(34):24414-24422.

206. Kayed R, *et al.* (2007) Fibril specific, conformation dependent antibodies recognize a generic epitope common to amyloid fibrils and fibrillar oligomers that is absent in prefibrillar oligomers. *Mol. Neurodegener.* 2:18.

207. Wu JW, *et al.* (2010) Fibrillar oligomers nucleate the oligomerization of monomeric amyloid beta but do not seed fibril formation. *J. Biol. Chem.* 285(9):6071-6079.

208. Iijima K, *et al.* (2004) Dissecting the pathological effects of human A beta 40 and A beta 42 in Drosophila: A potential model for Alzheimer's disease. *Proc. Natl. Acad. Sci. U. S. A.* 101(17):6623-6628.

209. Kimura N, *et al.* (2005) Age-related changes of intracellular A beta in cynomolgus monkey brains. *Neuropathol. Appl. Neurobiol.* 31(2):170-180.

210. Klyubin I, *et al.* (2005) Amyloid beta protein immunotherapy neutralizes A beta oligomers that disrupt synaptic plasticity in vivo. *Nat. Med.* 11(5):556-561.

211. Thakker DR, *et al.* (2009) Intracerebroventricular amyloid-beta antibodies reduce cerebral amyloid angiopathy and associated micro-hemorrhages in aged Tg2576 mice. *Proc. Natl. Acad. Sci. U. S. A.* 106(11):4501-4506.

212. Sarroukh R, *et al.* (2010) Transformation of amyloid β(1–40) oligomers into fibrils is characterized by a major change in secondary structure. *Cell. Mol. Life Sci.*:1-10.

213. Schmidt M, *et al.* (2009) Comparison of Alzheimer A beta(1-40) and A beta(1-42) amyloid fibrils reveals similar protofilament structures. *Proc. Natl. Acad. Sci. U. S. A.* 106(47):19813-19818.

214. Findeis MA (2000) Approaches to discovery and characterization of inhibitors of amyloid beta-peptide polymerization. *Biochimica Et Biophysica Acta-Molecular Basis of Disease* 1502(1):76-84.

215. Findeis MA & Molineaux SM (1999) Design and testing of inhibitors of fibril formation. *Amyloid, Prions, and Other Protein Aggregates,* Methods in Enzymology), Vol 309, pp 476-488.

216. Morinaga A, *et al.* (2011) Effects of sex hormones on Alzheimer's disease-associated beta-amyloid oligomer formation in vitro. *Exp. Neurol.* 228(2):298-302.

217. Ono K, *et al.* (2008) Effects of Grape Seed-derived Polyphenols on Amyloid beta-Protein Self-assembly and Cytotoxicity. *J. Biol. Chem.* 283(47):32176-32187.

218. Geng J, Li M, Ren J, Wang E, & Qu X (2011) Polyoxometalates as Inhibitors of the Aggregation of Amyloid β-Peptides Associated with Alzheimer's Disease. *Angew. Chem. Int. Ed.*:n/a-n/a.

219. Feng Y*, et al.* (2009) Ellagic acid promotes A beta 42 fibrillization and inhibits A beta 42-induced neurotoxicity. *Biochem. Biophys. Res. Commun.* 390(4):1250-1254.

220. Pollack SJ, Sadler IIJ, Hawtin SR, Tailor VJ, & Shearman MS (1995) Sulfonated dyes attenuate the toxic effects of beta-amyloid in a structure-specific fashion. *Neuroscience Letters* 197(3):211-214.

221. Avramovich-Tirosh Y*, et al.* (2007) Therapeutic targets and potential of the novel brain-permeable multifunctional iron chelator-monoamine oxidase inhibitor drug, M-30, for the treatment of Alzheimer's disease. *J Neurochem* 100(2):490-502.

222. Avramovich-Tirosh Y*, et al.* (2007) Neurorescue activity, APP regulation and amyloid-beta peptide reduction by novel multi-functional brain permeable iron- chelating-antioxidants, M-30 and green tea polyphenol, EGCG. *Curr Alzheimer Res* 4(4):403-411.

223. Lee S, Fernandez EJ, & Good TA (2007) Role of aggregation conditions in structure, stability, and toxicity of intermediates in the A beta fibril formation pathway. *Protein Science* 16(4):723-732.

224. Reznichenko L*, et al.* (2006) Reduction of iron-regulated amyloid precursor protein and beta-amyloid peptide by (-)-epigallocatechin-3-gallate in cell cultures: implications for iron chelation in Alzheimer's disease. *J Neurochem* 97(2):527-536.

225. Hudson SA, Ecroyd H, Kee TW, & Carver JA (2009) The thioflavin T fluorescence assay for amyloid fibril detection can be biased by the presence of exogenous compounds. *FEBS J.* 276(20):5960-5972.

226. Georgiou CD, Grintzalis K, Zervoudakis G, & Papapostolou I (2008) Mechanism of Coomassie brilliant blue G-250 binding to proteins: a hydrophobic assay for nanogram quantities of proteins. *Anal. Bioanal. Chem.* 391(1):391-403.

227. Hansen WH, Long EL, Davis KJ, Nelson AA, & Fitzhugh OG (1966) Chronic toxicity of three food colourings: Guinea Green B, Light Green SF Yellowish and Fast Green FCF in rats, dogs and mice. *Food Cosmet. Toxicol.* 4:389-410.

228. Chalker JM, Wood CSC, & Davis BG (2009) A Convenient Catalyst for Aqueous and Protein Suzuki−Miyaura Cross-Coupling. *J. Am. Chem. Soc.* 131(45):16346-16347.

229. Ojida A, Tsutsumi H, Kasagi N, & Hamachi I (2005) Suzuki coupling for protein modification. *Tetrahedron Lett.* 46(19):3301-3305.

230. Nowak MW*, et al.* (1998) In vivo incorporation of unnatural amino acids into ion channels in Xenopus oocyte expression system. *Ion Channels, Pt B,* Methods in Enzymology), Vol 293, pp 504-529.

231. Kitevski-LeBlanc JL & Prosser RS (2012) Current applications of F-19 NMR to studies of protein structure and dynamics. *Prog. Nucl. Magn. Reson. Spectrosc.* 62:1-33.

232. Hernandes MZ, Cavalcanti SMT, Moreira DRM, de Azevedo Junior WF, & Leite ACL (2010) Halogen Atoms in the Modern Medicinal Chemistry: Hints for the Drug Design. *Curr. Drug Targets* 11(3):303-314.

233. Ryan DM, Anderson SB, & Nilsson BL (2010) The influence of side-chain halogenation on the self-assembly and hydrogelation of Fmoc-phenylalanine derivatives. *Soft Matter* 6(14):3220-3231.

234. Burley SK & Petsko GA (1985) Aromatic-aromatic interaction - a mechanism of protein-structure stabilization. *Science* 229(4708):23-28.

235. Claessens CG & Stoddart JF (1997) pi-pi interactions in self-assembly. *J. Phys. Org. Chem.* 10(5):254-272.

236. Tartaglia GG, Cavalli A, Pellarin R, & Caflisch A (2004) The role of aromaticity, exposed surface, and dipole moment in determining protein aggregation rates. *Protein Science* 13(7):1939-1941.

237. Gazit E (2002) A possible role for pi-stacking in the self-assembly of amyloid fibrils. *FASEB J.* 16(1):77-83.

238. Porat Y, Abramowitz A, & Gazit E (2006) Inhibition of amyloid fibril formation by polyphenols: Structural similarity and aromatic interactions as a common inhibition mechanism. *Chemical Biology & Drug Design* 67(1):27-37.

239. Azriel R & Gazit E (2001) Analysis of the structural and functional elements of the minimal active fragment of islet amyloid polypeptide (IAPP) - An experimental support for the key role of the phenylalanine residue in amyloid formation. *J. Biol. Chem.* 276(36):34156-34161.

240. Gazit E (2002) Global analysis of tandem aromatic octapeptide repeats: The significance of the aromatic-glycine motif. *Bioinformatics* 18(6):880-883.

241. Park J-W*, et al.* (2008) Amyloid Fibrillar Meshwork Formation of Iron-Induced Oligomeric Species of Aβ40 with Phthalocyanine Tetrasulfonate and Its Toxic Consequences. *ChemBioChem* 9(16):2602-2605.

242. Williams AD*, et al.* (2005) Structural properties of Aβ protofibrils stabilized by a small molecule. *Proc. Natl. Acad. Sci. U. S. A.* 102(20):7115-7120.

243. Thapa A*, et al.* (2011) Biflavonoids Are Superior to Monoflavonoids in Inhibiting Amyloid-beta Toxicity and Fibrillogenesis via Accumulation of Nontoxic Oligomer-like Structures. *Biochemistry* 50(13):2445-2455.

244. Wahlström A*, et al.* (2012) Specific Binding of a β-Cyclodextrin Dimer to the Amyloid β Peptide Modulates the Peptide Aggregation Process. *Biochemistry* 51(21):4280-4289.

245. Wong HE & Kwon I (2011) Xanthene Food Dye, as a Modulator of Alzheimer's Disease Amyloid-beta Peptide Aggregation and the Associated Impaired Neuronal Cell Function. *PLoS ONE* 6(10):e25752.

246. Hirohashi T, Terasaki T, Shigetoshi M, & Sugiyama Y (1997) In vivo and in vitro evidence for nonrestricted transport of 2',7'-bis(2-carboxyethyl)-5(6)-carboxyfluorescein tetraacetoxymethyl ester at the blood-brain barrier. *J. Pharmacol. Exp. Ther.* 280(2):813-819.

247. Terasaki T & Hosoya K (1999) The blood-brain barrier efflux transporters as a detoxifying system for the brain. *Adv. Drug Del. Rev.* 36(2-3):195-209.

248. Wong HE, Qi W, Choi H-M, Fernandez EJ, & Kwon I (2011) A Safe, Blood-Brain Barrier Permeable Triphenylmethane Dye Inhibits Amyloid-β Neurotoxicity by Generating Nontoxic Aggregates. *ACS Chem. Neurosci.* 2(11):645-657.

249. Tomaselli S*, et al.* (2006) The α-to-β Conformational Transition of Alzheimer's Aβ-(1–42) Peptide in Aqueous Media is Reversible: A Step by Step Conformational Analysis Suggests the Location of β Conformation Seeding. *ChemBioChem* 7(2):257-267.

250. Jones GR, Cundall RB, Murray D, & Duddell DA (1984) Eosin Y-macromolecule complexes. Part 2.-Interactions between eosin Y and polycations, a cationic surfactant and proteins. *Journal of the Chemical Society, Faraday Transactions 2: Molecular and Chemical Physics* 80(10):1201-1213.

251. Ma CQ, Li KA, & Tong SY (1996) Determination of proteins by fluorescence quenching of erythrosin B. *Anal. Chim. Acta* 333(1–2):83-88.

252. Perez M*, et al.* (2005) Characterization of a double (amyloid precursor protein-tau) transgenic: tau phosphorylation and aggregation. *Neuroscience* 130(2):339-347.

253. Vlasova IM & Saletskii AM (2010) Dependence of the constants of binding for nanomarkers of the fluorescein family with human serum albumin on Ph. *Russ. J. Phys. Chem.* 84(6):1065-1070.

254. Waheed AA, Rao KS, & Gupta PD (2000) Mechanism of Dye Binding in the Protein Assay Using Eosin Dyes. *Anal. Biochem.* 287(1):73-79.

255. Wong HE, Irwin JA, & Kwon I (2013) Halogenation Generates Effective Modulators of Amyloid-Beta Aggregation and Neurotoxicity. *PLoS ONE* 8(2):e57288.

256. Irwin JA, Wong HE, & Kwon I (2013) Different Fates of Alzheimer's Disease Amyloid-β Fibrils Remodeled by Biocompatible Small Molecules. *Biomacromolecules* 14(1):264-274.

257. Wong HE, Qi W, Choi H-M, Fernandez EJ, & Kwon I (2011) A Safe, Blood-Brain Barrier Permeable Triphenylmethane Dye Inhibits Amyloid-β Neurotoxicity by Generating Nontoxic Aggregates. *ACS Chem. Neurosci.* 2(11):645-657.

258. Agarwala SS*, et al.* (2009) Chemoablation of melanoma with intralesional rose bengal (PV-10). *J. Clin. Oncol.* 27(15).

259. Thompson JF, Hersey P, & Wachter E (2008) Chemoablation of metastatic melanoma using intralesional Rose Bengal. *Melanoma Res.* 18(6):405-411.

260. Liu Y & Schubert D (1997) Cytotoxic Amyloid Peptides Inhibit Cellular 3-(4,5-Dimethylthiazol-2-yl)-2,5-Diphenyltetrazolium Bromide (MTT) Reduction by Enhancing MTT Formazan Exocytosis. *J. Neurochem.* 69(6):2285-2293.

261. Abe K & Saito H (1998) Amyloid [beta] protein inhibits cellular MTT reduction not by suppression of mitochondrial succinate dehydrogenase but by acceleration of MTT formazan exocytosis in cultured rat cortical astrocytes. *Neurosci. Res.* 31(4):295-305.

262. Hertel C, Hauser N, Schubenel R, Seilheimer B, & Kemp JA (1996) β-Amyloid-Induced Cell Toxicity: Enhancement of 3-(4,5-Dimethylthiazol-2-yl)-2,5-Diphenyltetrazolium Bromide-Dependent Cell Death. *J. Neurochem.* 67(1):272-276.

263. Bartolini M*, et al.* (2007) Insight Into the Kinetic of Amyloid β (1–42) Peptide Self-Aggregation: Elucidation of Inhibitors' Mechanism of Action. *ChemBioChem* 8(17):2152-2161.

264. Harada T & Kuroda R (2011) CD measurements of β-amyloid (1–40) and (1–42) in the condensed phase. *Biopolymers* 95(2):127-134.

265. Soto C, Castano EM, Frangione B, & Inestrosa NC (1995) The alpha-helical to beta-strand transition in the amino-terminal fragment of the amyloid beta-peptide modulates amyloid formation. *J. Biol. Chem.* 270(7):3063-3067.

266. Sarroukh R*, et al.* (2011) Transformation of amyloid β(1–40) oligomers into fibrils is characterized by a major change in secondary structure. *Cell. Mol. Life Sci.* 68:1429-1438.

267. Sreerama N, Venyaminov SY, & Woody RW (2000) Estimation of Protein Secondary Structure from Circular Dichroism Spectra: Inclusion of Denatured Proteins with Native Proteins in the Analysis. *Anal. Biochem.* 287(2):243-251.

268. Török B*, et al.* (2012) Structure–Activity Relationships of Organofluorine Inhibitors of β-Amyloid Self-Assembly. *ChemMedChem* 7(5):910-919.

269. Shin HJ*, et al.* (2000) Eosin interaction of alpha-synuclein leading to protein self-oligomerization. *Biochimica Et Biophysica Acta-Protein Structure and Molecular Enzymology* 1481(1):139-146.

270. Nussinov R, Tsai C-J, & Ma B (2013) The Underappreciated Role of Allostery in the Cellular Network. *Annual Review of Biophysics, Vol 42* 42:169-189.

271. Tsai C-J, del Sol A, & Nussinov R (2008) Allostery: Absence of a change in shape does not imply that allostery is not at play. *Journal of Molecular Biology* 378(1):1-11.

272. Bu Z & Callaway DJE (2011) Proteins move! Protein dynamics and long-range allostery in cell signaling. *Advances in Protein Chemistry and Structural Biology: Protein Structure and Diseases, Vol 83* 83:163-221.

273. Swain JF & Gierasch LM (2006) The changing landscape of protein allostery. *Current Opinion in Structural Biology* 16(1):102-108.

274. Cui Q & Karplus M (2008) Allostery and cooperativity revisited. *Protein Science* 17(8):1295-1307.

275. Tsai C-J, Del Sol A, & Nussinov R (2009) Protein allostery, signal transmission and dynamics: a classification scheme of allosteric mechanisms. *Molecular Biosystems* 5(3):207-216.

276. Jimenez-Oses G*, et al.* (2014) The role of distant mutations and allosteric regulation on LovD active site dynamics. *Nature Chemical Biology* 10(6):431-436.

277. Baldwin J & Chothia C (1979) Hemoglobin - structural-changes related to ligand-binding and its allosteric mechanism. *Journal of Molecular Biology* 129(2):175-+.

278. Edelstein SJ (1975) Cooperative interactions of hemoglobin. *Annual Review of Biochemistry* 44:209-232.

279. Kantrowitz ER & Lipscomb WN (1988) Escherichia-coli aspartate-transcarbamylase - the relation between structure and function. *Science* 241(4866):669-674.

280. Schachman HK (1988) Can a simple-model account for the allosteric transition of aspartate transcarbamoylase. *Journal of Biological Chemistry* 263(35):18583-18586.

281. Dowd JE & Riggs DS (1965) A comparison of estimates oc Michaelis-Menten kinetic constants from the various linear transformations. *The Journal of biological chemistry* 240:863-869.

282. Rubin MM & Changeux JP (1966) On the nature of allosteric transitions: implications of non-exclusive ligand binding. *Journal of molecular biology* 21(2):265-274.

283. Berger SA & Evans PR (1990) Active-site mutants altering the cooperativity of escherichia-coli phosphofructokinase. *Nature* 343(6258):575-576.

284. Schirmer T & Evans PR (1990) Structural basis of the allosteric behavior of phosphofructokinase. *Nature* 343(6254):140-145.

285. Schnappauf G, Lipscomb WN, & Braus GH (1998) Separation of inhibition and activation of the allosteric yeast chorismate mutase. *Proceedings of the National Academy of Sciences of the United States of America* 95(6):2868-2873.

286. Song ES*, et al.* (2005) Mutation of active site residues of insulin-degrading enzyme alters allosteric interactions. *Journal of Biological Chemistry* 280(18):17701-17706.

287. Pan H, Lee JC, & Hilser VJ (2000) Binding sites in Escherichia coli dihydrofolate reductase communicate by modulating the conformational ensemble. *Proceedings of the National Academy of Sciences of the United States of America* 97(22):12020-12025.

288. Boehr DD, McElheny D, Dyson HJ, & Wright PE (2006) The dynamic energy landscape of dihydrofolate reductase catalysis. *Science* 313(5793):1638-1642.

289. Basran J, Casarotto MG, Basran A, & Roberts GCK (1997) Effects of single-residue substitutions on negative cooperativity in ligand binding to dihydrofolate reductase. *Protein Engineering* 10(7):815-826.

290. Chen J, Dima RI, & Thirumalai D (2007) Allosteric communication in dihydrofolate reductase: Signaling network and pathways for closed to occluded transition and back. *Journal of Molecular Biology* 374(1):250-266.

291. Sawaya MR & Kraut J (1997) Loop and subdomain movements in the mechanism of Escherichia coli dihydrofolate reductase: Crystallographic evidence. *Biochemistry* 36(3):586-603.

292. Rod TH, Radkiewicz JL, & Brooks CL (2003) Correlated motion and the effect of distal mutations in dihydrofolate reductase. *Proceedings of the National Academy of Sciences of the United States of America* 100(12):6980-6985.

293. Reyes P & Huennekens FM (1967) Ion-dependent activation of dihydrofolate reductase from L1210 cells. *Biochemistry* 6(11):3519-3527.

294. Haber DA, Beverley SM, Kiely ML, & Schimke RT (1981) Properties of an altered dihydrofolate-reductase encoded by amplified genes in cultured mouse fibroblasts. *Journal of Biological Chemistry* 256(18):9501-9510.

295. Chunduru SK*, et al.* (1994) Methotrexate-resistant variants of human dihydrofolate-reductase - effects of phe31 substitutions. *Journal of Biological Chemistry* 269(13):9547-9555.

296. Cody V, Luft JR, & Pangborn W (2005) Understanding the role of Leu22 variants in methotrexate resistance: comparison of wild-type and Leu22Arg variant mouse and human dihydrofolate reductase ternary crystal complexes with methotrexate and NADPH. *Acta Crystallographica Section D-Biological Crystallography* 61:147-155.

297. Lewis WS, *et al.* (1995) Methotrexate-resistant variants of human dihydrofolate-reductase with substitutions of leucine-22 - kinetics, crystallography, and potential as selectable markers. *Journal of Biological Chemistry* 270(10):5057-5064.

298. Thillet J, Adams JA, & Benkovic SJ (1990) The kinetic mechanism of wild-type and mutant mouse dihydrofolate reductases. *Biochemistry* 29(21):5195-5202.

299. Ohmae E, Ishimura K, Iwakura M, & Gekko K (1998) Effects of point mutations at the flexible loop alanine-145 of Escherichia coli dihydrofolate reductase on its stability and function. *Journal of Biochemistry* 123(5):839-846.

300. Cameron CE & Benkovic SJ (1997) Evidence for a functional role of the dynamics of glycine-121 of Escherichia coli dihydrofolate reductase obtained from kinetic analysis of a site-directed mutant. *Biochemistry* 36(50):15792-15800.

301. Ohmae E, Iriyama K, Ichihara S, & Gekko K (1996) Effects of point mutations at the flexible loop glycine-67 of Escherichia coli dihydrofolate reductase on its stability and function. *Journal of Biochemistry* 119(4):703-710.

302. Gekko K, Kunori Y, Takeuchi H, Ichihara S, & Kodama M (1994) Point mutations at glycine-121 of escherichia-coli dihydrofolate-reductase- important roles of a flexible loop in the stability and function. *Journal of Biochemistry* 116(1):34-41.

303. Appleman JR, Howell EE, Kraut J, & Blakley RL (1990) Role of aspartate-27 of dihydrofolate-reductase from escherichia-coli in interconversion of active and inactive enzyme conformers and binding of NADPH. *Journal of Biological Chemistry* 265(10):5579-5584.

304. Dunn SMJ, Lanigan TM, & Howell EE (1990) Dihydrofolate-reductase from escherichia-coli - probing the role of aspartate-27 and phenylalanine-137 in enzyme conformation and the binding of NADPH. *Biochemistry* 29(37):8569-8576.

305. Appleman JR, Howell EE, Kraut J, Kuhl M, & Blakley RL (1988) Role of aspartate-27 in the binding of methotrexate to dihydrofolate-reductase from Escherichia-coli. *Journal of Biological Chemistry* 263(19):9187-9198.

306. Benkovic SJ, Fierke CA, & Naylor AM (1988) Insights into enzyme function from studies on mutants of dihydrofolate-reductase. *Science* 239(4844):1105-1110.

307. Thillet J, Absil J, Stone SR, & Pictet R (1988) Site-directed mutagenesis of mouse dihydrofolate-reductase - mutants with increased resistance to methotrexate and trimethoprim. *Journal of Biological Chemistry* 263(25):12500-12508.

308. Wang L, Brock A, & Schultz PG (2002) Adding L-3-(2-naphthyl)alanine to the genetic code of E-coli. *Journal of the American Chemical Society* 124(9):1836-1837.

309. Ricard J & Cornishbowden A (1987) Cooperative and allosteric enzymes - 20 years on. *European Journal of Biochemistry* 166(2):255-272.

310. Hillcoat BL, Nixon PF, & Blakley RL (1967) Effect of substrate decomposition on the spectrophotometric assay of dihydrofolate reductase. *Analytical biochemistry* 21(2):178-189.

311. Gauldie J, Marshall L, & Hillcoat BL (1973) Purification and properties of dihyrdofolate reductase from cultured mammalian-cells. *Biochemical Journal* 133(2):349-356.

312. Dion A, Linn CE, Bradrick TD, Georghiou S, & Howell EE (1993) How do mutations at phenylalanine-153 and isoleucine-155 partially suppress the effects of the aspartate-27 - serine mutation in escherichia-coli dihydrofolate-reductase.. *Biochemistry* 32(13):3479-3487.

313. Beard WA*, et al.* (1991) Role of the conserved active-site residue tryptophan-24 of human dihydrofolate-reductase as revealed by mutagenesis. *Biochemistry* 30(5):1432-1440.

314. Benkovic SJ & Hammes-Schiffer S (2003) A perspective on enzyme catalysis. *Science* 301(5637):1196-1202.

315. Appleman JR*, et al.* (1990) Unusual transient-state and steady-state kinetic-behavior is predicted by the kinetic scheme operational for recombinant human dihydrofolate-reductase. *Journal of Biological Chemistry* 265(5):2740-2748.

316. Goodey NM & Benkovic SJ (2008) Allosteric regulation and catalysis emerge via a common route. *Nature Chemical Biology* 4(8):474-482.

317. Eisenmesser EZ*, et al.* (2005) Intrinsic dynamics of an enzyme underlies catalysis. *Nature* 438(7064):117-121.

318. Hilser VJ & Thompson EB (2007) Intrinsic disorder as a mechanism to optimize allosteric coupling in proteins. *Proceedings of the National Academy of Sciences of the United States of America* 104(20):8311-8315.

319. Meiering EM, Li HJ, Delcamp TJ, Freisheim JH, & Wagner G (1995) Contributions of tryptophan-24 and glutamate-30 to binding long-lived water-molecules in the ternary complex of human dihydrofolate-reductase with methotrexate and nadph studied by site-directed mutagenesis and nuclear-magnetic-resonance spectroscopy. *Journal of Molecular Biology* 247(2):309-325.

320. Levitt M & Perutz MF (1988) Aromatic rings act as hydrogen-bond acceptors. *Journal of Molecular Biology* 201(4):751-754.

321. Oefner C, Darcy A, & Winkler FK (1988) Crystal-structure of human dihydrofolate-reductase complexed with folate. *European Journal of Biochemistry* 174(2):377-385.

322. Skacel N*, et al.* (2005) Identification of amino acids required for the functional up-regulation of human dihydrofolate reductase protein in response to antifolate treatment. *Journal of Biological Chemistry* 280(24):22721-22731.

323. Adamczyk AJ, Cao J, Kamerlin SCL, & Warshel A (2011) Catalysis by dihydrofolate reductase and other enzymes arises from electrostatic preorganization, not conformational motions. *Proceedings of the National Academy of Sciences of the United States of America* 108(34):14115-14120.

324. Zhang ZQ, Rajagopalan PTR, Selzer T, Benkovic SJ, & Hammes GG (2004) Single-molecule and transient kinetics investigation of the interaction of dihydrofolate reductase with NADPH and dihydrofolate. *Proceedings of the National Academy of Sciences of the United States of America* 101(9):2764-2769.

325. Bhabha G*, et al.* (2011) A Dynamic Knockout Reveals That Conformational Fluctuations Influence the Chemical Step of Enzyme Catalysis. *Science* 332(6026):234-238.

326. Dima RI & Thirumalai D (2006) Determination of network of residues that regulate allostery in protein families using sequence analysis. *Protein Science* 15(2):258-268.

327. Gunasekaran K, Ma BY, & Nussinov R (2004) Is allostery an intrinsic property of all dynamic proteins? *Proteins-Structure Function and Bioinformatics* 57(3):433-443.

328. Huang Z*, et al.* (2011) ASD: a comprehensive database of allosteric proteins and modulators. *Nucleic Acids Research* 39:D663-D669.

329. Francis K, Stojkovic V, & Kohen A (2013) Preservation of Protein Dynamics in Dihydrofolate Reductase Evolution. *Journal of Biological Chemistry* 288(50):35961-35968.

330. Park H-S*, et al.* (2011) Expanding the Genetic Code of Escherichia coli with Phosphoserine. *Science* 333(6046):1151-1154.

331. Xie JM*, et al.* (2004) The site-specific incorporation of p-iodo-L-phenylalanine into proteins for structure determination. *Nature Biotechnology* 22(10):1297-1301.

332. Cellitti SE*, et al.* (2008) In vivo incorporation of unnatural amino acids to probe structure, dynamics, and ligand binding in a large protein by nuclear magnetic resonance spectroscopy. *Journal of the American Chemical Society* 130(29):9268-9281.

333. Chen M*, et al.* (2008) Site-specific incorporation of unnatural amino acids into urate oxidase in Escherichia coli. *Protein Science* 17(10):1827-1833.

334. Taskent-Sezgin H*, et al.* (2009) Interpretation of p-Cyanophenylalanine Fluorescence in Proteins in Terms of Solvent Exposure and Contribution of Side-Chain Quenchers: A Combined Fluorescence, IR and Molecular Dynamics Study. *Biochemistry* 48(38):9040-9046.

335. Bailey SW & Ayling JE (2009) The extremely slow and variable activity of dihydrofolate reductase in human liver and its implications for high folic acid intake. *Proceedings of the National Academy of Sciences of the United States of America* 106(36):15424-15429.

336. Beard WA, Appleman JR, Delcamp TJ, Freisheim JH, & Blakley RL (1989) Hydride transfer by dihydrofolate-reductase - causes and consequences of the wide-range of rates exhibited by bacterial and vertebrate enzymes. *Journal of Biological Chemistry* 264(16):9391-9399.

337. Tsay JT*, et al.* (1990) Kinetic investigation of the functional-role of phenylalanine-31 of recombinant human dihydrofolate-reductase. *Biochemistry* 29(27):6428-6436.

338. Schweitzer BI, Dicker AP, & Bertino JR (1990) Dihydrofolate-reductase as a therapeutic target. *Faseb Journal* 4(8):2441-2452.

339. Liu CT*, et al.* (2013) Functional significance of evolving protein sequence in dihydrofolate reductase from bacteria to humans. *Proceedings of the National Academy of Sciences of the United States of America* 110(25):10159-10164.

340. Reva B, Antipin Y, & Sander C (2011) Predicting the functional impact of protein mutations: application to cancer genomics. *Nucleic Acids Research* 39(17):E118-U185.

341. Bordo D & Argos P (1991) Suggestions for safe residue substitutions in site-directed mutagenesis. *Journal of Molecular Biology* 217(4):721-729.

342. Guerois R, Nielsen JE, & Serrano L (2002) Predicting changes in the stability of proteins and protein complexes: A study of more than 1000 mutations. *Journal of Molecular Biology* 320(2):369-387.

343. Bowie JU, Reidhaarolson JF, Lim WA, & Sauer RT (1990) Deciphering the message in protein sequences - tolerance to amino-acid substitutions. *Science* 247(4948):1306-1310.

344. Ventura S*, et al.* (2002) Conformational strain in the hydrophobic core and its implications for protein folding and design. *Nature Structural Biology* 9(6):485-493.

345. Vandenburg B*, et al.* (1994) Protein stabilization by hydrophobic interactions at the surface. *European Journal of Biochemistry* 220(3):981-985.

346. Lim WA & Sauer RT (1989) Alternative packing arrangements in the hydrophobic core of lambda-repressor. *Nature* 339(6219):31-36.

347. Lazar GA, Desjarlais JR, & Handel TM (1997) De novo design of the hydrophobic core of ubiquitin. *Protein Science* 6(6):1167-1178.

348. Kellis JT, Nyberg K, & Fersht AR (1989) Energetics of complementary side-chain packing in a protein phdrophobic core. *Biochemistry* 28(11):4914-4922.

349. Jackson SE, Moracci M, Elmasry N, Johnson CM, & Fersht AR (1993) Effect of cavity-creating mutations in the phdrophobic core of chymotrypsin inhibitor-2. *Biochemistry* 32(42):11259-11269.

350. Eriksson AE*, et al.* (1992) Response of a protein-structure to caviting-creating mutations and its relation to the hydrophobic effect. *Science* 255(5041):178-183.

351. Desjarlais JR & Handel TM (1995) De-novo design of the pydrophobic cores of proteins. *Protein Science* 4(10):2006-2018.

352. Buckle AM, Cramer P, & Fersht AR (1996) Structural and energetic responses to cavity-creating mutations in hydrophobic cores: Observation of a buried water molecule and the hydrophilic nature of such hydrophobic cavities. *Biochemistry* 35(14):4298-4305.

353. Adamek DH, Guerrero L, Blaber M, & Caspar DLD (2005) Structural and energetic consequences of mutations in a solvated hydrophobic cavity. *Journal of Molecular Biology* 346(1):307-318.

354. Greenfie.Nj, Williams MN, Poe M, & Hoogstee.K (1972) Circular-dichroism studies of dihydrofolate reductase from a methotrexate-resistant strain of Escherichia-coli. *Biochemistry* 11(25):4706-&.

355. Rohl CA, Strauss CEM, Misura KMS, & Baker D (2004) Protein structure prediction using rosetta. *Numerical Computer Methods, Pt D* 383:66-+.

356. Kaufmann KW, Lemmon GH, DeLuca SL, Sheehan JH, & Meiler J (2010) Practically Useful: What the ROSETTA Protein Modeling Suite Can Do for You. *Biochemistry* 49(14):2987-2998.

357. Combs SA*, et al.* (2013) Small-molecule ligand docking into comparative models with Rosetta. *Nature Protocols* 8(7):1277-1298.

358. Kuhlman B & Baker D (2000) Native protein sequences are close to optimal for their structures. *Proceedings of the National Academy of Sciences of the United States of America* 97(19):10383-10388.

359. Ashworth J*, et al.* (2010) Computational reprogramming of homing endonuclease specificity at multiple adjacent base pairs. *Nucleic Acids Research* 38(16):5601-5608.

360. Ashworth J*, et al.* (2006) Computational redesign of endonuclease DNA binding and cleavage specificity. *Nature* 441(7093):656-659.

361. Cochran FV*, et al.* (2005) Computational de novo design and characterization of a four-helix bundle protein that selectively binds a nonbiological cofactor. *Journal of the American Chemical Society* 127(5):1346-1347.

362. Jiang L*, et al.* (2008) De novo computational design of retro-aldol enzymes. *Science* 319(5868):1387-1391.

363. Huang P-S, Love JJ, & Mayo SL (2007) A de novo designed protein-protein interface. *Protein Science* 16(12):2770-2774.

364. Gregoire S*, et al.* (2014) Cis-Suppression to Arrest Protein Aggregation in Mammalian Cells. *Biotechnology and Bioengineering* 111(3):462-474.

365. Gregoire S, Glitzos K, & Kwon I (2014) Suppressing mutation-induced protein aggregation in mammalian cells by mutating residues significantly displaced upon the original mutation. *Biochemical Engineering Journal* 91:196-203.

366. Cornette JL*, et al.* (1987) Hydrophobicity scales and computational techniques for detecting amphipathic structures in proteins. *Journal of Molecular Biology* 195(3):659-685.

367. Link AJ*, et al.* (2006) Discovery of aminoacyl-tRNA synthetase activity through cell-surface display of noncanonical amino acids. *Proceedings of the National Academy of Sciences of the United States of America* 103(27):10180-10185.

368. Wang P, Tang Y, & Tirrell DA (2003) Incorporation of trifluoroisoleucine into proteins in vivo. *Journal of the American Chemical Society* 125(23):6900-6906.

369. Zhao YH, Abraham MH, & Zissimos AM (2003) Fast calculation of van der Waals volume as a sum of atomic and bond contributions and its application to drug compounds. *Journal of Organic Chemistry* 68(19):7368-7373.

370. Gilis D & Rooman M (1997) Predicting protein stability changes upon mutation using database-derived potentials: Solvent accessibility determines the importance of local versus non-local interactions along the sequence. *Journal of Molecular Biology* 272(2):276-290.

371. Ahmad S, Gromiha M, Fawareh H, & Sarai A (2004) ASAView: Database and tool for solvent accessibility representation in proteins. *BMC Bioinformatics* 5(May 1).

372. Parthiban V, Gromiha MM, & Schomburg D (2006) CUPSAT: prediction of protein stability upon point mutations. *Nucleic Acids Research* 34:W239-W242.

373. Worth CL, Preissner R, & Blundell TL (2011) SDM-a server for predicting effects of mutations on protein stability and malfunction. *Nucleic Acids Research* 39:W215-W222.

374. Eisenberg D & McLachlan AD (1986) Solvation energy in protein folding and binding. *Nature* 319(6050):199-203.

375. Worth CL, Gong S, & Blundell TL (2009) Structural and functional constraints in the evolution of protein families. *Nature Reviews Molecular Cell Biology* 10(10):709-720.

376. Mirny LA & Shakhnovich EI (1999) Universally conserved positions in protein folds: Reading evolutionary signals about stability, folding kinetics and function. *Journal of Molecular Biology* 291(1):177-196.

377. Rausell A, Juan D, Pazos F, & Valencia A (2010) Protein interactions and ligand binding: From protein subfamilies to functional specificity. *Proceedings of the National Academy of Sciences of the United States of America* 107(5):1995-2000.

378. Kuhlman B*, et al.* (2003) Design of a novel globular protein fold with atomic-level accuracy. *Science* 302(5649):1364-1368.

379. Jiang X, Farid H, Pistor E, & Farid RS (2000) A new approach to the design of uniquely folded thermally stable proteins. *Protein Science* 9(2):403-416.

380. Kussell E, Shimada J, & Shakhnovich EI (2001) Excluded volume in protein side-chain packing. *Journal of Molecular Biology* 311(1):183-193.

381. Yasuda S*, et al.* (2010) Effects of side-chain packing on the formation of secondary structures in protein folding. *Journal of Chemical Physics* 132(6).

382. Lim WA, Farruggio DC, & Sauer RT (1992) Structural and Energetic consequences of disruptive mutations in a protein core. *Biochemistry* 31(17):4324-4333.

383. Ng PC & Henikoff S (2006) Predicting the effects of amino acid substitutions on protein function. *Annual Review of Genomics and Human Genetics,* Annual Review of Genomics and Human Genetics), Vol 7, pp 61-80.

384. Guo HH, Choe J, & Loeb LA (2004) Protein tolerance to random amino acid change. *Proceedings of the National Academy of Sciences of the United States of America* 101(25):9205-9210.

385. Wong KF, Selzer T, Benkovic SJ, & Hammes-Schiffer S (2005) Impact of distal mutations on the network of coupled motions correlated to hydride transfer in dihydrofolate reductase. *Proceedings of the National Academy of Sciences of the United States of America* 102(19):6807-6812.

386. Wang L, Goodey NM, Benkovic SJ, & Kohen A (2006) Coordinated effects of distal mutations on environmentally coupled tunneling in dihydrofolate reductase. *Proceedings of the National Academy of Sciences of the United States of America* 103(43):15753-15758.

387. Mauldin RV, Sapienza PJ, Petit CM, & Lee AL (2012) Structure and Dynamics of the G121V Dihydrofolate Reductase Mutant: Lessons from a Transition-State Inhibitor Complex. *Plos One* 7(3).

388. Tahar R, de Pecoulas PE, Basco LK, Chiadmi M, & Mazabraud A (2001) Kinetic properties of dihydrofolate reductase from wild-type and mutant Plasmodium vivax expressed in Escherichia coli. *Molecular and Biochemical Parasitology* 113(2):241-249.

389. Colquhoun D (1998) Binding, gating, affinity and efficacy: The interpretation of structure-activity relationships for agonists and of the effects of mutating receptors. *British Journal of Pharmacology* 125(5):924-947.

390. Luque I & Freire E (2000) Structural stability of binding sites: Consequences for binding affinity and allosteric effects. *Proteins-Structure Function and Genetics*:63-71.

391. Boehr DD*, et al.* (2013) A Distal Mutation Perturbs Dynamic Amino Acid Networks in Dihydrofolate Reductase. *Biochemistry* 52(27):4605-4619.

392. Adams J, Johnson K, Matthews R, & Benkovic SJ (1989) Effects of distal point-site mutations on the binding and catalysis of dihydrofolate-reductase from Escherichia-coli. *Biochemistry* 28(16):6611-6618.

393. Mayer RJ, Chen JT, Taira K, Fierke CA, & Benkovic SJ (1986) Importance of a hydrophobic residue in binding and catalysis by dihydrofolate-reductase. *Proceedings of the National Academy of Sciences of the United States of America* 83(20):7718-7720.

394. Adams JA, Fierke CA, & Benkovic SJ (1991) The function of amino-acid-residues contacting the nicotinamide ring of nadph in dihydrofolate-reductase from Escherichia-coli. *Biochemistry* 30(46):11046-11054.

395. Todd AE, Orengo CA, & Thornton JM (2001) Evolution of function in protein superfamilies, from a structural perspective. *Journal of Molecular Biology* 307(4):1113-1143.

396. Teilum K, Olsen JG, & Kragelund BB (2011) Protein stability, flexibility and function. *Biochimica Et Biophysica Acta-Proteins and Proteomics* 1814(8):969-976.

397. Schnell JR, Dyson HJ, & Wright PE (2004) Structure, dynamics, and catalytic function of dihydrofolate reductase. *Annual Review of Biophysics and Biomolecular Structure* 33:119-140.

398. Wang L, Goodey NM, Benkovic SJ, & Kohen A (2006) The role of enzyme dynamics and tunnelling in catalysing hydride transfer: studies of distal mutants of dihydrofolate reductase. *Philosophical Transactions of the Royal Society B-Biological Sciences* 361(1472):1307-1315.

399. Pelletier JN, Campbell-Valois FX, & Michnick SW (1998) Oligomerization domain-directed reassembly of active dihydrofolate reductase from rationally designed fragments. *Proceedings of the National Academy of Sciences of the United States of America* 95(21):12141-12146.

400. Shoichet BK, Baase WA, Kuroki R, & Matthews BW (1995) A relationship between protein stability and protein function. *Proceedings of the National Academy of Sciences of the United States of America* 92(2):452-456.

401. Ahrweiler PM & Frieden C (1991) Effects of point mutations in a hinge region on the stability, folding, and enzymatic-activity of Escherichia-coli dihydrofolate-reductase. *Biochemistry* 30(31):7801-7809.

402. Kuwajima K, Garvey EP, Finn BE, Matthews CR, & Sugai S (1991) Transient intermediates in the folding of dihydrofolate-reductase as detected by far-ultraviolet circular-dichroism spectroscopy. *Biochemistry* 30(31):7693-7703.

403. Grantham R (1974) Amino-acid difference formula to help explain protein evolution. *Science* 185(4154):862-864.

404. Monera OD, Sereda TJ, Zhou NE, Kay CM, & Hodges RS (1995) Relationship of Sidechain Hydrophobicity and alpha-Helical Propensity on the Stability of the Single-stranded Amphipathic alpha-Helix. *Journal of Peptide Science* 1(5):319-329.

405. Sereda TJ, Mant CT, Sonnichsen FD, & Hodges RS (1994) Reversed-phase chromatography of synthetic amphipathic alpha-helicaL peptides as a model for ligand/receptor interactions effect of changing hydrophobic environment on the relative hydrophilicity/hydrophobicity of amino-acid side-chains. *Journal of Chromatography A* 676(1):139-153.

406. Cody V, Pace J, Chisum K, & Rosowsky A (2006) New insights into DHFR interactions: Analysis of Pneumocystis carinii and mouse DHFR complexes with NADPH and two highly potent 5-(omega-carboxy(alkyloxy) trimethoprim derivatives reveals conformational correlations with activity and novel parallel ring stacking interactions. *Proteins-Structure Function and Bioinformatics* 65(4):959-969.

407. Touchette NA, Perry KM, & Matthews CR (1986) Folding of dihydrofolate-reductase from Escherichia-coli. *Biochemistry* 25(19):5445-5452.

408. Rajagopalan PTR, Lutz S, & Benkovic SJ (2002) Coupling interactions of distal residues enhance dihydrofolate reductase catalysis: Mutational effects on hydride transfer rates. *Biochemistry* 41(42):12618-12628.

Appendix A

Abbreviations

AD, Alzheimer's Disease; Aβ, Amyloid-beta; BBG, Brilliant Blue G; BBF, Brilliant Blue FCF; BBR, Brilliant Blue R; ThT, Thioflavin T; DMSO, dimethylsulfoxide; EC_{50}, Half-maximal enhancement value; FDA, U.S. Food and Drug Administration; HRP, Horseradish peroxidase; IC_{50}, Half-maximal inhibitory value; MTT, 3-(4,5-Dimethylthiazol-2-yl)-2,5-diphenyltetrazolium bromide; PBS, Phosphate-buffered saline; TBS, Tris-buffered saline; TBS-T, 0.1% Tween 20 in Tris-buffered saline; TEM, Transmission electron microscopy.

Acknowledgements

We thank Dr. Jan Redick and Dr. Stacey Guillot at the Advanced Microscopy Laboratory at the University of Virginia for assistance with TEM assays on Aβ samples. We are grateful to Dr. Theresa Good at the University of Maryland at Baltimore County for discussion and valuable comments on Aβ sample preparation and Aβ-associated cytotoxicity assay.

Supporting Information

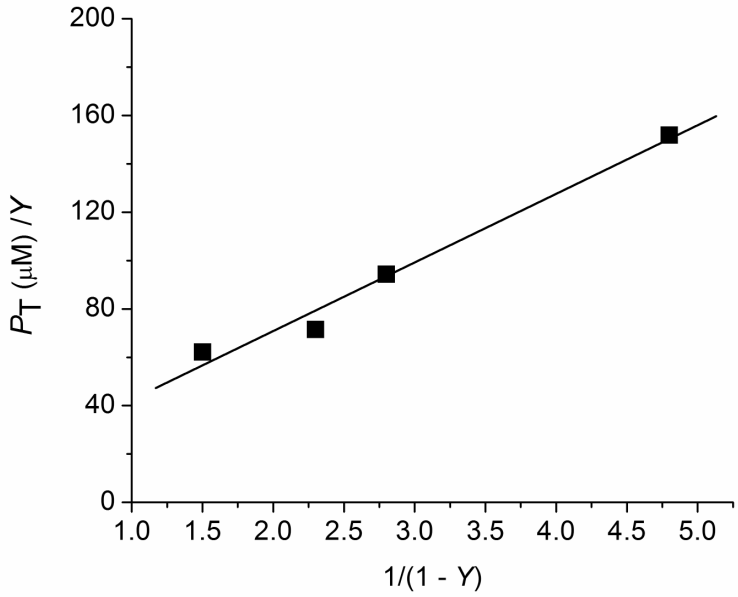

Figure A1. The data on the BBG-Aβ binding saturation curve (Figure 2.7) were fitted into a straight-line according to the equation, $P_T/Y = 1/(nk)\ [1/(1 - Y)] + D_T/n$ derived from $Y = nk(D)(P_T/D_T)/(1 + k(D))$ where Y, n, k, D, D_T, and P_T mean the fractional saturation of ligand binding sites, the number of binding sites, the binding constant, the dye concentration in solution, the total dye concentration, and the total protein concentration, respectively (*1*). The BBG concentration (D_T) was fixed at 49 μM. The Aβ concentration (P_T) was varied from 0 to 300 μM. The data at four P_T values between 20 μM and 120 μM were used for the fitting to a straight-line ($R^2 = 0.98$). The values of n and k were 3.2 and $1.1*10^4$ (M^{-1}), respectively.

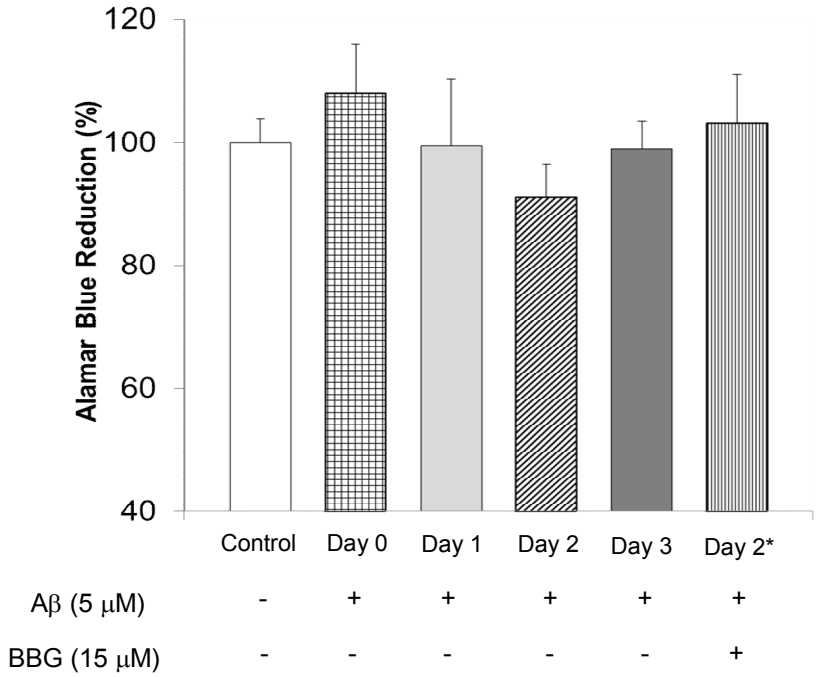

Figure A2. Alamar blue reducing activities of neuroblastoma SH-SY5Y cells incubated with pre-formed Aβ samples in the absence or presence of 3x BBG. Preformed Aβ aggregates were prepared by incubating 50 μM of Aβ monomer in the absence of BBG at 37 °C for 0 to 3 days or in the presence of 3x BBG for 2 days, as indicated in the graph. The Aβ aggregates were then administered to SH-SY5Y cells at a final concentration of 5 μM. After 3 days, cell viability was measured using alamar blue reduction. Cells administered with PBS as a control (*Control*), Aβ incubated without BBG for 0 (*Day 0*), 1 (*Day 1*), 2 (*Day 2*), or 3 days (*Day 3*), or Aβ incubated with 3x BBG for 2 days (*Day 2**). Values represent means ± standard deviation ($n \geq 3$). Values are normalized to the viability of cells administered with PBS only. One-sided Student's t-tests were applied to the data. * $P < 0.05$.

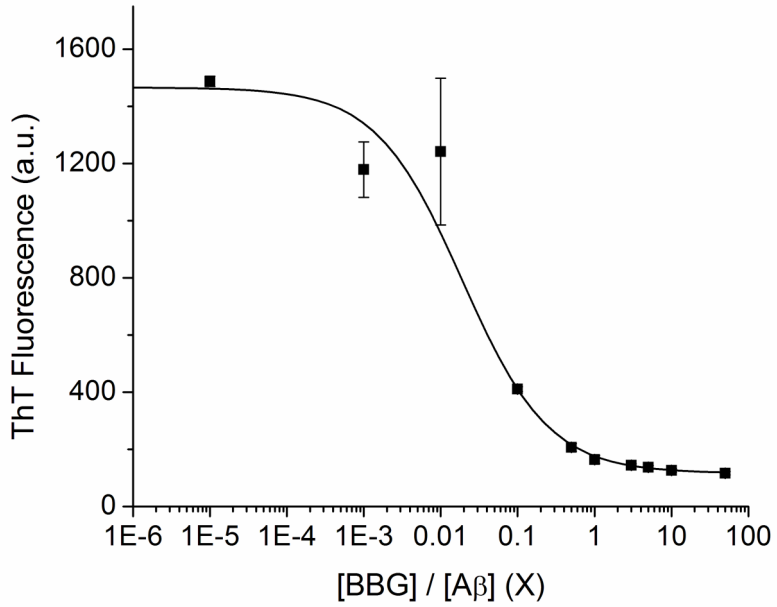

Figure A3. Dose-dependence inhibition of ThT fluorescence of Aβ samples by BBG. 50 μM of Aβ monomer was incubated at 37 °C in the absence (no BBG) or presence of the indicated concentrations of BBG (from 10^{-5}x to 50x). 5 μL of Aβ sample was taken at 72 hours of incubation. ThT fluorescence was measured in arbitrary units (a.u.). Values represent means ± standard deviation (n = 3). The data were fitted to a sigmoid curve ($R^2 = 0.99$).

Appendix B

Acknowledgements

We thank Dr. Alev Erisir and Anqi Fu at the Psychology Department at the University of Virginia for assistance with TEM assays for Aβ samples. We also thank Russell Baird for helping with preliminary experiments.

Abbreviations

Aβ, Amyloid-beta; AD, Alzheimer's Disease; CD, circular dichroism; DMSO, dimethylsulfoxide; EOB, eosin B; EOY, eosin Y; ERB, erythrosine B; FDA, U.S. Food and Drug Administration; FLN, fluorescein; HRP, Horseradish peroxidase; MTT, 3-(4,5-Dimethylthiazol-2-yl)-2,5-diphenyltetrazolium bromide; PBS, Phosphate-buffered saline; PHB, phloxine B; ROB, rose bengal; TBS, Tris-buffered saline; TBS-T, 0.1% Tween 20 in Tris-buffered saline; TEM, Transmission electron microscopy; ThT, Thioflavin T.

Supporting Information

Determination of Residual Dye Content During the MTT Assay

The MTT assay was carried out as described previously in the MTT methods section, but with 10 μL of each dye-only control (3x concentration - no Aβ) being added to each well. The absorbance of each dye was read at the respective absorbance maxima location (ERB – 540 nm, PHB – 554 nm, EOB – 520 nm, ROB – 562 nm, EOY – 530 nm, and FL – 492 nm) both before and after the washing steps described. After subtracting the appropriate background for both readings, the post-washing absorbance was normalized to the pre-wash absorbance in order to determine the fraction of each dye remaining after washing.

Determination of the Spectral Interference from Dyes During the MTT Assay

To quantify the interference that varying fractions of residual dye remaining in the cell wells have on the final reduced MTT absorbance signal, fresh media was first added to a new cell culture plate without cells. Next, 7 μL of 1 mg/mL reduced form of MTT (MTT-formazan) in DMSO was added to each well along with 0.01 and 0.05 fractions of each original dye amount or PBS. The absorbance of the samples was measured at 506 nm. After subtracting the background contribution of the media and DMSO, the absorbance values of the wells containing the varying dye fractions/MTT-formazan were normalized to the wells with PBS/MTT-formazan to obtain the change induced in the MTT signal by the dyes left behind after washing.

Table B1. Spectral interference in the MTT absorbance by the residual dyes in the plate after washing.

Dye		FLN	ERB	EOY	ROB	PHB	EOB
Residual dye after washing (%)		1.3	1.8	1.0	1.6	1.0	2.5
Change in the MTT absorbance with dye (%)	1% dye	1.4	0.4	-1.4	3.6	1.1	2.3
	5% dye	5.1	0.4	-1.8	3.8	0.9	3.9

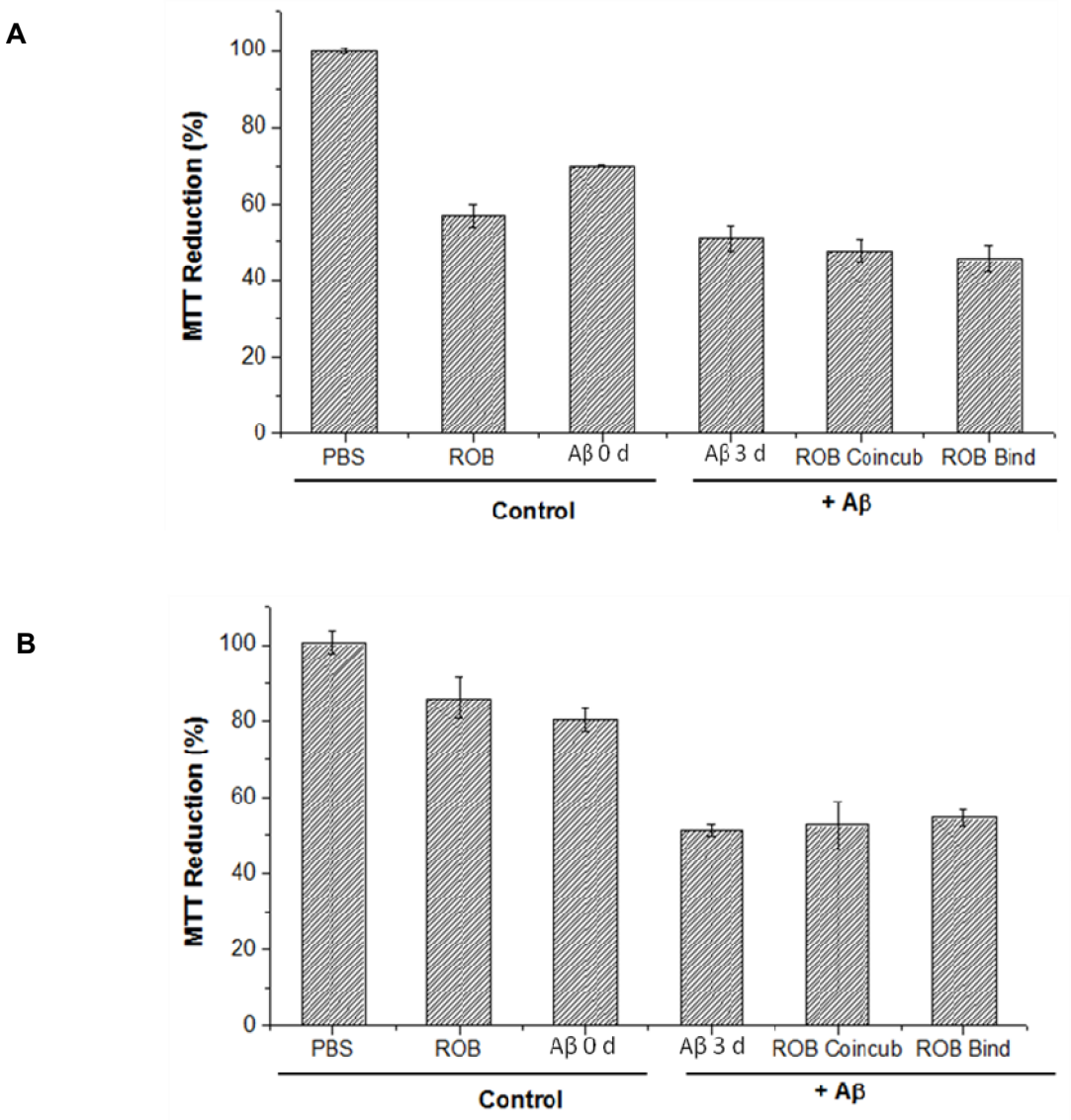

Figure B1. MTT assay for ROB to Assess Viability of Neuroblastoma SH-SY5Y Cells. Three controls (PBS buffer, ROB, and Aβ 0 d monomer) and two Aβ aggregates formed in the absence (Aβ 3 d) or presence (ROB Coincub) of 3x ROB at 37 °C for 3 days. (A) The Aβ and ROB concentrations used were 5 and 15 μM, respectively. (B) The Aβ and ROB concentrations used were 2.5 and 7.5 μM, respectively The ROB Bind sample refers to taking Aβ 3d aggregates formed in the absence of any dye and mixing them with 3x ROB immediately before addition to the cells. Values represent means ± standard deviation ($n \geq 3$). Values are normalized to the viability of cells administered with PBS buffer only.

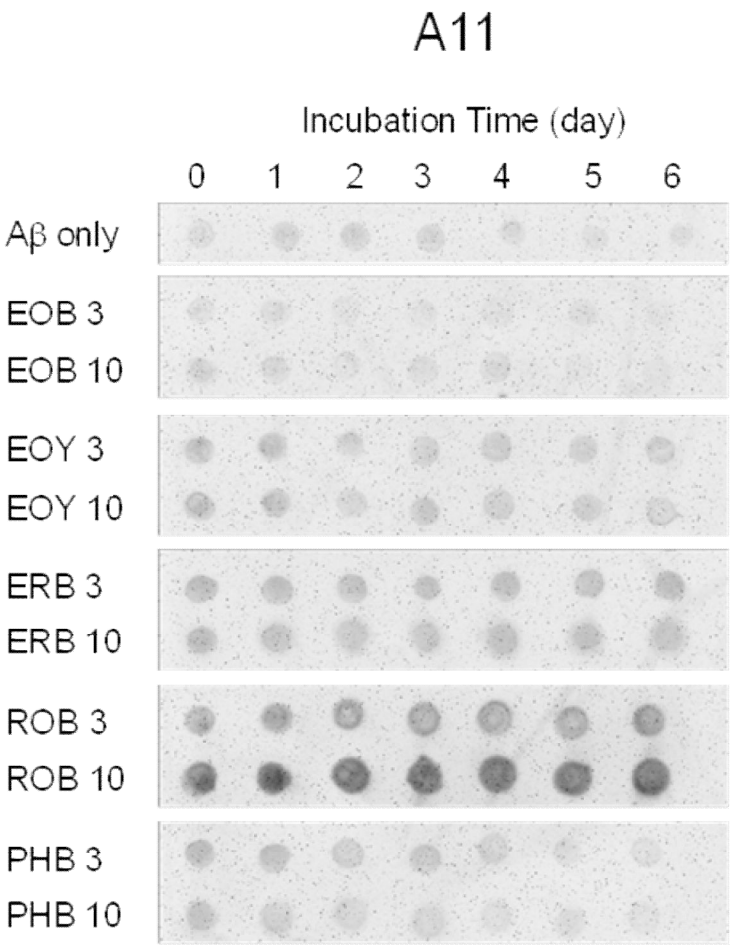

Figure B2. Dot blot assay results using the A11 antibody. 50 μM of Aβ monomer was incubated at 37 °C in the absence (Aβ only) or presence of 3x and 10x ERB analogs (EOB, EOY, ERB, ROB, and PHB) for up to 6 days. The samples were taken on the indicated day and the all samples were spotted onto one nitrocellulose membrane. The membrane was immuno-stained with the A11 antibody. For clearer presentation, the sections of the membrane were cut and re-arranged.

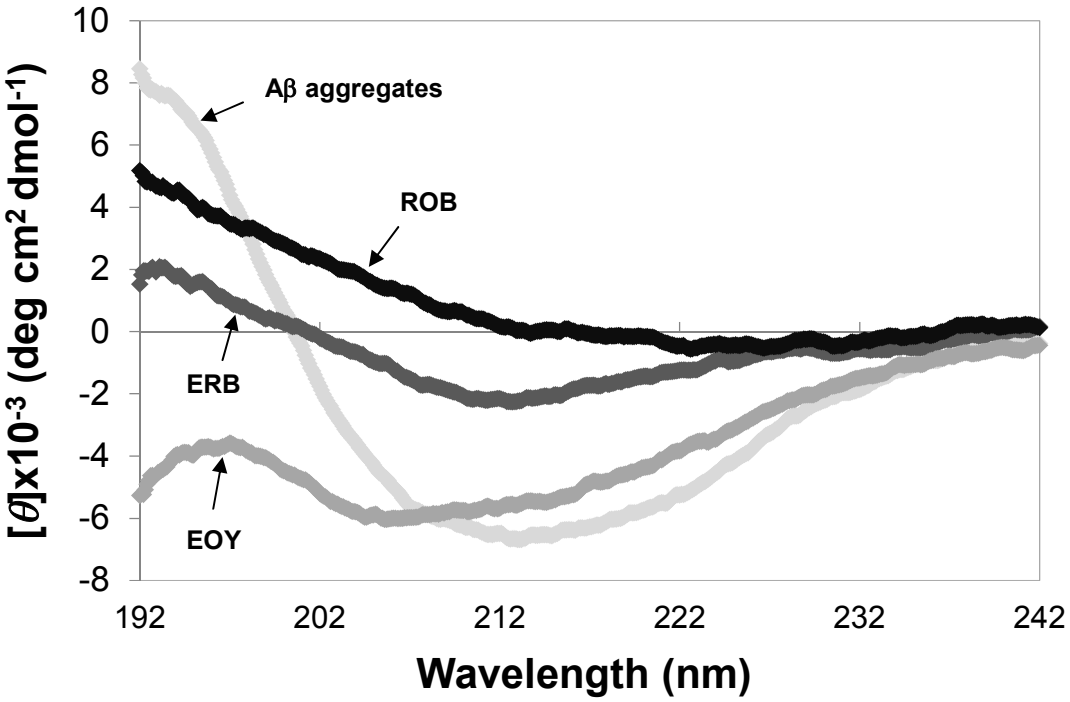

Figure B3. CD spectra of the Aβ aggregates formed in the absence (Aβ aggregates) or presence of 3x EOY, ERB, or ROB for 9 days at 37 °C.

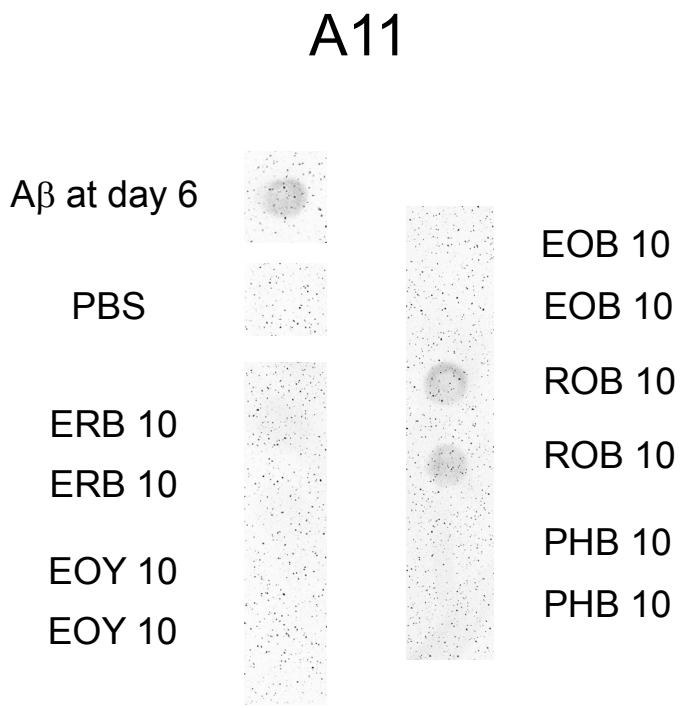

Figure B4. Dot-blot assay results using the A11 antibody. The A11-reactive Aβ aggregates (Aβ at day 6), PBS buffer, and 10x ERB analogs were spotted into one nitrocellulose membrane. Then, the membrane was immuno-stained with the A11 antibody. The sections from the same membrane were cut and re-arranged.

A

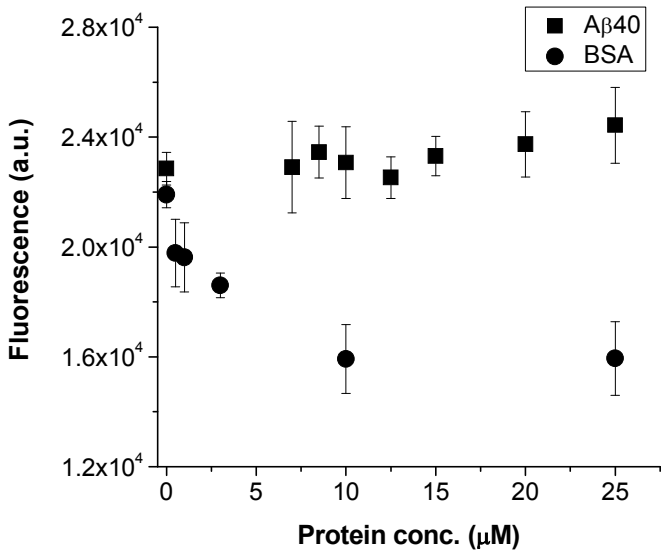

B

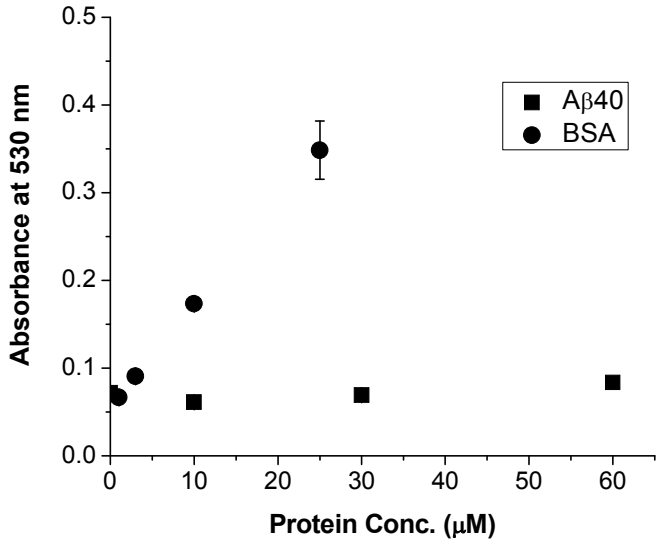

Figure B5. (A) Fluorescence of FLN with varying concentrations (0 to 25 μM) of BSA and Aβ40 (excitation at 432 nm and emission at 512 nm). (B) Absorbance of EOB with varying concentrations of BSA (0 to 25 μM) and Aβ40 (0 to 60 μM).

Appendix C

Abbreviations

Abbreviation	*Definition*
aaRS	Aminoacyl-tRNA synthetase
AFWK	Phenylalanine, tryptophan, lysine auxotroph
DHF	Dihydrofolate/dihydrofolic acid
[E]	Enzyme concentration
h	Hill number
IPTG	Isopropyl β-D-1-thiogalactopyranoside
k_{cat}	Substrate turnover rate (Michaelis-Menten or Hill)
K_h	Hill parameter
K_m	Michaelis-Menten parameter
M9-17AA	M9 media containing 17 amino acids at 50 mg/mL
M9-20AA	M9 media containing 20 amino acids at 50 mg/mL
MALDI-ToF	Matrix-assisted laser desorption/ionization-time of flight
DHFR	Dihydrofolate reductase
MS	Mass spectroscopy
nAA	Non-canonical amino acid
NADPH	Nicotinamide adenine dinucleotide phosphate
Nal	3-(2-naphthyl)-alanine
Ni-NTA	Nickel-nitrilotriacetic acid
[S]	Substrate concentration
SDS-PAGE	Sodium dodecyl sulfate polyacrylamide gel electrophoresis
THF	Tetrahydrofolate/tetrahydrofolic acid
tRNA	Transfer RNA

Trp	Tryptophan
Abbreviation	*Definition*
WT	Wild-type

Appendix D

Abbreviations

Abbreviation	*Definition*
aaRS	Aminoacyl-tRNA synthetase
AFWK	Phenylalanine, tryptophan, lysine auxotroph
DHF	Dihydrofolate/dihydrofolic acid
IPTG	Isopropyl β-D-1-thiogalactopyranoside
k_{cat}	Substrate turnover rate (Michaelis-Menten or Hill)
k_{cat}/K_m	Michaelis-Menten parameters; catalytic efficiency
K_m	Michaelis-Menten constant
M9-17AA	M9 media containing 17 amino acids at 50 mg/mL
M9-20AA	M9 media containing 20 amino acids at 50 mg/mL
MALDI-ToF	Matrix-assisted laser desorption/ionization-time of flight
DHFR	Dihydrofolate reductase
MS	Mass spectroscopy
nAA	Non-canonical amino acid
NADPH	Nicotinamide adenine dinucleotide phosphate
Nal	3-(2-naphthyl)-alanine
Ni-NTA	Nickel-nitrilotriacetic acid
OD_{600}	Optical density/absorbance at 600 nm.
SDS-PAGE	Sodium dodecyl sulfate polyacrylamide gel electrophoresis
THF	Tetrahydrofolate/tetrahydrofolic acid

Supporting Information

BSA Method Validation

Table D1. Comparison of wild-type DHFR kinetic parameters in the absence and presence of 0.1 mg/mL bovine serum albumin.

	-BSA	**+BSA**
k_{cat} (s^{-1})	3.20 ± 0.05	3.50 ± 0.02
K_m (µM)	2.00 ± 0.12	1.90 ± 0.04
k_{cat}/K_m (s^{-1}/µM)	1.56 ± 0.03	1.89 ± 0.01
Rel. Eff. (%)	100 ± 2	122 ± 1

1) (-BSA) and (+BSA) denote the absence and presence of bovines serum albumin (BSA), respectively.
2) Re. Eff. denotes the relative catalytic efficiency when compared against that of the sample without BSA.
3) In the absence of BSA, each substrate concentration was measured independently. In the presence of BSA, every substrate concentration was measured concurrently on the same plate.
4) Standard errors are shown (n = 3).

Results indicate that kinetic results are similar in the absence and presence of BSA.

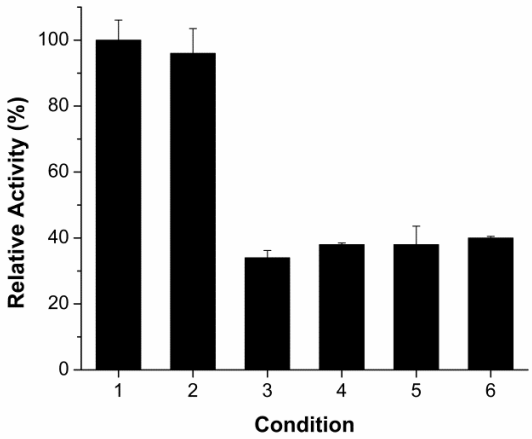

Condition	1	2	3	4	5	6
BSA (1 mg/mL)	No	Yes	No	Yes	No	Yes
DHF (50 µM)	Yes	Yes	Yes	Yes	No	No
NADPH (60 µM)	Yes	Yes	No	No	Yes	Yes

Figure D1. Evaluating the effect of bovine serums albumin (BSA) on DHFR substrate (DHF) and cofactor (NADPH) auto-degradation rates. Degradation rate was monitored over 15 minutes based on absorbance change at 340 nm. Raw values were compared against those of condition 1. Error bars denote standard error (n = 3).

Results indicate that BSA does not interact with or metabolize key kinetic assay reagents.

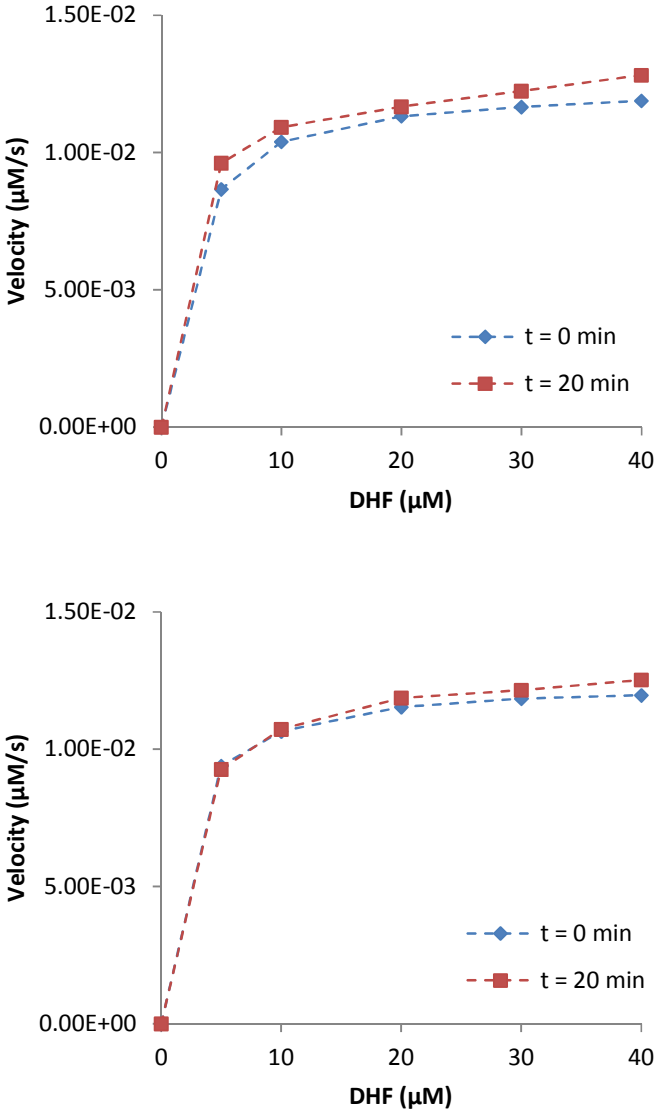

Figure D2. Wild-type DHFR kinetic measurements in the (Top) absence and (Bottom) presence of 0.1 mg/mL bovine serum albumin (BSA) at 0 mins and 20 mins after purification. 5 nM wild-type DHFR was freshly diluted at each time point to minimize incubation time in the diluted 5 nM concentration state. Wild-type DHFR stock concentration was greater than 1 µM. In the absence of BSA, each substrate concentration was measured independently. In the presence of BSA, every substrate concentration was measured concurrently on the same 96-well plate. For this work, n = 1.

Results suggest that degradation of enzyme stock solutions does not occur over the 20 min time period.

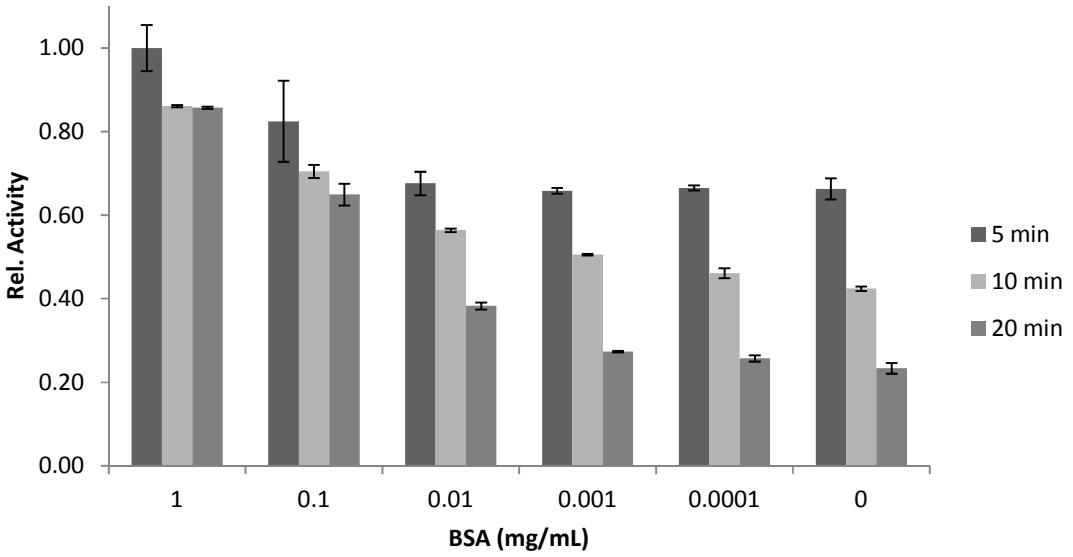

Figure D3. Relative activity of 5 nM wild-type DHFR after fixed incubation times in the presence of varying bovine serum albumin (BSA) concentrations. Activities were compared with that of 5nM DHFR co-incubated with 1 mg/mL BSA for 5 mins. A 20 minute incubation corresponds with the maximum time that sub-micromolar DHFR concentrations are used over the course of a kinetic measurement. Activities were determined at 50 μM DHF and 100 μM NADPH. Measurements at all substrate concentrations were performed concurrently on the same 96-well plate. Error bars denote standard errors (n = 3).

Over time, there is a loss of DHFR activity after dilution. BSA prevents this loss of activity. Since enzyme degradation does not occur in the stock, this suggests that there is an apparent loss of material.

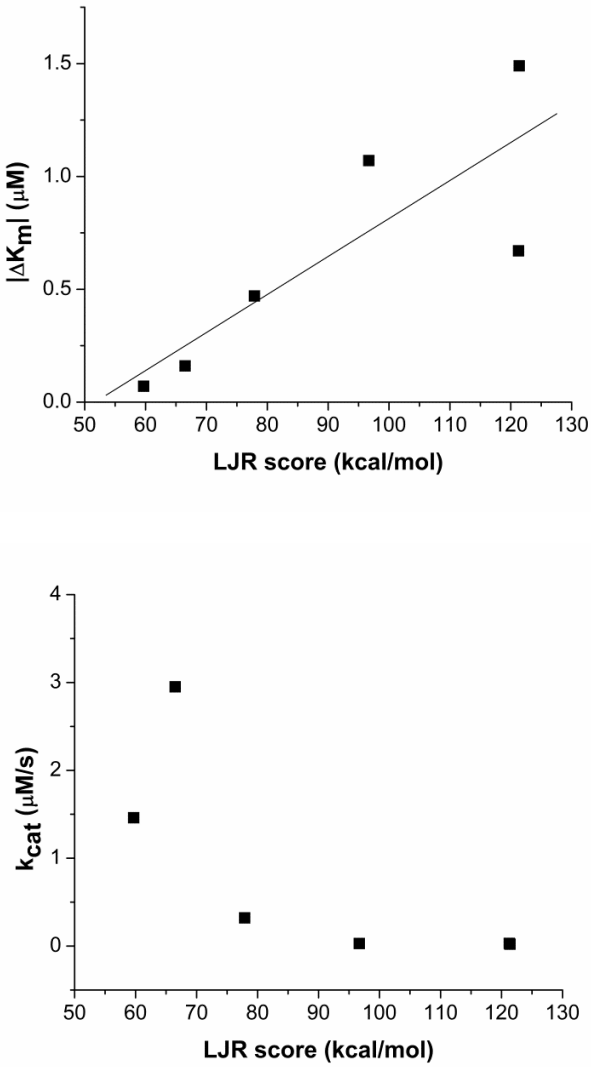

Figure D4. Statistically correlated parameters of mDHFR mutants. A) Statistical correlation between the LJR score and |ΔKm| based on the unpaired, two-tailed, Pearson's correlation constant (r = 0.831; p = 0.041), and B) statistical correlation between the LJR score and k_{cat} based on the two-tailed, unpaired, Spearman rho correlation coefficient (ρ = -0.886; p = 0.019).